Cranfield University

School of Engineering

Thesis submitted for the degree of Doctor of Philosophy

Year of submission: 2009

Richard John Reeves

Demodulation and De-multiplexing of a Fibre Bragg Grating Sensor Array using Volume Holograms

Supervisor: Dr. Stephen James and Prof. Ralph Tatam

Academic Years 2004 to 2009

This thesis is submitted in partial fulfilment of the requirements for the degree of Doctor of Philosophy

Abstract

The demodulation of a Wavelength Division Multiplexed FBG sensor array by a matching array of holograms hosted within a Volume Holographic (VH) material is considered within this thesis. The FBG sensor elements possess separate quiescent wavelengths and operate within different wavelength ranges. The edge of the transfer function of the demodulating holographic element is aligned with the operating range of the matching sensor element. The holographic element then diffracts a fraction of the sensor signal depending on its instantaneous wavelength. The signals from each of the sensor elements are also diffracted through separate angles to matching detectors so de-multiplexing the sensor array.

A scheme using narrow bandwidth holographic transfer functions to demodulate a two element strain sensor array fabricated 4nm apart is reported. The transfer functions and the hysteresis within the PZT actuator, applying the strain, are represented mathematically and used to process results. These are compared with a normalised saw-tooth voltage waveform applied to the PZT to achieve a high Pearson correlation factor of 0.9992. The holograms however possessed poor diffraction efficiency <1% so severely degrading strain resolution. The crosstalk between the sensors' channels is measured as -8.3dB.

The demodulation scheme is intensity based so is susceptible to fluctuations in source intensity and fibre bend losses. An intensity reference scheme is therefore demonstrated using two holograms to demodulate a single FBG strain sensor. The sensor's signal is divided by the two holograms and the intensity of the respective parts recorded on matched photo-detectors. Ratiometric detection is then used to identify changes in applied strain while disregarding fluctuations in source intensity and fibre bend losses. The standard difference over sum equation for ratiometric detection however is modified to take account of the respective holographic transfer functions.

To Theresa

I would like to firstly thank Professor Ralph Tatam for giving me the opportunity to study for a Ph.D. for the use of equipment, laboratory space and for financial support. I would like to thank my supervisor Dr Steve James for invaluable advice and direction, always available to offer a solution to any problem. I would also like to thank him for practical help including endless retuning of the Ti: Sapphire laser and comments on numerous sections of written work. I have gained much from conversations with my fellow students including Dr Daniel Francis and Dr Richard Murphy however specifically I would like to thank Dr Edmund Chehura. This is not only for fabricating FBG sensors and aiding in experimental configuration but for moral support encouraging me to complete this course of study. I would also like to thank Mr Steve Staines for fabricating vital parts at very short notice.

Table of Contents

Acronyms

AOTF Acoustic-Optic Tuneable Filter

APD Avanlanche Photo Diode

ASE Amplified Spontaneous Emission

AWG Array Wave Guide

BPX Broad-band Photodetector

BS Beam Splitter

CCD Charge Coupled Device

CDA Centroid Detection Algorithm

C-PFM Chirped Pulse Frequency Modulation

CTFBG Chirped and Tilted Fibre Bragg Grating

DAQ Data Acquisition Card

DBR Distributed Bragg Reflectors

DCF Dispersion Compensated Fibre

DFB Distributed Feed Back

DTG Drawn Tower Grating

DOE Diffractive Optic Element

EDFA Erbium Doped Fibre Amplifier

FBG Fibre Bragg Grating

FDM Frequency Division Multiplexing

FFP-TF Fibre Fabry-Perot Tunable Filter

FMCW Frequency Modulated Continuous Wave

FP Fabry-Perot

FPF Fabry-Perot Filter

FSR Free Spectral Range

FWHM Full Width Half Maximum

GPIB General Purpose Interface Bus

Hi-Bi Highly Bi-refringent

IM Intensity Modulator

IMG Index Matching Gel

L Lens

LPG Long Period Grating

MEMS Micro Electro Mechanical Systems

MZI Mach-Zender Interferometer

ND Neutral Density (filter)

YAG Yittrium Aluminium Garnet

OPD Optical Path Difference

OSA Optical Spectrum Analyser

PC Personal Computer

PCF Photonic Crystal Fibre

PM Polarisation Maintaining

PSC Polarisation State Controller

PSD Position Sensing Device

PVK Poly (*N*-vinylcarbazole)

PZT Piezo-Electric Transducer

RF Radio Frequency

RF-SA Radio Frequency Spectrum Analyser

RMS Root Mean Square

SA Spectrum Analyser

SDM Spatial Division Multiplexing

SLD Super Luminesent Diode

SM Single Mode

SNR Signal to Noise Ratio

SOA Semiconductor Optical Amplifier

TDM Time Division Multiplexing

TFBG Triangular Fibre Bragg Grating

TG Tracking Generator

UV Ultra Violet

VCO Voltage Controlled Oscillator

VH Volume Holographic

WDM Wavelength Division Multiplexing

ZCP Zero Crossing Point

Chapter 1 Introduction

1.1 Overview of Fibre Bragg Grating Sensor Technology

Fibre based optical sensors have emerged in recent years as a viable alternative to conventional electrical types. The sensors manipulate various aspects of the light transmitted through optical fibres to represent a measurand. Intrinsic properties of the fibre imply the sensors have considerable advantages over their electrical counterparts. For example they are robust, chemically inert, compact and immune to electro-magnetic interference. The sensors can also possess a superior specification for example, an Fibre Bragg Grating (FBG) strain sensor has a linear response from parts per billion to a few percent much greater than conventional strain gauges based on the elasticity of an electrical conductor (Othonos 1999).

Despite possessing numerous advantages optical sensors have not found widespread commercial success. They are still perceived as being costly to implement and difficult to handle and therefore have been limited to low volumes for use within hostile and hazardous environments. Bragg gratings are used, for example, for the monitoring of wind turbines (Ecke *et al.* 2008), structural health in building (Smeu *et al*. 2006) and bridges (Li *et al.* 2006) and transient strain in fuselages (Ecke *et al.* 2001). There has however been joint academic and commercial activity for example in a Norwegian government project strain in the composite hull of a newly commissioned patrol boat is monitored (Wang *et al.* 2001). Other academic studies have demonstrated possibilities for the widespread use of the sensors. For example, the monitoring of a gun barrel (James *et al*. 1999) and the absorption of moisture in concrete (Yeo *et al.* 2006). Recently however there have been reports of a number of novel applications such as the monitoring of wooden frame degradation in items of fine art (Falciai *et al.* 2003), parachute material (El-Sherif *et al.* 2000) whilst in use and ventilatory movements (Wehrle *et al.* 2001) in hospital patients.

FBG sensors are formed in the core of optical fibres by the periodic modulation of the refractive index. The sensor signal is a reflected portion of an illuminating spectrum typically one tenth of a nanometre in width (Othonos 1997). The sensors can detect a number of physical parameters including temperature, strain, and, pressure (Othonos 1999). When applying strain the pitch of the grating changes and therefore the instantaneous wavelength of reflection. When detecting temperature fluctuations the refractive index of the fibre core changes and hence the wavelength of reflection. The measurands are therefore wavelength encoded. In real applications wavelength fluctuations can be associated with changes in both temperature and strain. In this case the de-convolution of temperature and strain becomes necessary (Othonos 1999). When detecting exclusively strain thermal compensation is needed, however in a controlled laboratory environment the temperature can be fixed leading to a linear relationship between applied strain and instantaneous Bragg wavelength.

A standard fibre must be photosensitized before an FBG sensor can be inscribed. This can be achieved by the process of hydrogenation (Lemaire *et al.* 1993), i.e. immersion in a pressurised hydrogen rich environment for periods of a week of more. Photosensitivity can also be enhanced by co-doping with for example Boron that allows a saturated index change 4 times greater than that obtained with pure germanosilicate fibres (Williams *et al* 1993). Illumination from one side of the fibre by an interference pattern allows FBG inscription. A popular method to create an interference pattern is to cross two beams from a coherent source at a point of intersection with the fibre core. This technique allows the quiescent wavelength of the sensor to be changed by altering the angle between the interfering beams (Meltz *et al* 1989), thus changing the pitch of the grating.

Detecting the instantaneous value of the sensor wavelength as it changes with applied measurand is challenging. The wavelength encoded signal has to be demodulated so that the measurand value is represented by an electrical quantity for processing and storage (Kersey *et al.* 1997). An example of a simple demodulation device is an optical edge filter (Melle *et al.* 1993). The wavelength range of the sensor is aligned with either edge of the filter’s transfer function, the transfer function being the filter’s spectral response. As the wavelength of the sensor signal changes from the quiescent value the filter will alter the intensity of the signal beam. The beam intensity then changes with applied measurand and can be detected and represented by an electrical quantity. The demodulation scheme is shown in figure 1.1

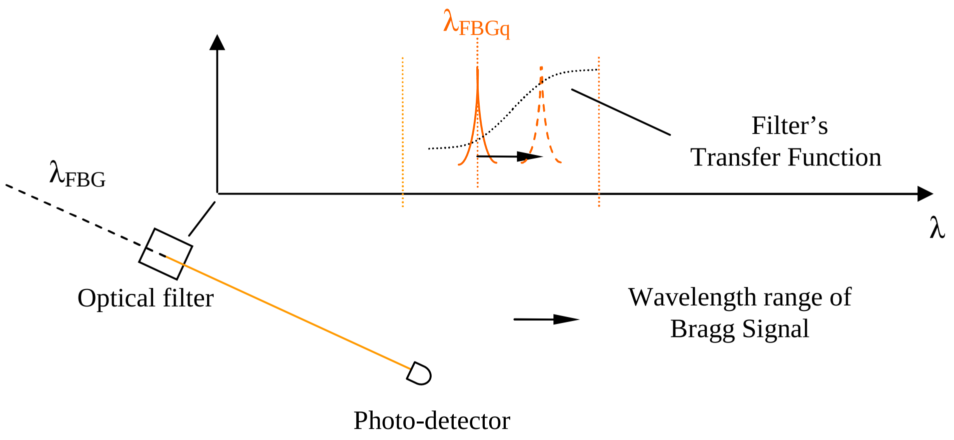

Figure 1.1 An FBG sensor demodulation scheme based on an optical filter. The filter's transfer function will modulate the intensity of the Bragg signal depending on the instantaneous wavelength. The quiescent wavelength of the Bragg signal is given by λ_{FBGq} (Melle *et al.* 1993)

A demodulation scheme for a single FBG sensor can be expensive requiring an optical source, a detector and a means of signal processing and storage (Othonos 1999). Multiplexing techniques allow the use of a single source to demodulate multiple sensors so reducing the cost per sensor of a scheme. An obvious choice is Wavelength-Division-Multiplexing (WDM) (Davis & Kersey 1995). Here each element of a sensor array is fabricated at a different quiescent wavelength and operates within a separate wavelength range. It is possible however to implement other techniques such as Time-Division-Multiplexing (TDM) (Berkoff & Kersey 2003), Frequency-Division-Multiplexing (FDM) (Chan, Jin & Demokan 2000) and Spatial-Division-Multiplexing (SDM) (Rao 1995(a)). The techniques can also be combined for example WDM and TDM (Davis, Bellemore & Kersey 1994), WDM and SDM (Kalli *et al.* 1995), and TDM and SDM (Rao 1995(b)). A means is then required to simultaneously de-multiplex and demodulate elements in the FBG sensor array.

A hologram can be inscribed by creating an interference pattern within the body of a Volume Holographic (VH) material (Kogelnik 1969). For this project a 5mm x 5mm x 5mm cube of photorefractive $BaTiO_3$ is available (Townsend & LaMacchia 1970). The refractive index of a photorefractive material can be changed by the application of an intense light beam. An interference pattern therefore produces a grating within the material by the periodic modulation of the refractive index that is otherwise known as a hologram. The grating, if subsequently illuminated with a single beam that matches the Bragg condition, will diffract a section of the beam (Leith & Upatnieks 1962). If the beam deviates from the Bragg wavelength or angle the diffracted intensity falls. The relationship between the change in angle or wavelength from the Bragg condition and the diffracted intensity is known as the transfer function. An array of holograms can be inscribed, each at a different wavelength and angle within a single block of VH material (Tao, Selviah & Midwinter 1993).

This thesis proposes a WDM FBG sensor array demodulation scheme based on a holographic array. Each element in the sensor array will be matched to an element in the holographic array, each hologram being inscribed at a different angle and wavelength. The transfer function of a hologram (Rakuljic & Leyva 1993) will provide demodulation in a similar way to the wavelength response of an edge filter. The separate sensor signals will be diffracted through different angles so de-multiplexing the array.

The operation of the FBG sensor array holographic demodulation scheme is similar to that of a passive filter and is therefore inexpensive, thermally stable and possesses the potential for high speed. The scheme however is susceptible to bend losses and fluctuations in source intensity. The development of an intensity referencing scheme is therefore a priority. Most importantly however the use of VH material allows the demodulation of a WDM sensor array by a single compact device. This allows the most efficient use of the source power spectrum, which is typically a Super Luminescent Diode (SLD) and can be used with other techniques such as TDM to maximise the number of sensors that can be demodulated by a single scheme.

1.2 FBG Sensor Demodulation Schemes

FBG sensor demodulation by the use of an edge filter is an example of a passive scheme. The intrinsic properties of the device provide the means of demodulation. It is possible however that a narrow optical bandwidth source can be used for demodulation for example a scanning laser. The source can be scanned continuously through a wavelength range and changes in wavelength recorded within each scan (Kersey, Berkoff & Morey 1993). This is an example of active demodulation as an electrical signal requires to be input to the scheme. A single passive edge filter cannot isolate sensor signals fabricated at different quiescent wavelengths. Active scanning techniques however can cover the wavelength ranges of two or more elements within a FBG sensor array so integrating readily with WDM techniques.

Within recently reported demodulation schemes a grating can be used to locate a signal beam from an FBG sensor array at a position on a photo-detector array or matrix (Chen 1997) (Jauregui 2004) (Kiesel *et al.* 2007). The beam then changes position as the signal wavelength varies with the applied measurand. The deviation in position can then be tracked and correlated to a change in wavelength. Beams from elements in a WDM FBG sensor array can be positioned at different locations on a detector matrix so allowing integration with WDM techniques. The resolution of the scheme relies on the ability to determine beam position precisely.

A generic demodulation scheme is shown in figure 1.2. The FBG is illuminated with a broadband source. The Bragg reflection is separated from the illuminating beam by a 3dB coupler as the beam is not present in the return path. The Bragg signal then undergoes demodulation before being incident on a photo-detector. The demodulating device can be a simple edge filter or interferometer. The device can also be a grating that locates the signal beam on a photo-detector array. Alternatively, shown in red a narrowband source is placed within a feed back loop that allows the wavelength changes to be tracked or scanned repeatedly through a range and the changes in wavelength recorded (Putnam *et. al.* 1998).

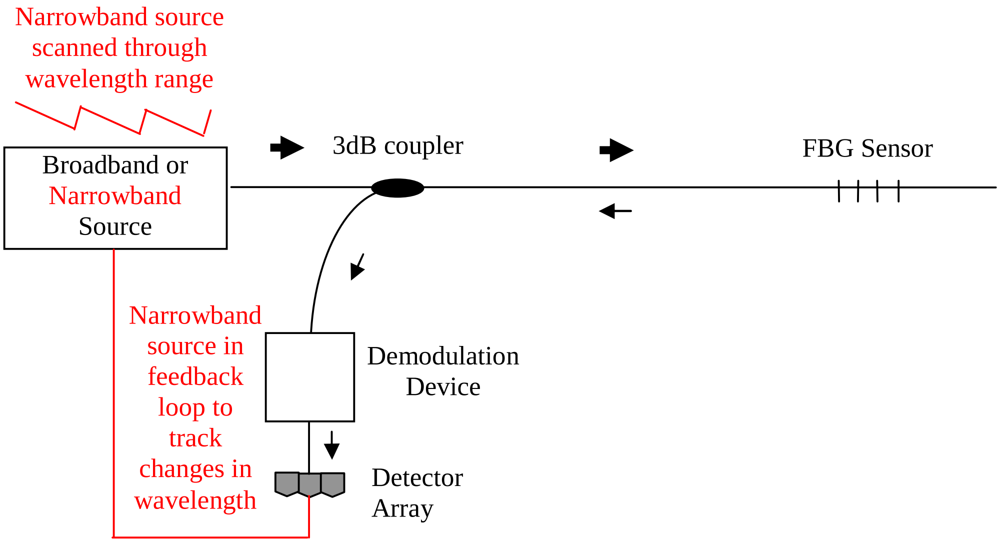

Figure 1.2 Generic Configuration of a single FBG sensor demodulation scheme.

The resolution of the physical quantity measured and the range over which it can be recorded are important factors that can be used when comparing FBG demodulation schemes. Another important factor is the speed of transient as well as qusai-static measurands that can be recorded. All demodulation devices are prone to instability to differing extents for an example an interferometer (Kersey, Berkoff & Morey 1992) possesses a large thermal instability. When comparing demodulation schemes therefore it is important to understand sources of instability and any techniques that can be used to overcome such drawbacks. Modern demodulation schemes should aim for a wavelength resolution of 1pm to resolve temperature and strain to 0.1°C and 1με respectively (Othonos 1999). The resolution being limited by the noise introduced to the sensor signal at the detector. Schemes are also compared on the range of which the mesurands can be taken. Finally as discussed earlier multiplexing techniques can reduce significantly the cost per sensor of a scheme. It is therefore important to understand if a demodulation scheme can readily integrate with any multiplexing techniques (Othonos 1999).

1.3 FBG Sensor Arrays

An FBG sensor array can be fabricated so each element operates within a separate wavelength range. The applicable demodulation scheme must then incorporate wavelength division de-multiplexing techniques. The scheme however will be limited by the optical bandwidth of a broadband source in passive schemes or the sweep width of a scanning device in active schemes. The operating range of each sensor element will then determine the number of elements that can be addressed.

Alternatively an FBG sensor array can be fabricated so each element operates within the same wavelength range. Each element can then be addressed using TDM techniques. Here the sensors are illuminated with a pulsed source. The system is designed so that the reflected pulse from each element arrives at the detector in a dedicated timeslot. Demodulation can then be achieved by a simple edge filter (Cooper & Smith 2003). The technique allows efficient use of the illuminating spectra however the reflectivity of each element is limited so that all sensor elements can be addressed.

A similar technique to TDM is FDM (Chan, Jin & Demokan 2000) where the signals from individual sensors are differentiated by frequency not time. The illuminating source is modulated by a linearly changing frequency so the signals reflected by the sensor elements are modulated in the same manner however there is a difference in instantaneous frequency detected due to time of travel to and from each element. The returning signals are mixed with the source to produce various constant beat frequencies matching each element in the FBG sensor array. FDM offers an advantage over TDM as a signal is detected continuously throughout the modulation cycle.

Logically the most efficient use of a broadband source is achieved by combining both TDM and WDM techniques (Kersey *et al*. 1997) within one demodulation scheme. Here FBG arrays fabricated at the same quiescent wavelength are demodulated using TDM techniques whilst those fabricated at different wavelengths are demodulated using WDM techniques. This will maximise the number of sensor elements that can be addressed.

1.4 The Proposed Demodulation Scheme

This thesis describes a WDM FBG sensor array demodulation scheme based on a holographic array. A holographic element inscribed within a VH material demodulates a matching element in an FBG sensor array in a similar fashion to an edge filter. Here the operating range of the element is aligned with the rising or falling edge of the holographic transfer function. Holograms can be inscribed at different wavelengths so allowing elements in a WDM FBG sensor array to be demodulated. The holograms can also be inscribed at different angles so each elemental signal is diffracted through a different angle toward a dedicated photo-detector, so completing de-multiplexing. Insufficient wavelength or angular separation between elements however will cause crosstalk between channels. The scheme is illustrated in figure 1.3.

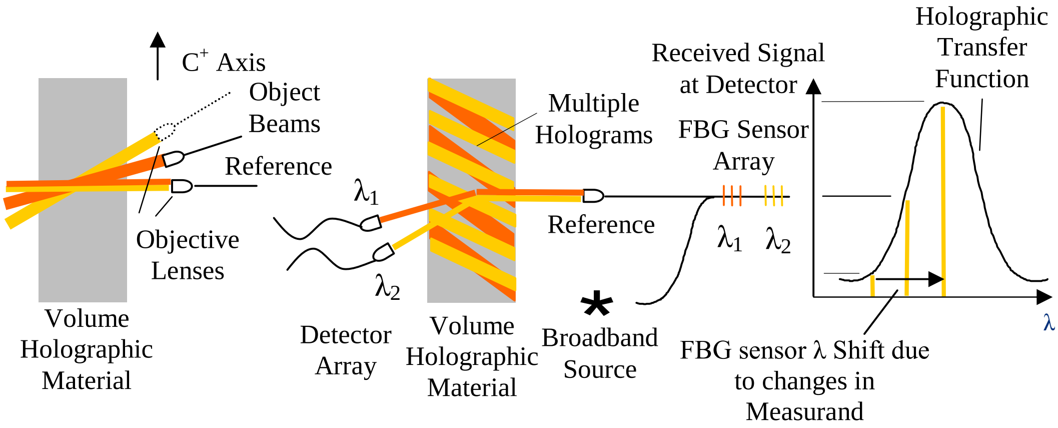

Figure 1.3 The proposed FBG sensor array demodulation scheme.

A hologram is inscribed by crossing two mutually coherent beams an object and a reference to produce an interference pattern within the body of a VH material. The multiple holograms are inscribed by changing the angle and wavelength of the two beams between each inscription. The holographic array de-multiplexes an FBG sensor array as the Bragg angle for different wavelengths varies and corresponds to a matching element in a photo-detector array. Each Bragg element is demodulated by the falling or rising edge of a matching holographic transfer function. (James, Dockney & Tatam 1996). A wavelength span of approximately 4nm is required for the demodulation of a single sensor and an SLD has an optical bandwidth of approximately 40nm the number of elements that can be realistically demodulated is 10 including a reference grating used for intensity referencing.

Many of the FBG sensor array demodulation schemes described above require optical scanning or tracking devices whilst others need pulsed optical sources. The schemes therefore need expensive optical components that can limit the speed of the dynamic response. Further schemes based on interferometers have the potential for high speed but are thermally unstable unless compensation is incorporated. The proposed scheme however has the potential for high speeds and is thermally stable as it is based on holograms that are similar to passive optical filters in operation. The scheme however has the added advantage of being able to demodulate a FBG sensor array in a compact device.

1.5 Polarisation Control

To maximise diffraction efficiency, the polarisation state of the inscribing beams must be controlled precisely. The electrical field vector of the interfering beams has to be within the plane of incidence. The plane of incidence is then to coincide with the c^+ axis, the optical axis within a uniaxial crystal (Ringhofer 1991). This ensures access to the r_{42} electro-optic coefficient and therefore the greatest diffraction efficiency, see section 3 for details.

The polarisation of sensor signals to be diffracted also need to be controlled precisely. The signal beam not only has to meet the Bragg condition for maximum diffraction efficiency but the polarisation has to match that of an inscription beam, with the e-field within the plane of incidence. This again ensures the access to the r_{42} electro-optic coefficient and therefore the greatest diffraction efficiency.

Polarisation control proved to be most challenging as the system for holographic inscription and interrogation is based on standard single mode fibre. Numerous Polarisation State Controllers (PSCs) were required to be placed in various positions throughout the experimental configuration. The polarisation states of beams traversing single mode fibre however, are susceptible to drift so reconfiguration of the PSCs is required before any experiment. This precaution however was still insufficient to ensure success. On many occasions experiments failed during execution due to the drift of the polarisation state. In reality this constraint would make the scheme impractical for real applications.

In an attempt to control polarisation, sensor elements were inscribed within Polarisation Maintaining (PM) fibre. This development however introduced an interferometer whose spectral response under certain conditions interfered with the holographic transfer function in the demodulation sensor signals. It is possible to envisage a scheme that is completely realised in PM fibre. This could lead to practical design that can be used in real applications however such schemes need to be tested and will be more expensive than ones based on single mode fibre.

1.6 Inscription of Multiple Holograms

When inscribing a hologram within a series, the process of inscription partially erases any presently hosted within the crystal (Strasser *et al.* 1989). A hologram takes time to grow to a steady state diffraction efficiency that depends on the total optical power present within the illuminating interference pattern (Solymar & Heaton 1984). The erasure time for a hologram also depends on the intensity of the erasing beam however the two time constants are not the same. This is due to a diffracted portion of the erasure beam interfering with the main portion initially reinforcing the hologram that is to be erased (Solymar 1996). To ensure all holograms in an array have the same diffraction efficiency the inscription and erasure time constants for various intensities are to be established (Strasser *et al.* 1989). A schedule of inscription including inscription times as well as wavelength and angle can then be derived. This requirement is difficult and time consuming and means the scheme is impractical for real applications.

1.7 Ratiometric Detection

Within simple filter demodulation schemes any change in power received is attributed to a change in measurand. Fluctuations in optical source power and fibre bend losses however also cause changes in received power leading to false readings. The scheme proposed within this thesis is based on the simple filter technique and therefore suffers from the same problem.

Ratiometric detection has been used in a number of reported schemes (Davis & Kersey 1994) (Huang et al. 2004) (Fallon et al. 1998) to overcome these drawbacks. Here a Bragg signal is demodulated simultaneously by the negative edge of one filter and the positive edge of another. A difference over sum ratio is then used to derive an output from the two detected intensities. If the change in received intensities is due to source fluctuations or fibre bend losses the ratio remains the same. Any changes in intensity due to wavelength variation in response to an applied measurand imply a change in the ratio.

1.8 Thesis Summary

The purpose of this thesis is to demonstrate that an FBG sensor array can be demodulated by a matching holographic array of gratings. It is important therefore to appreciate how a holographic array is inscribed and interrogated within a VH material such $BaTiO_3$. Central to the process of demodulation is the holographic transfer function. Established theory assumes that the hologram is uniform throughout the crystal. In reality however the inscribing Gaussian beams limit the hologram to a conic volume within the material. It is important to understand how both the Gaussian beam profile and the shape of the conic volume can affect the associated holographic transfer function.

The inscription of a specific hologram will partially erase any already hosted within the crystal. It is therefore important to understand how multiple holograms with the same peak diffraction efficiency can be inscribed.

All elements within the demodulation scheme possess a wavelength dependent response. It is important to understand how this will affect the system response and if it will disturb the demodulation process. A mathematical model of a transfer function is to be established from the inscription variable of a specific hologram. This will allow comparison between theory and experimental results. One objective of the work is to confirm earlier results for the demodulation of one FBG sensor by a single hologram (James *et al* 1996). These possess a 3rd order non-linearity due to the transfer function. The results can therefore be processed by the modelled transfer function to produce linear results. Upon demodulation of a FBG sensor the linearly applied measurand will be compared to the processed results to establish if the scheme can represent accurately a measurand value. Filter based schemes such as these possess the potential for high speed so there is an intention to establish transient performance.

The scheme is intensity based so changes in source intensity or fibre bend losses will be misrepresented as changes in measurand values. It is therefore necessary to incorporate an intensity referencing technique that will be based on ratiometric detection. The noise introduced by the detector causes fluctuation in the received signal and is detrimental to the resolution of the measurand. A review of presently reported demodulation schemes will therefore be presented and their performance compared with the scheme described within this thesis. Finally the scheme incorporates WDM techniques to allow an FBG array to be demodulated. A review of multiplexing techniques when applied to FBG sensor array demodulation also will be presented. Crosstalk between different channels will be reported to assess the performance of this particular aspect.

Chapter 2 describes the development of demodulation schemes. These range from a simple edge filter demodulating a single FBG sensor to high capacity schemes incorporating multiple multiplexing techniques for example WDM and TDM. The types of demodulation devices investigated include specialised filters and interferometers. Studied also are narrow bandwidth lasers or filters that demodulate by tracking wavelength changes or scanning a sensor's wavelength range. An emerging class of demodulator based on positional tracking of a signal beam with changes in wavelength is also described. The chapter describes other multiplexing techniques to allow the demodulation of FBG sensor arrays. These include WDM, TDM, FDM, and SDM. The chapter concludes with a comparison of the demodulation and de-multiplexing techniques.

Chapter 3 outlines the theory applicable to the proposed demodulation scheme. The chapter outlines holographic inscription and interrogation within photorefractive materials. Of particular interest is the use of Gaussian beams and their effect on the holographic transfer function. Holographic inscription and erasure times are discussed as an array inscription schedule is required to ensure all holograms possess the same diffraction efficiency.

Chapter 4 outlines the demonstration results of the proposed scheme. Primarily the spectral response of the demodulation system is discussed including the effect introduced by PM fibre. Ratiometric detection is described and how the basic difference over sum equation is modified to include the non-linearities within the holographic transfer function. The chapter then goes on to verify results previously obtained for the demodulation of an FBG sensor by a single hologram. Experiments are also described that characterise a single or multiple holograms to be used for demodulation. Inscription and erasure time constants are then established so a that schedule of holographic inscription can be derived. Factors affecting the wavelength response of the scheme are also discussed. The demodulation of an FBG sensor array is then described. Finally ratiometric detection is demonstrated using a modified difference over sum equation specifically derived to process readings from the scheme.

Chapter 5 summarises the experimental results in comparison to recently reported demodulation schemes. Progress in mathematical modelling is also summarised. The chapter then makes recommendations to improve results and allow a stable inexpensive system to be developed. Here the use of mixed de-multiplexing schemes are discussed specifically WDM and TDM. A recommendation to integrate that demonstrated with SDM techniques using a Charge Coupled Device (CCD) camera is also outlined. Finally conclusions are drawn about the scheme detailed and its potential to meet future requirements of sensor demodulation systems.

1.9 References

Chan, P.K.C., Jin, W. & Demokan, M.S. 2000, "FMCW multiplexing of fiber Bragg grating sensors", *IEEE Journal on Selected Topics in Quantum Electronics,* vol. 6, no. 5, pp. 756-763.

Chen, S. 1997, "Digital spatial and wavelength domain multiplexing of fibre Bragg grating based sensors", *Proceeding of the Optical Fibre Sensors Conference (OFS-12),* pp. 448-461.

Cooper, D.J.F. & Smith, P.W.E. 2003, "Simple high-performance method for large-scale time division multiplexing of fibre Bragg grating sensors", *Measurement Science and Technology,* vol. 14, no. 7, pp. 965-974.

Berkoff, T.A., & Kersey, A.D. 2003, "Simple high-performance method for large-scale time division multiplexing of fibre Bragg grating sensors", *Measurement Science and Technology,* vol. 14, no. 7, pp. 965-974.

Davis, M.A., Bellemore, D.G, and Kersey, A.D. 1994, "Structural strain mapping using a wavelength/time division addressed fibre Bragg grating array", Second European Conference on Smart Structures and Materials, Glasgow, Scotland, pp. 342-345.

Davis, M.A. & Kersey, A.D. 1995, "Matched-Filter Interrogation Technique for Fiber Bragg Grating Arrays", *Electron. Lett.,* vol. 31, no. 10, pp. 822-823.

Davis, M.A. & Kersey, A.D. 1994, "All-Fiber Bragg Grating Strain-Sensor Demodulation Technique using a Wavelength-Division Coupler", *Electron. Lett.,* vol. 30, no. 1, pp. 75-77.

Ecke, W., Grimm, S., Latka, I., Reutlinger, A. & Willsch, R. 2001, "Optical fiber grating sensor network basing on high-reliable fibers and components for spacecraft health monitoring", *Proc. SPIE Int. Soc. Opt. Eng.,* vol 4328.

Ecke, W. & Schroder, K. 2008, "Fiber Bragg grating sensor system for operational load monitoring of wind turbine blades", *Proc. SPIE Int. Soc. Opt. Eng.,* vol 6530.

El-Sherif, M., Fidanboylu, K., El-Sherif, D., Gafsi, R., Yuan, J., Richards, K. & Lee, C. 2000, "A novel fiber optic system for measuring the dynamic structural behavior of parachutes", *J. Intell. Mater. Syst. Struct.,* vol. 11, no. 5, pp. 351-359.

Falciai, R., Trono, C., Lanterna, G. & Castelli, C. 2003, "Continuous monitoring of wooden works of art using fiber Bragg grating sensors", *Journal of Cultural Heritage,* vol. 4, no. 4, pp. 285-290.

Fallon, R.W., Zhang, L., Everall, L.A., Williams, J.A.R. & Bennion, I. 1998, "All-fibre optical sensing system: Bragg grating sensor interrogated by a long-period grating", *Measurement Science and Technology,* vol. 9, no. 12, pp. 1969-1973.

Huang, R., Zhou, Y., Cai, H., Qu, R. & Fang, Z. 2004, "A fiber Bragg grating with triangular spectrum as wavelength readout in sensor systems", *Optics Communications,* vol. 229, no. 1-6, pp. 197-201.

Jauregui, C. 2004, "Interrogation of fibre Bragg gratings with a tilted fibre Bragg grating", *Measurement Science and Technology,* vol. 15, no. 8, pp. 1596-1600.

James, S.W., Dockney, M.L. & Tatam, R.P. 1996, "Photorefractive volume holographic demodulation of in-fiber Bragg grating sensors", *IEEE Photonics Technology Letters,* vol. 8, no. 5, pp. 664-666.

James, S.W., Tatam, R.P., Fuller, S.R. & Crompton, C. 1999, "Monitoring transient strains on a gun barrel using fibre Bragg-grating sensors", *Measurement Science and Technology,* vol. 10, no. 2, pp. 63-67.

Kalli, K., Brady, G.P., Webb, D.J., Jackson, D.A., Zhang, L. & Bennion, I. 1995, "Wavelength-division and spatial multiplexing using tandem interferometers for Bragg grating sensor networks", *Opt. Lett* , vol. 20, no. 24, pp. 2544-2546.

Kersey, A.D., Berkoff, T.A. & Morey, W.W. 1993, "Multiplexed Fiber Bragg Grating Strain-Sensor System with a Fiber Fabry-Perot Wavelength Filter", *Opt. Lett.,* vol. 18, no. 16, pp. 1370-1372.

Kersey, A.D., Berkoff, T.A. & Morey, W.W. 1992, "High-Resolution Fiber-Grating Based Strain Sensor with Interferometric Wavelength-Shift Detection", *Electron. Lett.,* vol. 28, no. 3, pp. 236-238.

Kersey, A.D., Davis, M.A., Patrick, H.J., LeBlanc, M., Koo, K.P., Askins, C.G., Putnam, M.A. & Friebele, E.J. 1997, "Fiber grating sensors", *Journal of Lightwave Technology,* vol. 15, no. 8, pp. 1442-1462.

Kiesel, P., Schmidt, O., Johnson, N., Mohta, S., 2006, "Compact, low cost, and high resolution interrogation unit for optical sensors", *Applied Physics Letters,* vol 89. pp 237-240.

Kogelnik, H.. 1969, "Coupled wave theory for thick hologram gratings ", *Bell System Tech J,* vol. 48, no. 9, pp. 2909-2947.

Leith, E.N. & Upatnieks, J. 1962, "Reconstructed wave-fronts and communication theory", *J. Opt. Soc. Am,* vol. 52, pp. 1377.

Lemaire, P.J., Atkins, R.M., Mizrahi, V. & Reed, W.A. 1993, "High-Pressure H-2 Loading as a Technique for Achieving Ultrahigh UV Photosensitivity and Thermal Sensitivity in Geo2 Doped Optical Fibers", *Electron. Lett.,* vol. 29, no. 13, pp. 1191-1193.

Li, H., Ou, J., Zhao, X., Zhou, W., Li, H., Zhou, Z. & Yang, Y. 2006, "Structural health monitoring system for the Shandong Binzhou Yellow River Highway Bridge", *Computer-Aided Civil and Infrastructure Engineering,* vol. 21, no. 4, pp. 306-317.

Melle, S.M., Alavie, A.T., Karr, S., Coroy, T., Liu, K.X. & Measures, R.M. 1993, "A Bragg Grating-Tuned Fiber Laser Strain Sensor System", *IEEE Photonics Technology Letters,* vol. 5, no. 2, pp. 263-266.

Meltz, G., Morey, W. W., Glen, W. H. 1989, "Formation of Bragg gratings in optical fibres by a transverse holographic method", *Opt. Lett.,* vol. 14, pp. 823-825.

Othonos, A. 1997, "Fiber Bragg gratings", *Rev. Sci. Instrum.,* vol. 68, no. 12, pp. 4309-4341.

Othonos, A. 1999, *Fiber Bragg gratings : fundamentals and applications in telecommunications and sensing,* Artech House, Boston, Mass. ; London.

Putnam, M. A., Dennis, M. L., Duling, I. N., Askins, C. G. and Friebele, E. J. (1998), "Broadband square-pulse operation of a passively mode-locked fiber laser for fiber Bragg grating interrogation", *Optics Letters,* vol. 23, no. 2, pp. 138-140.

Rakuljic, G.A. & Leyva, V. 1993, "Volume holographic narrow-band optical filter", *Opt. Lett.,* vol. 18, no. 6, pp. 459-461.

Rao, Y.J., *et al.*, 1995, "Spatially-multiplexed fibre-optic Bragg grating strain and temperature sensor based on interferometric wavelength-shift detection", *Electron. Lett.,* Vol 31, pp. 1009-1010.

Rao, Y.J., *et al.*, 1995, "Combined spatial- and time-division-multiplexing scheme for fibre grating sensors with drift compensated phase-sensitive detection", *Optics Letters.,* Vol. 20, pp 2149-2151.

Ringhofer, K.H., Tao, S., Takacs, J. & Solymar, L. 1991, "The role of the longitudinal component of the electric field vector in two-wave mixing in photorefractive $BaTiO_3$", *Applied Physics B Photophysics and Laser Chemistry,* vol. 52, no. 4, pp. 259-261.

Smeu, E., Gnewuch, H., Jackson, D.A. & Podoleanu, A. 2006, "High dynamic range, temperature compensated fibre Bragg gratings sensor for structural monitoring of buildings", *Proc. SPIE Int. Soc. Opt. Eng.,* vol 6345

Solymar, L. 1996, *The physics and applications of photorefractive materials,* Clarendon Press, Oxford.

Solymar, L. & Heaton, J.M. 1984, "Transient energy transfer in photorefractive materials; An analytic solution", *Optics Communications,* vol. 51, no. 2, pp. 76-78.

Strasser, A.C., Maniloff, E.S., Johnson, K.M. & Goggin, S.D.D. 1989, "Procedure for Recording Multiple-Exposure Holograms with Equal Diffraction Efficiency in Photorefractive Media", *Opt. Lett.,* vol. 14, no. 1, pp. 6-8.

Tao, S., Selviah, D.R. & Midwinter, J.E. 1993, "Spatioangular multiplexed storage of 750 holograms in an Fe:LiNbO3 crystal", *Opt. Lett.,* vol. 18, no. 11, pp. 912-914.

Townsend, R.L. & LaMacchia, J.T. 1970, "Optically induced refractive index changes in $BaTiO_3$", *Journal of Applied Physics,* vol. 41, no. 13, pp. 5188-5192.

Wang, G., Pran, K., Sagvolden, G., Havsgard, G.B., Jensen, A.E., Johnson, G.A. & Vohra, S.T. 2001, "Ship hull structure monitoring using fibre optic sensors", *Smart Materials and Structures*, vol. 10, no. 3, pp. 472-478.

Wehrle, G., Nohama, P., Kalinowski, H.J., Torres, P.I. & Valente, L.C.G. 2001, "A fibre optic Bragg grating strain sensor for monitoring ventilatory movements", *Measurement Science and Technology,* vol. 12, no. 7, pp. 805-809.

Williams, D.L. 1993, "Enhanced UV photosensitivity in boron co-doped germanosilicate fibres", *Electronic Letters,* vol. 29, pp. 45-47.

Yeo, T.L., Cox, M.A.C., Boswell, L.F., Sun, T. & Grattan, K.T.V. 2006, "Optical fiber sensors for monitoring ingress of moisture in structural concrete", *Review of Scientific Instruments,* vol. 77, no. 5, pp178-180.

Chapter 2 A review of FBG Sensor Demodulation and De-multiplexing Schemes

2.1 Introduction

The discovery of photosensitivity (Hill *et al.* 1978) within optical fibre has been a catalyst for considerable improvements in both telecommunication (Reekie *et al.* 1985) and sensing (Meltz *et al.* 1991) technology. The core of a photosensitised fibre demonstrates a permanent change in refractive index when illuminated with UV radiation. A Fibre Bragg Grating is formed by a periodic change in refractive index of the fibre core that allows the reflection of a narrow bandwidth section of an illuminating spectrum. The wavelength of reflection can be changed by the application of a measurand such as temperature or strain (Othonos 1999). The FBG demonstrates a linear response to an applied measurand over a wide range. The reflection of a narrow bandwidth is also useful in the selection of one channel of many transmitted within a Wavelength Division Multiplexed (WDM) telecommunication system (Bilodeau *et al.* 1995).

The introduction of dopants (Bilodeau *et al.* 1993) in small quantities during fabrication will allow the production of a photosensitised fibre. A standard fibre however can be photosensitised by the process of hydrogenation (Lemaire *et al.* 1993). Here the fibre is immersed in a hydrogen rich environment under pressure for a week or more. Hydrogen molecules diffuse into the core of the fibre and react with the glass. The process is known to increase the number of GeO defect centres (Awazu, Kawazoe & Yamane 1990). These are an optically absorbing species that can be bleached by UV illumination. The change in refractive index is linked to a change in absorption by the Kramer-Kronig principle (Williams *et al*. 1992).

A periodic change in refractive index and therefore the fabrication of an FBG can be achieved by illuminating the fibre core with an interference pattern. The pattern is created by splitting the amplitude (Meltz *et al* 1989) or wave-front (Kashyap *et al.* 1990) output from a coherent source and enabling the two sections to interfere. A two beam interferometer is a popular device for the inscribing of FBGs (Meltz *et al* 1989). Here a beam splitter creates two beams from the output of UV laser. The respective beams are then crossed by two tuning mirrors at a point of intersection with the fibre to produce an interference pattern. Cylindrical lenses are used to focus the beams on to the fibre core. The scheme is detailed in figure 2.1.

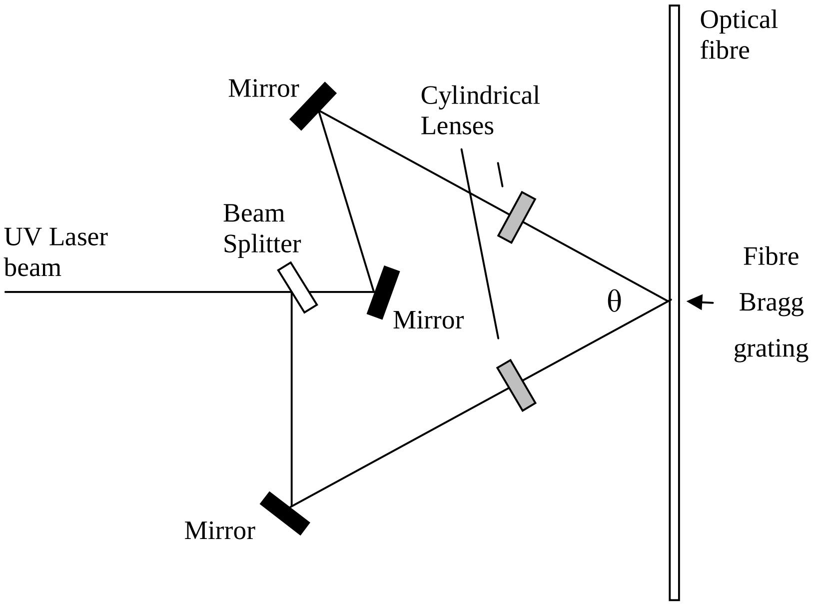

Figure 2.1 A two beam interferometer used to inscribe an FBG in an optical fibre. A beam splitter creates two beams from the same coherent source. Two mirrors cross the respective beams at a point of intersection with the fibre core to produce an interference pattern. The cylindrical lenses are used to focus beam intensity on to the fibre core (Meltz *et al* 1989).

This scheme ensures an equal number of reflections in each interferometer path, from the beam splitter to the point of interference on the fibre. The equal number of reflections eliminates different lateral orientations to allow high quality interference patterns. Unequal number of reflections in each path causes wave-front reversal of one beam with respect to the other resulting in a poor interference pattern. The Bragg wavelength of the of the FBG can be expressed in terms of the inscribing wavelength (Othonos 1999)

$$\lambda_B = \frac{n_{eff}\lambda_i}{\sin\theta} \qquad \textbf{2.1}$$

where λ_B is the quiescent Bragg wavelength, n_{eff} the effective refractive index of the fibre core, λ_i is the wavelength of inscription and θ is the half angle between the beams. The Bragg wavelength can then be changed by either altering the wavelength or half angle of inscription.

The technique can inscribe gratings at different quiescent Bragg wavelengths. The length of the FBG can also be shortened or extended allowing the widening or narrowing of the reflection spectrum respectively. The technique however is susceptible to submicron displacement during the inscription process in optical components such as mirrors and lenses. This will cause a drift in the fringe pattern so FBG inscription becomes problematic.

An alternative is to use a wave-front splitting interferometer based on a Lloyd mirror (Limberger *et al.* 1993) or a prism (Kashyap *et al.* 1990). Only one optical component is required reducing sensitivity to mechanical vibration. The physical arrangement of the interferometer however limits the quiescent Bragg wavelength tuning range.

A phase mask is a Diffractive Optical Element (DOE) that consists of a one dimensional relief pattern etched into a surface of a fused silica block. The pattern is regular with a period Λ. The profile of the surface-relief grating is chosen to suppress the zero order diffracted beam to ~3%. The plus and minus first order beams are maximised approximately to 30-35% and are used to form the interference pattern for grating inscription (Hill *et al.* 1993). The phase mask is placed in close proximity to or touching the fibre, the period of the grating created is one half that of the phase mask (Λ/2).

The use of a phase mask can greatly reduce the complexity of an FBG fabrication scheme as no beam splitting is required and is mechanically stable as only one optical element is used. The phase mask is fabricated with electron beam lithographic techniques so complex patterns and therefore reflection spectra can be formed. However, it is designed to inscribe at one Bragg wavelength only (Othonos 1999).

An FBG can be created point-by-point by (Malo *et al.* 1993) illuminating the fibre core with a single pulse of light. A translation stage then displaces the position of the point a distance equal to one period of the grating along the axis of the fibre before the core is again illuminated.

The point by point technique is flexible as the grating structure is built up over time. This allows the quiescent Bragg Wavelength and spectral response to be pre-determined as the grating pitch and length can be accurately fabricated. Chirped gratings can be formed by linearly changing consecutive pitch lengths. Complex reflection patterns can be achieved by altering the inscribing beam intensity between points. The technique however is long and tedious to implement and therefore is subject to thermal perturbations that vary pitch length. A major limitation is the requirement for high power objective lenses, the focusing has to be precise or the inscribed point will not be at the desired location. Moreover the spot size of the focused beam limits the grating period that can be inscribed. The point by point technique is therefore mainly used in the fabrication of Long Period Gratings. These are applicable to higher wavelength ranges approximately 1500nm and possess different reflection and transmission characteristics than standard FBGs (James 2006). The technique however has been used in the fabrication of grating with a shorter wavelength of reflection (Jonvanovic *et al* 2007).

An FBG consists of a periodic modulation typically of the order of 10^{-4} of the refractive index within the core of a fibre (Othonos 1999). The grating planes are perpendicular to the fibre axis and generally possess a constant period. An exception is a chirped grating where the period changes throughout length of the FBG. A range of wavelengths are therefore reflected from different sections of the FBG. A small amount of light traversing the fibre will be reflected by each plane due to the change in refractive index. The reflected light will constructively interfere to produce a narrow bandwidth signal centred at a specific wavelength. This wavelength is known to match the Bragg condition of the FBG. The operation of an FBG is shown in figure 2.2.

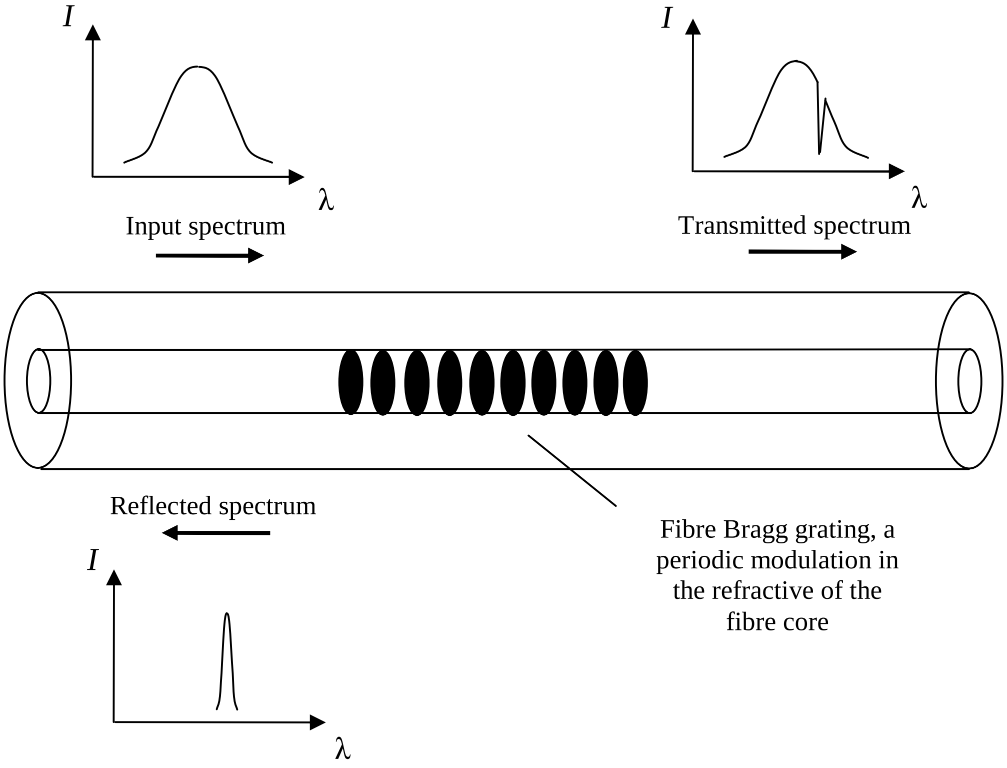

Figure 2.2 The operation of Fibre Bragg Grating.
The input broadband source spectrum is shown. The transmission spectrum demonstrates a gap at the Bragg wavelength as this reflected. The reflection spectrum is also shown (Othonos 1999).

At the Bragg condition the reflected light satisfies both energy and momentum conservation. Energy conservation requires the frequency of the reflected light to equal that of the incident. The conservation of momentum requires the wave-vector of the reflected light to equal that of the incident plus the grating wave-vector. The wave-vectors can be related to the grating period by equation 2.2 (Othonos 1999).

$$\mathbf{k}_i + \mathbf{K} = \mathbf{k}_r \tag{2.2}$$

Where $\mathbf{k}_i$ and $\mathbf{k}_r$ are the incident and reflected wave-vectors respectively and $\mathbf{K}$ is the grating-vector of the FBG. The reflected wave-vector however must be equal in magnitude but opposite in direction to the incident so equation 2.2 simplifies to the Bragg condition.

$$\lambda_{\mathrm{B}} = 2n_{\mathrm{eff}}\Lambda \tag{2.3}$$

where λ_B is the Bragg wavelength and Λ the grating period. The value n_{eff} is the effective refractive index of the fibre core at the free space wavelength.

The physical constants of a fibre can be changed by varying the fibre's environment. For example the thermal-optic coefficient governs the change in the effective refractive index n_{eff} of the fibre core with temperature. From equation 2.3 however the Bragg wavelength is related to the effective refractive index. The dimensions of the fibre will change with temperature due to the thermal coefficient of expansion. This will alter the grating period Λ. The FBG is therefore a temperature sensor where the measurand is wavelength encoded. A FBG can also act as a strain sensor as both the effective refractive index of the core and the grating period can be changed by stretching the fibre. Optical fibres are durable and possess a high temperature tolerance so can therefore detect measurands over an extended range. Importantly the sensors demonstrate a linear response to the measurand over this range.

A simple demodulation device is an optical filter where the edge of the filter's transfer function is aligned with the wavelength range of operation of the FBG sensor. The edge is a linear section of the transfer function of the filter which might lie either side of its transmission peak. The optical power transmitted through the filter changes depending on the value of the transfer function at the instantaneous Bragg wavelength. A photo-detector then produces an electrical signal proportional to the transmitted optical power and therefore the change in applied measurand (Kersey *et al.* 1997). The filter does not demodulate the Bragg signals outside the wavelength range of its transfer function. Filter based schemes therefore integrate poorly with Wavelength-Division-Multiplexed (WDM) sensor arrays. The filter however can demodulate sensor signals operating in the same wavelength range so integrate readily with Time-Division-Multiplexed (TDM) sensor arrays (Cooper & Smith 2003). The electrical signal received at the photo-detector will possess a component of noise. This represents high speed fluctuations in the measurand signal and will therefore limit resolution (Rao 1997). This demodulation scheme is passive as the filter's transfer function is not altered throughout the demodulation process. Passive schemes such as this have the potential for high bandwidth the limiting factor being the speed of the photo-detector. Currently available photo-detectors can operate within Giga-hertz range (Agethen *et al.* 2002). A high speed photo-detector however will increase the amount of noise received and degrade the resolution in comparison to a limited bandwidth detector. The operation of a passive filter demodulation scheme is outlined in figure 2.3(a).

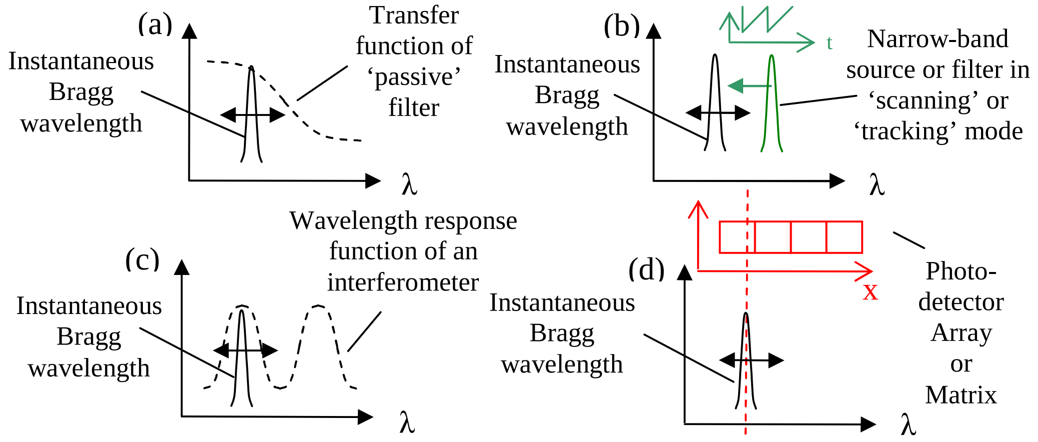

Figure 2.3 Different FBG sensor demodulation schemes
(a) A passive filter demodulation scheme. The transfer function of the filter modulates beam intensity depending on instantaneous Bragg wavelength. (b) An active filter or source demodulation scheme. A wavelength range is swept to determine Bragg wavelength or the device is used within a feedback loop to track the instantaneous value. (c) Demodulation scheme based on an interferometer. Output intensity depends on the state of interference at the Bragg wavelength. (d) A demodulation scheme using a photo-detector array. The position of the beam impinging on a detector array depends on instantaneous Bragg wavelength modified from (Othonos 1999).

Alternatively, a tuneable narrowband filter can be used for demodulation. This scheme is termed active as the filter's parameters are changed, usually by mechanical means, during the demodulation process. The filter can be scanned through a wavelength range to establish the instantaneous Bragg wavelength as a function of time. This is achieved by recording the peak value of the transmitted intensity at a particular position within a scan cycle, the position is then correlated to a wavelength. The scan can cover the different wavelength ranges associated with multiple sensors so readily integrates with WDM sensor arrays. The tuneable filter may also be deployed within a feedback loop and the instantaneous Bragg wavelength tracked. Multiple filters can be used to track multiple sensors operating in different wavelength ranges so a tracking filter scheme can readily integrate with WDM sensor arrays (Kersey, Berkoff & Morey 1993). Active schemes have a bandwidth that is limited to the scan repetition rate or the reaction time of the feedback loop (Rao 1997) and are more complex and expensive than their passive counterparts. A standard active filter is not designed to quickly locate wavelengths in the same wavelength range so therefore poorly integrates with TDM sensor arrays (Othonos 1999).

Instead of using a narrow band filter to scan the optical spectrum, a tuneable narrow band source can be deployed within an active demodulation scheme. Commercially available tuneable semiconductor lasers are available. However the bandwidth of these schemes is limited by the scan rate of the laser (Coroy *et al* 1997). The operation of an ‘active’ demodulation scheme is outlined in figure 2.3(b).

A two beam interferometer is another optical device that can be used within a demodulation scheme. The interferometer divides by amplitude a single beam from the same coherent source into two, the output being dependent on the phase difference introduced by the Optical Path Difference (OPD) between the two beams formed. If the paths are of different lengths the phase difference can also be changed by altering the source wavelength. An interferometer can detect maximum phase changes of $\pm\pi$ between constructive interference peaks that correlates to a wavelength span known as the Free Spectral Range (FSR). For a demodulation scheme based on an interferometer the FSR is the maximum detectable wavelength span and is therefore known as the unambiguous range (Kersey *et al.* 1997). The interferometer is at its most sensitive when in quadrature. However, small changes in device temperature will cause the loss of this condition. This means that a two path interferometer can only be used to demodulate dynamic measurands without thermal compensation (Kersey, Berkoff & Morey 1993). Interferometers are inexpensive and allow high bandwidths as no tracking or scanning is required. Multiple interferometers can be used to demodulate sensors operating in different wavelengths so the schemes readily integrate with WDM sensor arrays (Kalli *et al.* 1995). The output of an interferometer, if monitored by a high speed detector can differentiate sensors working at the same wavelength but allocated a different time slot. Interferometer based demodulation schemes therefore readily integrate to TDM sensor arrays (Weis, Kersey & Berkoff 1994). The use of an interferometer as a demodulation device is outlined in figure 2.3(c).

There is a class of demodulator emerging where the wavelength shift is translated into a positional change of a beam impinging on a photo-detector array or matrix. Sensors operating in different wavelength ranges can locate to different positions on the photo-detector array or matrix. The schemes therefore readily integrate to WDM sensor arrays (Chen *et al* 1997). Sensors operating in the same wavelength range however would locate to the same approximate location on the surface of the photo-detector array or matrix. The scheme would therefore not readily integrate to a TDM sensor array. The bandwidth of a scheme is dependent on the integration time of the photo-detector array or matrix (Chen *et al* 1997). The operation of these schemes is outlined in figure 2.3(d).

Simple filter and interferometer based demodulation schemes are inexpensive and possesses the potential for high speed in comparison to those based on active sources and filters as no complex optical components are required. Both however are intensity based and therefore require intensity referencing techniques to overcome fluctuations in source intensity and fibre bend losses. Interferometer based schemes are also unstable and require thermal compensation to detect quasi-static measurands. In general the resolution of the two schemes approach and in some cases exceeds that of 1με for strain and 0.1ºC for temperature. An interferometer is also a more sensitive device resulting in a range to resolution figures of 10^3-10^4 whilst the figures for a filter based techniques are 10^2-10^3. The resolution figures for active schemes are not as good as those possessed by passive ones and can be in the worst case 10με for strain and 1ºC for temperature. The resolution of however can be improved dramatically by the use of Centroid Detection Algorithms (CDAs) that locate a peak in a sensor signal precisely. The range figures for the active schemes reflect the narrow bandwidth components used and are 10^3-10^4 for filter and 10^3-10^5 for active source techniques. Finally the resolution of schemes that deflect a signal beam across a photo-detector array or matrix tend to be marginally better than 1με for strain and 0.1ºC for temperature however these also need a Centroid Detection Algorithm to achieve such levels. The resolution depends on the intensity of the sensor signal and therefore can be enhanced by powerful sources and FBGs of high reflectivity. These however do not need intensity referencing and are inexpensive as they are based on CCD devices.

The requirements of a particular application have to be considered when choosing the type of demodulation scheme. Passive filter schemes are suitable for high speed single sensor demodulation applications whilst scanning source or filter schemes are suitable for slower applications that require WDM sensor arrays to be demodulated. Interferometers without thermal compensation are more suitable for dynamic measurements. The particular scheme chosen then has attributes that have consequences for the range and resolution of the specific measurand. For simple filter demodulation scheme there is a trade off between speed and resolution, manifesting as noise at the photo-detector. For scanning filter or source schemes the range depends on the wavelength span of the device.

The most widely used multiplexing technique is Wavelength Division Multiplexing (WDM). Here each element in a FBG sensor array is fabricated at a different quiescent Bragg wavelength and operates within a separate wavelength range. Consecutive ranges are separated by a stop-band that limits crosstalk between different channels. The number of elements that can be addressed is limited by the bandwidth of the illuminating source or the tuning range of the demodulating device (Davis & Kersey 1995). Within Time Division Multiplexing (TDM) the FBGs can use the same quiescent Bragg wavelength and operate within the same wavelength range. The FBG elements however are separated physically by a sufficient distance to ensure the returning pulses do not overlap (Weis, Kersey & Berkoff 1994). For a 10ns pulse separation this would correspond approximately to a distance of 1m. The Bragg signals then arrive at the detector within allocated time-slots. As the FBGs operate within the same wavelength range, Bragg signals can experience multiple reflections. These signals then arrive at the detector in a time-slot allocated to another sensor and so represent crosstalk. Crosstalk will increase with number of FBG sensors limiting the number of elements that can be addressed. The effects of crosstalk can be limited by reducing reflectivity of sensor elements so increasing the number of elements that can be addressed (Wilson, James & Tatam 2001).

The different multiplexing schemes are summarised in figure 2.4.

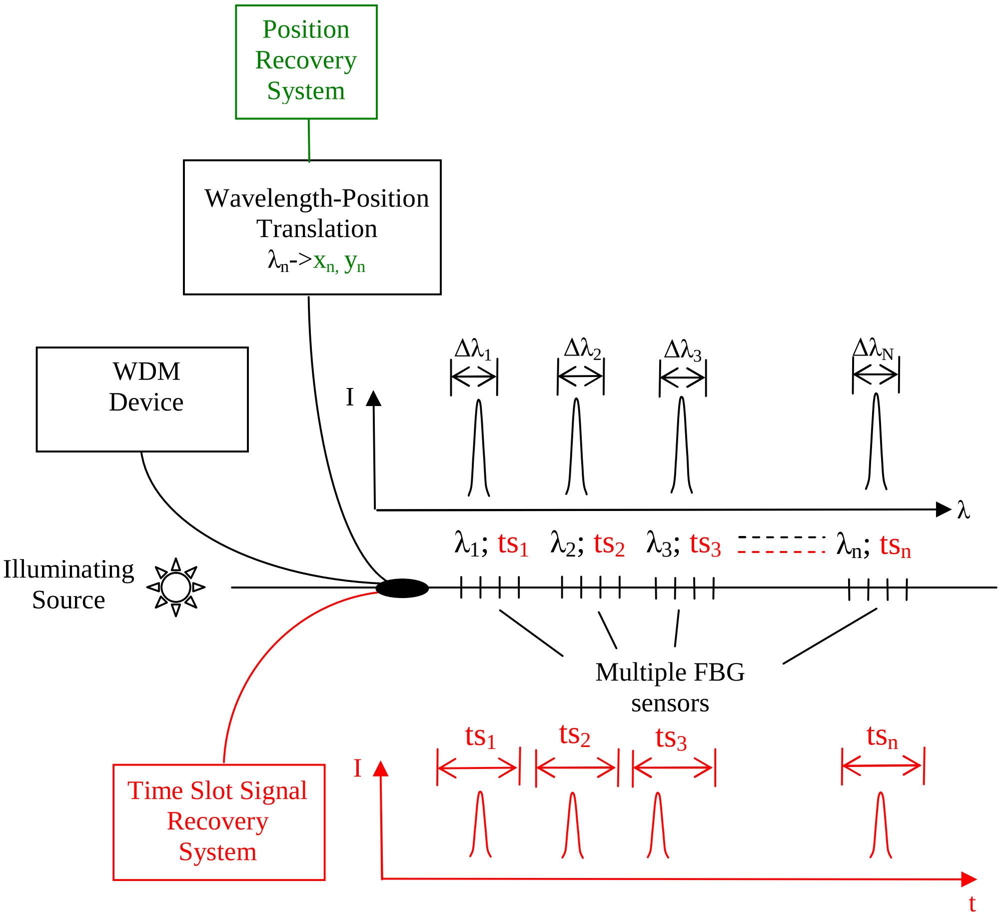

Figure 2.4 Different FBG sensor array multiplexing techniques.
(-) Wavelength Division Multiplexing (WDM). Each element in a FBG sensor array is fabricated at a different quiescent Bragg wavelength and operates within a separate wavelength range. (-) Time Division Multiplexing (TDM). The reflected Bragg signals are separated in time as the round trip delay to each element is different. (-) Combined Wavelength Division Multiplexing and Spatial Division Multiplexing (WDM/SDM). The instantaneous Bragg wavelengths are translated into a change in multiple beam positions impinging on a photo-detector array.

The spectrum of a pulsed broadband source used for the illumination of FBG sensor arrays can be efficiently used by combining WDM/TDM techniques. Here TDM techniques can be used to address FBG sensor elements operating within the same wavelength range. The broadband source however can address FBG sensors operating within different wavelength ranges. This combined technique has the potential to address large numbers of sensors (Kersey *et al.* 1997). Various topologies have been proposed that include serial, parallel and branching networks. Each is outlined in figure 2.5.

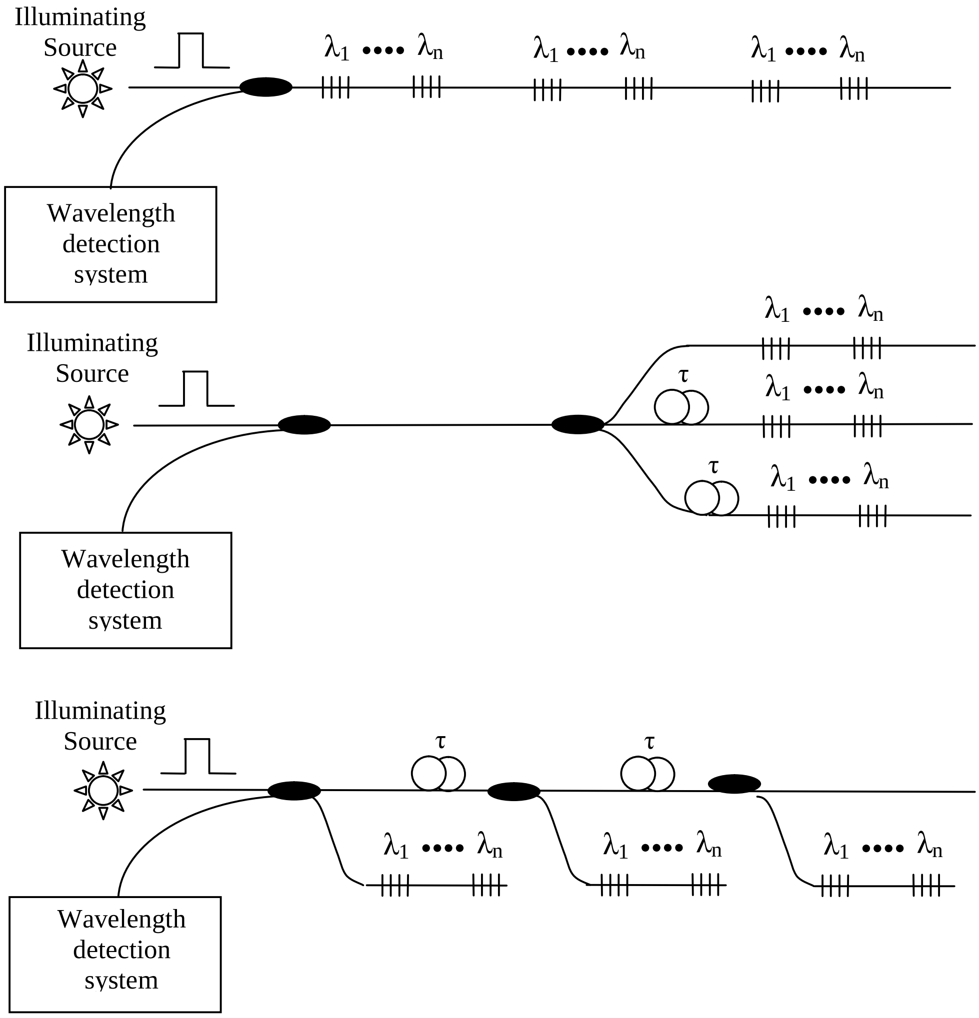

Figure 2.5 Combined WDM/TDM multiplexing topologies for FBG sensor arrays. (a) Serial system with low reflectivity gratings, (b) parallel network, and (c) branching network (Kersey *et al.* 1997)

The advantage of using topologies as described in figure 2.5(b) and 2.5 (c) is that multiple reflection crosstalk can be eliminated. The reflectivity of sensor elements however has to be maximised as the incident and reflected beam intensity is divided by the couplers.

2.2 Passive Demodulation Scheme

2.2.1 Passive Filter Demodulation Schemes

A demodulation scheme has been demonstrated using a bulk-optic filter. This is shown in figure 2.6 (Melle, Liu & Measures 1992). The Bragg signal reflected from the FBG sensor is split by a coupler into beams of equal intensity. One is collimated into a free space beam and demodulated by the edge of the filter’s transfer function, the sensor signal being represented by the current I_S. The other is detected directly and used as a reference I_R.

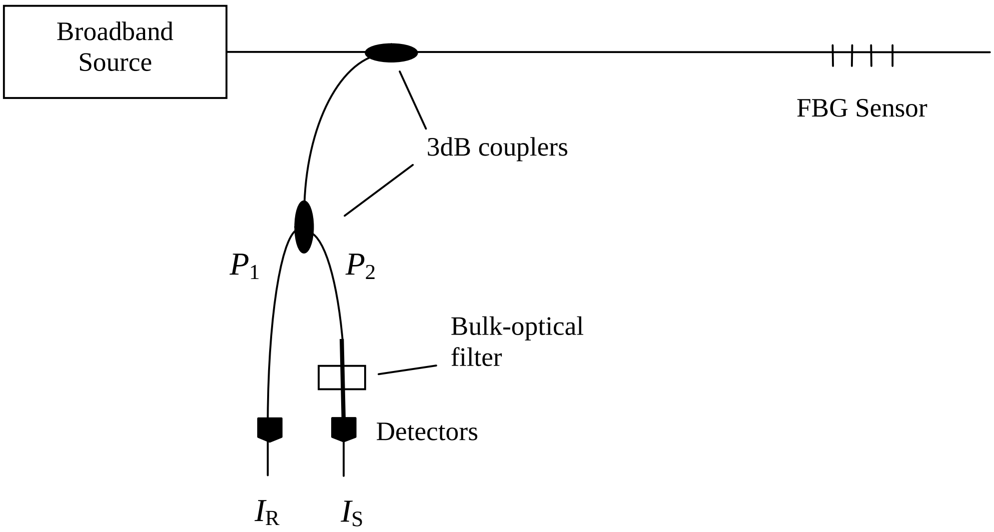

Figure 2.6 An FBG sensor demodulation scheme based on a bulk-optical filter
The Bragg signal reflected from the FBG sensor is split by a coupler into beams of equal intensity. One is collimated into a free space beam and demodulated by the edge of the filter's transfer function, the sensor signal being represented by the current I_S. The other is detected directly and used as a reference I_R (Melle, Liu & Measure 1992).

Passive filter schemes such as this suffer from fluctuation in source intensity and fibre losses. These phenomena cause changes in signal intensity that is not due to wavelength variation and therefore implies a false measurand reading. The reference signal allows compensation for the fluctuations by using the equation

$$\frac{I_S}{I_R} = A(\lambda_B - \lambda_o + \frac{\Delta\lambda}{\sqrt{\pi}}) \qquad \textbf{2.4}$$

where λ_B is the instantaneous Bragg wavelength and $\Delta\lambda$ is the optical bandwidth of the FBG. The values λ_o and A are the starting wavelength and the gradient of the filter's transfer function, respectively. This is otherwise known as an intensity referencing technique and is required for all intensity based demodulation schemes. The quasi-static strain resolution achieved was 375με over a range of ±5500με. The junction capacitance of the photo-detector limited the speed of the scheme to 100Hz.

Transient strain on a gun barrel has been monitored using FBG sensors (James *et al.* 1999). This used a filter as the means of demodulation of a transient signal. The scheme was implemented with two channels using Avalanche Photo-Detectors (APDs) to detect the sensor signals. The bandwidth of the scheme is limited to 100kHz by the response time of the APDs.

The performance of this scheme is limited by the alignment of the bulk-optical filter as small changes in angle may cause a significant change in transmitted intensity. The change in intensity is due the central wavelength of the filter depending on the angle of incidence. A considerable proportion of the Bragg signal is also lost due to reflections at fibre ends and at the filter’s material interface (Melle, Liu & Measures 1992). It also possible to increase the resolution of a filter demodulation scheme by using fibre based devices. A scheme based on a biconic fibre filter reports a resolution of ±3.5με over a 16,000με range.

An all fibre approach has been demonstrated by using a wavelength dependent fibre coupler. The scheme together the transfer function of the coupler is shown in figure 2.7 (Davis & Kersey 1994). As the instantaneous Bragg wavelength of the sensor changes with applied measurand the split ratio of the incident beam changes due the transfer function of the wavelength dependent fibre coupler. The wavelength encoded signal is then changed into an intensity encoded one to be recorded by a photo-detector. The signal is then demodulated by the edge of the coupler’s transfer function. The output ports of the coupler are monitored by a pair of matched detectors. Here ratiometric detection is used to provide intensity referencing. The scheme achieved a quasi-static strain resolution of ±3με over a measurement range of 1050με.

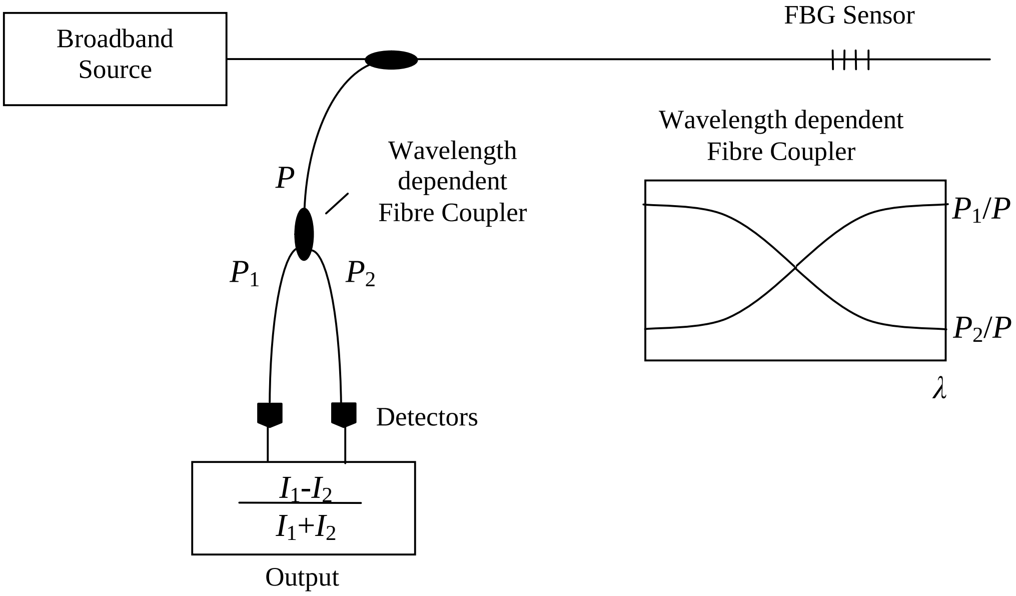

Figure 2.7 An FBG sensor demodulation scheme based on a WDM fibre coupler
A pair of matched detectors monitors the output ports of the WDM coupler. Intensity referencing is provided by ratiometric detection (Davis & Kersey 1994).

A similar scheme has been demonstrated using an over-coupled coupler (Zhang *et al.*, 1995). The transfer function has a greater maximum gradient than the WDM fibre coupler detailed in figure 2.7, so increasing sensitivity. The transfer function demonstrates a constant period sinusoidal variation with wavelength possessing approximately four periods within a 20nm range. Each half cycle from transmission peak to trough can then demodulate a FBG sensor element within a WDM sensor array. Each Bragg signal however would need to be differentiated by a WDM device before being detected.

Long period gratings (LPGs) are inexpensive fibre based devices that possess optical bandwidths that can extend to over 10nm. A demodulation scheme based on a single sensor and a single LPG used in transmission has been demonstrated (Fallon *et al.* 1998), the scheme also incorporates an intensity referencing technique. Here a reference as well as a demodulated signal is received. The signal is then simply divided by the reference to provide intensity referencing. The quasi-static strain resolution of the scheme is reported to be 0.5με within a maximum range of 8100με.

An FBG sensor is fabricated by irradiation of a photosensitive fibre by a regular UV interference pattern. The coupling coefficient between forward and backward propagating modes is constant along the length of the FBG however the coefficient at any point can be made to vary. This allows reflection spectra of a predetermined shape to be designed. A profile has been established that produces a Triangular FBG (TFBG) with an FWHM optical bandwidth of 5nm. Such a triangular grating is used with a circulator for the demodulation of a single FBG sensor (Huang *et al.* 2004), as is shown in figure 2.8. The intensity recorded at PD_1 is divided by that received at PD_2 to compensate for fluctuations in source intensity and bend losses in the fibre. The technique reports a quasi-static strain resolution of 1.5με demonstrated over a 200με range. An array of TFBGs can be used to demodulate a WDM array of FBG sensors. This would use the same configuration detailed in figure 2.8 in a cascaded fashion. The spectrum transmitted through the FBG sensor would be the input to the following circulator.

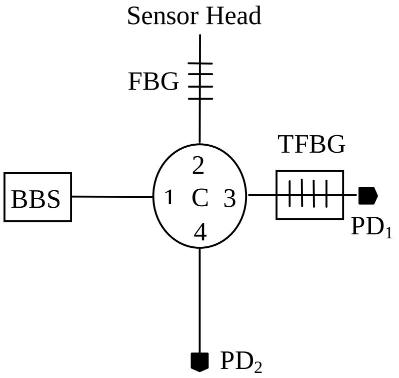

Figure 2.8 An FBG sensor demodulation scheme based on a Triangular FBG (TFBG)
BBS: Broadband source, C: Circulator, PD1, PD2: Photo-detectors. The edge in the spectral response of the TFBG modulates beam intensity depending on the instantaneous Bragg wavelength. The intensity recorded at PD1 is divided by that received at PD2 to compensate for fluctuations in source intensity and losses in the fibre (Huang *et al.* 2004).
.

2.2.2 Passive Filter Spatial Translation Demodulation Schemes

A scheme similar to the bulk optical filter has been demonstrated using a volume hologram written in a photorefractive crystal ($BaTiO_3$) (James *et al.* 1996). The holographic transfer function demodulates the Bragg signal; however the hologram also diffracts the demodulated signal through a pre-determined angle to a photo-detector. Here approximately 20% of signal power is lost by interface reflections, the refractive index of $BaTiO_3$ being 2.424. A crystal of $BaTiO_3$ is fragile with properties that depend heavily on temperature. The use of the crystal is therefore unrealistic for an actual demodulation scheme but can be used for the demonstration of an approach based on holographic techniques. When demodulating a single FBG sensor, a quasi-static strain resolution of 2με was achieved within a maximum range of 2500με. The crystal however can host an array of volume holograms. Each can be matched to an element in a WDM FBG sensor array to provide simultaneous demodulation and de-multiplexing. The holographic transfer function provides demodulation similar to the single sensor scheme whilst each Bragg signal is diffracted through a separate angle to a separate detector thus providing de-multiplexing. The demonstration of this principle forms the main focus of this thesis.

The scheme based on holographic techniques represents a deviation from those discussed in section 2.2.1. The signals from individual elements are translated into different beam directions therefore the scheme represents a combined WDM/SDM technique. Numerous passive filter schemes are emerging that use combined WDM/SDM techniques each will be discussed in the following paragraphs.

A WDM FBG array demodulation scheme has been demonstrated using a curved free space grating and a CCD camera (Chen *et al* 1997). The Bragg reflections from five FBG sensors are diffracted toward different points on a 512 x 512 pixel CCD camera by a free space grating. The configuration allows a change in beam position to be recorded for a shift in Bragg wavelength. The scheme is illustrated in figure 2.9.

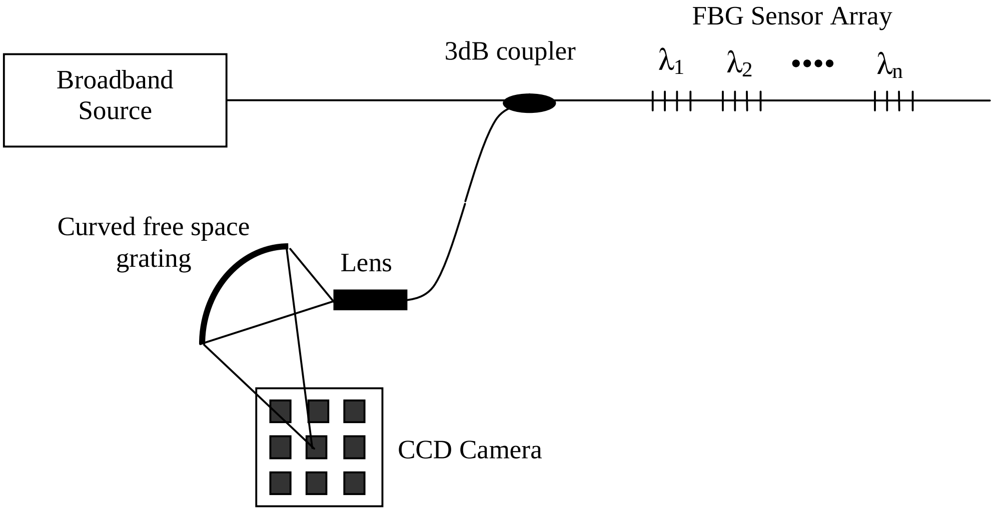

Figure 2.9 A WDM FBG sensor array demodulation scheme based on a curved free space grating and a CCD camera
The Bragg reflections from five FBG sensors are diffracted toward different points on a 512 x 512 pixel CCD camera by a free space grating. The configuration allows a change in beam position to be recorded for a shift in Bragg wavelength (Chen *et al.* 1997).

A Centroid Detection Algorithm (CDA) is used to process the image that is represented by equation

$$\lambda_{\mathrm{B}} = \frac{\sum_{\mathrm{j}} \lambda_{\mathrm{j}} I_{\mathrm{j}}}{\sum_{\mathrm{j}} I_{\mathrm{j}}} \qquad \textbf{2.5}$$

where λ_j and I_j and represent the central wavelength and the incident intensity of the j*th* CCD pixel. This expression represents a moving average that points to the Bragg wavelength to within a fraction of one pixel (Davis *et al.* 1996(a)). The number of pixels chosen for processing determines the wavelength resolution. The wavelength resolution increases with Bragg signal intensity therefore FBGs sensors each with a different reflectivity demonstrate different accuracies. This type of resolution improvement algorithm is beginning to be used in FBG sensor demodulation in both passive and active schemes. This scheme however demonstrates a quasi-static resolution of 1.5με over a 600με range. The major limitation however is the frame rate available for the CCD camera, in this case 30 frames per second limiting the bandwidth to 30Hz. The scheme is inexpensive in comparison with active ones due to the use of readily available CCDs. Furthermore no intensity referencing is required.

Another scheme uses a Chirped and Tilted Fibre Bragg Grating (CTFBG) with a 512 element linear detector array to interrogate three FBG sensors (Jauregui 2004), see figure 2.10. The reflected signals from the sensors are diffracted through the fibre cladding to form an image on the detector array. The image processing has three consecutive stages; a de-multiplexing algorithm, a peak detection algorithm and finally a wavelength correction stage. The image recorded is a composite of images from individual sensor elements. Individual sensor images are recorded during a calibration exercise by sweeping each FBG sensor through its entire wavelength range in 1 nm steps. Pattern recognition software then uses adaptive filtering techniques to derive a combination of individual images which is the best match to the composite. A spectrum including the instantaneous Bragg wavelengths of all sensors is then derived. Peak detection software is used to determine the Bragg wavelengths. There is however a discrepancy between the calculated and actual wavelengths. Correction is achieved by a calibration curve created by a sweeping a tuneable narrowband laser through the interrogation range and correlating calculated to actual Bragg wavelengths. The quasi-static resolution of 0.6με is demonstrated by the scheme over a 1000με range. The bandwidth of the scheme is limited by the integration time of the linear array to 80Hz.

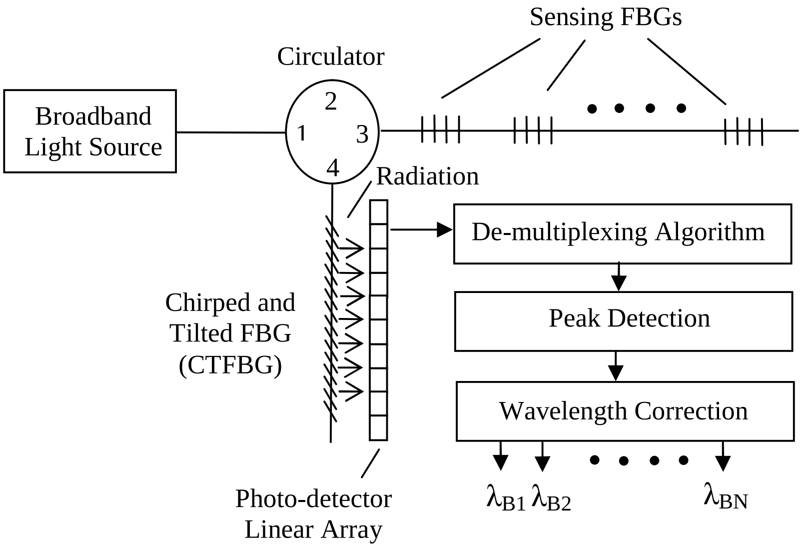

Figure 2.10 Demodulation and de-multiplexing of an FBG sensor array by a Chirped and Tilted FBG (CTFBG)
The Chirped and Tilted FBG reflects the combined spectrum of a three element FBG sensor array through the cladding of the fibre onto a linear array. From the image the peak wavelength is established for each sensor element (Jauregui 2004).
.

Another interesting demodulation scheme based on a tilted Fabry-Perot (FP) cavity has been demonstrated (Kiesel *et al.* 2007). The filters are fabricated from alternate thin layers deposited on the surface of the material to form distributed Bragg reflectors (DBR). Two such filters separated by a layer of bulk material forms an FP cavity. Here the filters are not parallel but offset by a small angle allowing light of different wavelengths to interfere constructively at different locations on the surface of the filters. Any change in wavelength of a Bragg reflection can be then tracked as the location of constructive interference changes, see figure 2.11. Tracking is achieved by a Position Sensing Device (PSD) that derives two currents representing the central position of the impinging beam and therefore wavelength precisely. The scheme demonstrates a temperature resolution of 0.1°C over a 20ºC range.

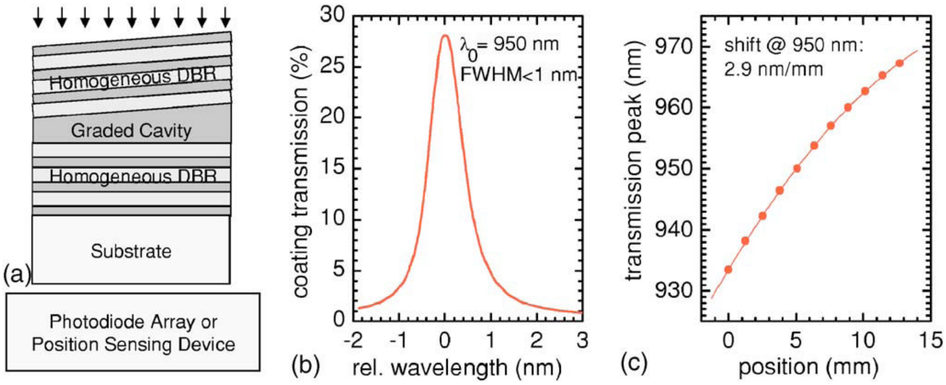

Figure 2.11 Demodulation scheme based on a tilted Fabry-Perot (FP) cavity. The cavity is formed by two distributed Bragg reflectors (DBRs) with a section of bulk material between. (a) A Filter with laterally varying transmission properties transforms spectral into spatial information. A photo-detector array records a change in position depending on the instantaneous Bragg wavelength (b) Transmission properties of the GaAs/ AlAs Fabry-Pérot cavity. (c) Dependence of spectral peak on lateral filter position (Kiesel *et al.* 2007).

2.2.3 Summary of Passive Filter Demodulation Schemes

Passive filter demodulation techniques are inexpensive, stable and possess the potential for high speed. They do however require intensity referencing techniques to compensate for fluctuations in source and fibre losses. Quasi-static resolutions are good, approaching and in some cases exceeding 1με for strain. Few electrical bandwidth measurements are available so it is unclear whether the potential for high speed can be achieved. Finally passive filter schemes do not readily integrate to WDM techniques without a specific demultiplexing device.

A summary of passive filter demodulation schemes is shown in Table 2.1.

Table 2.1 Summary of passive filter demodulation schemes

	Fibre-optic Filter	**WDM Coupler**	**Long Period Grating**	**Triangular FBG**
Resolution	±0.1 -3.5με	±3-5με	0.13-0.5με	1.5με
Range	±8000-10000με$^{(1)}$	1050-1200με$^{(1)}$	8100-12000με$^{(1)}$	200με$^{(1)}$
Bandwidth	100kHz$^{(2)}$	Unavailable	Unavailable	Unavailable

(1) Not representative the maximum possible range but the range used to establish resolution figure.
(2) Limited by the speed of the APD.

Schemes that translate the instantaneous Bragg wavelength into a shift in beam position possess better resolution figures than those based on standard passive filters as real time signal or image processing is used. The translation schemes are robust, inexpensive, stable and do not require intensity referencing. Importantly the schemes can be readily integrated into WDM techniques as multiple beam positions can be tracked. Their bandwidth however is severely limited by the integration time of the linear array or matrix of photo-detectors.

A summary of passive spatial translation demodulation schemes is shown in Table 2.2.

Table 2.2 Summary of passive spatial translation demodulation schemes

	Holographic	**Curved Grating with CCD Camera**	**Chirped and Tilted FBG**	**Tilted Fabry-Perot (FP) Cavity**
Resolution	2με	1.5με	0.6με	0.1ºC
Range	2500με	600με$^{(1)}$	1000με$^{(1)}$	20ºC$^{(1)}$
Bandwidth	Unavailable	30Hz$^{(2)}$	80Hz$^{(2)}$	Unavailable

(1) Not representative the maximum possible range but the range used to establish resolution figure.
(2) Limited by the integration time of the array or matrix of photo-detectors.

2.3 Active Demodulation Schemes

2.3.1 Active Filter Demodulation Schemes

A fibre based Fabry-Perot Filter (FPF) has been used to demodulate a single FBG sensor (Kersey, Berkoff & Morey 1993). The filter possesses a finesse of 120 and an FSR of 40nm and is used to demodulate in both scanning and tracking modes. A feedback loop consisting of the filter and a dither signal allows the instantaneous Bragg wavelength to be tracked. The scheme is shown in figure 2.12. The insertion of a dither frequency at the resonant Fabry-Perot wavelength by a fraction of its pass-band produces a modulation at the output of the FPF that contains components of the frequency and its harmonics. When the transmission peak of the FPF and the reflection peak of the FBG sensor are aligned the fundamental component is annulled. The amplitude of the fundamental frequency component therefore acts as an error signal that can be used to lock the FPF pass-band to the Bragg wavelength, and the control voltage is used to give a measure of the applied measurand. Within a demonstration a low frequency 1Hz signal was applied to the sensor. The results demonstrate a detectable strain better than 0.3με when used in tracking mode.

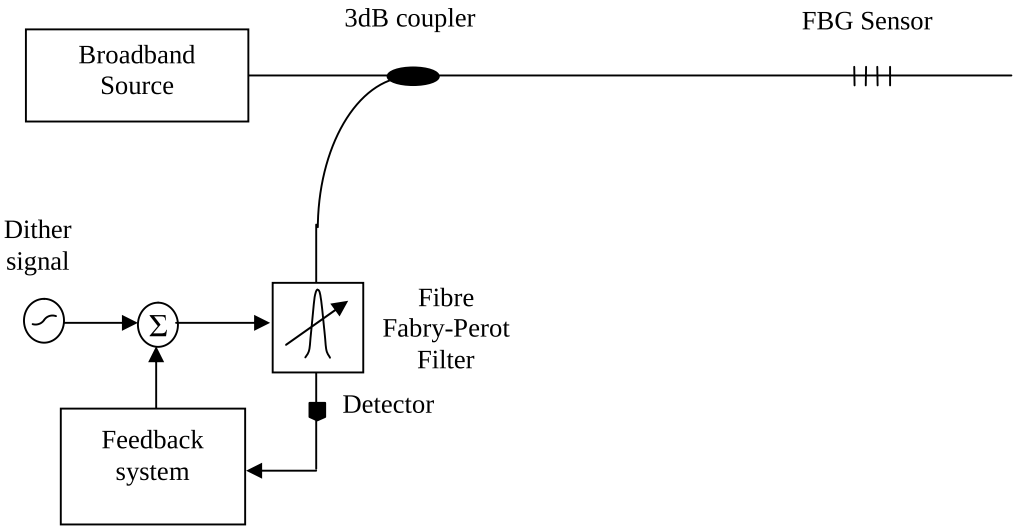

Figure 2.12 Demodulation of a FBG sensor by a fibre based Fabry-Perot Filter. A feedback loop consisting of the filter and a dither signal allows the instantaneous Bragg wavelength to be tracked (Kersey, Berkoff & Morey 1993).

When operating in scanning mode multiple FBG sensors can be demodulated. Here the spectrum of the source and the FSR of the scanning filter must incorporate the operating wavelength range of the sensor array. The filter is swept through the wavelength range and peaks in the received signal correlated to the instantaneous wavelengths of each of the sensor elements. The use of optical switches allows several serial arrays to be addressed simultaneously. For example 60 sensors constructed of 5 strings of 12 WDM arrays can be addressed with a frequency of 20 per second (Davis *et al.* 1996(b)). The scheme is outlined in figure 2.13 and demonstrates a resolution of ±1με over a 400με range. It represents a combination of WDM and SDM techniques.

Typically the bandwidth of a broadband source is 50nm. The wavelength range of an FBG sensor operating at 1300nm is 2-4nm with a guard band between consecutive ranges of 0.5nm. This implies the number of elements in the array that can be addressed is 11-20. The FSR of the interrogating filter is to match that of the broadband source 50nm so all of the elements can be addressed. The optical bandwidth of the filter is to be similar or less than that of the FBG Bragg signal 0.1 nm to ensure the best possible resolution. This implies the filter must have Finesse of 500. Filters with these specifications are presently available that operate at high speeds of over 2kHz (Venghaus, 2006).

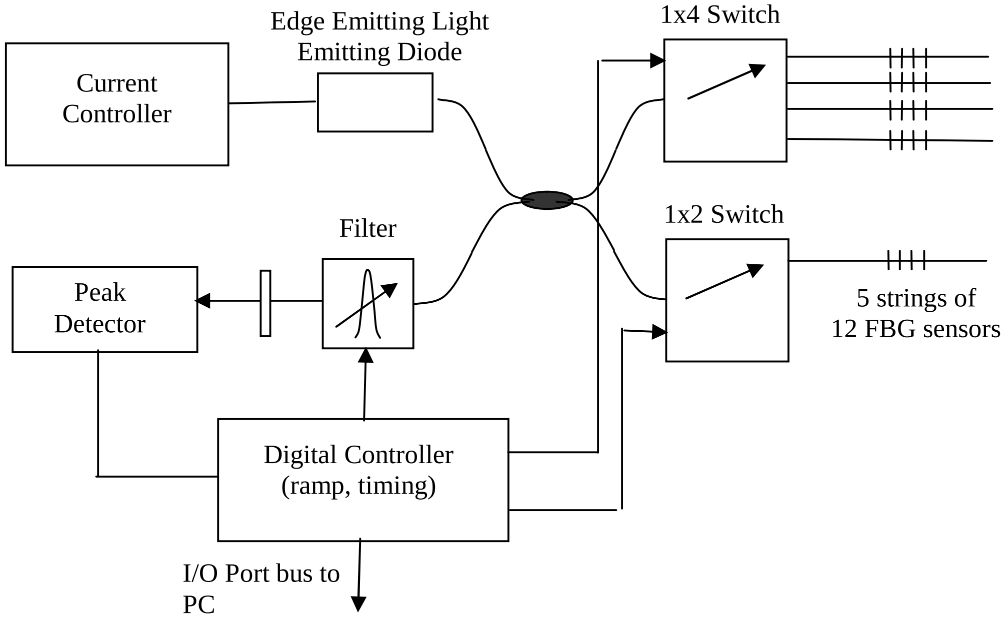

Figure 2.13 Demodulation of 60 FBG sensors by a scanning filter.
The 60 sensors are constructed in 5 strings of 12 WDM sensor arrays. The optical switches allow the filter to scan each string consecutively. The scheme represents a combination of WDM and SDM techniques (Davis *et al.* 1996).

An array of tuneable FBG filters can be used to demodulate an array of FBG sensors (Jackson *et al.* 1993). Here each element in a WDM sensor array is matched to an element in the filter array. The technique has been demonstrated using a parallel configuration as shown in figure 2.14. Here the Bragg signals from the sensor elements are divided by a network of 3dB couplers. The signals are reflected by the matched filter and detected via a 3dB coupler. The filter is tuned by a Piezo-Electric Transducer (PZT) to track the changes in Bragg wavelength or scan through the sensor's wavelength range. The minimum detectable quasi-static strain achieved was 4.12με when the Bragg wavelength was being tracked.

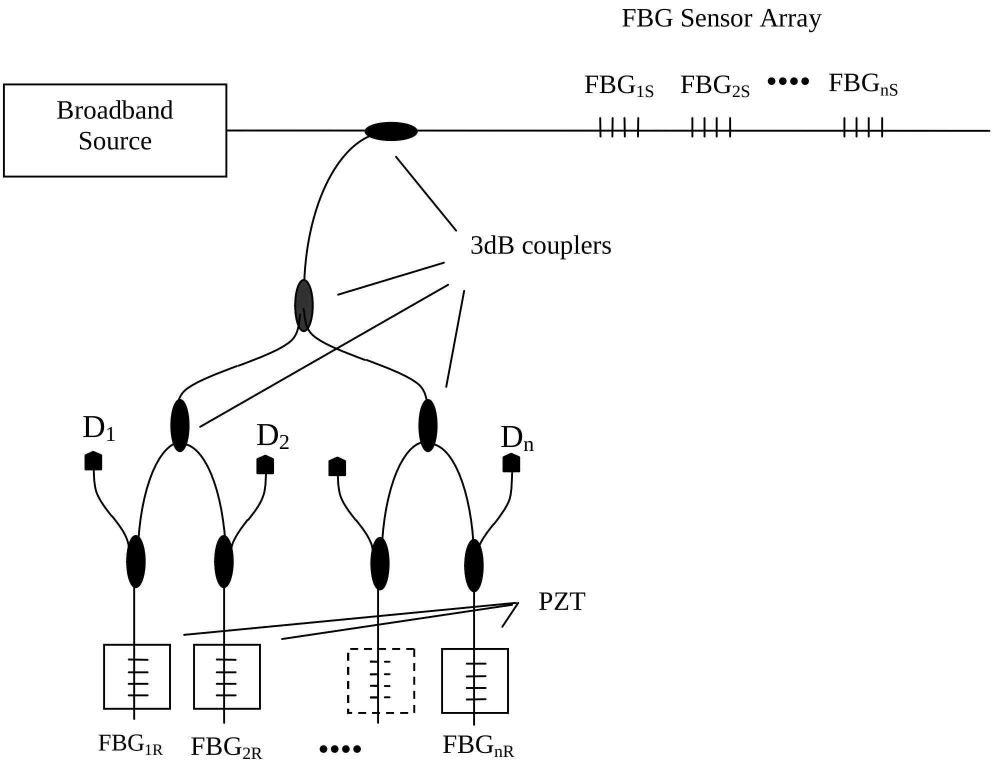

Figure 2.14 Demodulation of an FBG sensor array by matched FBG filters. The Bragg signals from a WDM sensor array are directed by a network of 3dB couplers to matching filters. Each filter is tuned by a PZT. If the PZT is wthin a feedback loop the Bragg wavelength can be tracked. The PZT can also be scanned through a wavelength range to detect the Bragg wavelength (Jackson *et al.* 1993).

A major disadvantage with this configuration is the use of the parallel coupler network that degrades the intensity of the Bragg signals. This can be improved by using serial FBG filters (Brady *et al.* 1994). Here the filters are connected in series to reflect the respective Bragg signals. The scheme is shown in figure 2.15. The quasi-static temperature resolution achieved by the scheme was 0.2ºC over a 170ºC range whilst the strain resolution was 2.8με over an 800με range. The dynamic resolution was reported to be 67nε/√Hz at a frequency of 86Hz.

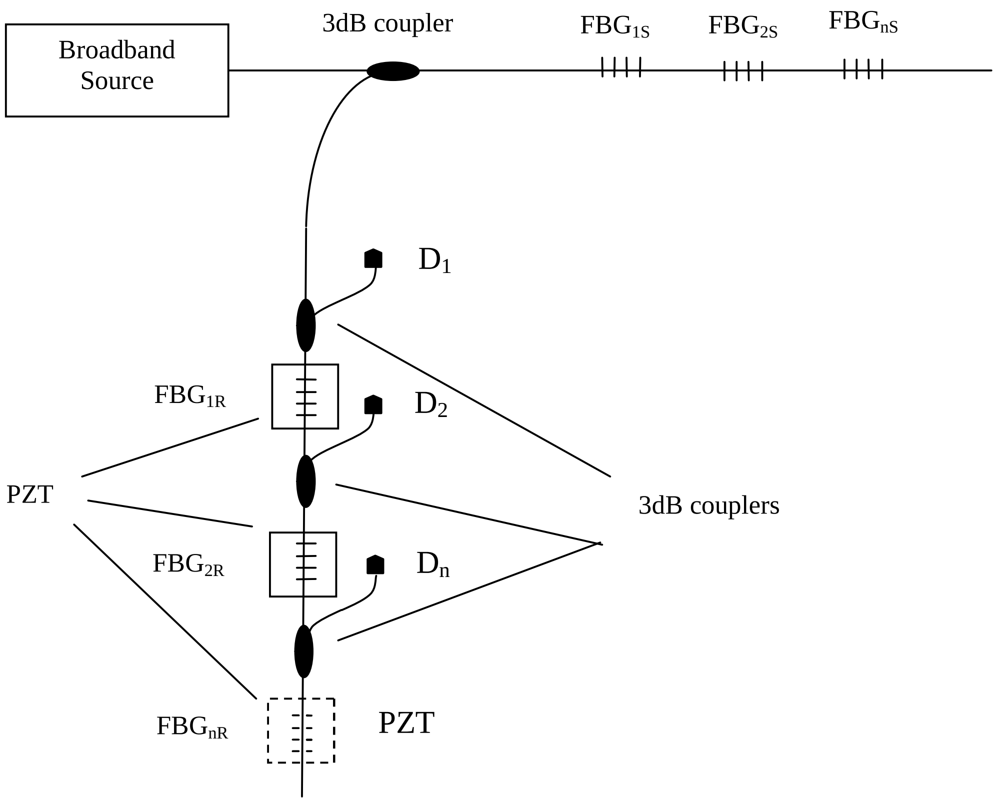

Figure 2.15 Demodulation of an FBG sensor array by a serial array of matched FBG filters. This demodulation scheme has the same operation as that depicted in figure 2.14. The serial matched filter array however allows a higher proportion of the Bragg signal to be detected (Brady *et al.* 1994).

The use of a PZT however represents a major disadvantage. The device limits the range and frequency of the measurand to be detected. A PZT driven stage can also introduce hysteresis into a demodulation scheme. Due to hysteresis the relationship between applied voltage and instantaneous Bragg wavelength may not be linear. Moreover the instantaneous wavelength is dependent not only on the applied voltage but on the speed and direction of stage movement (Fu *et al*. 2006). Reference FBGs have been used to compensate for hysteresis when detecting wavelength shifts (Fu *et al.* 2006). This FBG sensor demodulation scheme uses a Fibre Fabry Perot Tuneable filter (FFP-TF) in conjunction with two reference FBGs as shown in figure 2.16.

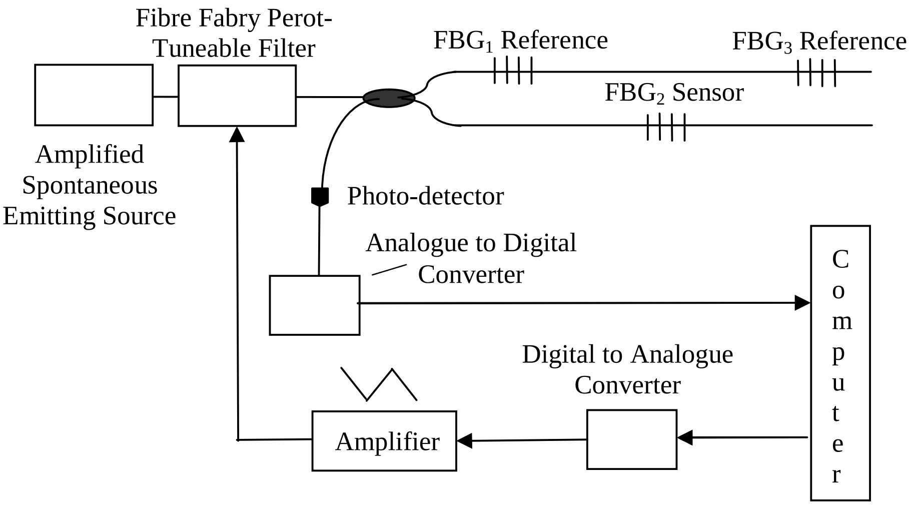

Figure 2.16 A single FBG sensor demodulation scheme with two reference FBGs and a Fibre Fabry-Perot Tuneable Filter (FFP-TF).

A voltage is applied to a PZT to tune the fibre based filter. The voltage is in the form of a triangular waveform varying from 0-30v. The intensity peaks from the two reference FBGs and the sensor are recorded only on the rising edge of the waveform. The voltage range which the peaks are recorded is also limited to 21.5-25.5v. Given these conditions the correlation of applied voltage to wavelength can be considered as quasi-linear (Fu *et al.* 2006).

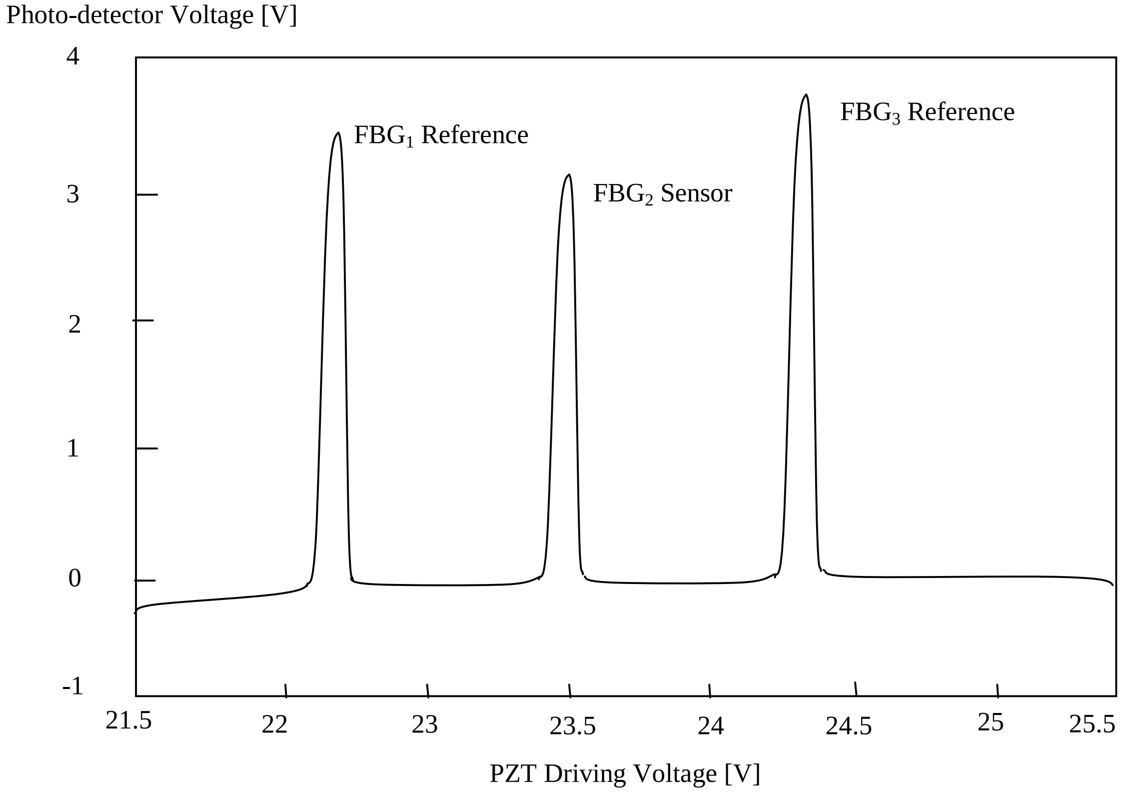

Figure 2.17 Response of the demodulation scheme detailed in figure 2.16 within a limited section of the PZT driving voltage.

The reference FBGs are shown with the FBG sensor. The peaks are recorded on the positive half cycle of the 0-30v triangular waveform and the applicable section of the scan is limited to 21.5-25.5v. Under these conditions the correlation of applied voltage to wavelength can be considered as quasi-linear (Fu *et al.* 2006).

The reference FBGs 1 and 3 have quiescent Bragg wavelengths of 1550.01 nm and 1556.03 nm respectively whilst the sensor has a quiescent Bragg wavelength of 1552.81nm. A voltage applied to the PZT sweeps the FP filter through the wavelength range associated with all three FBGs, the output scan being shown in figure 2.17. The lower and upper peaks represent the reference gratings whilst the centre peak is the sensor. The voltage applied to the PZT is detailed on the x-axis. The full width of the scan however is from 0-30V so the peaks are recorded in the middle of the scan. The peaks are also recorded on forward half cycle 0-30V not the reverse. Both these measures minimise the non-linear effects introduced by the PZT. Given these conditions the correlation of applied voltage to wavelength can be considered as quasi-linear. All FBGs have the same wavelength response to temperature.

The scan voltages that correlate to the central wavelength of the reflection are enhanced by data processing (Fu *et al.* 2006). Three methods are outlined Central Detection Algorithm (CDA), Differential method and the Gaussian technique. The Central Detection Algorithm is a simple moving average that points to the location of the peak. The differential method takes the first differential of the recorded data. The zero crossing point then coincides with the location of the peak. The Gaussian-fit technique finds the best-fit Gaussian curve to the recorded data for peak location.

Once the peak voltages have been located the wavelength shift of the sensor can be determined by equation 2.6

$$\lambda_2=\lambda_1+(\lambda_3-\lambda_1)\frac{(V_{p2}-V_{p1})}{(V_{p3}-V_{p1})} \qquad \textbf{2.6}$$

where V_{px} represent the location of the three peaks x=1,2,3 associated with the reference FBGs 1 and 3 and the FBG sensor 2. λ_x where x=1,2,3 are the Bragg wavelengths of the reference FBGs 1 and 3 and the FBG sensor 2. The Gaussian-fit technique achieved the best resolution of ±0.3ºC for the measurement of temperature over the range 50ºC-120ºC. The scheme was expanded to simultaneously de-multiplex and demodulate two FBG sensors demonstrating resolution figure of ±1ºC over the same range.

An Acoustic-Optic Tuneable Filter (AOTF) allows a diffraction grating to be created within a material by acoustic waves through the application of a Radio Frequency (RF) voltage. The grating transfer functions possess a narrow bandwidth of

0.3 nm whilst the tuning range extends to several micrometers (Othonos 1999). Similar to other active filter schemes, an AOTF can be operated in scanning or tracking mode. In scanning mode access times of 5kHz are achievable. In tracking mode a resolution of 2.24με has been achieved over a measurement range of 2000με (Coroy *et al.* 1995). A major advantage of an AOTF is that it can host multiple gratings by the application of different RF signals. An AOTF has therefore been used in the demodulation of a two element FBG sensor array (Volanthen *et al.,* 1996) however the quiescent Bragg wavelengths were 200nm apart. AOTFs possess great potential for use within demodulation schemes however; they are expensive to fabricate and require thermal compensation.

2.3.2 Active Source Demodulation Schemes

Lasers are high power narrow bandwidth sources ideal for use in active demodulation schemes. A commercially available semiconductor gain coupled distributed feedback (DFB) tuneable laser with an 8nm tuning range was used to address a single FBG sensor (Coroy *et al* 1997). The scheme achieved a resolution of ±0.76με over a 2000με measurement range. Alternatively, highly reflective FBGs (98%) are used in combination with an Erbium Doped Fibre Amplifier (EDFA) to produce an easily fabricated tuneable fibre laser within the 1550nm range (Ball, Morey & Cheo 1994). The FBGs act as the mirrors that create the cavity whilst the EDFA provides the gain medium. The fibre laser produced a 100μW of power within a 0.03nm optical bandwidth and was scanned through the sensor's range by a pair of PZTs straining the cavity FBGs. The laser demodulated a three element FBG sensor array with a resolution of 0.18ºC over a 180ºC range. The range was limited by the maximum 1% strain that can be applied to the FBGs because of surface contaminates and physical damage incurred upon inscription. Above 1% the FBGs are liable to deform or break.

To overcome the limited tuning range of the FBG cavity, fibre loop lasers are used within demodulation schemes (Kersey & Morey 1993). In one such scheme four FBG sensors in a WDM array are interrogated by a fibre loop laser where the gain is provided by an EDFA. The scheme is shown in figure 2.18. Each FBG sensor acts as a reflection point within a unidirectional loop allowing lasing at the elements' instantaneous Bragg wavelengths. A narrow-band tuneable Fabry Perot (FP) filter maximises loop gain at the Bragg wavelengths by addressing the elements sequentially. The Bragg signals are detected by an Optical Spectrum Analyser (OSA) that limits the resolution to ±25με.

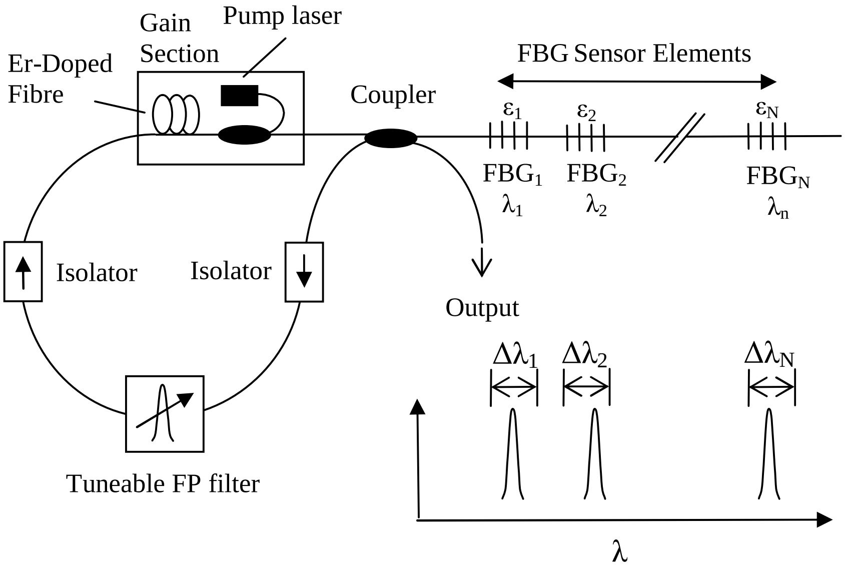

Figure 2.18 Demodulation of a FBG sensor array by a fibre loop laser.
Each sensor element forms a unidirectional loop at its Bragg wavelength. The filter is then scanned through a wavelength span incorporating the sensor ranges of all elements maximising the gain at the respective instantaneous Bragg wavelengths. The Bragg signals are detected by an optical spectrum analyser (OSA) that limits the resolution to ±25με (Kersey & Morey 1993).

A scanning fibre loop laser has been used to demodulate a single FBG sensor (Yun *et al*. 2006), the laser being tuned by a voltage controlled FP filter. The laser produces 130mW of power within 0.2nm line-width that can be tuned over a 43nm range. The scheme is enhanced by a Centroid Detection Algorithm to improve the correlation between voltage applied to the filter and the Bragg wavelength. Without the algorithm the resolution was measured at 10.1με but this was improved to 1.39με with the algorithm, the resolution being established over a 1400με range. It is envisaged that the scheme can be scaled to demodulate an FBG sensor array as the wavelength range of the FP filter can detect Bragg signals from multiple sensors.

An actively mode locked fibre loop laser has been used to demodulate a three element FBG sensor array (Yamashita & Inaba 2004). The diagram explaining the scheme is shown in figure 2.19.

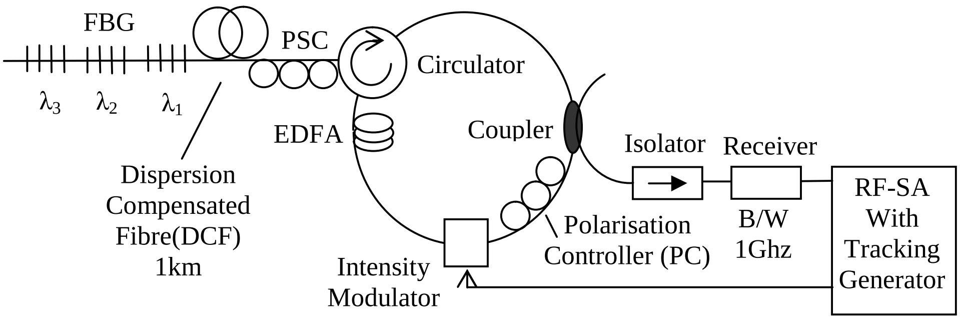

Figure 2.19 Demodulation of a three element FBG sensor array by an actively mode locked fibre laser loop.
Laser loop cavities are constructed from the three FBG sensor elements, a circulator,1km of Dispersion Compensated Fibre (DCF), an EDFA and two polarisation state controllers (PSCs). The scheme operates by recording the change in the FSR of the cavities as the measurand is applied to the sensor elements. The FSR of each cavity is interrogated by a scanning RF source derived from a Tracking Generator (TG) and applied to an Intensity Modulator. The change in FSR is recorded by a change in the mode locked Radio Frequency on a Radio Frequency Spectrum Analyser (RF-SA) (Yamashita & Inaba 2004).

The laser loop cavities are constructed from a circulator, a 1km length of Dispersion Compensated Fibre (DCF), an EDFA, two polarisation controllers (PSCs) and the three FBG sensor elements. As the measurand is applied to the sensor elements the change in the FSR of the cavities are recorded. The FSR of each cavity is interrogated by a scanning RF source derived from a Tracking Generator and applied to an Intensity Modulator (IM). The IM modulates the light intensity within the laser loop. The change in FSR is recorded by a change in the mode locking Radio Frequency on a Radio Frequency Spectrum Analyser, with the change in Bragg wavelength being related to the change in Radio Frequency by equations 2.7 and 2.8.

$$\Delta \mathrm{F} = \mathrm{F}_0 \frac{cD}{n} \Delta\lambda_s \qquad \textbf{2.7}$$

where ΔF is the change in the FSR and F_o is the quiescent FSR of a cavity. The shift in Bragg wavelength is given by $\Delta\lambda_S$, n is the refractive index of the fibre, c is the speed of light and D is the averaged chromatic dispersion within a laser cavity. The change in FSR (ΔF) is then related to the change in RF frequency by

$$\Delta f_N = \mathrm{N}\Delta\mathrm{F} \qquad \textbf{2.8}$$

The laser is mode locked when the drive frequency matches an integer multiple of the change in FSR (N). Demodulation of three FBG sensors with quiescent Bragg wavelengths of 1550 nm, 1556nm and 1559 nm is demonstrated by sweeping the RF frequency around a central figure of 200MHz. The scheme reported a resolution of 10με over a measurement range of 7500με.

Until recently, tuneable fibre lasers using FBG cavities have been considered unfit for FBG sensor demodulation due to the limited tuning range. There has been progress however in FBG fabrication leading to a significant improvement in the maximum strain that can be applied. As a rule of thumb an FBG inscribed by conventional means can be stretched by approximately 1% (Paterno *et al.* 2007). A FBG can be inscribed within a fibre when it is being drawn allowing maximum stretching ratio of 4% (Hagemann *et al.* 1998). These have been used within a tuneable wavelength source to allow the demodulation of an array of FBG sensors (Paterno et al. 2007). The configuration of the scheme is shown in figure 2.20.

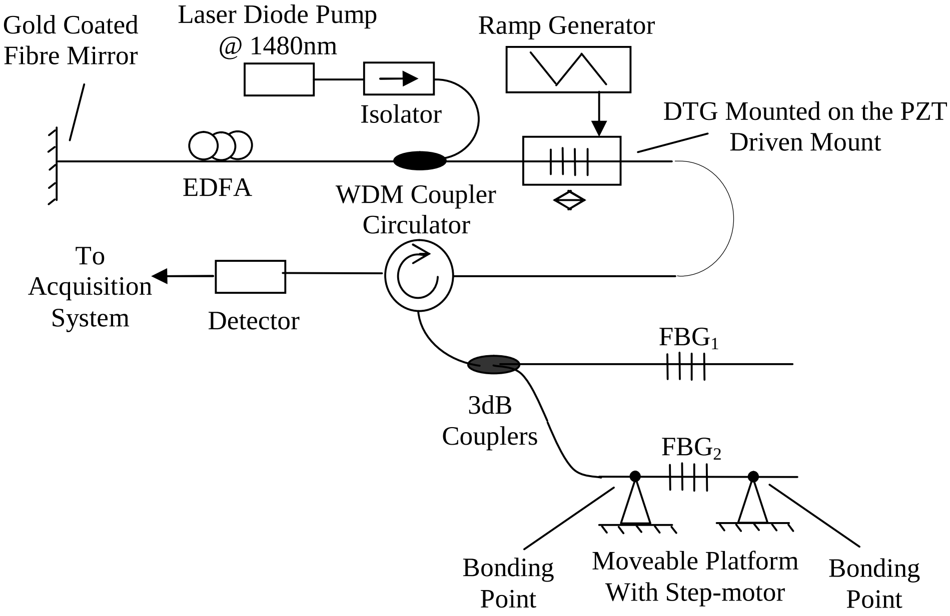

Figure 2.20 Demodulation of an FBG sensor array by a Drawn Tower Grating (DTG) tuneable fibre laser.
A tuneable laser is formed between a DTG and a gold coated mirror. By applying a saw-tooth waveform to the PZT the laser is swept through a wavelength range. The Bragg wavelengths are located by establishing peaks in the detected signal or by using a Zero Crossing Point (ZCP) algorithm applied to a derivative of the signal (Paterno *et al.* 2007).

A tuneable laser is formed between a gold covered fibre mirror and a drawn tower grating (DTG) attached to a PZT. The laser is swept through a wavelength range by applying a saw-tooth waveform to the PZT. The laser is calibrated before experimentation so an instantaneous applied voltage is correlated to a wavelength. The two FBG sensors demodulated possess quiescent wavelengths of 1543nm and 1547nm. The Bragg wavelengths are located by establishing peaks in the detected signal or by using a Zero Crossing Point (ZCP) algorithm applied to a derivative of the signal. The results were taken over a 2000με range, fitted to a straight line and the root mean square (RMS) deviation established. The RMS deviation in the peaks located is 9.6με/√Hz however using ZCP the deviation is 4.9με/√Hz.

The use of Micro Electro Mechanical Systems (MEMS) is beginning to transform swept laser technology allowing sweep speed to increase rapidly. A study has been undertaken that uses a Santec HSL-2000 with an output power of 14mW to interrogate 5 FBG sensors in the 1300nm range (Chehura 2009). Figure 2.21 shows a typical output scan of the wavelength range using an 114nm width and a scan rate of 20kHz.

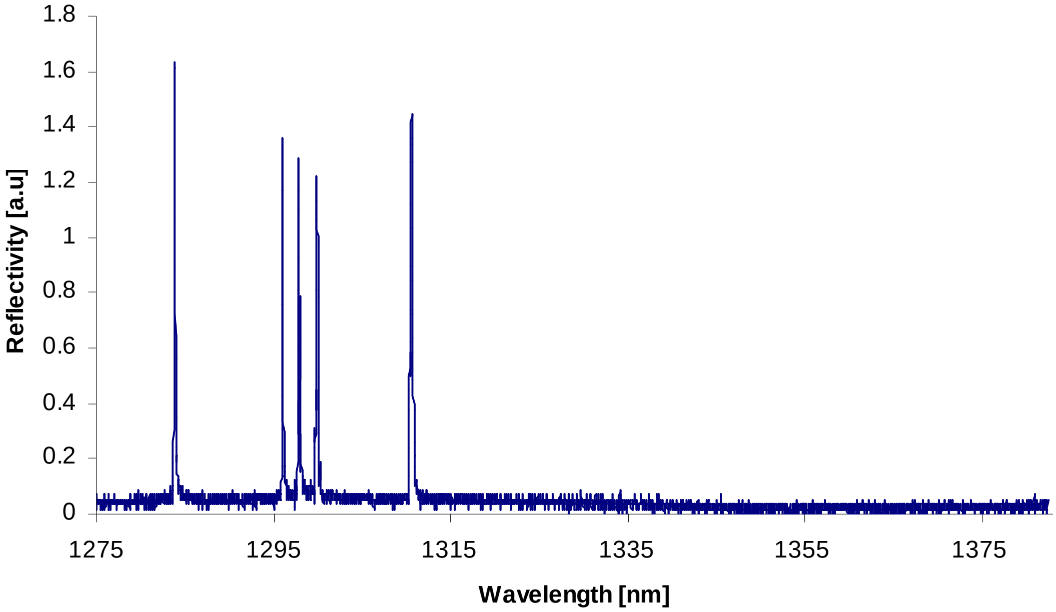

Figure 2.21 Typical output scan of a HSL-2000 Santec scanning laser interrogating 5 FBG sensors in the 1330nm range.
A 114nm wavelength range is scanned by the laser at 20kHz (Chehura 2009).

The resolution of the scheme has not been established however it is likely to reflect the optical bandwidth of the FBG sensor as the laser has a resolution of 3pm.

2.3.3 Summary of Active Demodulation Schemes

Active demodulation schemes generally are more complex than passive ones as they either use lasers or narrow bandwidth filters. The schemes either track the instantaneous Bragg wavelength of a single sensor by the use of a feedback loop or demodulate a sensor array by scanning through an extended wavelength range. The schemes are limited by the response time of the device if implemented in a feedback loop. If the device is swept through a wavelength range then the demodulation scheme is limited by the scan rate. Active filters however are becoming available with sweep cycles of 2kHz and active sources are emerging with scan rates of 20kHz.

The resolution of the peak intensity detected in scanning schemes determines the measurand resolution. Data processing techniques however are available that enhances the resolution of the recorded peak and therefore that of the measurand. An example of a simple method is to take a derivative of scan data and determine the zero crossing point to determine the peak intensity position.

The PZT that applies strain to FBGs is non-linear and introduces a systematic error into a demodulation scheme. This is particularly true of FBGs that are scanned through an extended wavelength. Attempts have been made however to overcome this issue with reference FBGs. This assumes that the response of a PZT is quasi-linear by using data from a small central section of a scan moving in one direction alone.

FBGs that have been inscribed within the fibre core after fibre fabrication possess maximum strains limited to 1% (Paterno *et al.* 2007). This limits the measurement range of FBG sensors and the tuning range fibre based cavity lasers. It is possible however to combine the processes of fibre and FBG fabrication. Here an FBG is inscribed within the core as the fibre pre-form is being pulled. Using this technique the maximum possible strain is increased to 4% (Hagemann *et al.* 1998). Another technique to overcome the limited tuning range of a FBG cavity is to use a loop laser. Here the FBG sensor is the single reflection point in a unidirectional loop determining laser wavelength. Other ingenious schemes for example use a mode locked loop laser, the mode lock frequency being related to the instantaneous Bragg wavelength of an FBG sensor array element. Active demodulation schemes are summarised in table 2.3.

Table 2.3 Summary of active filter demodulation schemes.

	Fibre Based FP Filter	FBG Filter	AOTF
Resolution	±10με(1); 0.3°C(2)	2.8με, 0.2°C	2.24με
Range	300με(3), 70°C(3)	800με(3), 170°C(3)	2000με(3)
Bandwidth	200Hz(4), 2.2kHz(5)	86Hz(4)	5kHz(5)
Dynamic Range	Unavailable	67nε/√Hz@86Hz	Unavailable

(1) Strain resolution without Centroid Detection Algorithm.
(2) Temperature resolution with Centroid detection Algorithm.
(3) Represents range reported not maximum possible range.
(4) Represents bandwidth reported not maximum possible bandwidth.
(5) Represents maximum possible bandwidth.

The active source demodulation schemes that have been detailed earlier in the section have been summarised in Table 2.4.

Table 2.4 Summary of active source demodulation schemes.

	Semi-conductor DFB Laser	Fibre Based FBG Cavity Laser	Loop Laser	Mode Locked Laser
Resolution	±0.76με	0.18°C	10.1με(4), 1.38με(5)	10με
Range	2000με(1)	180°C(1)	1400με(1)	7500με(1)
Bandwidth	10kHz(2)	Unavailable(3)	Unavailable	Unavailable

(1) Represents range reported not maximum possible range
(2) Represents maximum possible bandwidth.
(3) Severely limited by PZT diving FBG cavity.
(4) Strain resolution without Centroid Detection Algorithm.
(5) Strain resolution with Centroid Detection Algorithm.

2.4 Interferometer Based Demodulation Schemes

2.4.1 Introduction

A fibre based Mach-Zender Interferometer (MZI) has been used in the demodulation of FBG sensors (Kersey, Berkoff & Morey 1992). The device is at its most sensitive held in quadrature by a low gain feedback loop but in this state can only detect high speed changes in a measurand. Fibre based interferometers such as the MZI are preferred to free space types as no intensity is lost in reflection at material interfaces. The strain induced phase shift within an MZI is given by equation 2.9 (Othonos 1999).

$$\Delta\psi(\mathrm{t}) = \frac{2\pi\Delta L_{\mathrm{MZI}}}{\lambda_{\mathrm{B}}^{2}} \Delta\lambda_{\mathrm{B}} \sin\omega\mathrm{t} \qquad \mathbf{2.9}$$

where $\Delta L_{\mathrm{MZI}} = nd$ the optical path difference (OPD) of a Mach-Zender interferometer, n is the effective refractive index of the fibre core, d is the physical length imbalance between the fibre paths, λ_{B} is the quiescent Bragg wavelength of the sensor whilst $\Delta\lambda_{\mathrm{B}}$ is the measurand induced wavelength shift. The term $\sin(\omega\mathrm{t})$ represents the frequency of the high speed fluctuations in the measurand to be demodulated. The strain induced phase shift is a measure of the sensitivity of the demodulation scheme. For a MZI the unambiguous range is given by equation 2.10 (Othonos 1999).

$$FSR_{\mathrm{MZI}} = \frac{\lambda_{\mathrm{B}}^{2}}{\Delta L_{\mathrm{MZI}}} \qquad \mathbf{2.10}$$

all symbols have been previously defined for equation 2.9. As explained in section 2.1 the unambiguous range is the wavelength span between constructive peaks in the response of an interferometer. The sensitivity is proportional to the OPD whilst the unambiguous range is inversely proportional to the OPD. Hence there is trade-off between operational range and sensitivity. Figure 2.22 below shows the strain to phase shift conversion ratio for different values of OPD.

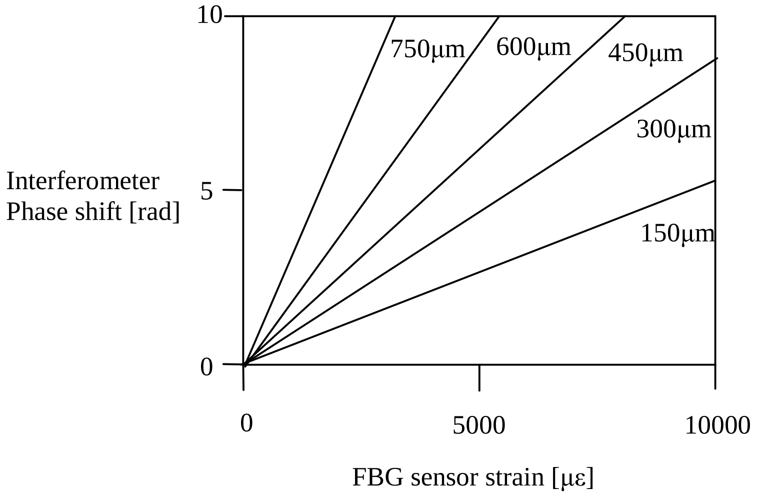

Figure 2.22 Strain to phase shift conversion for an integrated optic Mach-Zehnder detection scheme for various OPDs.
The figure shows the strain to phase shift conversion ratio for different values of OPD (Kersey, Berkoff & Morey 1992).

Demodulation of FBG sensors by interference techniques can prove to be an inexpensive way to achieve high sensitivity and resolution. For a free space OPD of 1cm the typical strain-to-phase response for a FBG sensor operating at 1.55μm is 0.031με/rad. An interferometer can detect phase changes of μrad/√Hz. Under these conditions a demodulating interferometer has a dynamic resolution of 30pε/√Hz. A MZI based demodulator of a single FBG sensor has been demonstrated using a feedback loop (Kersey *et al.*, 1992). The MZI was held in quadrature by a PZT that altered the OPD. The minimum detectable strain was 0.6 nε/√Hz for frequencies from 100Hz to 100kHz.

2.4.2 Comparison of Demodulation Schemes

Temperature fluctuations within an interferometer are a major source of instability. However thermal compensation would allow quasi-static as well as dynamic measurands to be detected. An MZI based FBG sensor demodulator has been demonstrated that includes a local temperature reference grating (Kersey, Berkoff & Morey 1993). Thermal compensation is achieved by measuring the phase difference between the sensor and reference gratings. Using this scheme a quasi-static resolution of 0.05ºC was demonstrated within a 60ºC range.

A fibre base Sagnac loop is created by a 3dB coupler that divides an incident beam and transmits the respective portions in counter-propagating directions around the same loop. The beams then coincide again at the coupler were they interfere. An OPD can be introduced by the use of a highly birefringent (Hi-Bi) fibre as the counter-propagating beams will experience n_f and n_s respectively, the values n_f and n_s being the effective refractive indices of the fibre core for the fast and slow axis respectively. The FSR of a Sagnac loop using Hi-Bi fibre is given by equation 2.11

$$\Delta\lambda = \frac{\lambda^2}{\left(n_s - n_f\right)L} \tag{2.11}$$

where $\Delta\lambda$ is the FSR, λ is the wavelength of operation and L is the length of the fibre loop. Importantly the Sagnac loop is thermally stable compared to other interferometers as the beams traverse the same fibre. The scheme however may demonstrate instability in extreme environments and therefore may need thermal compensation. The configuration of the interferometer is also simple and inexpensive.

A FBG sensor demodulation scheme based on a fibre Sagnac loop has been demonstrated (Chung *et al.* 2001). The loop contained two short lengths of single mode fibre spliced on to a long length of Hi-Bi fibre. A Polarisation State Controller (PSC) modified the polarisation of each beam, one beam was aligned to the slow axis whilst the other to the fast. The difference in refractive indices at the operational wavelength of 1550nm was approximately $2\text{x}10^{-4}$ whilst the length of the fibre was 5m giving a FSR of approximately 2.5nm. The scheme is enhanced by the detection of the power transmitted as well reflected from the loop to provide intensity referencing. The paper reports quasi-static resolution of 2.12 με over a 160με measurement range and a dynamic resolution of 77nε/√Hz at a frequency of 350Hz.

A modification to the scheme has been demonstrated using crystal fibre (Kim & Kang 2004) as illustrated in figure 2.23. A diagram outlining a cross-section of the fibre is shown as is the length of the fibre 44.6cm. The difference in refractive indices between the major axes is approximately 10^{-3}so the FSR at 1550nm is approximately 5nm. The fibre is also known to possess high thermal stability. No information about the temperature stability of the scheme is reported, however in other studies a Sagnac loop using crystal fibre report a change in birefringence with temperature of d(Δn)/dT = $-2\text{x}10^{-9}$/K (Yang *et al.*, 2005). This is more stable by a factor three than a loop constructed of standard birefringent fibre. Again both the powers transmitted through and reflected from the loop are recorded to provide intensity referencing. The scheme demonstrates a quasi-static resolution of 1.54με over a 1000με range.

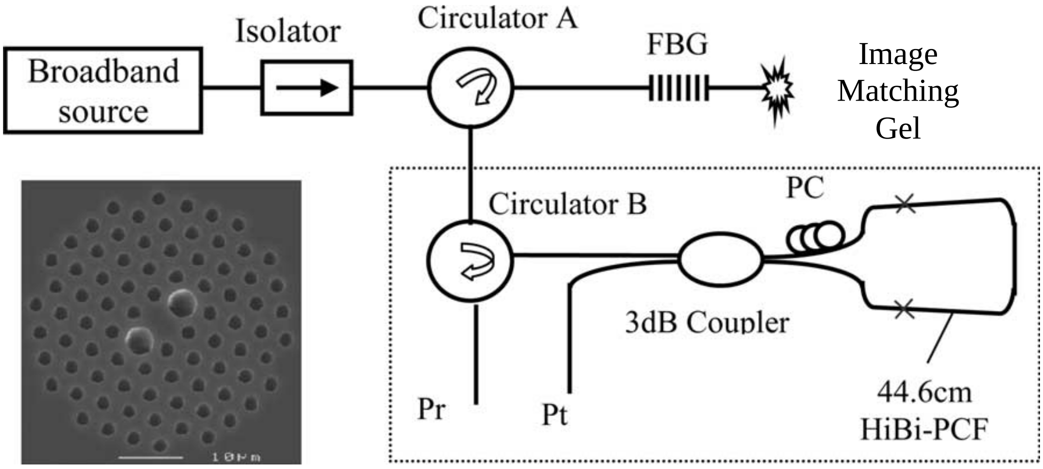

Figure 2.23 FBG sensor demodulation by a fibre Sagnac loop interferometer based on Highly Bi-refringent Photonic Crystal Fibre (HiBi-PCF).
Within the Sagnac loop the counter-propagating beams will experience n_f and n_s respectively. These are effective refractive indices of the fibre core for the fast and slow axis respectively. The FSR of the resulting interferometer at 1550nm is approximately 5nm (Kim & Kang 2004).

The use of a fibre based Sagnac loop provides a stable interferometer for the demodulation of a single FBG sensor. Multiple cascaded Sagnac loops however have been demonstrated to demodulate a two element FBG sensor array (Kim *et al.* 2006). The scheme is shown in figure 2.24.

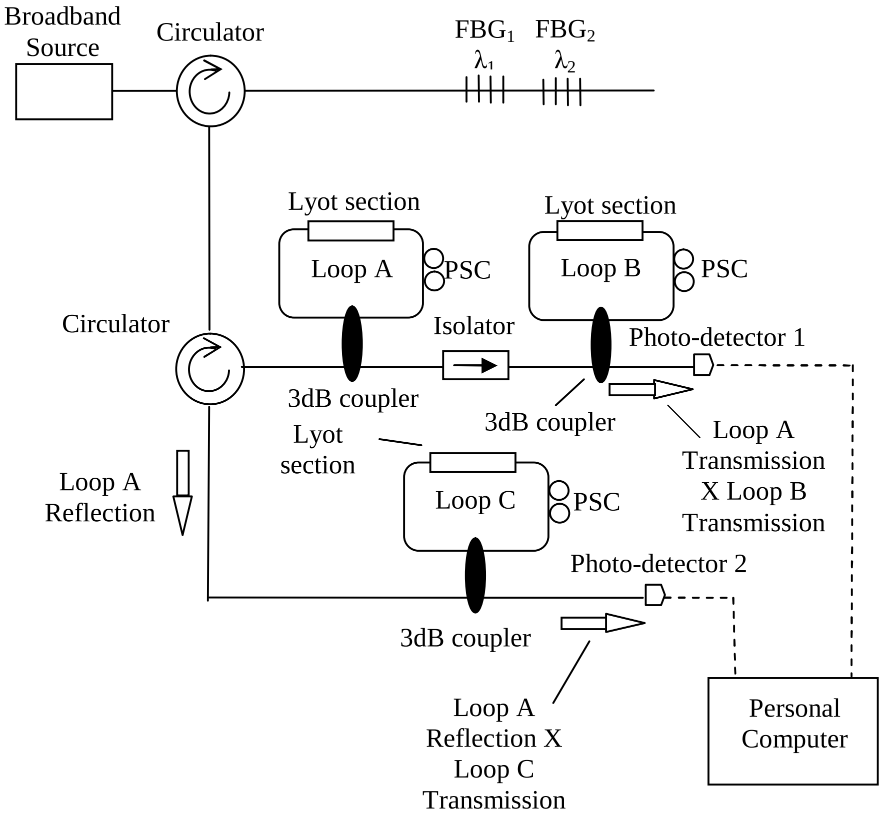

Figure 2.24 A two element FBG Sensor array demodulation scheme based on cascaded fibre Sagnac loops**.**
The configuration allows multiplication of the transmission spectra of loops A and B. The reflection of A and the transmission of C are also multiplied. A Polarisation State Controller (PSC) within each loop is used to change its phase bias so the minima of the spectral responses within a pair coincide. This creates a sharp edge within the multiplied spectra with approximately a 20dB change over a 1.5nm range which used for the demodulation of an FBG sensor (Kim *et al.* 2006).

The configuration consists of three Sagnac loops, two circulators, two detectors and an isolator. Each of the Sagnac loops is connected via a 3dB coupler and contains a Lyot section and a Polarisation State Controller (PSC). The Lyot sections contain multiple lengths of Polarisation Maintaining (PM) fibre between each length is a PSC that changes the orientation of one fibre section with respect to the next.

The transmission and reflection interference spectra of the Sagnac Loops can be found by using Jones matrixes. These are given by equations 2.12 and 2.13

$$T(\lambda) = \cos^2\left(\frac{\pi}{\lambda}\Delta n L_{\text{eff}} + \varphi\right) \qquad \textbf{2.12}$$

and

$$R(\lambda) = 1 - T(\lambda) \qquad \mathbf{2.13}$$

where Δn represents the birefringence of the PM fibre and φ the phase bias of the interferometer. The PSCs within a Lyot section are used to orientate the axes of one length of PM fibre with respect to the next manipulating the effective length L_{eff}. For example a section could contain two different lengths L_1 and L_2 of fibre. If the orientation between the major axes is 0° then $L_{\mathrm{eff}}=L_1+L_2$, if however the orientation is 90° then $L_{\mathrm{eff}}=L_1-L_2$. The FSR of an individual Sagnac loop is given by

$$\Delta\lambda_{\text{peak-peak}} = \frac{\lambda^2}{\Delta n L_{\mathrm{eff}}} \qquad \mathbf{2.14}$$

where all variables have been defined except for λ which is the wavelength of operation. The minima of the spectral response can occur at any wavelength. The PSC shown in the figure within each loop but outside a Lyot section changes the phase bias φ so the minima occur at a desired wavelength. The configuration allows the interference spectra from loops A and B to be multiplied together. The reflection of loop A and the transmission of C are also multiplied. The phase bias associated with each loop can be manipulated so that the minima of the spectra within a pair coincide. This creates a sharp edge in the multiplied spectra, approximately a 20dB intensity change over a 1.5nm wavelength range which is used for the demodulation of an FBG sensor element.

No performance figures were reported; however the scheme demonstrates the principle of FBG sensor array demodulation by cascaded Sagnac loops. The scheme can be scaled to interrogate an FBG sensor array with more elements by adding more loops.

An Array Wave-Guide (AWG) is a de-multiplexing device originally designed for telecommunications applications. An AWG is fabricated on a single chip and consists of multiple waveguides of specific but different lengths. Multiple wavelengths traversing a single fibre are then simultaneously coupled into all elements of the waveguide array. Upon exiting the array individual wavelengths constructively interfere at different points predetermined by the optical path difference introduced by the waveguide elements as the different wavelengths of light do not interfere. These points coincide with elements of a detector array, thus enabling de-multiplexing. The principle AGW operation is shown in figure 2.25

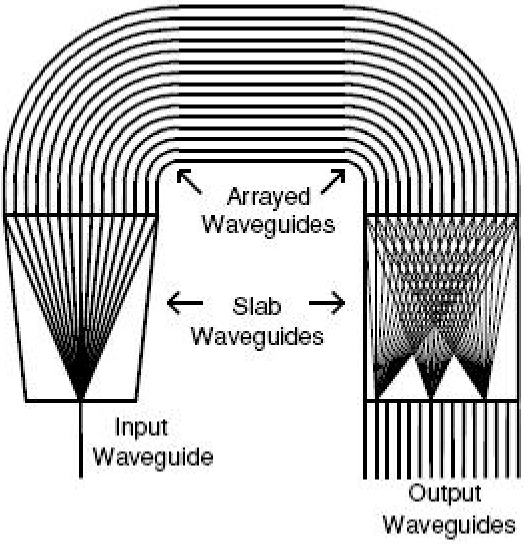

Figure 2.25 The operation of an Array Wave Guide (AWG).
Multiple wavelengths traversing a single fibre are simultaneously coupled into all elements of a waveguide array. The individual wavelengths after exiting the fibre then constructively interfere at different points predetermined by the optical path difference introduced by the waveguide elements. These points coincide with elements of a detector array, thus enabling de-multiplexing (Norman, Webb & Pechstedt 2005).

A Bookham Technology AWG originally designed for telecommunication applications has been used for the demodulation of an FBG sensor (Norman, Webb & Pechstedt 2005). The AWG possesses narrow channels of 250pm that are 1.6nm apart. When demodulating, the reflected Bragg spectrum overlaps with different channel pass-bands increasing or decreasing power within a specific channel depending on the instantaneous Bragg wavelength. The optical bandwidth of a channel is small in comparison with the wavelength range of an FBG sensor, so the AWG requires to be calibrated to relate power in consecutive channels to an instantaneous Bragg wavelength. The quasi-static resolution was demonstrated to be 0.35με achieved over a range of 1890με. The use of an NTT Electronics AWG for FBG demodulation has also been reported for the detection high speed signals. This scheme could detect a signal originally applied by an ultrasonic cleaner of 27.5kHz (Fujisue, Nakamura & Ueha 2006).

2.4.3 Summary of Demodulation Schemes Based On Interferometer Devices

Fibre based two beam interferometers are preferred for demodulation schemes as no intensity is lost in reflections at material interfaces. Such devices however are thermally unstable so only dynamic measurands can be detected by holding the interferometer in quadrature within a feedback loop. Temperature compensation however can be achieved by utilizing a reference grating with a demodulating interferometer. The use of Sagnac loops also improves the thermal stability of fibre based schemes. These devices also allow simple integration with WDM techniques by cascading loops.

At present AWGs are specifically fabricated for telecommunication applications. This implies that demodulation requires processing of signal information in various channels to determine the instantaneous Bragg wavelength however this means an AWG based demodulation scheme will readily integrate to WDM techniques. AWGs are also monolithic devices that require thermal compensation to be built in. The interferometer based demodulation schemes that have been detailed earlier in the section have been summarised in Table 2.5.

Table 2.5 Summary of demodulation schemes based on an interferometer.

	Mach Zender Interferometer	**Sagnac Loop**	**AWG**
Resolution	0.05°C(1)	2.12με	0.35με
Range	60°C(1,2)	160με(2)	1890με(2)
Dynamic Range	Unavailable	77nε/√Hz@350Hz	Unavailable

(1) Requires referencing grating.
(2) Represents range reported not maximum possible range.

2.5. Multiplexing Techniques

2.5.1 Introduction

An obvious choice for the multiplexing of FBG sensors is Wavelength Division Multiplexing (WDM). Within an FBG sensor demodulation scheme the illuminating source usually has an optical bandwidth much greater than the operational wavelength range of a single sensor. This means the source can be used to illuminate an array of sensors each allocated a different wavelength range with a stop band between consecutive ranges to limit crosstalk. An FBG sensor array demodulation scheme however is limited by the source bandwidth and needs to differentiate the signals from each of the sensor elements.

Within Time Division Multiplexing (TDM) techniques FBG sensors are fabricated at the same quiescent wavelength and operate within the same wavelength range. The FBG elements however are separated by long lengths of fibre whilst the illuminating source is pulsed. The Bragg signals then arrive at the detector within allocated time-slots. Within TDM schemes however the pulsed source is still broadband with an optical bandwidth much greater than the operating range of the sensor array. To maximise the use of the spectrum therefore combined WDM/ TDM schemes are being investigated.

A technique similar to TDM is Frequency Division Multiplexing (FDM). Here the source is modulated with different frequencies that allow the Bragg signals to be differentiated in the frequency domain. The Bragg signal is detected throughout a cycle increasing Signal to Noise Ratio (SNR) and therefore performance.

2.5.2 Wavelength-Division-Multiplexing (WDM) Techniques

Sensor array demodulation schemes based on free space or fibre based passive filters require a device to differentiate the Bragg signals from the sensor elements. This is possible with a device such an AWG however these are not designed to be used within demodulation schemes see section 2.4. Passive filter demodulation schemes therefore integrate poorly into WDM techniques. It is possible however to extend the filter scheme based on Triangular FBGs (TFBGs) to cascade the devices and allow the demodulation of a sensor array. This is similar to the cascaded Sagnac loop de-multiplexing scheme outlined in section 2.4.

Active filter or source schemes allow multiple FBGs to be demodulated. The filter or source can be scanned through a wavelength range that hosts multiple FBG sensors. The wavelength range that can be scanned however limits the number of sensor elements that can be addressed. The resolution of the Bragg wavelength can be improved by using algorithms such as the Centroid Detection Algorithm (CDA) and the Zero Crossing Point (ZCP) algorithm applied to the of the differential of a recorded scan. The dynamic range of the scheme is limited by the scan rate however fibre based FP filters are now available with rates that exceed 2kHz whilst laser sources have rates that can exceed 20kHz.

Demodulation schemes based on simple interferometers are emerging that allow uncomplicated scaling for the demodulation of WDM sensor arrays. An example is the cascaded Sagnac loops detailed section 2.4.

The number of sensor elements within WDM array demodulating schemes is limited by the optical bandwidth of the illuminating source or the tuning range of the demodulating narrowband device. In the case of interferometer based schemes the unambiguous range is the limiting factor. The majority of the demodulating schemes discussed are intensity based, the instantaneous Bragg wavelength being changed into an analogue electrical value. To minimise the effect of noise the electrical value has to be maximised. A sensor array therefore has to be illuminated with a source of high intensity and the FBG reflectivity has to be close to 100%.

2.5.3 Time-Division-Multiplexing (TDM) techniques

Illumination for TDM schemes is from a pulsed high intensity broadband source. Sensors within the schemes can also possess the same instantaneous Bragg wavelength so an upstream sensor will disturb the signal reflected from a downstream sensor. This phenomenon causes crosstalk that limits the number of sensors that can be supported by a TDM scheme. To minimise this disturbance the reflectivity of the sensors within such schemes are limited to approximately 10%.

A scheme has been demonstrated using a mode locked laser (Putnam *et al.*, 1998) however an inexpensive option using a Semiconductor Optical Amplifier (SOA) and an EDFA has also been reported (Cooper & Smith 2003). The SOA is pulsed to provide a broadband source whilst the EDFA provides amplification. The signal level received from some elements however was near to the noise floor. To rectify this problem source intensity was increased however the EDFA saturated at high pulse intensities causing a broadening of the spectrum. This caused a decrease in the power spectral density and therefore a reduced Bragg signal level. To overcome this problem a configuration with two EDFAs was tested one located before sensor illumination and one after. This allowed post illumination amplification of the Bragg signals so increasing signal levels without broadening. The instantaneous Bragg wavelengths can possess the same. The configuration is shown in figure 2.26.

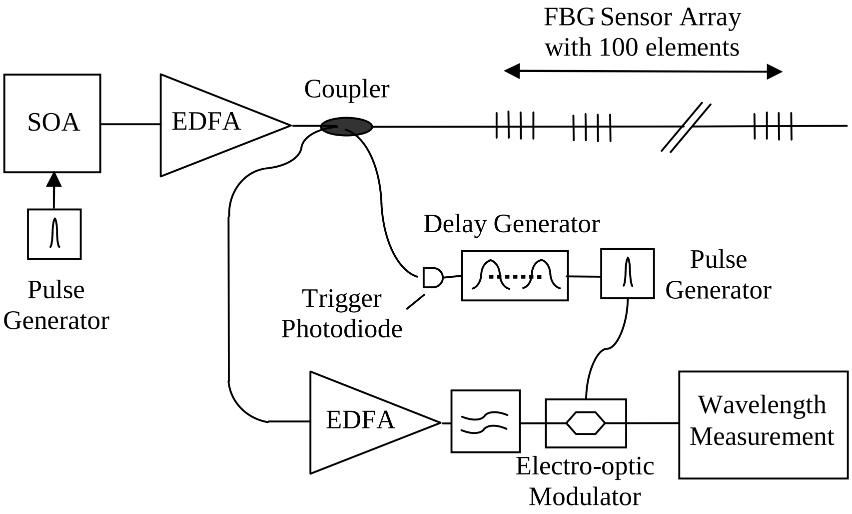

Figure 2.26 A TDM based FBG array demodulation scheme. Light from a pulsed source is amplified by two Erbium Doped Fibre Amplifiers (EDFAs) before and after sensor array illumination. A delay line triggers an Elctro-optic modulator to provide optical gating. Demodulation is provided by a passive filter (Cooper & Smith 2003).

A pulse generator feeds an SOA to provide a pulsed low power broadband source. Two EDFAs provide signal amplification before and after sensor array illumination. An Electro-optic modulator is triggered from the source via a delay line to provide optical gating. Demodulation is provided by a passive filter.

The use of an EDFA introduced a noise source into the system. The noise was due to spontaneous emission from the EDFA being amplified, therefore called Amplified Spontaneous Emission (ASE). Different spectral aspects of the noise mix to create ASE self beat noise and therefore fluctuations at the detector. The fluctuations are intensity noise that limits the resolution of the scheme. This can be overcome by using short duty cycle pulses, the duty cycle being the ratio of the pulse time to the period. The specific configuration allowed 100 FBG sensors to be demodulated. The dynamic resolution reported was 38 nε/Hz$^{1/2}$ at 300 Hz no quasi-static or crosstalk figures are available.

Recently a scheme has been reported that uses only one SOA (Lloyd *et al.* 2005). Cavities are created between four elements in a sensor array and a back reflector. This allows signal amplification by multiple passes of the SOA. The configuration is shown in figure 2.27. A pulse generator drives the SOA, the pulses being synchronised to the reflected Bragg signals. The Bragg signals reach equilibrium when the amplification introduced by the SOA is balanced by the round trip loss. Demodulation is by a simple passive filter and the system incorporates an intensity referencing technique. The reflectivity of the FBG sensors is limited to 4% with a FWHM optical bandwidth of 70pm so limiting crosstalk. The quasi-static resolution is given to be 0.1ºC over a 60ºC range. No crosstalk figures were reported.

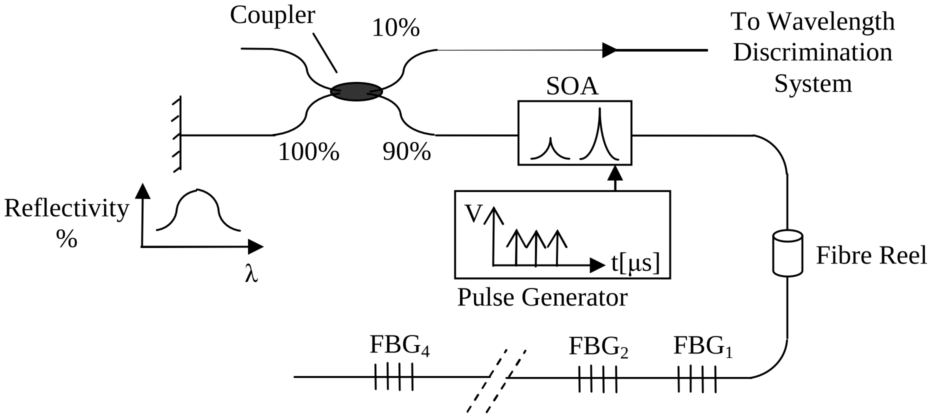

Figure 2.27 A TDM based FBG array demodulation scheme based on a single SOA. The SOA is driven by a pulsed generator. The pulses are synchronised to the reflected Bragg signals so the signal intensity reaches equilibrium when the amplification introduced by the SOA is balanced by the round trip loss. The system incorporates an intensity referencing technique and demodulation is by a simple passive filter (Lloyd *et al.* 2005).

2.5.4. Frequency Division Multiplexing (FDM) Techniques

An FDM scheme is reported that relies on a ramped RF oscillator modulating a broadband source (Chan, Jin & Demokan 2000). The change in frequency modulating the source is represented by a saw-tooth waveform. The frequency of the signal reflected by an element is then mixed with the source to produce a beat frequency. There is a constant time lag between the received and source signal due to the round-trip delay leading to a constant beat frequency, the round-trip delay to another sensor element is different producing a separate beat frequency. Demodulation is achieved by scanning a tuneable filter and correlating the position in the scan to the intensity peak of the beat frequency. The scheme is illustrated in figure 2.28 and is referred to as the Frequency Modulated Continuous Wave (FMCW) technique. Three FBG sensors with the same quiescent wavelength where reported to be successfully de-multiplexed. A six element array deployed in pairs possessing the same quiescent wavelength was also de-multiplexed. The scheme demonstrated a 2με quasi-static strain resolution. No range or dynamic resolution figures were reported. The crosstalk between channels was reported to be -30dB.

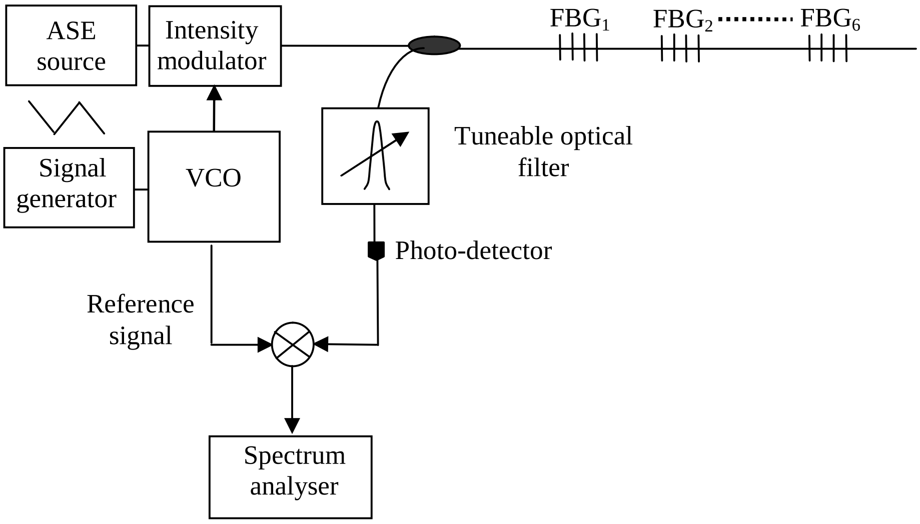

Figure 2.28 The Frequency Modulated Continuous Wave (FMCW) de-multiplexing and demodulation scheme.

The source is modulated by a ramped frequency represented by a saw-tooth waveform. The frequency of the source and the reflected signals are mixed to produce a beat frequency. Separate beat frequencies are produced by the different sensor elements due to a different round trip delays (Chan, Jin & Demokan 2000).

A similar technique modulates the broadband source with pulse of chirped radio frequencies and is referred to as the Chirped-Pulse Frequency Modulation (C-PFM) (Breglio *et al.,* 2006) technique. The reflected signal is then correlated with a reference pulse. A difference in round-trip delay implies that the each sensor signal will be separated in time. Demodulation is achieved with a simple edge filter and the scheme incorporates an intensity referencing technique. The reported quasi-static resolution for strain and temperature was 1με over a range of 1000με and 0.1ºC over a range of 100ºC respectively. A two element FBG sensor array was demodulated. The maximum crosstalk between the channels was reported to be -10dBs.

2.5.5 Combined WDM/ TDM Techniques

The number of elements in an FBG sensor array that can be addressed by TDM techniques can be as many as 100 (Cooper and Smith 2003) as shown in section 2.5.2. Combined TDM/ WDM schemes have even greater potential as the use of a broadband spectrum is maximised. A recent study has modelled a TDM/WDM scheme to assess the potential (Nunes *et al.* 2007). A combined WDM/TDM sensor de-multiplexing scheme is represented in figure 2.29.

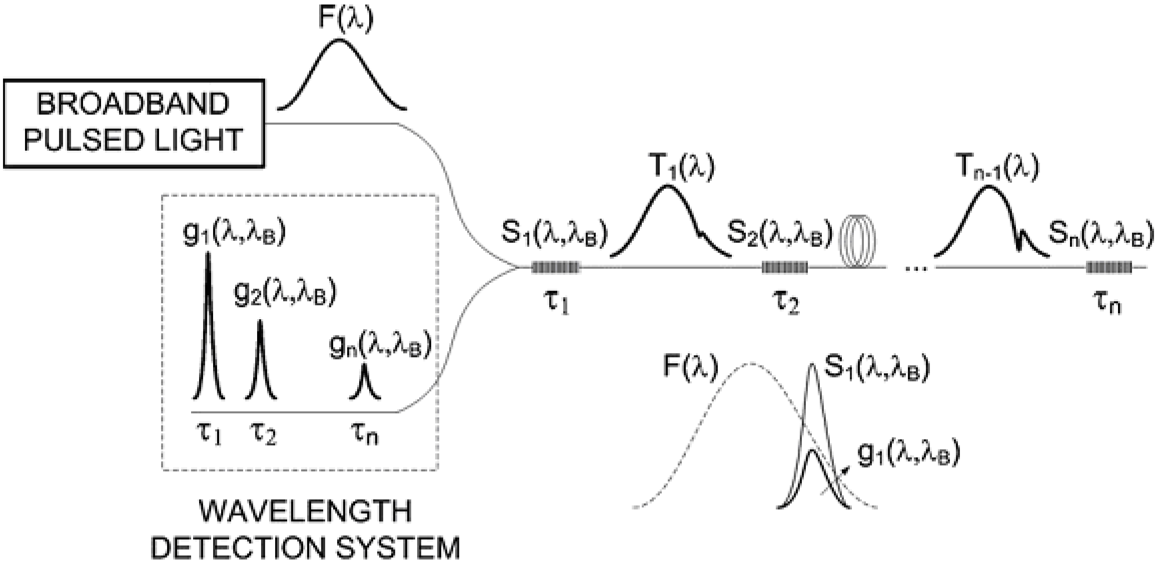

Figure 2.29 Combined WDM/TDM Multiplexing.
The source spectrum passes through identical sensors $S_i(\lambda,\lambda_B)$ so the transmitted spectrum $T_i(\lambda)$ is disturbed. Consequently the reflected spectrum $g_{i+1}(\lambda, \lambda_B)$ generated by the interrogation of the sensor group $S_{i+1}(\lambda,\lambda_B)$ will also be disturbed. The groups of sensors $S_i(\lambda,\lambda_B)$ and $S_{i+1}(\lambda,\lambda_B)$ separated by a distance that allows the time discrimination τ_i (Nunes *et al.* 2007)..

The broadband source $F(\lambda)$ can interrogate a group of identical sensors $S_i(\lambda,\lambda_B)$ with a Bragg wavelength λ_B and a reflectivity r_i positioned along a fibre, separated by a distance that allows the time discrimination τ_i.. When the source spectrum passes through the identical sensors the transmitted spectrum $T_i(\lambda)$ is disturbed and consequently the reflected spectrum $g_{i+1}(\lambda, \lambda_B)$ generated by the interrogation of the sensor group $S_{i+1}(\lambda,\lambda_B)$ will also be disturbed. The spectrum of light reaching sensor group *n*, after passing through (*n*-1) sensors is given by equation 2.15, multiple reflections are not considered.

$$T_{n-1}(\lambda,\lambda_{\mathrm{B}}) = F(\lambda)\left[\prod_{\mathrm{i}=1}^{n-1}(1-r_{\mathrm{i}}S_{\mathrm{i}}(\lambda,\lambda_{\mathrm{B}}))\right] \tag{2.15}$$

The reflected spectrum reaching the wavelength detection system from the sensor group $S_{\mathrm{i+1}}(\lambda,\lambda_B)$ is given by equation 2.16.

$$g_{\mathrm{n}}(\lambda,\lambda_{\mathrm{B}}) = r_{\mathrm{n}}S_{\mathrm{n}}(\lambda,\lambda_{\mathrm{B}})F(\lambda)\left[\prod_{\mathrm{i}=1}^{n-1}(1-r_{\mathrm{i}}S_{\mathrm{i}}(\lambda,\lambda_{\mathrm{B}}))\right]^2 \tag{2.16}$$

Where $F(\lambda)$ is the source spectrum, $S_{\mathrm{i}}(\lambda,\lambda_B)$ and $S_{\mathrm{n}}(\lambda,\lambda_{\mathrm{B}})$ are the normalised FBG sensor spectra, and r_{i} and r_{n} are the reflectivity of sensor groups i and n respectively, where i=1..(n-1).

The reflection peak from an FBG illuminated with a distorted spectrum will present a deviation compared with the reflection generated when illuminated by the original source. The deviation D is given by equation 2.17

$$D = \lambda_{\mathrm{B}} - \lambda_{\mathrm{BI}} \tag{2.17}$$

where λ_{B} and λ_{BI} are the Bragg wavelength measured when the Bragg grating is interrogated using undistorted and distorted spectrum respectively. The deviation is then calculated for peak position, as used in active scanning schemes, and passive filter schemes. Equations 2.16 and 2.17 are used to calculate the deviation. The results consider the worse case when all of the Bragg signals are centred at 1545nm. The wavelength range of operation is from 1543nm to 1547nm. Figure 2.30 shows the deviation of fixed filter and peak positions schemes demodulating arrays of 40 and 100 sensors. All sensors possess a reflectivity of 1%.

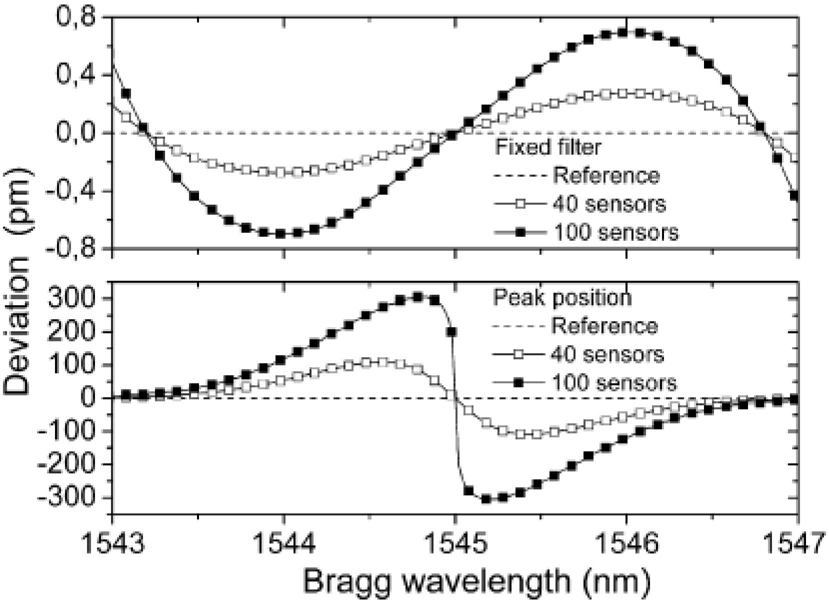

Figure 2.30 Maximum deviation of Bragg wavelength.
This is upon demodulating 40 and 100 identical sensors with 1% reflectivity using fixed filter and active scanning demodulation techniques (Nunes *et al.* 2007).

The results indicate that a fixed filter scheme creates considerably less deviation. In reality the Bragg wavelengths will be centred at random positions within the operating range. Here the deviation increases to a 5pm maximum for an array of 100 sensors. Considering a maximum deviation of 5pm a combined TDM/WDM scheme using fixed filters across a 75nm range at 1550nm can easily accommodate 10 different nominal wavelengths leading to a demodulation scheme with a capacity of up to 1000 FBG sensors.

2.6 Conclusions

Recently reported passive filter and interferometer based demodulation schemes are similar. They are both stable, possess a potential for high speed and require intensity referencing techniques to compensate for fluctuations in source and fibre losses. Thermal drift, an issue for earlier interferometer based schemes, has been overcome by the use of a reference grating. Recently thermal stable Sagnac loops have also been investigated for demodulation. Both types of scheme however demonstrate quasi-static resolutions of approximately 1με for strain. The resolution being limited by noise introduced to the sensor signals by the photo-detector. Dynamic measurements for passive filters have shown bandwidths up to 100kHz whilst interferometers demonstrate dynamic resolutions of 0.6nε/√Hz for frequencies in the range 100Hz-100kHz. Both do not readily integrate to WDM techniques however a cascaded Sagnac loop configuration can demodulate a two element wavelength multiplexed sensor array. The cascaded configuration can be extended to passive filters for the schemes based on Triangular FBGs (TFBGs) for example.

The use of scanning sources and filters imply active demodulation schemes are more complex than passive ones. The dynamic range of the schemes however is limited by the same components. A filter or source can be scanned through a wavelength range to readily demodulate a WDM FBG sensor array. Scanning schemes however can be enhanced by the use of Centroid Detection Algorithms (CDA). In one example when used within an active filter scheme an algorithm achieved approximately a ten fold increase in quasi-static resolution. The performance figures of the active schemes approximate to 1με for strain and 0.1°C for temperature. The schemes also possess the potential for a high dynamic range. Modern fibre based Fabry Perot filters can operate at 2kHz whilst MEMS based external cavity lasers can interrogate a 100nm wavelength range at 20kHz.

Schemes that translate the instantaneous Bragg wavelength into a shift in beam position possess better resolution figures than passive filter schemes. Such schemes are inexpensive, stable and do not require intensity referencing. Here however the intensity of the Bragg signal is to be maximised as the resolution depends on incident beam intensity. They can be readily integrated into WDM techniques as multiple beam positions can be tracked. Their bandwidths however are severely limited by the integration time of the linear array or matrix of photo-detectors tracking the beam position.

A comparison for the different demodulations schemes is shown in Table 2.6.

Table 2.6 Comparison of demodulation schemes

	Passive Filter	**Tuneable Filter**	**Tuneable Laser**	**Interferometric**	**Wavelength to Spatial Translators**
Resolution(1)	0.5-6με	4-20με, 0.2-0.6ºC(2)	1.39-10με(2)	0.35-2.12με	0.6-2με(2)
Range	8000-10000με	Unavailable(3)	Unavailable(3)	Unavailable(3)	2500με
Bandwidth	High	Medium(4)	Medium(4)	High	High
Stability	Good(5)	Good	Good	Good(5)	Good
WDM Compatibility	Low	High	High	Low	High

(1) Quoted in με and ºC where available.
(2) Performance is enhanced by peak detection algorithms.
(3) Maximum range unavailable as it is not reported in references.
(4) Limited by the maximum scanning speeds of approximately 2kHz.
(5) Requires intensity referencing scheme.

The optical bandwidth of the source or the tuning range of the narrowband device limits the number of sensor elements within WDM array demodulating schemes. The unambiguous range is the limiting factor in the case of interferometer based demodulating schemes. The majority of the schemes discussed are intensity based, the instantaneous Bragg wavelength being changed into an analogue electrical value. To minimise the effect of noise the electrical value has to be maximised. A sensor array therefore has to be illuminated with a source of high intensity and the FBG reflectivity has to be close to 100%.

TDM techniques have the potential of de-multiplexing a large number of sensor elements. The number of elements supported however is limited by sensors of high reflectivity. The effects of crosstalk can be limited by reducing the reflectivity of the sensors however this increases the SNR of individual Bragg signals. Noise present in TDM demodulation schemes however can be minimised by using short duty cycle pulses.

FDM techniques use the difference in round-trip delay to differentiate between individual array elements as for TDM. They detect power throughout each cycle and therefore demonstrate an increased SNR in comparison to TDM techniques.

Combined WDM/TDM schemes demonstrate the greatest potential to support the largest number of sensor elements. This is because the schemes make the most efficient use of the illuminating spectrum. A detailed study concludes that a combined WDM/TDM scheme can support 1000 FBG sensors if passive filter demodulation techniques are used.

A comparison for the different de-multiplexing techniques studied is shown in Table 2.7.

Table 2.7 Comparison of de-multiplexing techniques

	WDM	**TDM**	**FDM**	**WDM/SDM**	**WDM/TDM**
Capacity (No of FBGs)	5(1.4)	100(5)	6(6)	60(7)	1000(2.8)
Use of optical power	Good	Poor(3)	Poor(3)	Good	Good

(1) Limited by the optical bandwidth of the illuminating source.
(2) Theoretical maximum number of FBGs using respective multiplexing scheme
(3) The quiescent Bragg wavelengths of all FBGs are the same and their reflectivity limited.
(4) (Chehura 2009).
(5) (Cooper & Smith 2003).
(6) (Chan, Jin & Demokan 2000).
(7) (Davis *et al.* 1996).
(8) (Nunes *et al.* 2007).

Active demodulation schemes are expensive and possess slow response times however scanning filters and sources are becoming available that have the potential for high speed operation. These need to be evaluated as possible sensor array demodulation devices. Passive filters in contrast are inexpensive and have the potential for high speed but do not readily integrate with WDM techniques. This would be a natural partner as a filter element would match the wavelength range of operation of a FBG sensor element within an array. A de-multiplexing device however would be required to differentiate the signal elements. The resolution is limited in such schemes by noise introduced by the photo-detector. It is possible to integrate the filter scheme with TDM techniques however this would be expensive due to the need for a pulsed source. An FBG sensor array demodulation scheme based on holograms allows ready integration with WDM as each holographic element will diffract a matched signal element through a separate angle to a dedicated detector. The holographic transfer function will then provide signal element demodulation. All holograms will be hosted within a single block of VH material. This type of demodulation scheme is intended to be demonstrated within this thesis.

A crystal of $BaTiO_3$ is available for experimentation however this VH material does not readily allow holograms to be fixed and those inscribed will be erased overnight by thermal excitation of carriers. A means to inscribe holograms therefore needs to be incorporated into experiments. To create holograms of sufficient diffraction efficiency access has to be gained to the r_{42} electro-optic coefficient therefore the inscribing beams and the sensor signals have to be of a specific polarisation. Furthermore demodulation relies on the transfer function of the hologram to be of a particular bandwidth therefore factors effecting bandwidth and diffraction efficiency need to be understood. Finally the inscriptions of a hologram will partial erase any already hosted within the material so a writing schedule is required so that all elements in the holographic array possess the same diffraction efficiency.

2.7 References

Agethen, M., Keiper, D., Janssen, G., Brennemann, A., Velling, P., Van den Berg, C. & Bertenburg, R.M. 2002, "InGaAs PIN detectors for frequencies above 100 GHz", *International Conference on InP and Related Material*, pp. 673-676.

Awazu, K., Kawazoe, H. & Yamane, M. 1990, "Simultaneous generation of optical absorption bands at 5.14 and 0.452 eV in 9 SiO2: GeO2 glasses heated under an H2 atmosphere", *Journal of Applied Physics*, vol. 68, no. 6, pp. 2713-2718.

Ball, G.A., Morey, W.W. & Cheo, P.K. 1994, "Fiber Laser Source Analyzer for Bragg Grating Sensor Array Interrogation", *Journal of Lightwave Technology.,* vol. 12, no. 4, pp. 700-703.

Bilodeau, F., Johnson, D.C., Theriault, S., Malo, B., Albert, J. & Hill, K.O. 1995, "All-fiber dense-wavelength-division multiplexer/demultiplexer using photoimprinted Bragg gratings", *IEEE Photonics Technology Letters*, vol. 7, no. 4, pp. 388-390.

Bilodeau, F., Malo, R., Albert, J., Johnson, D.C., Hill, K.O., Hibino, Y., Abe, M. & Kawachi, M. 1993, "Photosensitization of optical fiber and silica-on-silicon/silica waveguides", *Opt. Lett.*, vol. 18, no. 12, pp. 953-955.

Brady, G.P., Hope, S., Ribeiro, A.B.L., Webb, D.J., Reekie, L., Archambault, J.L. & Jackson, D.A. 1994, "Demultiplexing of fibre Bragg grating temperature and strain sensors", *Optics Communications*, vol. 111, no. 1-2, pp. 51-54.

Breglio, G., Irace, A., Cusano, A. and Cutolo, A. (2006), "Chirped-pulsed frequency modulation (C-PFM) for fiber Bragg grating sensors multiplexing", *Optical Fiber Technology*, vol. 12, pp. 71-86.

Chan, P.K.C., Jin, W. & Demokan, M.S. 2000, "FMCW multiplexing of fiber Bragg grating sensors", *IEEE Journal on Selected Topics in Quantum Electronics*, vol. 6, no. 5, pp. 756-763.

Chen, S. 1997, "Digital spatial and wavelength domain multiplexing of fibre Bragg grating based sensors", *Proceeding of the Optical Fibre Sensors Conference (OFS-12)*, pp. 448-461.

Chehura, E 2009 Personal communication

Chung, S., Kim, J., Yu, B.-. & Lee, B. 2001, "A fiber Bragg grating sensor demodulation technique using a polarization maintaining fiber loop mirror", *IEEE Photonics Technology Letters*, vol. 13, no. 12, pp. 1343-1345.

Cooper, D.J.F. & Smith, P.W.E. 2003, "Simple high-performance method for large-scale time division multiplexing of fibre Bragg grating sensors", *Measurement Science and Technology*, vol. 14, no. 7, pp. 965-974.

Coroy, T., Ellerbrock, P.J., Measures, R.M. & Belk, J.H. 1995, "Active wavelength demodulation of Bragg fibre-optic strain sensor using acousto-optic tunable filter", *Electron. Lett.,* vol. 31, no. 18, pp. 1602-1603.

Coroy, T, 1997 "Peak detection demodulation of a Bragg fiber optic sensor using gain-coupled distributed feedback tunable laser", *Proceeding of the Optical Fibre Sensors Conference (OFS-12),* pp. 210-212.

Davis, M.A., Bellemore, D.G., Putnam, M.A. & Kersey, A.D. 1996, "Interrogation of 60 fibre Bragg grating sensors with microstrain resolution capability", *Electron. Lett.,* vol. 32, no. 15, pp. 1393-1394.

Davis, M.A., Bellemore, D.G., Kersey, A.D., Putnam, M.A., Friebele, E.J., Idriss, R.L. & Kodindouma, M.B. 1996, "High-sensor-count Bragg grating instrumentation system for large-scale structural monitoring applications", *Proc. SPIE Int. Soc. Opt. Eng*., vol 2718, pp. 303-319.

Davis, M.A. & Kersey, A.D. 1995, "Matched-Filter Interrogation Technique for Fiber Bragg Grating Arrays", *Electron. Lett.,* vol. 31, no. 10, pp. 822-823.

Davis, M.A. & Kersey, A.D. 1994, "All-Fiber Bragg Grating Strain-Sensor Demodulation Technique using a Wavelength-Division Coupler", *Electron. Lett.,* vol. 30, no. 1, pp. 75-77.

Fallon, R.W., Zhang, L., Everall, L.A., Williams, J.A.R. & Bennion, I. 1998, "All-fibre optical sensing system: Bragg grating sensor interrogated by a long-period grating", *Measurement Science and Technology,* vol. 9, no. 12, pp. 1969-1973.

Fu, J.-., Xiao, L.-., Zhang, Y.-., Zhao, X.-. & Chen, H.-. 2006, "A new method for fiber bragg grating wavelength demodulation with calibration", *Proc. SPIE Int. Soc. Opt. Eng*., vol 6027, pp. 186-191.

Fujisue, T., Nakamura, K. & Ueha, S. 2006, "Demodulation of acoustic signals in fiber bragg grating ultrasonic sensors using arrayed waveguide gratings", *Japanese Journal of Applied Physics, Part 1: Regular Papers and Short Notes and Review Papers,* vol. 45, no. 5, pp. 4577-4579.

Hagemann, V., Trutzel, M.N., Staudigel, L., Rothhardt, M., MuÌˆller, H.-. & Krumpholz, O. 1998, "Mechanical resistance of draw-tower-Bragg-grating sensors", *Electron. Lett.,* vol. 34, no. 2, pp. 211-212.

Hill, K.O., et al. 1978, "Photosensitivity in optical fibre waveguides: Application to reflection filter fabrication", *Applied Physics Letters,* vol. 32, pp. 647-649.

Hill, K.O., Malo, B., Bilodeau, F., Johnson, D.C. & Albert, J. 1993, "Bragg gratings fabricated in monomode photosensitive optical fiber by UV exposure through a phase mask", *Applied Physics Letters*, vol. 62, no. 10, pp. 1035-1037.

Huang, R., Zhou, Y., Cai, H., Qu, R. & Fang, Z. 2004, "A fiber Bragg grating with triangular spectrum as wavelength readout in sensor systems", *Optics Communications,* vol. 229, no. 1-6, pp. 197-201.

Jackson, D.A., Ribeiro, A.B.L., Reekie, L. & Archambult, J.L. 1993, "Simple Multiplexing Scheme for a Fiberoptic Grating Sensor Network", *Opt. Lett.,* vol. 18, no. 14, pp. 1192-1194.

Jauregui, C. 2004, "Interrogation of fibre Bragg gratings with a tilted fibre Bragg grating", *Measurement Science and Technology,* vol. 15, no. 8, pp. 1596-1600.

James, S.W., Dockney, M.L. & Tatam, R.P. 1996, "Photorefractive volume holographic demodulation of in-fiber Bragg crating sensors", *IEEE Photonics Technology Letters,* vol. 8, no. 5, pp. 664-666.

James, S.W., Tatam, R.P., Fuller, S.R. & Crompton, C. 1999, "Monitoring transient strains on a gun barrel using fibre Bragg-grating sensors", *Measurement Science and Technology,* vol. 10, no. 2, pp. 63-67.

James, S.W. & Tatam, R.P., 2006, "Fibre Optic sensors with Nano-Structured coatings", *Journal of Optics A, Pure and Applied Optics,* 8 S340.

Jovanovic, N., Fuerbach, A., Marshall, M.J., Withford, S.D., Jackson, A., “Stable high-power continuous wave Yb3+-doped silica fiber laser utilizing a point-by-point inscribed fiber Bragg grating,” *Optics Letters*, vol 32, 1486-1489 (2007).

Kalli, K., Brady, G.P., Webb, D.J., Jackson, D.A., Zhang, L. & Bennion, I. 1995, "Wavelength-division and spatial multiplexing using tandem interferometers for Bragg grating sensor networks", *Opt. Lett.,* vol. 20, no. 24, pp. 2544-2546.

Kashyap, R., Armitage, J.R., Wyatt, R., Davey, S.T. & Williams, D.L. 1990, "All-fibre narrowband reflection gratings at 1500nm", *Electron. Lett.,* vol. 26, no. 11, pp. 730-732.

Kersey, A.D., Berkoff, T.A. & Morey, W.W. 1993, "Fiber-optic Bragg grating strain sensor with drift-compensated high-resolution interferometric wavelength-shift detection", *Optics Letters,* vol. 18, no. 1, pp. 72-74.

Kersey, A.D., Berkoff, T.A. & Morey, W.W. 1993, "Multiplexed Fiber Bragg Grating Strain-Sensor System with a Fiber Fabry-Perot Wavelength Filter", *Opt. Lett.,* vol. 18, no. 16, pp. 1370-1372.

Kersey, A.D., Berkoff, T.A. & Morey, W.W. 1992, "High-Resolution Fiber-Grating Based Strain Sensor with Interferometric Wavelength-Shift Detection", *Electron. Lett.,* vol. 28, no. 3, pp. 236-238.

Kersey, A.D., Davis, M.A., Patrick, H.J., LeBlanc, M., Koo, K.P., Askins, C.G., Putnam, M.A. & Friebele, E.J. 1997, "Fiber grating sensors", *Journal of Lightwave Technology,* vol. 15, no. 8, pp. 1442-1462.

Kersey, A.D. & Morey, W.W. 1993, "Multi-element Bragg-grating based fiber-laser strain sensor", *Electron. Lett.,* vol. 29, no. 11, pp. 964-966.

Kiesel, P., Schmidt, O., Johnson, N., Mohta, S., 2006, "Compact, low cost, and high resolution interrogation unit for optical sensors", *Applied Physics Letters,* vol 89. pp 237-240.

Kim, C.-., Lee, T.H., Yu, Y.S., Han, Y.-., Lee, S.B. & Jeong, M.Y. 2006, "Multi-point interrogation of FBG sensors using cascaded flexible wavelength-division Sagnac loop filters", *Optics Express,* vol. 14, no. 19, pp. 8546-8551.

Kim, D.-. & Kang, J.U. 2004, "Sagnac loop interferometer based on polarization maintaining photonic crystal fiber with reduced temperature sensitivity", *Optics Express,* vol. 12, no. 19, pp. 4490-4495.

Lemaire P.J., Atkins, R.M., Mizrahi, V. & Reed, W.A. 1993, "High-Pressure H-2 Loading as a Technique for Achieving Ultrahigh Uv Photosensitivity and Thermal Sensitivity in Geo2 Doped Optical Fibers", *Electron. Lett.,* vol. 29, no. 13, pp. 1191-1193.

Limberger, H.G., Fonjallaz, P.Y. & Salathe, R.P. 1993, "Photosensitivity and Self-Organization in Optical Fibre and Waveguides", *Proc. of SPIE,* vol 2044, pp. 272-274.

Lloyd, G., Everall, L., Sugden, K. & Bennion, I. 2005, "Resonant cavity based fibre Bragg grating sensor interrogation using rationmetric detection", *Optics Communications.,* vol. 244, no. 1-6, pp. 193-197.

Lobo Ribeiro A. B, L.A. Ferreira, M. Tsvetkov, J.L. Santos, 1996 “All-fibre interrogation technique for fibre Bragg sensors using a biconical fibre filter”, *Electron. Lett.* 32 (4),pp 382–383.

Malo, B., Hill, K.O., Bilodeau, F., Johnson, D.C. & Albert, J. 1993, "Point-by-point fabrication of micro-Bragg gratings in photosensitive fibre using single excimer pulse refractive index modification techniques", *Electron. Lett.,* vol. 29, no. 18, pp. 1668-1669.

Melle, S.M., Liu, K.X. & Measures, R.M. 1992, "A Passive Wavelength Demodulation System for Guided-Wave Bragg Grating Sensors", *IEEE Photonics Technology Letters,* vol. 4, no. 5, pp. 516-518.

Meltz, G., Morey, W. W., Glen, W. H. 1989, "Formation of Bragg gratings in optical fibres by a transverse holographic method", *Opt. Lett.,* vol. 14, pp. 823-825.

Meltz, G., Morey, W. W., Glen, W. H. 1991, "Bragg grating formation and germanosilicate fibre photosensitivity", *Proc. of SPIE,* vol 1516, pp. 185-199.

Norman, D.C.C., Webb, D.J. & Pechstedt, R.D. 2005, "Interrogation of fibre Bragg grating sensors using an arrayed waveguide grating", *Measurement Science and Technology,* vol. 16, no. 3, pp. 691-698.

Nunes, L.C.S., Olivieri, B.S., Kato, C.C., Valente, L.C.G. & Braga, A.M.B. 2007, "FBG sensor multiplexing system based on the TDM and fixed filters approach", *Sensors and Actuators, A: Physical*, vol. 138, no. 2, pp. 341-349.

Othonos, A. 1999, *Fiber Bragg gratings : fundamentals and applications in telecommunications and sensing,* Artech House, Boston, Mass.; London.

Paterno, A.S., Haramoni, N., Silva, J.C.C. & Kalinowski, H.J. 2007, "Highly reliable strain-tuning of an Erbium-doped fiber laser for the interrogation of multiplexed Bragg grating sensors", *Optics Communications,* vol. 273, no. 1, pp. 187-192.

Putnam, M. A., Dennis, M. L., Duling, I. N., Askins, C. G. and Friebele, E. J. (1998), "Broadband square-pulse operation of a passively mode-locked fiber laser for fiber Bragg grating interrogation", *Optics Letters,* vol. 23, no. 2, pp. 138-140.

Rao, Y.J. 1997, "In-fibre Bragg grating sensors", *Measurement Science and Technology,* vol. 8, no. 4, pp. 355-375.

Reekie, L., Mears, R.J., Payne, D.N. & Poole, S.B. 1986, "Tuneable single-mode fibre lasers", *Journal of Lightwave Technology,* vol LT4, pp.956-957.

Venghaus. R, 2006, *Wavelength Filters in Fibre Optics (Springer Series in Optical Sciences),* 1st ed, Springer.

Volanthen, M., Geiger, H., Xu, M. G. and Dakin, J. P. 1996, "Simultaneous monitoring of multiple fibre gratings with a single acousto-optic tunable filter", *Electronics Letters,* vol. 32, no. 1, pp. 1228-9.

Weis, R.S., Kersey, A.D. & Berkoff, T.A. 1994, "A 4-Element Fiber Grating Sensor Array with Phase-Sensitive Detection", *IEEE Photonics Technology Letters,* vol. 6, no. 12, pp. 1469-1472.

Williams, D.L., Davey, S.T., Kashyap, R., Armitage, J.R. & Ainslie, B.J. 1992, "Direct observation of UV induced bleaching of 240 nm absorption band in photosensitive germanosilicate glass fibres", *Electron. Lett.,* vol. 28, no. 4, pp. 369-371.

Wilson, A., James, S.W. & Tatam, R.P. 2001, "Time-division-multiplexed interrogation of fibre bragg grating sensors using laser diodes", *Measurement Science and Technology,* vol. 12, no. 2, pp. 181-187.

Yamashita, S. & Inaba, A. 2004, "FBG laser sensor with intracavity dispersive fibre based on mode-locking frequency interrogation", *Measurement Science and Technology,* vol. 15, no. 8, pp. 1536-1538.

Yang, X., Chun-Liu Zhao, Peng, Q., Zhou, X. and Lu, C. (2005), "FBG sensor interrogation with high temperature insensitivity by using a HiBi-PCF Sagnac loop filter", *Optics Communications,* vol. 250, no. 1, pp. 63-8.

Yun, B.F., Wang, Y.P., Li, A.M. & Cui, Y.P. 2006, "Tunable fiber laser based fiber Bragg grating strain sensor demodulation system with enhanced resolution by digital signal processing", *Microwave Opt Technol Lett,* vol. 48, no. 7, pp. 1391-1393.

Zhang, Q., Brown, D. A., Kung, H., Townsend, J. E., Chen, M., Reinhart, L. J. and Morse, T. F. (1995), "Use of highly overcoupled couplers to detect shifts in Bragg wavelength", *Electronics Letters,* vol. 31, pp. 480-482.

Chapter 3 Volume Holograms in Photorefractive Materials

3.1 Introduction

This chapter provides a theoretical background to the experiments that will be described in chapter 4. It is proposed that an array of FBG sensors is demodulated by an array of holograms inscribed within a photorefractive material. A photorefractive material allows holograms of different central wavelengths and bandwidths to be inscribed and subsequently erased. This allows sensor arrays with different elemental quiescent wavelengths to be demodulated and the performance of holograms with different bandwidths to be assessed. The sensor array will be constructed of FBG elements operating in separate wavelength ranges. Each hologram will match an FBG sensor element and will diffract each signal through a different angle to a matching photo-detector so completing de-multiplexing. The wavelength range of operation for a particular sensor element is aligned with a linear section of the holographic transfer function either side of the diffraction efficiency peak. The change in the Bragg wavelength will alter the intensity of the Bragg signal so completing demodulation.

The refractive index of the photorefractive material may change by a photo-induced space-charge field via the electro-optic effect. The photorefractive effect was first demonstrated within $\mathrm{LiNbO_3}$ (Ashkin *et al.* 1966) and has been observed within other ferroelectric oxides such as $\mathrm{LiTaO_3}$ (Ashkin *et al.* 1966) and $\mathrm{KNbO_3}$ (Gu□nter 1987). Photorefractivity has been verified within semiconductors such as GaAs (Partovi *et al.* 1993) and InP (Gravey, Picoli & Labandibar 1989). Recently, cheap and readily available polymers such as PVK (poly (*N*-vinylcarbazole)) (Kippelen *et al.* 2002) have also been shown to demonstrate the effect. A photorefractive ferroelectric oxide of particular interest is Barium Titanate ($\mathrm{BaTiO_3}$) (Townsend & LaMacchia 1970) due to the large electro-optic tensor element possessed by the material, which allows significant change in refractive index.

Volume holograms can be can be recorded within a photo-refractive material by interfering mutually coherent laser beams within a volume, as shown in figure 3.1(a) (Kogelnik, H 1969), and is therefore referred to as a Volume Holographic (VH) material. One beam is referred to as the object beam and the other as the reference beam. The beams are incident at an angle θ and produce an interference pattern with a period Λ within the material as shown in figure 3.1(b). If the wave-vectors of the beams are $\mathbf{k_1}$ and $\mathbf{k_2}$ then the interference pattern has a wave-vector **K** as shown in figure 3.1(c). In this particular example the bisector of the interfering beams is normal to the surface of the crystal so the direction of the wave-vector **K** coincides with the z axis. In reality the bisector will not be normal to the crystal's surface as explained later in this section.

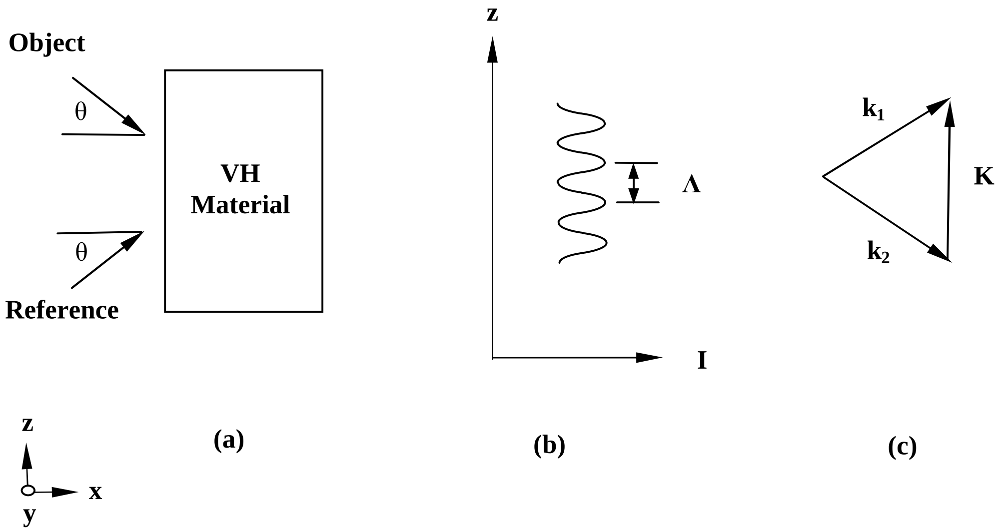

Figure 3.1 Creation of a grating in a Volume Holographic Material
(a) The interference pattern is created by an object and a reference beam crossing within a VH material. The beams are incident at an angle of *θ*. **(b)** The beams produce an interference pattern with a period Λ within the material. **(c)** The beams possess wave-vectors of $\mathbf{k_1}$ and $\mathbf{k_2}$ to produce an interference pattern and therefore a grating with a wave-vector **K.** (Solymar, L 1996)

Assuming that the beams are plane waves the electric fields are represented by (Solymar 1996)

$$\varepsilon_x = \varepsilon_{x0} e^{-\mathrm{jk_x} \bullet \mathrm{r} + \varphi_\mathrm{x}} \qquad \mathbf{3.1}$$

where x=1,2 for the reference and object beams respectively. ε_x is the electric field of the respective beams, $\varepsilon_{\mathrm{x}0}$ are the respective amplitudes, φ_x the respective phases, $\mathbf{k_x}$ the respective wave-vectors, and **r** is the radius vector.

The intensity of the interference pattern created by the two beams shown in figure 3.1(b) is given by (Solymar, 1996)

$$I = |\varepsilon_1 + \varepsilon_2|^2 = \varepsilon_{10}^2 + \varepsilon_{20}^2 + 2\varepsilon_{10}\varepsilon_{20}\cos(\mathbf{K.r} + \phi_2 - \phi_1) \qquad \mathbf{3.2}$$

where **K** is the wave-vector of the interference pattern, given by

$$\mathbf{K} = \mathbf{k_1} - \mathbf{k_2} \qquad \textbf{3.3}$$

where $\mathbf{k_1}$ and $\mathbf{k_2}$ are the wave-vectors of the incident beams. The magnitude of the wave-vectors are

$$k_1 = k_2 = \frac{2n\pi}{\lambda} \qquad \textbf{3.4}$$

where λ is the wavelength of the interfering beams and n is the refractive index of the material. Equation 3.4 can then be simplified to

$$\Lambda = \frac{\lambda_i}{2n\sin\theta_i} \qquad \textbf{3.5}$$

where Λ is the period of the interference pattern, λ_i and θ_i is the wavelength and half-angle of inscription respectively.

Within the photorefractive material, mobile charge carriers are photo-generated in high intensity regions of the interference pattern. The carriers diffuse to the dark regions where they subsequently recombine with ionised donors. Periodic areas of high and low charge density are therefore formed. Between these areas an electric field is created leading to a periodic space charge field. The formation of the space charge field is examined in Section 3.2.1. In general the inscribing beams possess a Gaussian profile, modifying the profile of the interference pattern in a radial direction. The impact of the Gaussian beam on the space charge field is detailed in Section 3.2.2.

A VH material of particular interest is $BaTiO_3$ a crystal of which is available for experimentation. This material can host holograms of elevated diffraction efficiency because of the high r_{42} electro-optic tensor co-efficient. Within an anisotropic material such as $BaTiO_3$ the electro-optic tensor can be reduced to a single effective coefficient r_{eff} (Ringhofer *et al.* 1991) applicable to a specific hologram, the value of which depends on the orientation of the space-charge field with respect the c-axis.

Consider the inscription of a volume hologram within $BaTiO_3$, illustrated in figure 3.2. It is assumed that the interfering beams are of extraordinary polarisation with the e-fields lying in the z,y plane. It is assumed that the z and c axes coincide, the c-axis being the optical axis of a uniaxial crystal such as $BaTiO_3$. The axis was determined by a simple beam fanning experiment detailed in Section 4.x. The bisector of the interfering beams $(\alpha+\beta)/\ 2$ is not $\pi/2$ so allowing a component of the space charge field in the y direction to access the large r_{42} coefficient. To maximise holographic diffraction efficiency the bisector of the beams is configured to be at an angle of approximately 20° to a normal to the crystal's front facet (Solymar 1996). This angle does not coincide to where the r_{eff} is at a maximum as the crystal's dielectric constant, a tensor value also has to be considered. The values of the electro-optic tensor elements within $BaTiO_3$ and how to access specific components have been detailed (Solymar 1996).

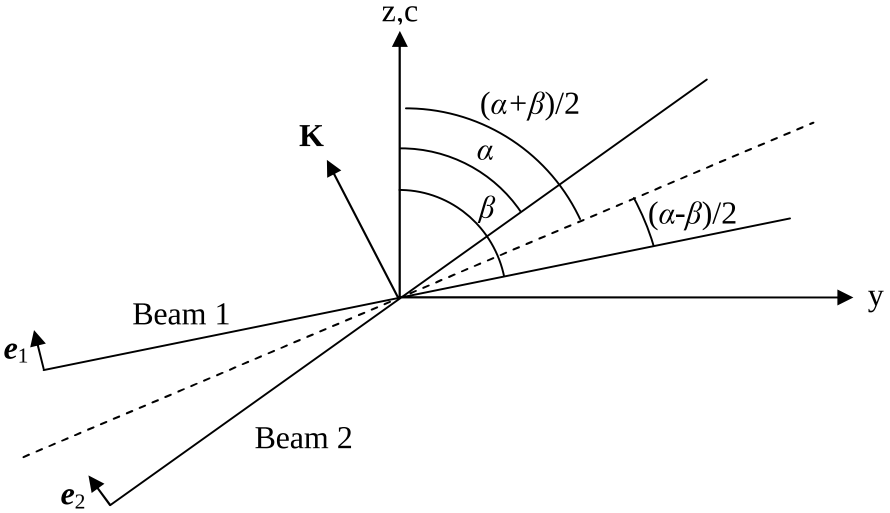

Figure 3.2 Determination of r_{eff} within $BaTiO_3$.
The interfering beams are of extraordinary polarisation with the e-fields being in the z,y plane. The z and c axes coincide, the c-axis being the optical axis in a uniaxial crystal such as $BaTiO_3$. This specific arrangement allows a component of the space charge field in the y direction to access the large r_{42} coefficient if the bisector of the interfering beams $(\alpha+\beta)/\ 2$ is not $\pi/2$ (Ringhofer et al. 1991).

A hologram is formed by the periodic space field E_s inducing a change in refractive index Δn. The refractive index change is related to the space charge field via the effective electro-optic coefficient r_{eff}.

$$\Delta n \approx \frac{1}{2} n_o^3 r_{\text{eff}} E_s \qquad \textbf{3.6}$$

where E_s is the space change field, r_{eff} is the effective electro-optic coefficient, Δn is the change in refractive index and n_o is the refractive index of the crystal.

The hologram has to be illuminated with a reference beam to allow holographic reconstruction. To maximise the diffraction efficiency the beam has to meet the Bragg condition that requires the angle and wavelength to equal that of the reference beam used within inscription. The Bragg condition can be summarised by the equation

$$\Lambda = \frac{\lambda_b}{2n\sin\theta_b} \qquad \textbf{3.7}$$

where λ_b and θ_b are the Bragg wavelength and angle respectively. If the wavelength or angle deviates from the Bragg condition the diffraction efficiency will fall. The relationship between incident wavelength or angle and the diffraction efficiency is known as the transfer function. The diffraction efficiency and the holographic transfer function are examined in detail in section 3.3 and will be used in the demodulation the FBG sensor array.

A VH material can host multiple holograms, the holograms being multiplexed by angle or wavelength or both angle and wavelength. Inscription of multiple holograms is simply achieved by changing the wavelength or angle of inscription between consecutive holograms (Anderson & Lininger 1987). The number of holograms that can be simultaneously hosted by the crystal can be up to 5000 (Mok 1993). The inscription of one hologram however can partially erase any already hosted within the material (Strasser *et al.* 1989). The time constants for inscription and erasure therefore must be established so a schedule of inscription can be derived. The schedule will ensure all the holograms have the same diffraction efficiency. Inscription and erasure times are examined in detail in section 3.2.3 whilst the schedule of inscription is detailed in section 3.3.3.

Considering a wavelength span of 4nm is required for the demodulation of a single sensor and an SLD has an optical bandwidth of approximately 40nm the number of elements that can be realistically demodulated is 10 including a reference grating used for intensity referencing. In practice the erasure time are considerably greater than inscription times so it is envisaged that 10 holograms can readily be inscribed within the crystal.

3.2 Grating Formation

3.2.1 Space Charge Field

A space charge field is established in a photorefractive material by the photo-generation and subsequent diffusion and recombination of charge carriers (Kukhtarev & Odoulov 1980). An electric field then exists between regions of excess and depleted static charge.

The creation of the space charge field is described in figure 3.3. Here the majority carriers are assumed to be electrons and there is no applied electric field. The interference pattern (Fig. 3.3(a)) creates electron-donor pairs the number of pairs being proportional to the intensity of the interference pattern. The electrons are mobile and will diffuse from areas of high to areas of low density (Fig. 3.3(b)). The diffusing electrons will recombine to leave an excess of ionised donors in areas of high intensity. A periodic net charge density is then established in phase with the interference pattern (Fig. 3.3(c)). An electric field is also created 90° out of phase with the interference pattern between the areas of high and low charge density (Fig. 3.3(d)). A drift current is produced that opposes the diffusion current (Fig. 3.3(e)). When the diffusion and drift currents are equal the electric field reaches a steady state. The effective electro-optic coefficient r_{eff} then causes a periodic change in refractive index due to the electrical field that is 90° out of phase with the interference pattern (Fig. 3.3(f)) (Solymar 1996).

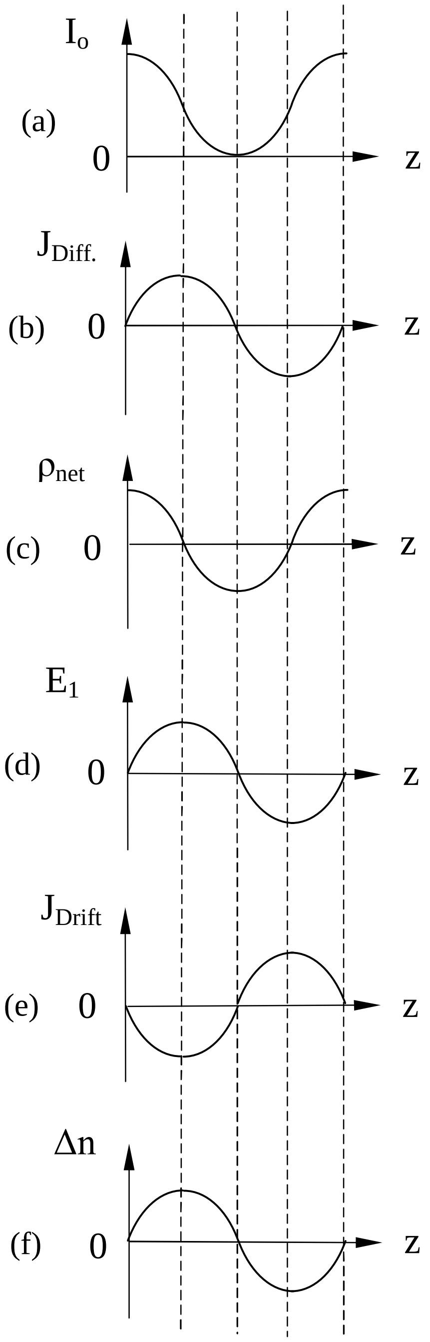

Figure 3.3 The process of Holographic inscription.
(a) The interference pattern creates electron-donor pairs the number being proportional to the intensity I_o. (b) The charge difference causes the drift J_{Diff} of electrons from areas of high intensity to areas of low intensity where the carriers recombine. (c) This creates areas of high and low static charge density ρ_{net} in phase with the interference pattern. (d) An electric field E_1 is then established between these areas. (e) The electric field will cease growth when the resulting drift current J_{Drift} equals the diffusion current J_{Diff}. (f) The effective electro-optic coefficient r_{eff} then causes a periodic change in refractive index Δn due to the electrical field that is 90° out of phase with the interference pattern (Solymar 1996).

A derivation of an expression for the space charge field has been reported (Kukhtarev & Odoulov 1980). This uses equations applicable to the carrier generation, diffusion and subsequent recombination to derive a value of the field. The derivation assumes that the majority carriers are electrons.

The space change field is considered to grow to a steady state value given by the complex equation (Kukhtarev & Odoulov 1980).

$$E_s = jm\frac{E_\mathrm{D}E_\mathrm{q}}{E_\mathrm{D}+E_\mathrm{q}} \qquad \textbf{3.8}$$

where $m=I_1/I_0$ is the modulation of the interference pattern given by the ratio of the interfering beams, j is the unit complex number.

The value E_D is known as the diffusion field that is inversely proportional to grating period Λ. As the period decreases, the greater the gradient of electron distribution and so the forces of diffusion are stronger. The diffusion field is given by the equation

$$E_\mathrm{D} = \frac{k_\mathrm{B}TK}{e} \qquad \textbf{3.9}$$

where k_B is Boltzmann’s constant, T is temperature, K is the magnitude of the grating vector and e is the eletronic charge.

The parameter E_q is the saturation field. It is the maximum space charge field that can exist within the crystal for a sinusoidal charge distribution and is given by

$$E_\mathrm{q} = \frac{eN_\mathrm{A}^-}{\varepsilon_\mathrm{s}K} \qquad \textbf{3.10}$$

here N_A^- is the ionised acceptor density and ε_s is the relative permittivity of the material, all other variable have been defined.

The maximum negative charge occurs at a point when all donors are filled with electrons and the full charge of the ionised acceptors is seen. The maximum positive charge occurs when the density of ionised donors is twice the density of ionised acceptors. The saturation field must occur half way between these two points where the distance is governed by the grating period Λ.

The limiting values for the space charge field E_s are jmE_q for small grating periods and jmE_D for large grating periods. These two values are applicable if the saturated or non-saturated regimes prevail respectively. The inscription geometry for the holograms detailed within experimentation assumes that the grating period is large above 3μm and therefore the non-saturated regime prevails (Solymar 1996).

3.2.2 Effect of Beam Profile on Space Charge Field

An expression for the space-charge field is derived above by considering the interference pattern formed by two uniform beams. In reality however the inscribing beams will have a Gaussian Profile. Consider therefore two Gaussian beams an object and a reference being represented by ε_1 and ε_2.respectively. The beams are crossed to form a hologram within a photorefractive material. A cross section of the holographic region is delineated by a parallelogram as shown in figure 3.4.

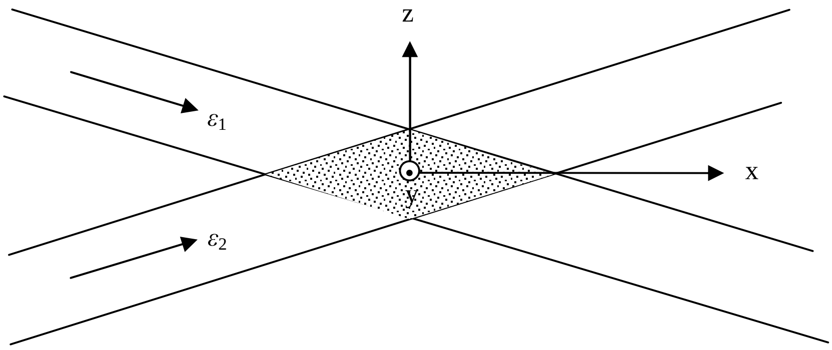

Figure 3.4 Cross section of a holographic region..
Consider a reference and an object beam being represented by ε_1 and ε_2.respectively. Both possess a Gaussian profile. The beams are crossed to form a hologram within photorefractive material. The holographic region is delineated by a parallelogram (Hamad & Wicksted 1997).

The spatial profile of beam 1 can be represented by the equation.

$$\varepsilon_1 = \varepsilon_{10} \exp\left[-\frac{y^2 + (z\cos\theta - x\sin\theta)^2}{w_o^2} - jk(x\cos\theta + z\sin\theta) \right] \qquad \textbf{3.11}$$

where the fall in intensity from the centre of the beam is represented by the first term within the exponential whist the second term describes the cyclical nature of the electrical field change along the axis of propagation. The value w_o is the beam-width. To represent beam 2 the angle θ within equation 3.11 is simply replaced by $-\theta$.

The intensity of the interference pattern created by the two beams is then given by

$$I(\mathrm{x,y,z}) = \frac{1}{4}\left(\varepsilon_1 + \varepsilon_2^*\right)\left(\varepsilon_1^* + \varepsilon_2\right) \qquad \textbf{3.12}$$

where the superscript * denotes the complex conjugate where $j \rightarrow -j$. The term of interest is $\varepsilon_1\varepsilon_2^*$ as this has the phase variation exp($-j2\ k$ z sinθ). The normalised modulated intensity pattern can then be defined as $M(\mathrm{x,y,z}) = (\frac{1}{4}|\varepsilon_o|)\varepsilon_1\varepsilon_2^*$ and can be expressed by

$$M(\mathrm{x,y,z}) = \frac{1}{4}\exp\left(-2\frac{\mathrm{y}^2 + \mathrm{z}^2\cos^2\theta + \mathrm{x}^2\sin^2\theta}{w_o^2} - j2k\mathrm{z}\sin\theta\right) \qquad \textbf{3.13}$$

Considering only the radial variation in the interference pattern in the z direction and assuming that the angle between the beams within the crystal is small so that cos$\theta \approx 1$. The normalised modulated intensity pattern becomes

$$M(\mathrm{z}) = \frac{1}{4}\exp\left(-2\frac{\mathrm{z}^2}{w_\mathrm{o}^2} - jK\mathrm{z}\right) \qquad \textbf{3.14}$$

The creation of a space charge field by a single Gaussian beam has been reported (Lindsay 1989). In the non-saturated regime the expression for the space change field is given by

$$E_s(\mathrm{z}) = \frac{k_\mathrm{B}T}{e}\frac{1}{I}\frac{\mathrm{d}I}{\mathrm{dz}} \qquad \textbf{3.15}$$

When applied to equation 3.14 the space charge field becomes

$$E_\mathrm{s} = jmE_\mathrm{D} + m\frac{k_\mathrm{B}T}{e}\frac{\mathrm{z}}{w_\mathrm{o}^2} \qquad \textbf{3.16}$$

for the non-saturated regime. The value of the space charge field is therefore complex with real and imaginary parts. This implies that there is a deviation in the 90° phase shift between the inscribing interference pattern and the grating implied by equation 3.8. The value of the space charge field under these conditions is related to the first spatial differential of the interference pattern. The grating is therefore approximately uniform as the largest rate of change in intensity due to the interference pattern is much greater than that of the Gaussian profile.

3.2.3 Inscription and Erasure Times

The dielectric relaxation time is the mean free time of majority carriers within a conducting material and is given by the equation

$$\tau_{\mathrm{d}} = \frac{\varepsilon_{\mathrm{s}}}{e\mu n_{\mathrm{o}}} \qquad \textbf{3.17}$$

where μ is the mobility of and n_{o} the number of the majority carriers, which is assumed to be electrons, all other variables have been defined. The number of carriers can be calculated by the equation

$$n_{\mathrm{o}} = sI_{\mathrm{o}}(N_{\mathrm{D}} - N_D^+)/\gamma_{\mathrm{R}} N_D^+ \qquad \textbf{3.18}$$

where s is the photo-ionisation coefficient, I_{o} is the combined intensity of the interfering beams, N_{D} is the donor density, N_{D}^+ is the ionised donor density and γ_{R} is the recombination constant.

The dielectric relaxation time equates to the rise time of the space charge field in a photorefractive material operated within the non-saturated regime (Solymar 1996)

$$\tau_r = \tau_d = \frac{\varepsilon_{\mathrm{s}}}{e\mu n_{\mathrm{o}}} \qquad \textbf{3.19.}$$

The material processes that govern erasure times are the same as those for inscription. This implies that the inscription and erasure time constants have the same value. A single erasure beam impinging on a hologram however will be separated into diffracted and un-diffracted parts. The diffracted and un-diffracted sections of the beam interfere initially reinforcing the hologram present within the crystal. In the long time period the beam will erase the hologram. The erasure time constant however will be greater than that of inscription. The mathematical modelling of the erasure time constant is therefore difficult (Solymar 1996). Thermal excitation of carriers will ensure that all holograms within the crystal will be erased overnight.

3.3 Holographic Reconstruction

3.3.1 Holographic Transfer Function

The hologram is illuminated with single beam that has the same wavelength and incident angle of the inscribing reference beam as shown in figure 3.5 (Kogelnik 1969). The diagram shows the hologram inscribed within a VH material by the process described in figure 3.1. As the illuminating beam meets the Bragg condition the amount diffracted by the hologram is at a maximum. The hologram inscribed within the VH material is assumed to be uniform with the direction of the grating-vector coinciding with the z-direction. The holographic depth therefore is assumed to be the depth of the material bounded by the physical dimensions in the x-direction.

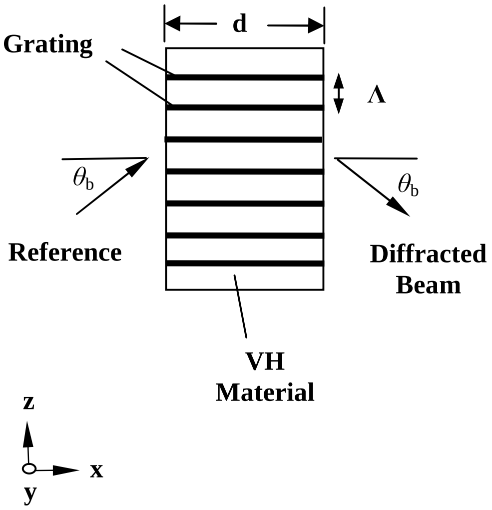

Figure 3.5 Interrogation of a holographic grating by a single reference beam. The beam meets the Bragg condition so the power diffracted by the hologram is at a maximum. The grating vector of the hologram coincides with the z-direction and the beam is diffracted through an angle twice that of the Bragg angle. The hologram is assumed to be uniform in the VH material with the holographic depth equalling the physical dimensions of the material in the x-direction (Solymar 1996).

The holographic transfer function plots the change in the diffraction efficiency of the hologram as the interrogating reference beam detunes from the Bragg condition. The diffraction efficiency depends on two variables Φ and χ which are the coupling coefficient and the detuning parameter respectively. The coupling coefficient depends on the maximum change in refractive index Δn and the holographic depth *d*. The change in refractive index is related to the space charge field and the effective electro-optic coefficient as given in equation 3.6. The detuning parameter determines the change in the diffraction efficiency as the interrogating beam deviates from the Bragg condition.

The holographic transfer function is given by the equation

$$Diffraction\_Efficiency = \eta(d) = \frac{\sin^2(\sqrt{\Phi^2+\chi^2})}{1+\frac{\chi^2}{\Phi^2}} \qquad \textbf{3.20}$$

Where the coupling coefficient

$$\Phi = \frac{\pi \Delta n d}{\lambda_b \cos\theta_b} \qquad \textbf{3.21}$$

and the detuning coefficient

$$\chi = \frac{Kd}{2\cos\theta}\left[\Delta\theta\cos\theta - \frac{\Delta\lambda}{2\Lambda}\right] \qquad \textbf{3.22}$$

The values $\Delta\lambda$ and $\Delta\theta$ are small changes from the angle and wavelength of inscription and represents deviation from the Bragg condition. The Bragg angle and wavelength are given by θ_b and λ_b respectively. The symbol η represents diffraction efficiency.

A typical transfer function for a transmission hologram is shown in figure 3.6. Here the Bragg wavelength λ_b and angle θ_b are shown as is the deviation from the Bragg condition in wavelength $\Delta\lambda$ and angle $\Delta\theta$. As the detuning parameter χ ncreases the diffraction falls to a zero minima due to the $\sin^2$ function in equation 3.20. The function then continues to fluctuate due to the $\sin^2$ function however the side-lobes reduce with increasing deviation due to the factor χ being present in the denominator of equation 3.20.

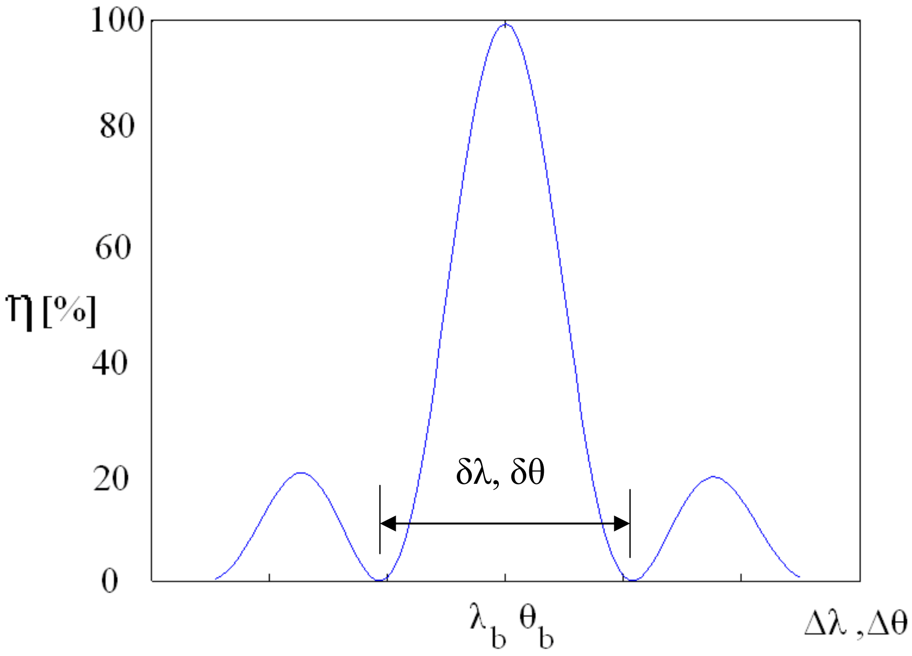

Figure 3.6 Diffraction efficiency η of a transmission hologram.
Here the deviation from the Bragg condition in both wavelength $\Delta\lambda$ and angle $\Delta\theta$ is shown. The $\sin^2$ function in equation 3.20 determines the fall in diffraction efficiency to zero minima with increasing deviation from the Bragg condition. The function then continues to fluctuate however the side-lobes reduce with increasing deviation due to the factor χ being present in the denominator.

The angular or wavelength selectivity is defined as the difference between the first minima either side of the diffraction efficiency peak. The equations for wavelength $\delta\lambda$ and angular $\delta\theta$ selectivity are given by equations 3.23 and 3.24 respectively.

$$\delta\lambda \approx \frac{\lambda_{\mathrm{b}}{}^2 \cos\theta_{\mathrm{b}}}{2nd\sin^2\theta_{\mathrm{b}}} \qquad \mathbf{3.23}$$

$$\delta\theta \approx \frac{\lambda_{\mathrm{b}}}{2d\sin\theta_{\mathrm{b}}} \qquad \mathbf{3.24}$$

where λ_{b} and θ_{b} represent the Bragg wavelength and angle respectively, d is the holographic depth and n is the refractive index of the crystal.

3.3.2 Transfer Function of Holograms Written With Gaussian Beams

The holograms used for demodulation are formed by two Gaussian beams that overlap on the front facet of the crystal as shown in figure 3.7. Both beams are of extraordinary polarisation to allow the resultant space-charge field to access the r_{42} tensor element. Both beams are refracted at the crystal's front and rear facets. The hologram therefore forms a conical volume within the material with a triangular cross-section also shown in figure 3.7. The depth of the hologram d is the length of the triangular cross-section.

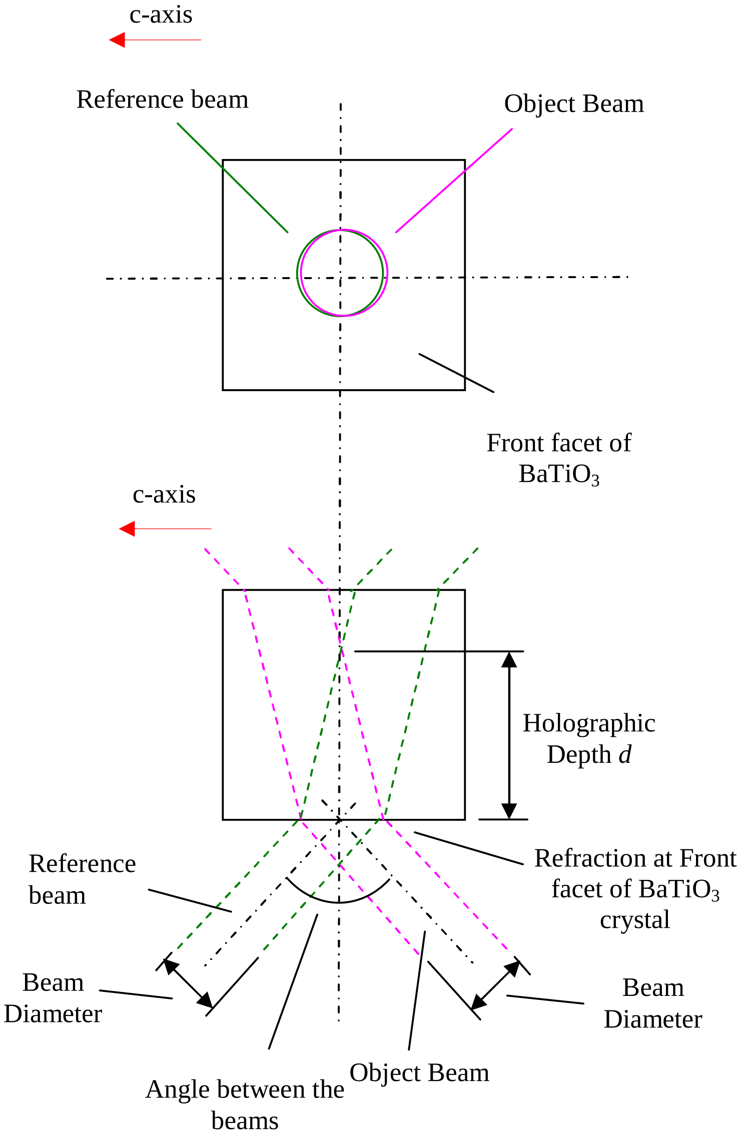

Figure 3.7 Conic hologram formed by the interference of the two Gaussian beams within a crystal of BaTiO$_3$.
The inscribing Gaussian beams overlap on the front of the crystal and are refracted by both the crystal's front and rear facets. The interfering beams inscribe a hologram that is bounded by a conic volume. The conic hologram has a triangular cross-section with a holographic depth *d*.

To interrogate the hologram a beam of the same wavelength, angle and diameter as the inscribing reference beam is considered. The rays on the extreme right of the beam experience a hologram of limited depth however rays on the extreme left traverse the full depth. The resulting transfer function is then the integral of transfer functions applicable the different depths from zero to the length of the conic section. The model is therefore a development of the simple two dimensional one presented in figure 3.5. It is assumed that the hologram is uniform within the conic volume so the

Gaussian form of the beams is disregarded. The resulting transfer function is evaluated by the integral

$$I(\%) = \int_0^1 \eta(X)dX \qquad \textbf{3.25}$$

where $\eta(X)$ is the transfer function of a hologram with a normalised depth $X=d/d_{\mathrm{Max}}$, d_{Max} being the maximum holographic depth determined by the conic section. The integral can then be represented by

$$I(\%) = \frac{1}{1+\frac{\chi^2_{d\max}}{\Phi^2_{d\max}}} \int_0^1 \sin^2(\sqrt{\Phi^2_{d\max} + \chi^2_{d\max}}\,X)dX \qquad \textbf{3.26}$$

The denominator in equation 3.20 can be taken outside the integral as both Φ and χ are proportional to depth (d). The values $\Phi_{d\max}=\Phi(d=d_{\mathrm{Max}})$ and $\chi_{d\max}=\chi(d=d_{\mathrm{Max}})$. The integral is then completed over the range of normalised depths from zero to one. The indefinite integral is then

$$I(\%) = \frac{1}{1+\frac{\chi^2_{d\max}}{\Phi^2_{d\max}}} \left[\frac{u}{2} - \frac{sin(\sqrt{\Phi^2_{d\max} + \chi^2_{d\max}}\,u)}{4(\sqrt{\Phi^2_{d\max} + \chi^2_{d\max}})} \right]_0^1 \qquad \textbf{3.27}$$

The result is given by the equation

$$I(\%) = \frac{1}{1+\frac{\chi^2_{d\max}}{\Phi^2_{d\max}}} \left[\frac{1}{2} - \frac{sinc\left(\frac{2}{\pi} \left(\Phi^2_{d\max} + \chi^2_{d\max} \right)^{\frac{1}{2}} \right)}{2} \right] \qquad \textbf{3.28}$$

where all variables have been previously defined. The function is plotted on a three dimensional graph shown in figure 3.8.

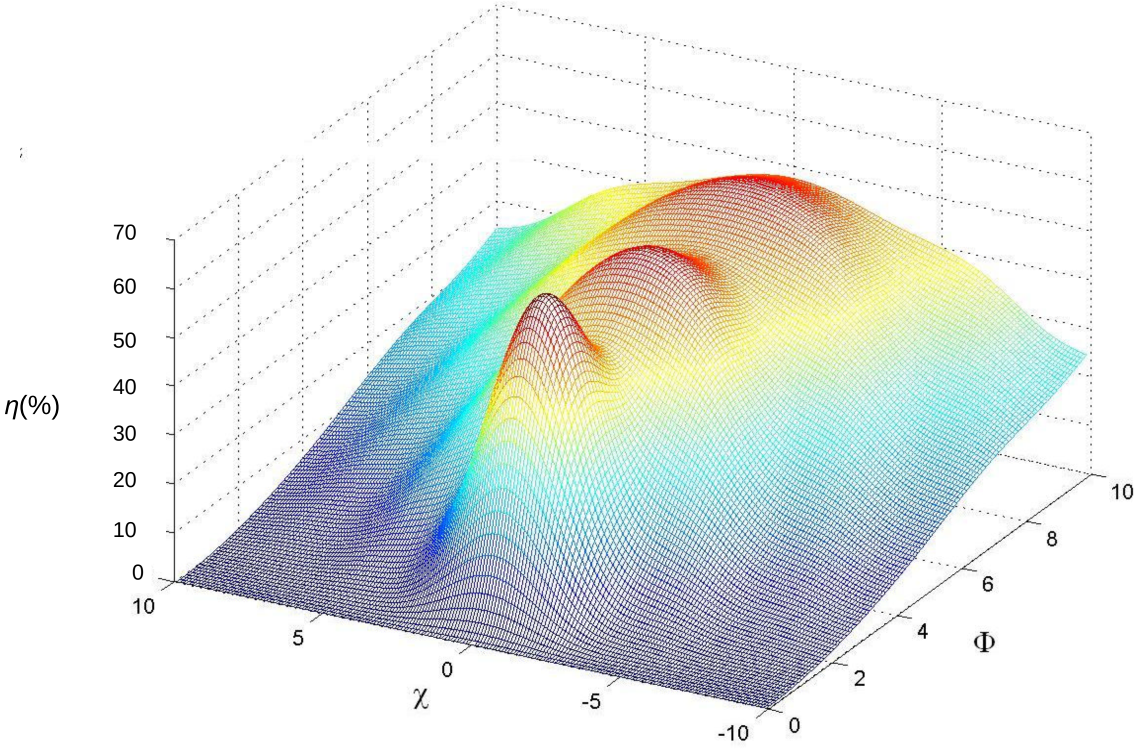

Figure 3.8 Diffraction efficiency of a conic shaped volume hologram. As the beam detunes from the Bragg condition $|\chi|\rightarrow\infty$ the diffraction efficiency falls to zero. There is no evidence of significant side-lobes in the normalised transfer function. The diffraction efficiency tends to ½ as the coupling coefficient $\Phi\rightarrow\infty$.

The integral demonstrates an increase in maximum diffraction efficiency as the coupling coefficient Φ increases from zero. The form however is of a ½(1/2-*sinc*) function that tends to ½ as $\Phi\rightarrow\infty$. As the beam begins to detune the diffraction efficiency falls and tends to zero as $|\chi|\rightarrow\infty$. There is no evidence of significant side-lobes in the normalised transfer function.

The maxima, minima and the points of inflection of this function inscribe a circle in the Φ-χ plane as $(\Phi^2+\chi^2)^{1/2}=\pm n\pi$ where n=1, 2, 3….∞ at these points. The transfer function can then be established by considering the coupling coefficient at a constant value $\Phi \ll \pi$ and allowing χ to vary. The bandwidth $\Delta\lambda$ is then the wavelength difference between the points $\chi=\pi$ and $\chi=-\pi$. This is analogous to considering the first minima either side of the peak diffraction efficiency shown in figure 3.6 to derive the wavelength bandwidth given in equation 3.23 (Kogelnik 1969). The bandwidth is therefore given by the equation

$$\delta\lambda \approx \frac{\lambda_{\mathrm{b}}^{2}\cos\theta_{\mathrm{b}}}{2nd\sin^{2}\theta_{\mathrm{b}}} \qquad \mathbf{3.29}$$

where all variables are defined for equation 3.23. The bandwidth however represented by equation 3.29 is greater than that of 3.23 because the wavelength difference between points of inflections either side of the peak diffraction efficiency are considered not between the minima. The points of inflection represent a diffraction efficiency approximately one third that of the peak. The bandwidth given by equation 3.29 therefore is increased by approximately one third of that given by equation 3.23.

3.3.3 Multiple Holograms

A photorefractive material can host multiple holograms. Each hologram is multiplexed by angle and wavelength or a combination of both. The proposed demodulation scheme allows the signals from a wavelength multiplexed FBG sensor array to be diffracted through different angles to matching elements in a photo-detector array. The holograms therefore require to be multiplexed by both wavelength and angle.

A tuneable single wavelength laser is available for inscription so the holograms are required to be inscribed sequentially. Between each inscription both the wavelength and the angle between the inscribing beams are altered. The inscription of a hologram however will partially erase any that is already hosted within the crystal so it is important to establish holographic inscription and erasure times. This will allow a schedule of inscription to be derived so each hologram will have the same diffraction efficiency.

The inscription time of the n^{th} hologram is related to the inscription time of the first hologram by (Strasser *et al.* 1989).

$$\tau_{\mathrm{n}} = \frac{\tau_1}{1+\dfrac{n-1}{\beta}} \qquad \mathbf{3.30}$$

where τ_1 is the inscription time of the first hologram and τ_n is the inscription time of subsequent holograms. $\beta = \tau_e / \tau_r$ where τ_r is the holographic inscription time and τ_e is the erasure time both to be established by experimentation.

In reality the erasure time is considerably greater than that of inscription. The inscription time of a hologram within a sequence therefore is fractionally shorter than the previous one. All holograms are erased by the thermal generation of carriers overnight therefore hologram inscription has to be completed each day to allow experimentation.

3.6 Summary

The theory of photorefractive materials is complex however an understanding is required to assess the impact on the experimental configuration for both holographic inscription and interrogation by a sensor signal. Established theory assumes a uniform grating throughout the body of a VH material however in reality the hologram is inscribed by two Gaussian beams. The beams limit the volume hologram to a conic section that causes the broadening and apodisation of the associated transfer function compared with that of a uniform grating. The radial intensity distribution of the inscribing beams has no impact on the associated transfer function. Finally the inscription of a hologram will imply the partial erasure of any already hosted within the crystal. A schedule therefore has to be derived depending holographic inscription and erasure times that allows all holograms simultaneously hosted to possess the same diffraction efficiency.

The next section uses the theory presented here to define experimental variables or process results. Specifically holographic inscription and erasure time constants are established and used to derive a writing schedule for an array of holograms. The spectral responses of all components in the demodulation scheme are considered to derive a system response which approximates to the holographic transfer function. The hologram introduces a third order non-linearity therefore a mathematical model of the associated transfer function is used to derive measurand results from readings output from the demodulation system. The modelled transfer function also modifies the standard difference over sum equation used for intensity referencing, the two readings being recorded from two holograms simultaneously demodulating one FBG sensor element.

3.7 References

Anderson, D.Z. & Lininger, D.M. 1987, "Dynamic optical interconnections: Volume holograms as optical two-port operators", *Appied Optics,* vol. 26, no. 23, pp. 5031-5038.

Ashkin, A., Boyd, G.D., Dziedzic, J.M., Smith, R.G., Ballman, A.A., Levinstein, J.J. & Nassau, K. 1966, "Optically-induced refractive index inhomogeneities in LiNbO3 and LiTaO3", *Applied Physics Letters,* vol. 9, no. 1, pp. 72-74.

Gravey, P., Picoli, G. & Labandibar, J.Y. 1989, "Stabilization of photorefractive two-beam coupling in InP:Fe under high dc fields by temperature control", *Optics Communications,* vol. 70, no. 3, pp. 190-194.

Günter, P. and Huignard, J. (1987), *Photorefractive Materials and Their Applications 1: Fundamental Phenomena (Springer Series in Optical Sciences).*

Hamad, A.Y. & Wicksted, J.P. 1997, "Volume grating produced by intersecting Gaussian beams in an absorbing medium: A Bragg diffraction model", *Optics Communications,* vol. 138, no. 4-6, pp. 354-364.

Kippelen, B., Blanche, P., Schulzgen, A., Fuentes-Hernandez, C., Ramos-Ortiz, G., Wang, J.-., Peyghambarian, N., Marder, S.R., Leclercq, A., Beljonne, D. & Bredas, J.-. 2002, "Photorefractive polymers with non-destructive readout", *Advanced Functional Materials,* vol. 12, no. 9, pp. 615-620.

Kogelnik, H., 1969, "Coupled wave theory for thick hologram gratings", *Bell System Tech J,* vol. 48, no. 9, pp. 2909-2947.

Kukhtarev, N.V. & Odoulov, S.G. 1980, "Wavefront conjugation via degenerate four-wave mixing in electro-optic crystals", *Proc. SPIE,* vol 213, pp 2-9

Lindsay, I. 1989, *Optical phase conjugation in photorefractive materials and its application to image,* Ph.D., London, Imperial College of Science and Technology, 43-3490.

Mok, F.H. 1993, "Angle-multiplexed storage of 5000 holograms in lithium niobate", *Opt. Lett.,* vol. 18, no. 11, pp. 915-917.

Partovi, A., Glass, A.M., Zydzik, G.J., O'Bryan, H.M., Chiu, T.H. & Knox, W.H. 1993, "Effect of carrier escape time on the performance of semi-insulating photorefractive self-electro-optic effect devices", *Applied Physics Letters,* vol. 62, no. 24, pp. 3088-3090.

Ringhofer, K.H., Tao, S., Takacs, J. & Solymar, L. 1991, "The role of the longitudinal component of the electric field vector in two-wave mixing in photorefractive $BaTiO_3$", *Applied Physics B Photophysics and Laser Chemistry,* vol. 52, no. 4, pp. 259-261.

Solymar, L. 1996, *The physics and applications of photorefractive materials,* Clarendon Press, Oxford.

Strasser, A.C., Maniloff, E.S., Johnson, K.M. & Goggin, S.D.D. 1989, "Procedure for Recording Multiple-Exposure Holograms with Equal Diffraction Efficiency in Photorefractive Media", *Opt. Lett.,* vol. 14, no. 1, pp. 6-8.

Townsend, R.L. & LaMacchia, J.T. 1970, "Optically induced refractive index changes in $BaTiO_3$", *Journal of Applied Physics,* vol. 41, no. 13, pp. 5188-5192.

Chapter 4 Demonstration of the FBG Array Demodulation Scheme

4.1 Introduction

A single FBG sensor can be demodulated by illuminating a volume hologram, previously inscribed, within a photorefractive crystal with the Bragg reflection from the sensor (James *et al.* 1996). As the central wavelength of the Bragg reflection changes with an applied measurand, the transfer function of the volume hologram modulates the intensity of the diffracted signal as shown in figure 4.1. In a similar manner a WDM FBG sensor array can be demodulated by an array of volume holograms. In this case the properties of each volume hologram ensure that the element's signal is diffracted through a different angle to a matching element in a photo-detector array. The process of de-multiplexing is shown in figure 4.2. To demonstrate the feasibility of this approach, an available 5mm x 5mm x 5mm crystal of photorefractive $BaTi0_3$ is used to host the array volume holograms.

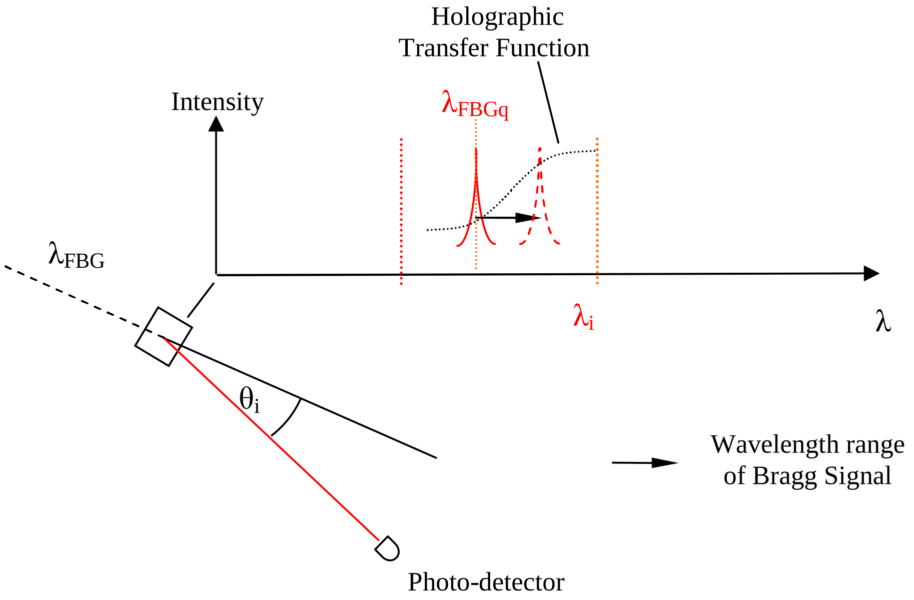

Figure 4.1 An FBG sensor demodulation scheme based on a single volume hologram. The holographic transfer function inscribed at λ_i will modulate the intensity of the Bragg signal depending on the instantaneous wavelength. The quiescent wavelength of the Bragg signal is given by λ_{FBGq}. The Bragg signal will be diffracted through the angle of holographic inscription θ_i before impinging on a photo-detector.

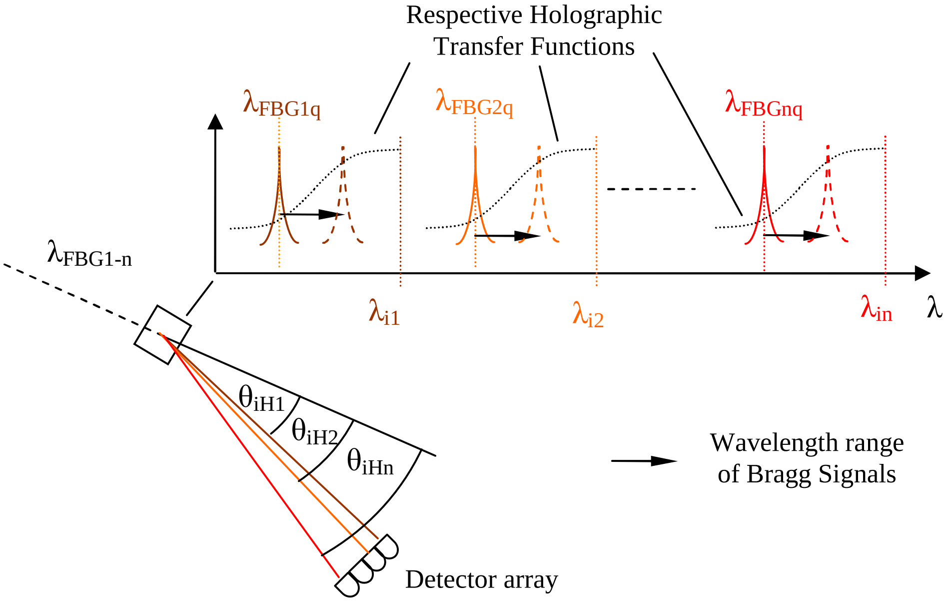

Figure 4.2 An FBG sensor array demodulation scheme based on an array of volume holograms. The holographic transfer functions inscribed at λ_{in} will modulate the intensity of the matching element's signal depending on the instantaneous wavelength. The quiescent wavelengths of the matching Bragg elements are given by λ_{FBGnq}. The Bragg signals will be diffracted through angles of holographic inscription θ_{iHn} before impinging on a matching element in a photo-detector array.

A demodulating hologram possesses a transfer function with a central wavelength and a FWHM bandwidth. The edge of the transfer function will coincide with the operational wavelength range of the element. The signal intensity diffracted by a hologram is therefore related to the Bragg wavelength and so the instantaneous value of the measurand. The wavelength range of each element in an FBG sensor array is then to be separated with a stop-band between consecutive ranges. This will limit crosstalk between different channels in an array demodulation scheme. The operating range of an FBG is typically 2-2.5nm whilst the band-stop can vary from 2nm to in excess of 10nm. The band-stop varies depending not only on the bandwidth of the demodulating transfer function but also which edge of the function positive or negative is used for demodulation. Such limitations do not apply to other schemes for example an active filter scheme can demodulate a sensor array with overlapping ranges if the individual elements can be identified within each sweep of the filter.

The quiescent wavelength and operating range of each element in the FBG sensor array determine the centre wavelength and FWHM bandwidth of the demodulating volume hologram. An inscription wavelength, beam angle and beam width are then chosen to inscribe a hologram with the correct centre wavelength and bandwidth to match the array element.

The proposed system requires the hosting of multiple holograms within the crystal. The first hologram is inscribed by interfering laser beams at the desired angle and wavelength with an inscription time that ensures maximum diffraction efficiency. The two interfering beams are blocked and the wavelength and angle of inscription changed for the next hologram within the sequence. Typically beam width is not altered for a specific holographic array. Each hologram in the array is then inscribed with consecutively smaller times to ensure each element has the same diffraction efficiency. The inscription times for each subsequent hologram are related to the first by equation 3.30, as detailed in section 3.3.3. The process for the inscription of an array of volume holograms is shown in figure 4.3 (Strasser 1989). For experiments described within this thesis however the number of elements in a holographic array is limited to two.

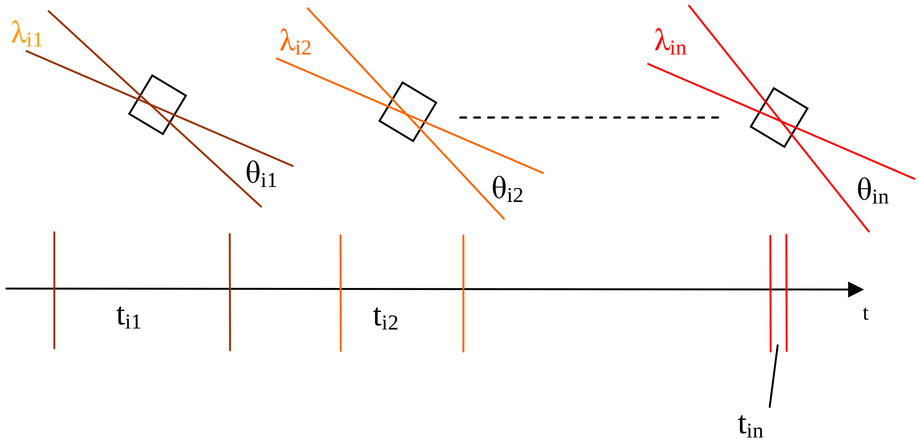

Figure 4.3 Process for the inscription of a holographic array.
The first hologram is inscribed at the desired angle θ_{i1} and wavelength λ_{i1} with an inscription time t_{i1} that ensures maximum diffraction efficiency. Each subsequent hologram is inscribed at a different wavelength λ_{in} and angle θ_{in} with consecutively smaller inscription times t_{in}.

To allow the schedule to be derived the inscription and erasure time constants have to be established. These are related to the crystal’s material constants and to the inscribing beam intensities, as outlined in section 3.2.3.

To achieve maximum diffraction efficiency the space charge field that forms the hologram must be orientated to gain access to the r_{42} coefficient of the $BaTi0_3$ crystal. This implies that the interfering beams that create the hologram are of extraordinary polarisation, with the beam bisector being at an angle other than 90° to the crystal’s c-axis, as outlined in section 3.1 (Ringhofer 1991).

A beam interrogating the hologram has to match the Bragg condition to achieve maximum diffraction efficiency. This means the incident angle and wavelength of the beam is identical to the reference beam used in holographic inscription. The beam is also to be of extraordinary polarisation. The instantaneous Bragg wavelength of a sensor signal will change in response to an applied measurand. The transfer function will then modulate intensity of the signal depending on the instantaneous wavelength.

Polarisation control is therefore important in both hologram inscription and interrogation. The majority of experiments use Single Mode (SM) fibre where the state of polarisation is related to the birefringence within the fibre. The birefringence is subject to change with temperature causing a drift in the polarisation state. Polarisation within the SM fibre however can be manipulated by the use of Polarisation State Controllers (PSCs). Due to the sensitivity of the demonstration system the incorporated PSCs need to be adjusted before and during the execution of any experiment.

The FBGs used in latter experiments are fabricated in Polarisation Maintaining (PM) fibre to ensure the sensor signals possess a stable state of polarisation. The PM fibre however introduces an interferometer created by the difference in refractive indices between the fibre’s Eigen-axes. There is an inverse relationship between the FSR of the interferometer and the distance travelled in the PM fibre by a sensor signal. The distance includes that travelled by the illuminating spectrum as well as the reflected signal. The depth of interference depends on the state of polarisation of the broadband spectrum with respect to the orientation of the Eigen-axes. To reduce the effect of the interferometer the main state of polarisation of SLD is to align with either of the Eigen-axes whilst the distance travelled in the PM fibre is to be minimised. The effects of the interferometer however cannot be negated as the SLD has approximately a 10:1 polarisation extinction ratio between the main state of polarisation and the orthogonal state.

A ratiometric intensity referencing scheme (Davis & Kersey 1994) was investigated as the proposed demodulation plan is susceptible to fibre bend losses and changes in source intensity. Here two holograms simultaneously demodulate a single sensor. The wavelength range of the FBG sensor is aligned with the positive slope of one transfer function and the negative slope of the other. The two holograms then divide the Bragg signal and diffract the respective parts through separate angles to two photo-detectors. The scheme is outlined in figure 4.4.

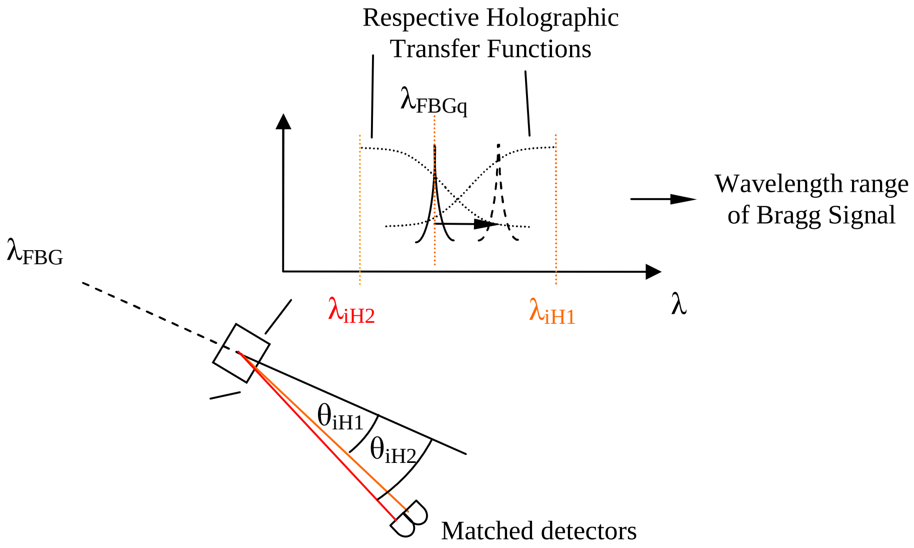

Figure 4.4 The proposed intensity referencing scheme.
Two holograms simultaneously demodulate a single FBG sensor, the wavelength range of the sensor being aligned with the positive slope of one transfer function and the negative slope of the other. The two holograms are inscribed at wavelengths of λ_{iH1} and λ_{iH2} and angles θ_{iH1} and θ_{iH2} respectively. The Bragg signal is divided and the respective parts diffracted through separate angles to two matching photo-detectors.

The intensity referencing scheme assumes that the photo-detectors used are matched and that the holograms possess equal but opposite transfer function gradients throughout the sensor's wavelength range of operation. In this scheme ratiometric detection will be used for intensity referencing. Ratiometric detection is governed by the equation (Davis & Kersey 1994)

$$S(\varepsilon) = \frac{I_{APD1} - I_{APD2}}{I_{APD1} + I_{APD2}} \qquad \textbf{4.1}$$

where I_{APD1} and I_{APD2} are the currents in two matched APDs. The quantity S is a function of the applied measurand which in this case is strain (ε).

An understanding of the intensity referencing technique can be gained from equation 4.1. The currents I_{APD2} and I_{APD1} are determined by the operating point of the respective demodulating transfer functions. If the intensity change is due to bend losses or source fluctuations the currents are in proportion $I_{\mathrm{APD2}}=kI_{\mathrm{APD1}}$ and the difference over sum quotient remains unchanged. If however the respective currents are modified by deviation in applied strain the change in the respective currents are equal but opposite $\Delta I_{\mathrm{APD1}}=-\Delta I_{\mathrm{APD2}}$. Under these conditions the change in S is proportional to twice the change I_{APD1} or I_{APD2}. The operation of the intensity referencing scheme is shown in figure 4.5.

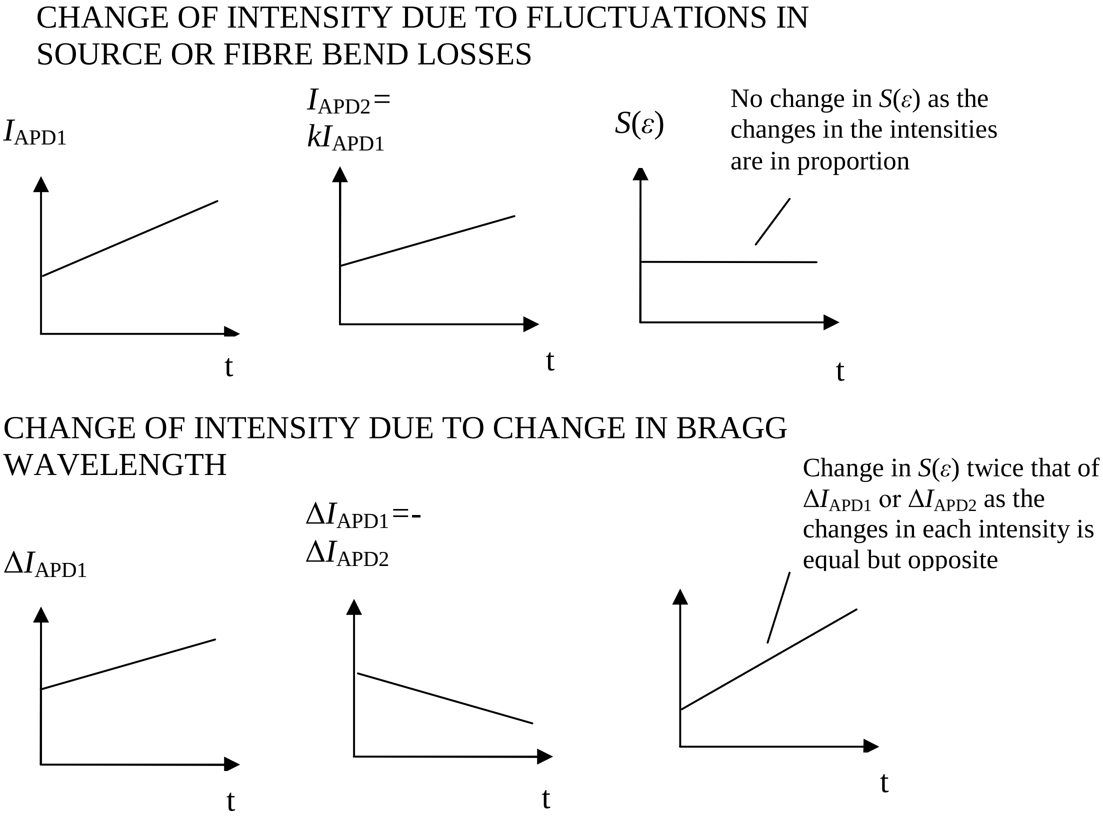

Figure 4.5 The operation of the proposed intensity referencing scheme.
If the current changes at the two detectors are in proportion then the changes are due to source power or fibre loss fluctuations and the value of $S(\varepsilon)$ remains unchanged. If the current changes are equal and opposite then this is due to changes in the instantaneous Bragg wavelength.

The operation detailed in figure 4.5 above is only applicable if the slope of the transfer functions are equal and opposite. If the slopes are not equal a constant factor is to be incorporated into the equation to allow for compensation. This factor is the quotient of the slopes applicable to each transfer functions $\left(\frac{d\eta_2/d\lambda}{d\eta_1/d\lambda}\right)$, where η_1 and η_2 are the respective holographic transfer functions associated with I_{APD2} and I_{APD1}.

It is possible to see from figure 4.5 however that the slope of the transfer functions is not constant throughout the sensor's wavelength range of operation. The compensation factor is the differential of the one transfer function with respect to wavelength divided by the differential of the other. Equation 4.1 can therefore be altered for this particular intensity referencing scheme.

$$S(\varepsilon) = \frac{I_{APD1}\left(\frac{d\eta_2(\lambda)/d\lambda}{d\eta_1(\lambda)/d\lambda}\right) - I_{APD2}}{I_{APD1}\left(\frac{d\eta_2(\lambda)/d\lambda}{d\eta_1(\lambda)/d\lambda}\right) + I_{APD2}} \qquad \mathbf{4.2}$$

where $d\eta_x/d\lambda$ is the differential of the transfer function with respect to wavelength. The subscript x=1,2 refer to the respective demodulating holographic transfer functions.

An FBG sensor demodulation scheme based on a Volume Hologram is shown in figure 4.6. An SLD illuminates the fibre based FBG sensor. The Bragg reflection is separated from the illuminating beam via a 3dB coupler. The holographic transfer function modulates the intensity of the Bragg signal depending on the instantaneous wavelength. A current proportional to the intensity of the Bragg signal is then produced by an APD.

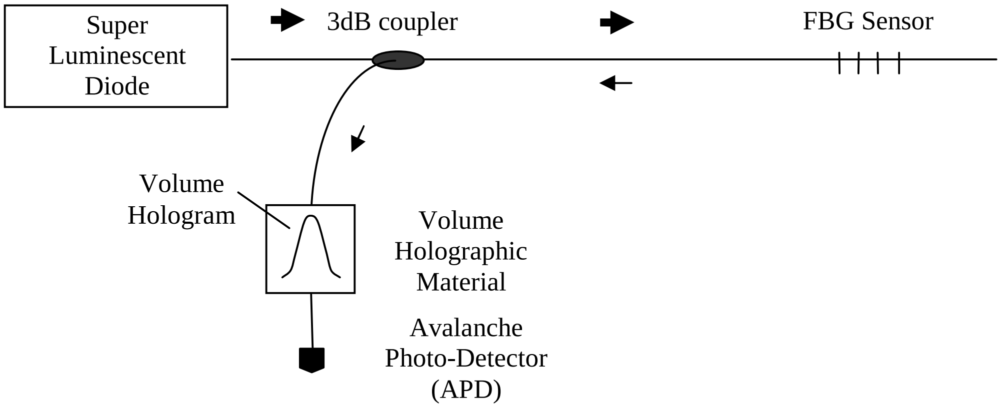

Figure 4.6 The configuration of a single FBG sensor demodulation scheme. The 3dB coupler separates the illuminating broadband beam from the SLD from the reflected Bragg signal. The volume hologram then modulates Bragg signal intensity depending on the instantaneous wavelength. A current proportional to the intensity of the Bragg signal is then created within the APD.

When applied to the demodulation scheme outlined in figure 4.6 the signal intensity diffracted is the integral of the reflected sensor spectrum at the instantaneous Bragg wavelength and the holographic transfer function. The transfer function is symmetrical about the wavelength of inscription whilst the sensor spectrum is symmetrical about the instantaneous Bragg wavelength. Consider therefore a FBG sensor signal whose central wavelength can vary from -∞ to ∞. The intensity of the diffracted signal is then the convolution of the reflected sensor spectrum and the holographic transfer function.

The convolution of two functions is defined in terms of a dummy variable for example *X*. The convolution is then given by the equation

$$(f \otimes g)(x) = \int_{-\infty}^{\infty} f(X)g(x-X)dX \qquad \textbf{4.3}$$

The convolution is then represented by figure 4.7.

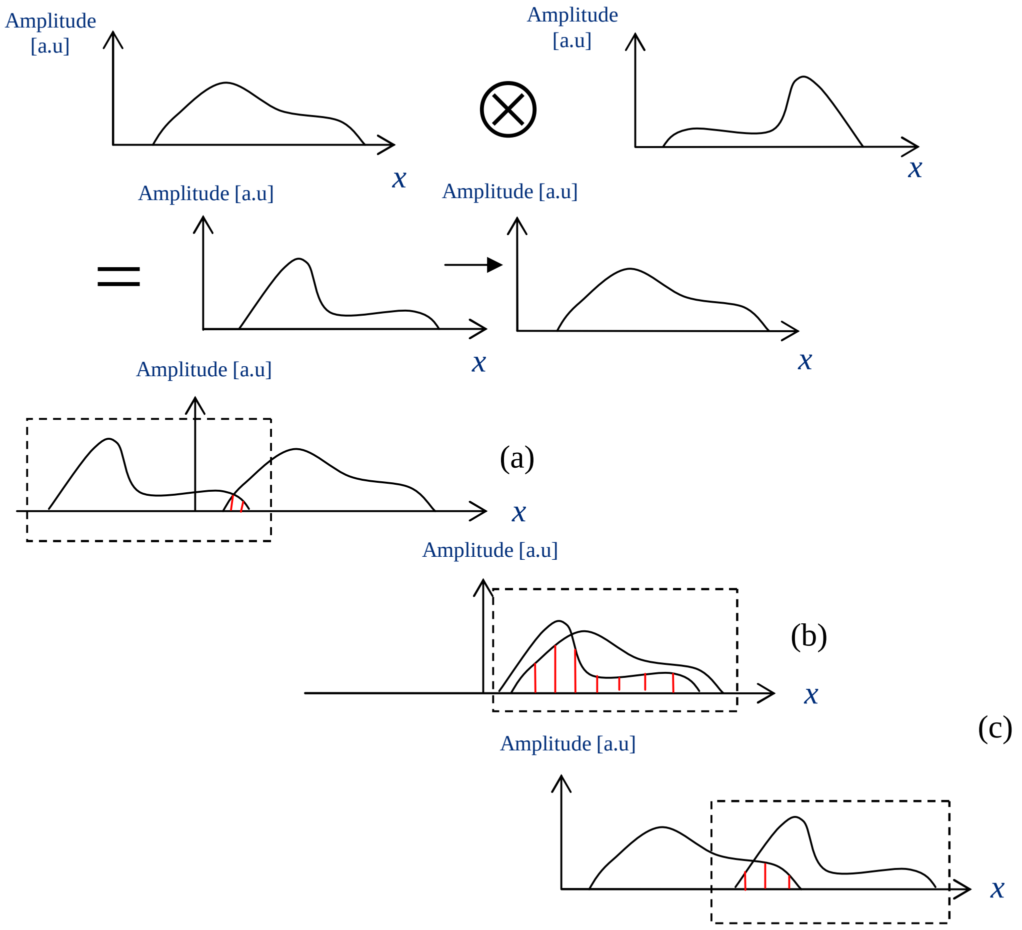

Figure 4.7 Convolution of two functions f(*x*) and g(*x*).
A space-offset is added to one function to allow variation along the *x*-axis from -∞ to ∞. Wherever the functions intersect the integral of their product is determined, this is shown by the shaded area in examples (a), (b) and (c). The convolution is then a function whose value at a specific value of *x* is the area of the intersection between the functions.

One of the two functions is transposed $g(X)\rightarrow g(-X)$. A space-offset is added $g(x\text{-}X)$ to allow the function to vary along the *x*-axis from -∞ to ∞. Wherever the two functions intersect the integral of their product is determined. This is shown by the shaded area in the three examples (a), (b) and (c). The convolution is then a function whose value at a specific value *x* is the area of the intersection between the functions $g(x\text{-}X)$ and $f(X)$.

The intensity of the sensor signal however also depends on the power spectrum of the SLD and the split ratio of coupler at the instantaneous Bragg wavelength. The intensity recorded also depends on the responsivity of the APD at the instantaneous wavelength. The response of the system over all wavelengths can then be summarised by the equation

$$I_{\mathrm{APD}}(\varepsilon) = R_{\mathrm{APD}}(\lambda)\left[\Re(\lambda(\varepsilon)) \otimes \eta_{\mathrm{VH}}(\lambda) P_{\mathrm{SLD}}(\lambda) S_{\mathrm{3dB}}(\lambda)\right] \qquad \mathbf{4.4}$$

where η_{VH} is the transfer function of the volume hologram, P_{SLD} is the power spectrum of the SLD, $\Re$ is the reflection spectrum of an FBG sensor, S_{3dB} is the split ratio of a 3dB coupler and R_{APD} is the responsitivity of the APD. I_{APD} is the current produced in the APD. The instantaneous Bragg wavelength of reflection is assumed to be proportional to the applied measurand which in this case is strain ($\lambda \alpha \ \varepsilon$).

The FBG sensors fabricated possess an FWHM optical bandwidth of approximately 0.2nm. However the holographic transfer function has an optical bandwidth much greater than that of the FBG sensors. The bandwidth of the transfer function is also considerably less than the power spectrum of the SLD and the responsitivity of the APD. The split ratio of the coupler is considered constant over the sensor's wavelength range of operation. In this case the response of the scheme is dominated by the transfer function of the hologram. The wavelength response of the SLD, the APD and the 3dB coupler are discussed in section 4.8.

The APD introduces noise into the system that limits the resolution of the mesurand value. This manifests as high speed fluctuations in recorded data. The average measurand value represented by a straight line can then be found by linear regression techniques. The noise is then the standard deviation from the average value that can be found by the least squares method. The resolution depends on the Signal to Noise Ratio (SNR) of a sensor signal and therefore depends on the peak diffraction efficiency of the demodulating hologram. The maximum error in the measurand can also established by comparing that applied to the average straight line measurand value derived from results. The applied measurand can be established by the voltage applied to PZT driven stage.

The scheme described in figure 4.6 is realised in Single Mode (SM) fibre however the polarisation control of sensor signals within this media is problematic. In an attempt to control polarisation FBG sensors are fabricated within a length of PM fibre. The PM fibre then replaces a length of SM fibre hosting the FBG sensor detailed in figure 4.6. The PM fibre is then spliced on to the SM fibre connected to the 3dB coupler. Ideally the light from the SLD illuminating the sensor is coupled into one Eigen axis alone however the polarisation extinction ratio of the SLDs used are approximately 10:1 so despite best efforts some light will always be coupled into both

Eigen axes. The signal reflected from the FBG sensor therefore will have two orthogonal components associated with each axis that will arrive at the fibre splice at slightly different times. The polarisation of the two components however is subject to rotation upon propagating a distance within the SM fibre. The two components then interfere due to the OPD introduced by the difference in refractive indices between the Eigen axes.

The interferometer created possess a raised cosine response R_{inf} and a Free Spectral Range (FSR) given by the equation

$$\Delta\lambda = \frac{\lambda^2}{(n_{\mathrm{s}} - n_{\mathrm{f}})2d} \qquad \textbf{4.5}$$

where d is the distance between the splice of the SM and PM fibres and the FBG sensor. The OPD is proportional to twice this distance as the illuminating beam has to travel a distance d to the sensor from the splice whilst the Bragg reflection has to travel this distance back to the splice. As the distance d increases the FSR of the interferometer $\Delta\lambda$ reduces. At lengths of $d \geq 0.35$m the FSR is 4nm or smaller, the difference in refractive indices between Eigen-axes being available from fibre specifications and is given as $(n_{\mathrm{s}}\text{-}n_{\mathrm{f}}) = 0.43\mathrm{x}10^{-3}$. This is approximately the same as the optical bandwidth of the holographic transfer functions used for sensor demodulation so the interferometer can disturb the demodulation process.

Equation 4.4 can then be modified to incorporate the interferometer

$$I_{\mathrm{APD}}(\varepsilon) = R_{\mathrm{APD}}\left[\Re(\lambda(\varepsilon)) \otimes \eta_{\mathrm{VH}}(\lambda) P_{\mathrm{SLD}}(\lambda) S_{\mathrm{3dB}}(\lambda) R_{\mathrm{Inf}}(\lambda)\right] \qquad \textbf{4.6}$$

where $R_{\mathrm{Inf}}(\lambda)$ is the response of the interferometer. The impact can be minimised by shortening length d and ensuring as far as possible that light is coupled into only one Eigen-axis.

To demonstrate the principles of the demodulation system, the initial experiment focused on the demodulation of one sensor by a single volume hologram. The process for inscribing a single hologram is detailed in section 4.2. The hologram is then characterised in section 4.3. This is important as the transfer function introduces nonlinear aspects into the results. The transfer function is also mathematically modelled, as detailed in section 3.3.2. Comparisons between experimental and theoretical results are made.

Inscription of the FBG sensors is detailed in section 4.4 and response of the sensors to strain in section 4.5. A PZT controlled stage is used to apply strain to the FBG sensor. This introduces hysteresis that is characterised and then mathematically modelled by two simple quadratic equations applicable to the forward and reverse directions respectively. The process for the demodulation of a single FBG sensor is detailed in section 4.6. The results exhibit the effects of both the non-linearity within the holographic transfer function and hysteresis due to the PZT driven stage. A look-up table combining these nonlinearities can then compensate for errors. Here the normalised photo-detector signals representing raw results are processed to create normalised sensor signals that are correlated to the applied voltage.

Section 4.7 details the process used to establish the inscription and erasure time constants, knowledge of which is necessary to optimise diffraction efficiency when inscribing a holographic array. The measured times constants are then compared to the modelled constants detailed in section 3.2.3.

Many optical components possess a wavelength dependent response. These responses can disturb the demodulation of the FBG sensor by a holographic transfer function and are discussed in section 4.8.

A scheme for the demodulation of a two element FBG sensor array is demonstrated in section 4.9. An FBG sensor array has also been fabricated in PM fibre to control the state of polarisation of sensor signals. A scheme for the demodulation of a two element array fabricated in PM fibre is therefore demonstrated in section 4.10.

The ratiometric intensity reference scheme is investigated in section 4.11. A demonstration is detailed that allows demodulation of a single FBG sensor by two holograms. The raw results are primarily processed to compensate for hysteresis within the PZT driven stage. The results are further processed using equation 4.2 to compensate for the non-linearity within the transfer functions. The processed data is then correlated to the voltage applied to the PZT. An intensity reference scheme however should not be affected by fluctuations in source intensity and fibre losses. Another experiment is therefore detailed where the source intensity is modulated by a sinusoidal signal as different static strains are applied to the sensor. The results are processed using equation 4.2 to reconstruct the static signals.

4.2. Inscription of a Single Hologram

The configuration used to inscribe a volume hologram is shown in figure 4.8. Two tuneable lasers have been used during the course of the experiments. The first is a Coherent Innova 70C-4 Argon-ion laser running on all lines with an output power of 5W that was used to pump a tuneable Schwartz Electro-Optic Titan Ti: Sapphire laser. The Ti: Sapphire was configured in a ring cavity with a specific mirror set to allow a coherence length of 500m, an optical bandwidth of 40MHz and a wavelength range of 790-850nm. The output power was approximately 300mW. The incremental steps in wavelength are limited to approximately 0.5nm by the cavity length. The Argon-ion laser developed a catastrophic fault midway through experiments and was replaced by a Sacher-LaserTechnik TEC500 Littman external cavity laser. Here the light source is a broadband diode that limits the wavelength range to 768-784nm but with no constraints on wavelength increments. The output power is approximately 12mW with an optical bandwidth of 1MHz.

Light from the laser is coupled into a SM fibre using a x20 microscope objective. Two types of fibre were used, with cut off wavelengths of 780nm and 750nm for use with the Ti: Sapphire and external cavity lasers respectively. For the external cavity laser the maximum power coupled was 6mW whilst for the Ti: Sapphire it was 12mW. The coupling efficiency was severely limited for the Ti: Sapphire laser due to the non-circular beam profile. The quality of an inscribed hologram is impaired by beam fanning. This is a phenomenon where light in the inscribing beam is deflected away from a straight-line by the electro-optical properties of the crystal. The amount of light subject to fanning increases proportional with beam intensity therefore degrading hologram quality in proportion.

A 3dB coupler created beams of equal intensity, a reference and an object. Two different couplers were used one with a central wavelength of 820nm and another of 780nm for use with the Ti: Sapphire and external cavity lasers respectively. The couplers used were Sifam models PS78 and PS82 for operation at 780nmm and 820nm respectively.

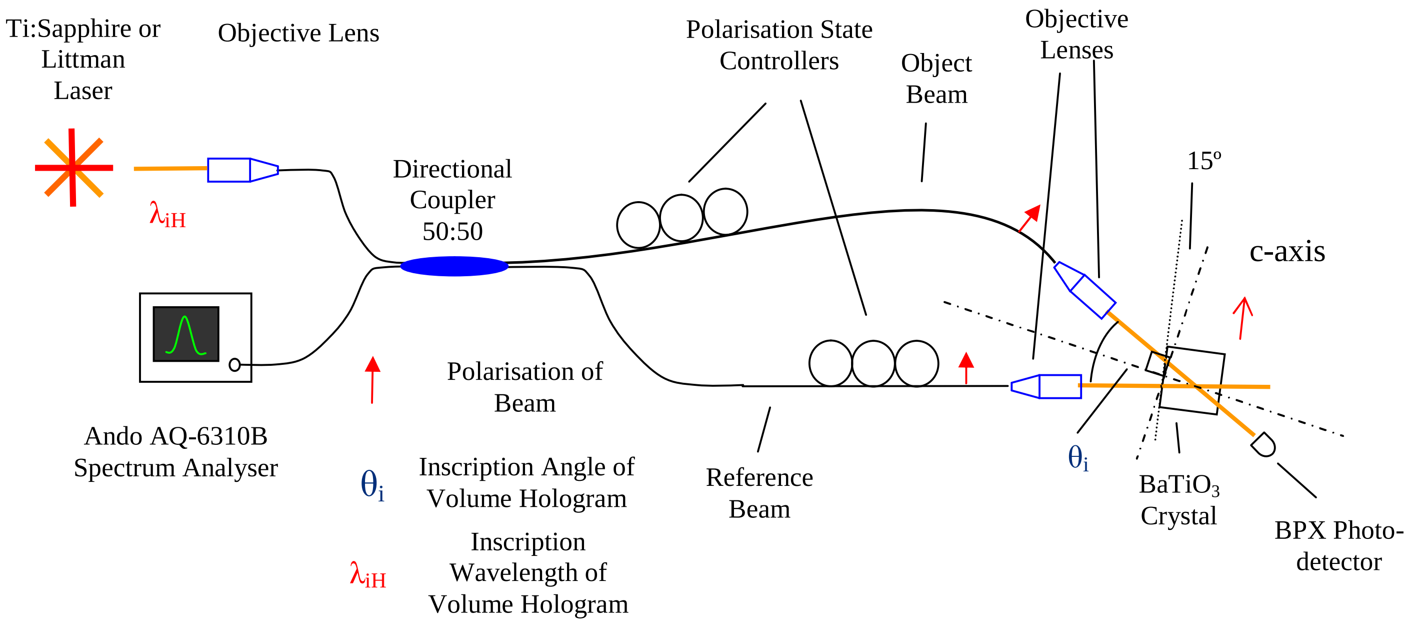

Figure 4.8 Experimental configuration for the inscription of a single Volume Hologram.

The polarisation of the beams in the fibre is controlled by Polarisation State Controllers (PSCs). A PSC consists of three metal rings of a specific diameter determined by the wavelength of operation. They are in series connected to a base plate and can be rotated around a common axis tangential to all rings. Each is wrapped with SM fibre in series one turn around the first, two turns around the central and single turn around the third. The first and third rings act as ¼ wave-plates whilst the central ring acts as a ½ wave-plate. Rotating the rings around a common axis changes linearly polarised light of an arbitrary orientation to one desired.

The beams exist the fibre end and were collimated by a x20 microscope objective and directed to create an interference pattern within the body of the 5mm x 5mm x 5mm $BaTiO_3$ crystal. The beams were of extraordinary polarisation. The bi-sector of the beams was rotated by approximately 20º by an OptoSigma 40mm rotation stage (Part Number 124-00500) with respect to a normal to the crystal's c-axis to maximise diffraction efficiency (Solymar 1996). The crystal is also tilted backward by approximately 5º to minimise the effect of spurious gratings caused by interface reflections (Rajbenbach 1991). This was achieved by placing a thin metal strip under the front facet of the crystal.

In practice the crystal has been previously characterised and so c-axis can be readily found by damage of a specific nature at the corners of the crystal. The c-axis however can be found by directing a beam from a He-Ne at the front facet of the crystal. Beam incidence is at the Brewster angle determined by the refractive index of the photorefractive material. This allows the maximum beam intensity to the transmitted through the crystal. The s-polarised beam is therefore offset from the suspected c-axis by the same angle. If the suspected is the actual c-axis the beam will experience fanning. Stands of the light will be diffracted away from the main beam direction perpendicular to the plane of beam incidence.

A spectrum analyser was connected to the unused coupler port. This allows the wavelength of inscription to be monitored. The coupler port also represents the output of an interferometer formed by beam reflections from the fibre ends. When the beams interfere the OPD can be changed by placing a hand in close proximity to one fibre. This changes subtly the refractive index of the fibre core and therefore alters the polarisation state of the transmitted light. The result is a change in the received intensity seen on the analyser as a fringe is traversed. Subsequently the interferometer is shown to a stable by removing the hand and waiting for power fluctuations to subside. If there are no changes in received intensity when a hand is placed over the fibre either the beams are mutually incoherent and the respective state of polarisation do not match or the tuneable laser is operating with multiple longitudinal modes. If the intensity fluctuations do not stabilise this is an indication that the laser is mode hopping. This simple test gives an indication if holographic inscription is possible.

A Broadband Photo-detector (BPX) is positioned to monitor changes in object beam intensity due to two-beam coupling (Refregier 1985). Two beam coupling is due to grating formation and allows hologram growth to be monitored. The object beam intensity decays to a steady state value. The decay can be recorded by computer running a standard LabView module, the signal being input to the computer via a Data Acquisition Card (DAQ) card. Inscription times are discussed in Section 4.7.

4.3. Characterisation of a Single Hologram

Once the hologram is inscribed it can be characterised by using the output of the tuneable laser. The configuration is shown in figure 4.9. The laser output is split by a 3dB coupler, one port being connected to a spectrum analyser to record output wavelength. The other is directed toward the crystal by a x20 objective lens in the same direction as the reference beam used at inscription. The beam has to be of the extraordinary polarisation as discussed in section 4.1.

The output of the interrogating laser fluctuates with wavelength and time so a beam splitter creates a monitor signal to allow for compensation. The monitor beam is detected by a BPX photo detector and recorded in Labview.

The main beam was attenuated by a variable neutral density filter before impinging on the crystal to reduce intensity and ensure that the process of characterising did not result in hologram erasure. The un-diffracted portion of the beam passing through the crystal was recorded by a Photon Control photo-detector. The diffracted portion was recorded on a Hamamatsu C5460 APD module. This had a responsitivity of 0.5 A/W within the 800nm range and an internal gain of 30. The signal is then recorded in LabView via a Stanford Research SR560 preamplifier. The signal was recorded at 20 readings per second and averaged over a 1 second period. The division of the diffracted power by the un-diffracted power then determines the diffraction efficiency of the hologram.

The lasers are stepped through a range of wavelengths to determine the transfer function. A shutter then blocks the main beam between wavelength increments. The Littman cavity laser can be tuned to any desired wavelength within its operating range however the Ti: Sapphire allows wavelength increments of 0.5nm. Readings are taken continuously throughout the experiment so blocking the beams between increments allows ready location of data pertaining to a specific wavelength.

The laser is initially tuned to the inscription wavelength of the hologram. The angular bandwidth of the hologram can then be established with the same experimental configuration. The objective lens is mounted on a rotational stage and rotated fractions of a degree to determine change in diffraction efficiency from the Bragg angle.

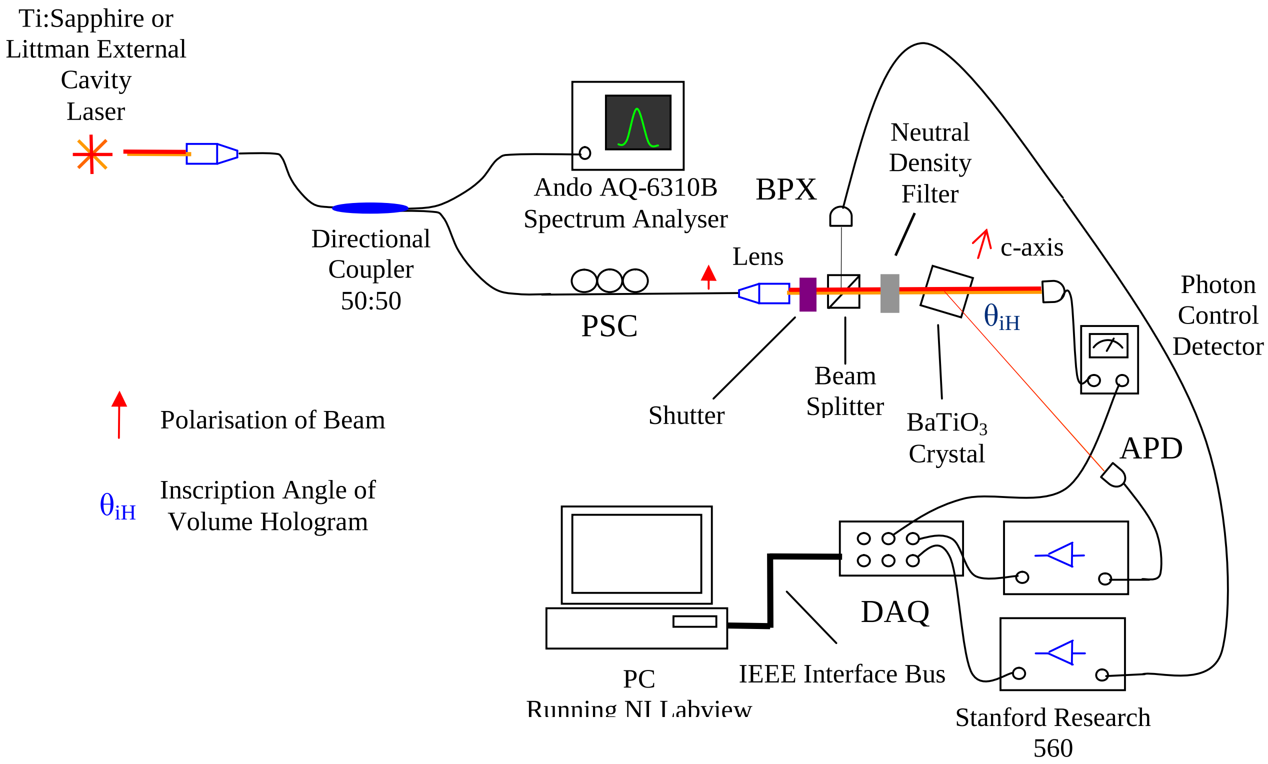

Figure 4.9 Characterisation of the holographic transfer function.

A theoretical model of a holographic transfer function inscribed with Gaussian beams and based coupled model theory is outlined in section 3.3. A theoretic function can then be derived using experimental variables and compared with results, the variables include wavelength, angle and beam width of inscription. The width of the beam is measured by a number of circular reference holes drilled into a plastic template. The measurement of beam diameter is therefore approximate and will possess an associated error. This causes an error in the wavelength and angular bandwidth of the transfer function.

The holographic diffraction efficiency depends on the change in refractive index achieved when inscribing a hologram. In turn the change in refractive index depends on the value of the space charge field and the effective electro-optic co-efficient r_{eff} as determined by equation 3.6. The diffraction efficiency however throughout experimentation is much less than expected by theoretical calculations. Theory assumes an absorption rate that determines the number of mobile carriers. The space charge field then depends on the number of mobile carries relocated due to the inscription process. The absorption rate however is known to be a function of wavelength (Günter 1987). Theory presented in literature (Solymar 1996) assumes a wavelength of operation of 500nm however experiments described in this thesis were executed at approximately 800nm where the absorption coefficient is known to be much less. This leads to fewer carriers being available for relocation, a lower space charge field and therefore reduced diffraction efficiency. Other aspects for example scattering and reflections at front and back crystal facets also contribute to the low diffraction efficiency. The resolution of the measurand within intensity based demodulation schemes such as this depend on the on the signal to noise ratio (SNR). Very low diffraction efficiency causes sensor signals to be susceptible to noise and therefore possess low resolution figures.

Figures 4.10 and 4.11 show typical wavelength and angular transfer functions respectively for holograms inscribed within the 800nm wavelength range. The inscription variables and the resulting holographic parameters are shown in Table 4.1.

Table 4.1 Parameters used to inscribe the hologram and the resulting key holographic parameters. λ_i is the wavelength, $\theta_i/2$ the half angle and w the beam width radius of inscription. The FWHM wavelength and angular bandwidth is given by $\delta\lambda$ and $\delta\theta$ respectively.

Parameter	**Value**
λ_i	815.4nm
$\theta_i/2$	10°
w	0.25±0.03mm
$\delta\lambda$	3.65±0.3nm
$\delta\theta$	1±0.1°

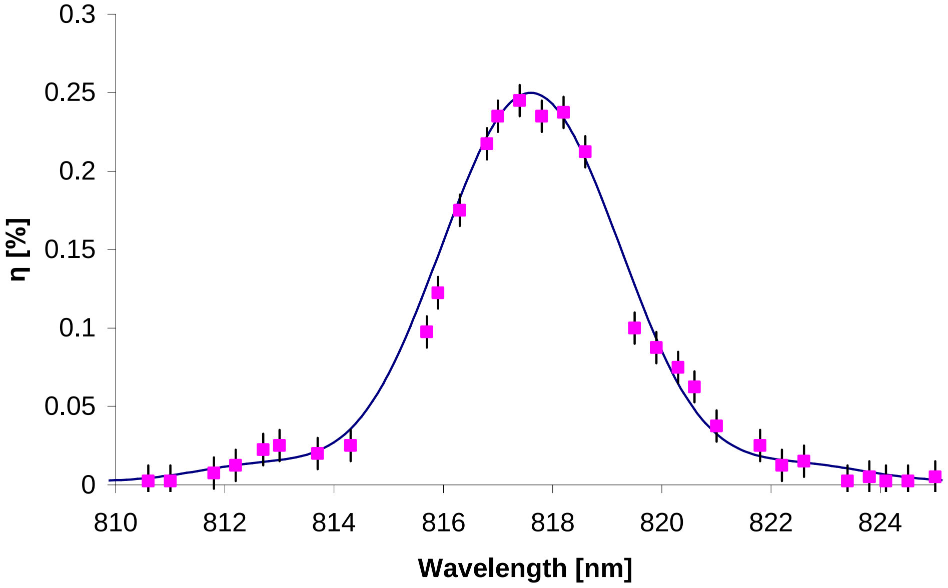

Figure 4.10 The wavelength transfer function of a volume hologram inscribed within $BaTiO_3$. The hologram was inscribed and interrogated with a Ti: Sapphire laser. The experimental results are given by the set of points (■) whilst the theoretical results from equation 3.28 are given by the continuous line (—). The inscription variables and the resulting holographic parameters are shown in Table 4.1.

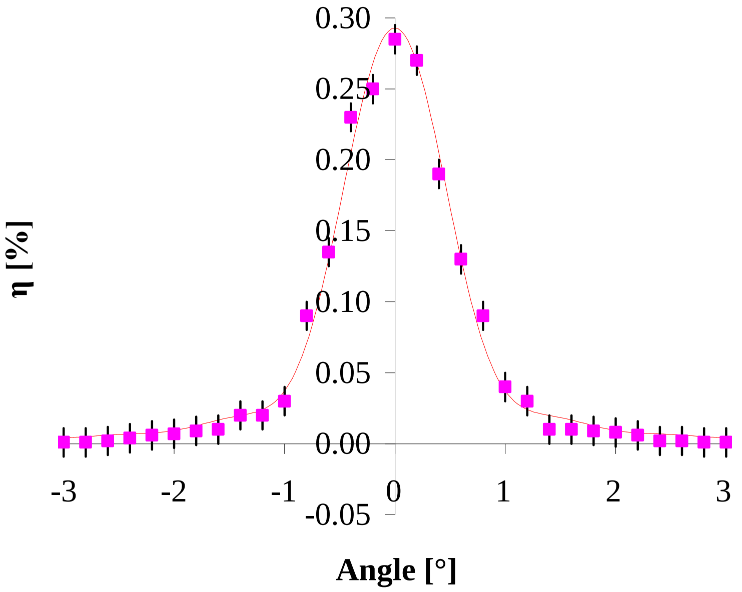

Figure 4.11 The angular transfer function of a volume hologram inscribed within $BaTiO_3$. The hologram was inscribed and interrogated with a Ti: Sapphire laser. The experimental results are given by the set of points (■) whilst the theoretical results from equation 3.28 are given by the continuous line (—). The inscription variables and the resulting holographic parameters are shown in Table 4.1.

There is a good correlation between the experimental results and theoretical model as demonstrated within figures 4.10 and 4.11. A reference beam is monitored to compensate for fluctuations in laser power at different wavelengths. The experimental results however demonstrate deviation from the theoretical transfer function. This can be attributed to the differences in the averaging process. Sometimes the readings were taken over a period slightly less than 1 second. The beams were blocked by a manual shuttering process that sometimes limited the data collection period to less than 1 second.

The peak diffraction efficiency however is of the order of 0.25%. FBG sensors are characterised in Section 4.5; however a Bragg signal has an approximate intensity of 10^{-6} W so the diffracted signal will be approximately 10^{-8} W. This implies a low intensity signal that is susceptible to noise that is introduced by the APD. Noise present in the results can be seen as an error in the measured diffraction efficiency.

The FWHM bandwidth of the wavelength transfer function is 3.65nm. The edges of the transfer function either side of the peak in diffraction efficiency are approximately linear and therefore suitable for the demodulation of a single FBG sensor. When fitted to a straight line the edges the transfer function showed an r^2 coefficient of determination value of 0.973 (Rodgers 1988) when considered between 10% and 90% of the peak diffraction efficiency. The transfer function can therefore be considered linear over this section. Importantly the transfer function also demonstrates heavily suppressed side-lobes so ensuring limited crosstalk between channels if the hologram is used for the demodulation of an FBG sensor array. The side-lobes are heavily suppressed due to the conical nature of the inscribed hologram as explained in section 3.3. The bandwidth of the angular transfer function however is 1°. This restricts the difference of inscription angles between holograms within an array to approximately twice the angular bandwidth 2°.

4.4. Inscription of an FBG Sensor Array

The fibres identified to host the FBG sensors are photosensitised by saturation in a hydrogen rich environment at a pressure of 175 atmospheres at room temperature for a period of two weeks prior to inscription. Three types of fibre are photosensitised. Two were SM fibres with cut off wavelengths of 750nm and 780nm respectively. The third is a PM fibre with a cut off wavelength of 750nm.

A frequency quadrupled Nd: YAG (Yittrium Aluminium Garnett) laser pulsed at 10Hz was used to inscribe the FBG sensors. The output beam had a Gaussian profile and a power of 60mW at a wavelength of 266nm. A beam splitter derives two beams of equal power. Two mirrors direct the respective beams to a point of intersection with the photosensitised fibre. Cylindrical lenses then focus the beams on the point of intersection forming an interference pattern. This pattern allows the inscription of an FBG within the fibre core. A selected length of fibre is stripped of its protective cover before being placed in the interference pattern as shown in figure 4.12. The wavelength of inscription is given by equation 2.1. The FBGs where fabricated at Cranfield University by Dr Edmund Chehura.

To monitor the growth of the FBG, the spectrum of an SLD transmitted through the fibre is recorded. A spectrum analyser then normalises the instantaneous spectrum to one recorded before inscription began. The peak reflectivity can be determined from the normalised spectrum. The reflectivity depends on the change in refractive index Δn achieved by inscription and the length of the FBG (Lam & Garside, 1981).

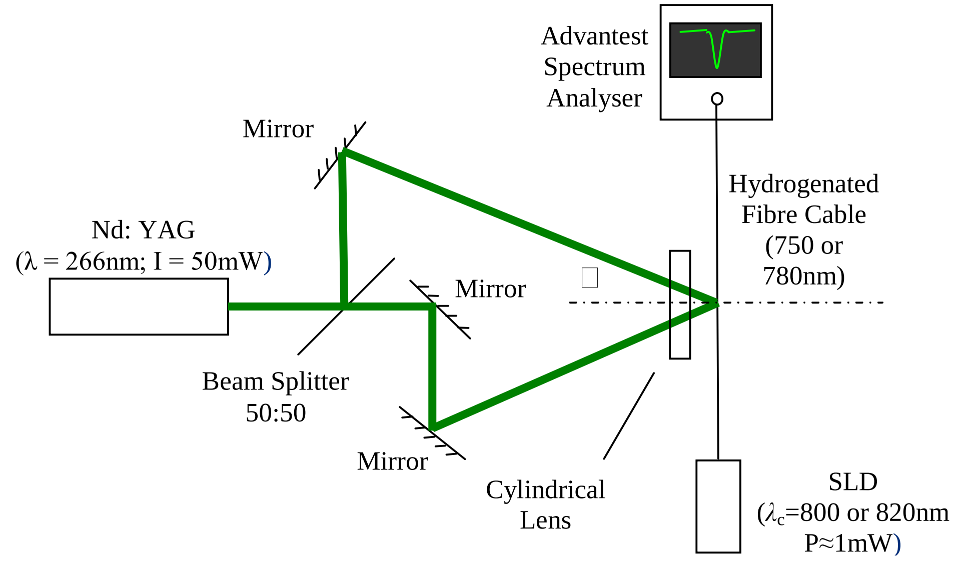

Figure 4.12 Inscription of a Fibre Bragg Grating (FBG).
A Nd: YAG laser with an output power of 50mW and a wavelength of 266nm is used to inscribe the FBG sensors. A beam splitter derives two Gaussian beams of equal power to form an interference pattern at an intersection with the fibre. The beams are directed and focused on to the fibre by mirrors and a cylindrical lens respectively. A selected length of photosensitised fibre is stripped of its protective cover before being placed in the interference pattern.

Two different SLDs were used to monitor inscription. These are a Superlum SLD-38-HP1-TOW2-PD SLD with a peak output wavelength of 820nm and a Qphotonics QSDM-790-2 SLD with a peak wavelength of 800nm. These have spectra that cover the operating range of the Ti: Sapphire and Littman external cavity lasers respectively and are shown in figure 4.13. The Superlum SLD is coupled into a fibre using a x20 objective, the Qphotonics SLD however is provided with a SM fibre pigtail. Both provide a maximum beam power within the fibre of approximately 2mW.

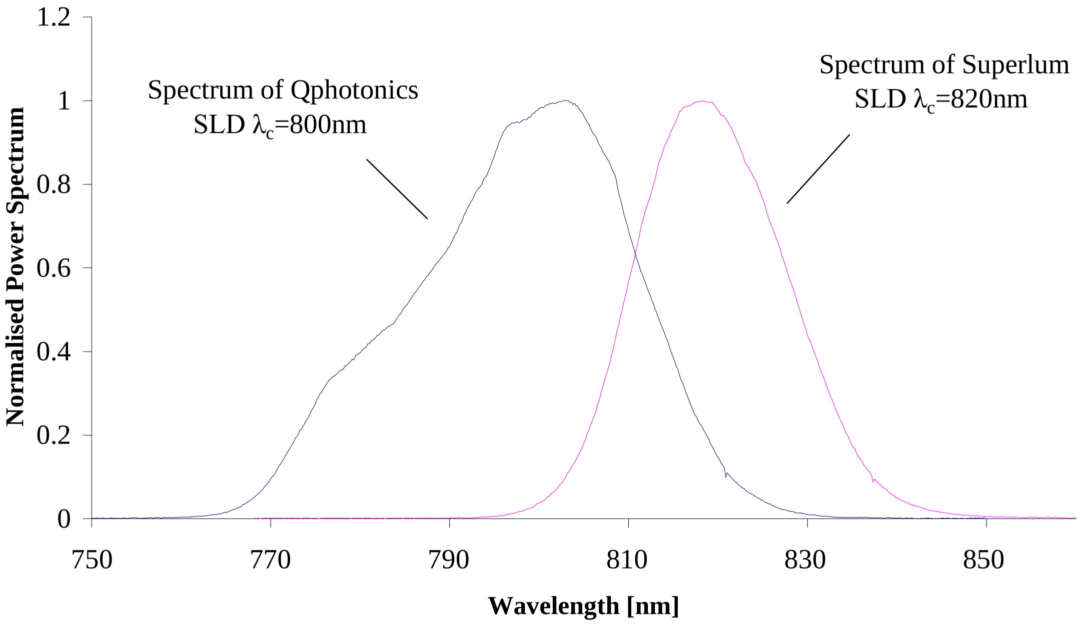

Figure 4.13 Super Luminescent Diode (SLD) Spectra used within experimentation. The spectrum of the Qphotonics SLD (—) is centred at 800nm whilst the Superlum SLD (—) is centred at 820nm.

The FBG sensor array was made by fabricating individual sensor elements with appropriate Bragg wavelengths in short lengths of fibre. After heat treatment to remove excess hydrogen, the lengths of fibre containing the sensors are spliced together to create the array.

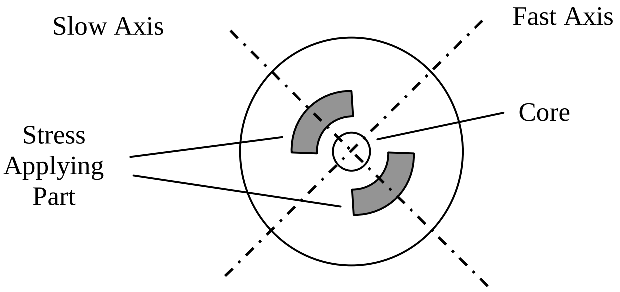

Figure 4.14 Construction of a Bow-Tie Polarisation Maintaining (PM) fibre showing fast and slow axes

The fabrication of a sensor array in PM fibre is more problematic. The PM fibre used to host FBG arrays is of a Bow-Tie construction. This is shown in figure 4.14 and shows the fast and slow axes respectively. When the fibre is illuminated from the side with an UV interference pattern to inscribe a grating the stress applying parts can disturb the pattern and degrade the resulting FBG. To overcome this issue the fibre is to be rotated before inscription begins so the illuminating pattern is incident in the plane of the fast axis. To determine the fast axis prior to inscription the fibre is illuminated from the side by a He-Ne laser. If the light is incident to a stress applying part it will result in a feature in the diffraction pattern. The fibre can then be rotated until the feature is no longer present and the diffraction pattern is similar to if the laser illuminated a standard fibre. At this point the fast axis is located.

Joining lengths of PM fibre is possible however a fusion splicer designed specifically for working with PM fibre was not available. As explained in section 4.1 the length of PM fibre hosting a sensor array is important. The PM fibre introduces an interferometer that can compete with the volume hologram in the demodulation of the sensor elements. A sensor array is therefore fabricated in a single length of PM fibre with predetermined spectral and spatial separations.

The FBG were inscribed in three fibres, two were single mode with operating wavelengths of 750nm and 780nm. These were Fibrecore fibres SM750 (reference number 10328/B-00A) and SM 780 (reference number 10229/A-00BA) respectively. The third is a Fibrecore bow-tie highly birefringent fibre HB750 (reference number 50395/B-00BAC) designed for operation at 750nm.

4.5. Characterisation of the Strain Sensitivity of an FBG Sensor

An FBG is illuminated by the output from an SLD. The reflected signal is separated from the illuminating beam by a coupler and recorded on a spectrum analyser with a resolution of 0.1nm. The data was extracted to a PC running Labview via a General Purpose Interface Bus (GPIB) port. A typical spectrum is shown in figure 4.15. The spectrum has a FWHM bandwidth of approximately 0.2nm and a peak reflectivity of 67%. The quiescent wavelength λ_q of the sensor is 776.3nm.

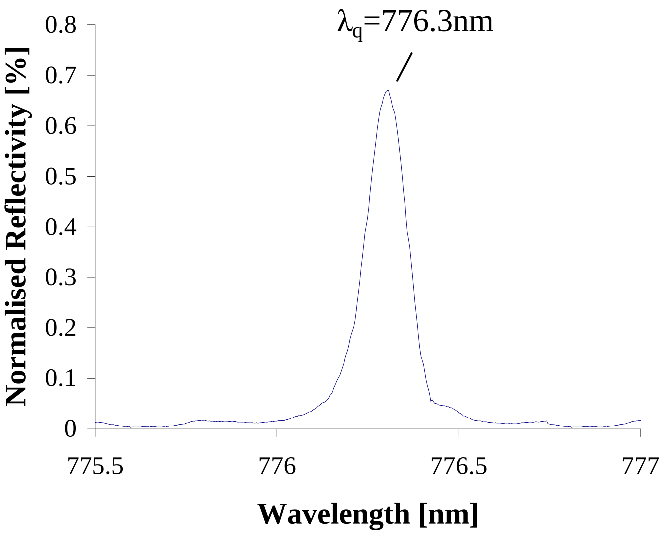

Figure 4.15 Reflection Spectrum of a typical FBG sensor.

It is important to fabricate an FBG sensor with a high peak reflectivity as the diffraction efficiency of the demodulating hologram is of order 1%, as discussed in section 4.3. This will maximise the diffracted signal power. The peak reflectivity is established when inscribing the sensor as explained in section 4.4.

Throughout the demonstration of the sensor array demodulation scheme strain is used as a measurand. This can be easily applied to the FBG sensor elements using a 'push'-'pull' configuration shown in figure 4.16. A moveable stage is located between two fixed stages, the displacement of which is controlled by a voltage driven PZT actuator. The PZT actuator is a Newport 17PAS 013 which is controlled by a Photon Control Piezo Controller MD3-750. The voltage applied can be determined remotely by a signal present on a PZT Controller port. A PC running LabView can then dictate the applied strain via a DAQ card.

V-grooves are placed on both the fixed and movable stages. Individual FBG sensors are attached between a fixed and a movable stage, the host fibre being stripped of its protective cover before being attached to individual V-grooves with Cyanoacrylate adhesive. The V-grooves are separated by 12.5mm.

A free space Michelson interferometer is constructed to measure the movement of the PZT driven stage. The interferometer is formed by a He-Ne laser, a beam splitter and two mirrors, one being fixed to an immovable post whilst the other is attached to the moveable stage. The fringes are monitored via a BPX photo-detector positioned at the centre of a circular fringe pattern. The fringes are then recorded in on a PC running Labview.

A voltage of 40V applied to the PZT controlled translation stage creates a displacement of 52.2μm, corresponding to a strain of 4170με applied to the 'pull' section of the configuration. The 'push' section however is pre-strained. The stage is displaced by the application of 40V before the FBG is attached. The sensor therefore has an applied strain of 4170με for 0V applied. The host fibre was proved to be strong able to withstand this level of strain over periods of months without significant deformation and therefore degradation in the properties of the sensor. The strain reduces to 0με as the applied voltage increases.

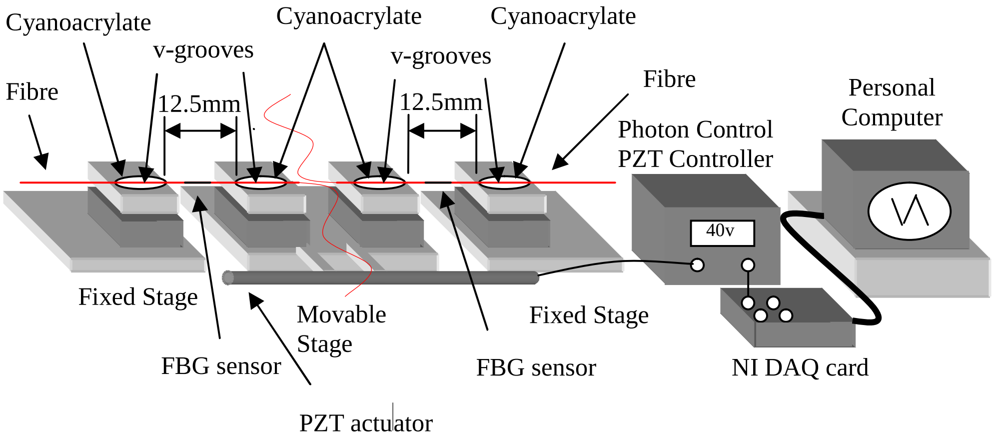

Figure 4.16 A **'**push'-'pull' configuration to apply strain to a FBG sensor array.

The 'push'-'pull' configuration is used to characterise the strain response of three FBG sensors. Two are within the 780nm range whilst another is in the 820nm range. For the two FBGs within the 780nm range, one is fabricated within SM fibre and the other within PM fibre. Here the shift in Bragg wavelength was recorded from the quiescent value as the strain is applied. Changes in the Bragg wavelength are recorded on a spectrum analyser. The results are shown in figure 4.17.

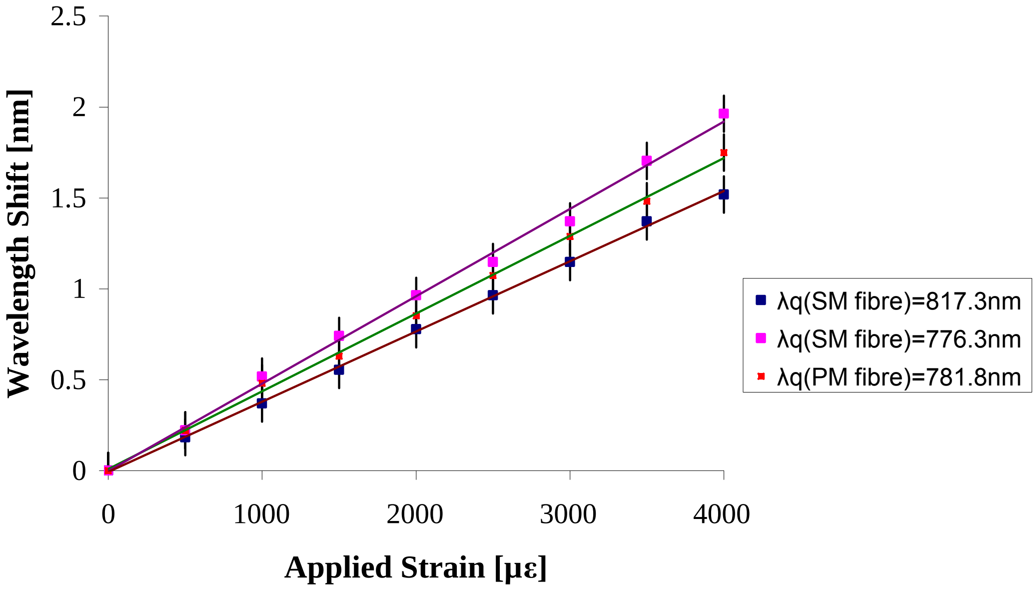

Figure 4.17 Strain response of three typical FBG strain sensors.
The quiescent wavelengths λ_q are shown for the FBG sensors fabricated in SM and PM fibre.
Best-fit straight lines are fitted to the data points for the quiescent Bragg wavelengths of 817.3nm (—), 776.3nm (—) and 781.8nm (—).

The results are similar for the all the sensors characterised. The change in applied strain from 0 to 4000με caused a wavelength shift of 1.5±0.05nm to 1.95±0.05nm depending on the specific sensor. This equates to a strain response of $3.75\pm0.125\times10^{-4}$ nm/με to $4.9\pm0.125\times10^{-4}$ nm/με. The maximum resolution of the spectrum analyser is 0.1nm causing an error associated with the wavelength shift. The responses of the FBG sensors are linear as expected. Included on the chart are fitted straight lines for all three sensors. It is possible to determine the standard deviation of the readings from the fitted straight line. These are 0.151nm, 0.151nm and 0.143nm for the sensors with quiescent wavelengths of 817.3nm, 776.3nm and 781.8nm respectively.

4.5.1 Characterisation of the ‘Push’-‘Pull’ Stage used for Quasi-Static Strain Measurements

Quasi-static measurements are also possible with the ‘push’-‘pull’ configuration, by applying a slowly varying voltage to the PZT actuator. A 30mHz saw-tooth waveform varying from 0-40V is applied to the PZT, the displacement of the stage is then measured using the interferometer described in section 4.5. The applied voltage is limited to 40V as above this figure the stage becomes highly non-linear. The moveable stage stores energy throughout the displacement cycle, resulting in hysteresis. This is demonstrated in figure 4.18 where one FBG sensor is attached to the ‘pull’ section of the system. The errors in displacement are associated with the fringe plots and represent a strain of 40με too small to be detailed on the figure. Shown also is the fit of experimental data to two quadratic equations. These equations map applied voltage to strain in both the forward and reverse directions and will subsequently be used in the processing of results for compensation of this systematic error. The representing quadratic equations are

$$\text{Applied strain } [\mu\varepsilon] = 2.7V^2 + 89.7V + 19.6 \qquad \textbf{4.7}$$

for the forward direction and

$$\text{Applied strain } [\mu\varepsilon] = -2V^2 + 277.5V + 21.5 \qquad \textbf{4.8}$$

in the reverse direction. The applied voltage is given by V whilst the applied strain is given in με.

The hysteresis can be reduced by attaching two sensors one to the ‘pull’ and another to the ‘push’ section of the stage. The results are shown in figure 4.19. The quadratic equations that represent the best fit to the experimental results in both the forward and reverse directions are also shown. The quadratic equations are

$$\text{Applied strain } [\mu\varepsilon] = 1.4V^2 + 149.8V - 29.7 \qquad \textbf{4.9}$$

for the forward direction and

$$\text{Applied strain } [\mu\varepsilon]=-1.3V^2+245.7V+23.6 \tag{4.10}$$

in the reverse direction.

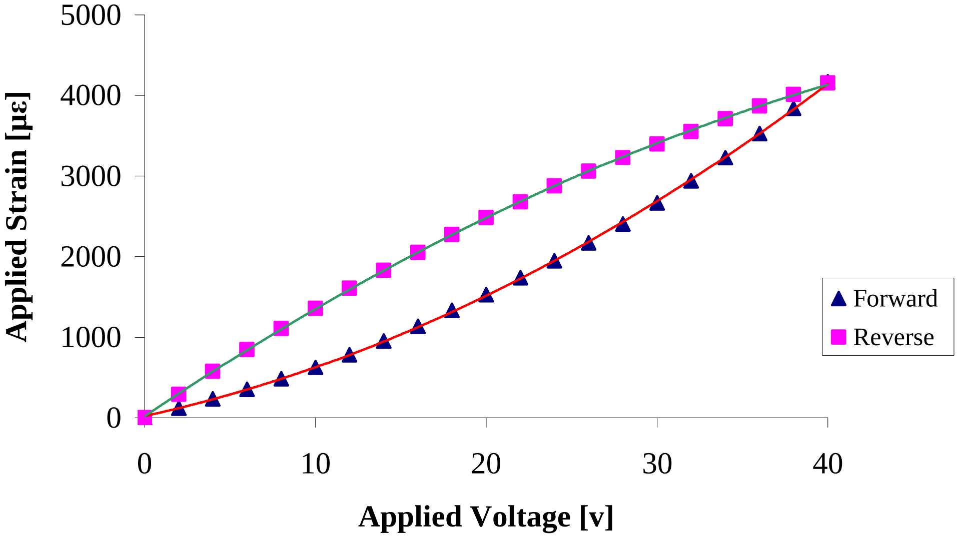

Figure 4.18 Displacement of a PZT controlled stage in response to a slowly varying voltage. The best-fit quadratic equations to the experimental results are also shown for the forward (—) and reverse (—) directions.

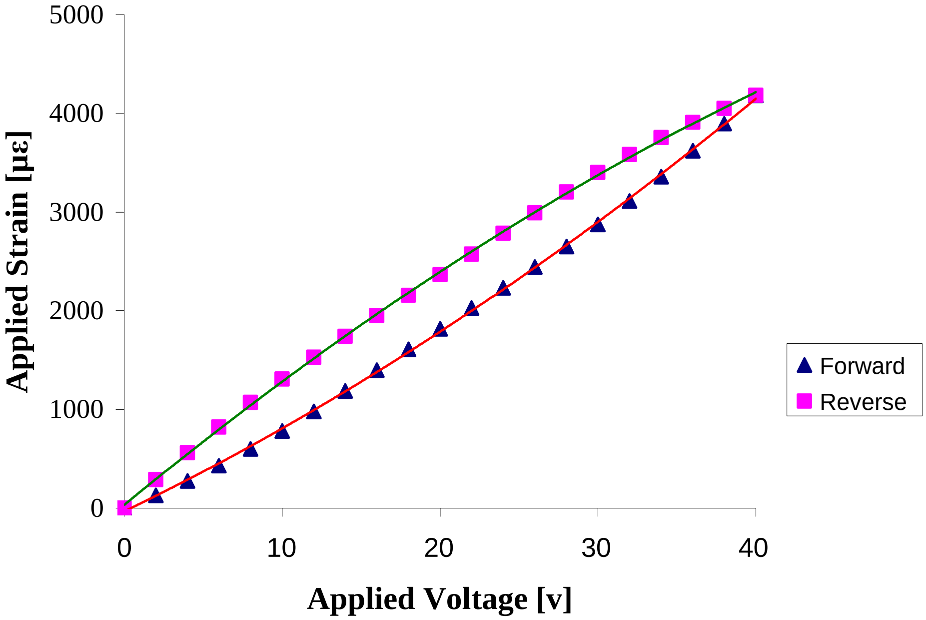

Figure 4.19 Displacement of a PZT controlled stage in response to a slowly varying voltage. The hysteresis can be reduced by attaching two sensors one to the ‘pull’ and another to the ‘push’ section of the stage. The best-fit quadratic equations to the experimental results are shown the forward (—) and reverse (—) directions.

Each section of fibre hosting the sensors on either side of the stage counteract, the tension increases on the 'pull' side of the stage for example as the tension on the 'push' side falls. This reduced the effect of hysteresis on results.

4.6. Demodulation of an FBG Sensor

Volume holograms have been previously inscribed using the configuration detailed in figure 4.8. The half angle of inscription and the beam width determines the bandwidth of the holographic transfer function. The wavelength of inscription is then chosen so an edge of the transfer function coincides with the operational range of the matching FBG sensor. The hologram is inscribed for a time to allow the greatest diffraction efficiency, inscription time constants being discussed in section 4.7. The inscription process however is not assured, the volume hologram can start to form, erase and then form again. This is due to small phase changes in either of the inscribing beams. Therefore even if the inscription time is equal or greater than the time constant maximum diffraction efficiency is not guaranteed.

During sensor inscription, the anisotropic nature of the photo-induced refractive index change produces a birefringence within the FBG (Parent & Michel 1985). The polarisation of the beam from the SLD illuminating the FBG sensor is therefore manipulated to ensure that the reflected Bragg signal is linearly polarised. This is achieved using a PSC for the fibre pig-tailed Qphotonics SLD and a half-wave plate for the free space beam from the Superlum SLD. In initial experiments, an FBG sensor is connected to either the 'push' or the 'pull' section of the stage. A 0-40V 30mHz saw-tooth waveform is then applied to the voltage controlled PZT actuator by a PC running Labview via a DAQ card.

The Bragg signal is separated from the illuminating beam by the 3dB coupler and directed toward the crystal in the same direction as the reference beam used in holographic inscription. The configuration used Sifam 3 dB couplers models PS78 and PS82 for operation at 780nmm and 820nm respectively. A PSC ensures that the Bragg signal is of extraordinary polarisation to allow maximum diffraction efficiency. The hologram then diffracts a portion of the beam towards a Hamamatsu C5460 APD module.

This introduces a Noise Equivalent Power level of 0.02pW/√Hz. As the instantaneous Bragg wavelength changes with applied strain, the power of the diffracted beam is modulated by the holographic transfer function. The signal from the APD is fed to the PC via a Stanford Research SR560 pre-amplifier and a DAQ card. The application of the quasi-static strain and the measurement of the demodulated signal are controlled by a single virtual instrument run within LabView. The demodulation scheme is illustrated in figure 4.20.

To prevent stray light from causing errors the free space configuration from the objective lens to the detectors is encased within a box. Further precautions are taken for example extinguishing all light sources within the laboratory.

Figure 4.21 illustrates the processes involved in the characterisation of the demodulation system. A saw-tooth 0-40V waveform is applied to the PZT controlled stage. The stage stores energy so the strain applied to the sensor demonstrates hysteresis that manifests as a different second order non-linear response in the forward and reverse directions. The wavelength of the FBG will also demonstrate this non-linear variation. Finally the holographic transfer function introduces further third order non-linearity. The amount depends on the bandwidth and the section of the transfer function used.

The hysteresis associated with the stage is represented by two quadratic equations applicable to the forward and reverse directions respectively. The mapping between applied strain and wavelength shift is linear (Meltz *et al* 1989) whilst the transfer function is represented by equation 3.28. The experimental results are represented by a normalised signal where the instantaneous Bragg signal is divided by the peak signal value. A look-up table is derived by multiplying the mathematical models for the hysteresis within the stage and the holographic transfer function. The normalised results can then be processed by the table to derive a normalised sensor signal. The procedure compensates for both the non-linear effects and the results can then be correlated to the linear voltage applied to the PZT actuator.

The level of correlation is measured by the establishing the Pearson correlation coefficient (Rodgers 1988). A set of results can be represented by a vector that is a best fit straight line to the data recorded. The Pearson correlation coefficient is then the cosine of the angle between two such vectors. In this case one vector will represent the normalised sensor signal whilst the other is the normalised voltage applied to the PZT. It is assumed however that these parameters possess a normal distribution. The Pearson correlation coefficient is a parametric statistic that is most useful when parameters possess a normal distribution. The value of the Pearson correlation coefficient therefore varies between -1 and 1. Values near -1 or 1 represent a very high level of correlation between the two vectors. In general the results demonstrate a high level of correlation that approaches 1 or -1 as discussed in Sections 4.6 and 4.9.

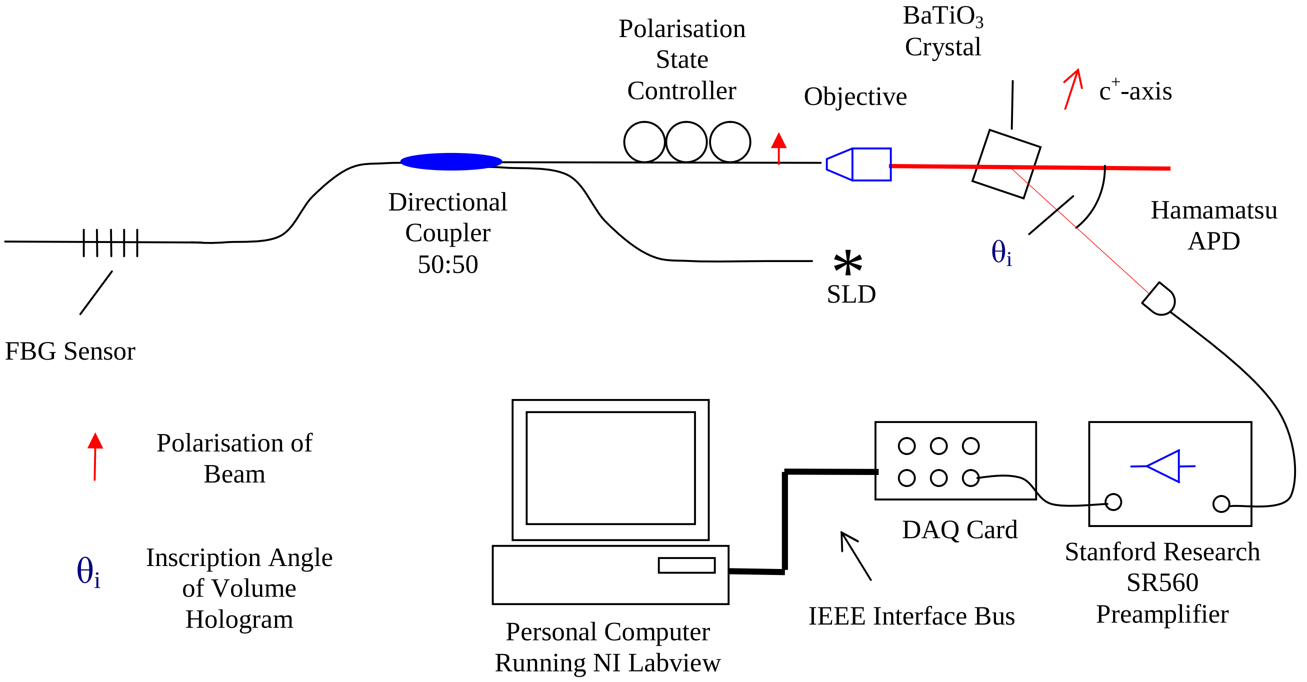

Figure 4.20 Experimental configuration for the demodulation of an FBG strain sensor by a volume hologram.

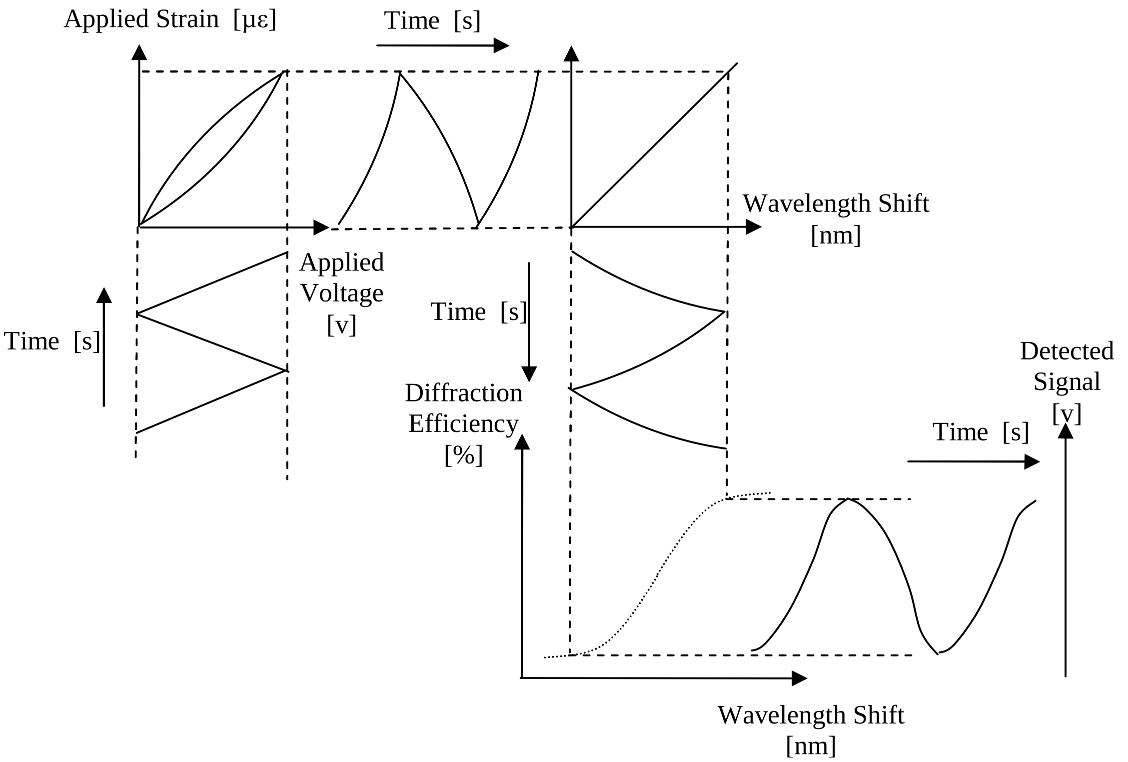

Figure 4.21 The process of demodulation by a volume hologram of a single FBG strain sensor.

A saw-tooth 0-40V waveform is applied to the PZT controlled stage which demonstrates hysteresis. The strain applied to the FBG sensor reflects these characteristics by demonstrating a second order non-linearity in contrast to the linearly applied voltage. The non-linearity will be different in the forward and reverse directions of movement due to hysteresis. The relationship between wavelength shift and applied strain is linear so the wavelength shift also demonstrates the non-linearity with respect to time. Finally the holographic transfer function introduces a further third order non-linearity. The amount depends on the bandwidth and the section of the transfer function used.

Table 4.2 represents the inscription parameters for a volume hologram with a central wavelength of 817.8nm along with the resulting bandwidth of the transfer function. The FBG sensor to be demodulated on the positive edge of the transfer function is also detailed.

Table 4.2 Parameters used to inscribe the demodulating hologram and the resulting key holographic parameters. λ_i is the wavelength, $\theta_i/2$ the half angle and w the beam width radius of inscription. The FWHM wavelength and angular bandwidth is given by $\delta\lambda$ and $\delta\theta$ respectively. The FBG is attached to the 'push' section of the stage and is pre-strained. λ_q is the quiescent wavelength of the FBG whilst $\lambda_{fbg}(4170\mu\varepsilon)$ is the wavelength when strained to 4170με. The peak reflectivity of the FBG sensor is given by $R_{fbg.}$

Parameter	Value
λ_i	817.8nm
$\theta_i/2$	10°
w	0.25±0.03mm
$\delta\lambda$	3.65±0.3nm
$\delta\theta$	1.05±0.1°
λ_q	814.6nm
$\lambda_{fbg}(4170\mu\varepsilon)$	817.3nm
R_{fbg}	59%

The measurement of beam diameter is approximate and will possess an associated error. This causes the error in the wavelength and angular bandwidth of the resulting transfer function. Figure 4.22 is a representation of the proposed demonstration scheme. It includes the transfer function of the demodulating volume hologram and the spectrum of the FBG sensor. The holographic transfer function is characterised experimentally as detailed in the figure along with the mathematical model. The characterisation shows an error associated with signal noise recorded by the APD. The sensor is attached to the 'push' section of the stage and is pre-strained to 4170με. The Bragg wavelength is shown when the FBG sensor is pre-strained to this level.

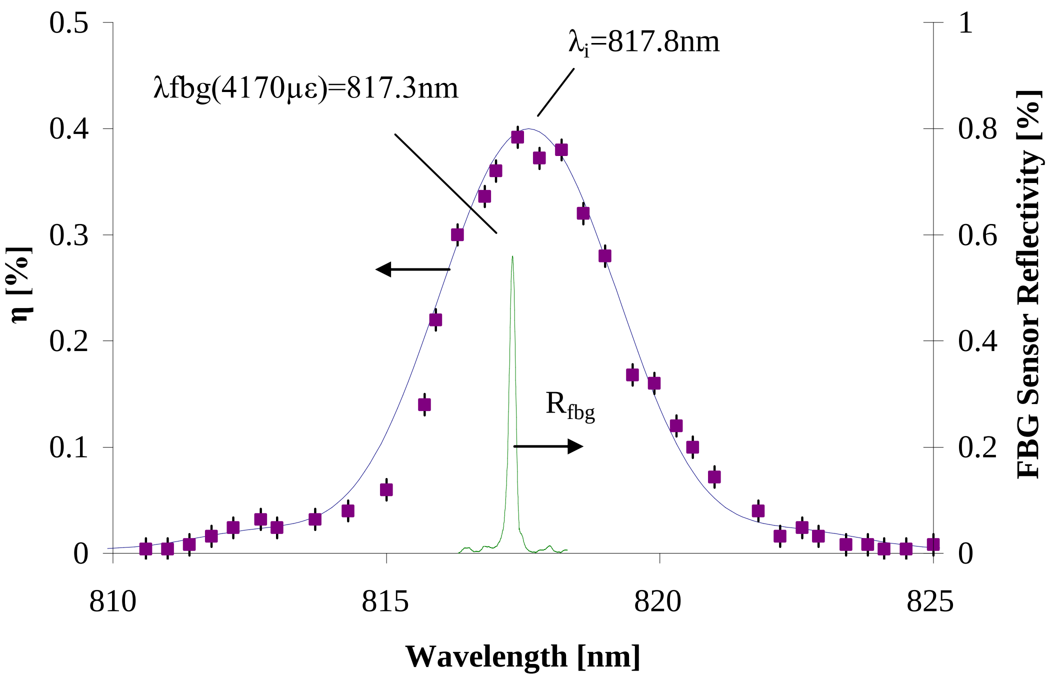

Figure 4.22 The holographic transfer function used to demodulate an FBG sensor. The inscription variables and the resulting holographic parameters are shown in Table 4.2. The experimental diffraction efficiency is given by the points (■) whilst the theoretical diffraction efficiency is given by the line (—).

A normalised 30mHz 0-40V saw-tooth waveform is applied to the PZT as shown in figure 4.23 whilst the response of the system is shown by the normalised APD signal. The results demonstrate the effect of hysteresis associated with the PZT controlled stage. It is also possible to identify the effects of the third order non-linearity present within the holographic transfer function. This is from the S shaped non-linearity shown in the normalised APD signal.

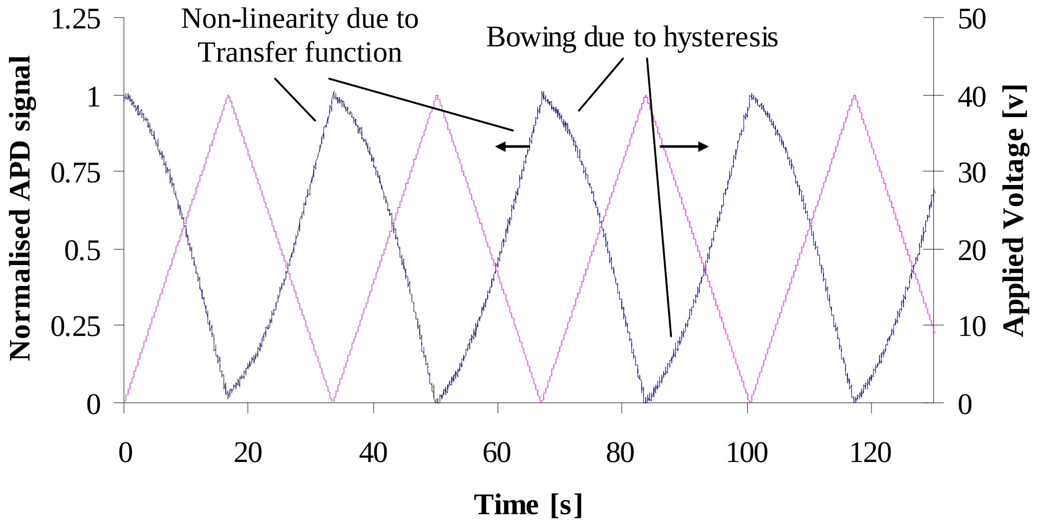

Figure 4.23 Demodulation of an FBG strain sensor by a volume hologram.
The normalised voltage applied to the PZT actuator (—) is shown with the normalised APD signal (—). The results show both the second order non-linearity associated with hysteresis within the stage and third order non-linearity associated with the holographic transfer function.

The mapping of the experimental results represented by the normalised APD signal to a normalised sensor signal is shown in figure 4.24. The mapping is the multiplication the holographic transfer function over the sensor’s wavelength range of operation and two quadratic equations representing the response of the stage in the forward and reverse directions.

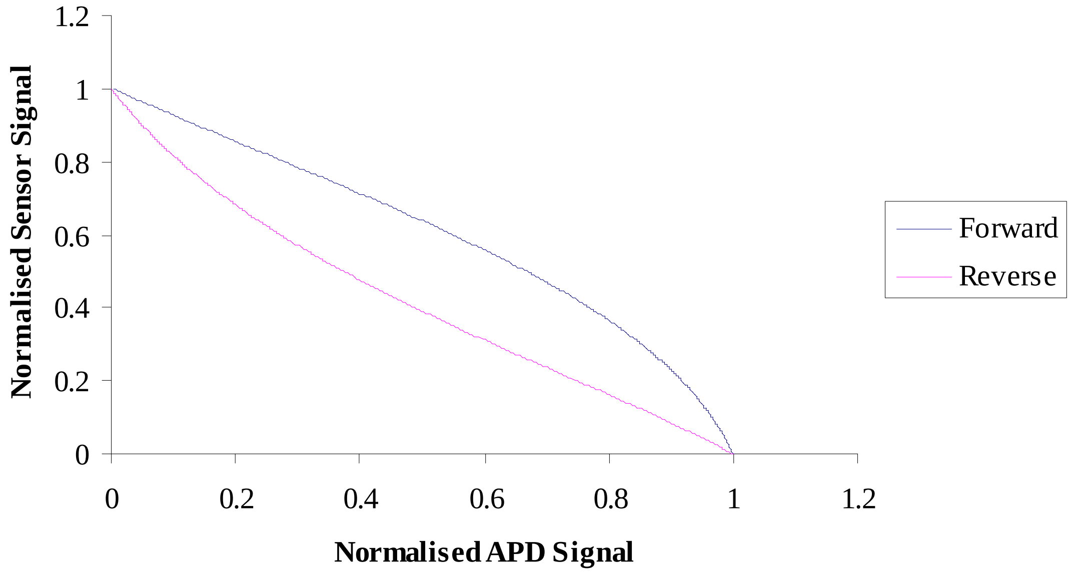

Figure 4.24 The mapping of the normalised APD signal to a normalised sensor signal. The mapping is the multiplication the holographic transfer function over the sensor's wavelength range of operation and two quadratic equations representing the response of the stage in the forward and reverse directions.

The normalised sensor signal is shown in figure 4.25 with the applied voltage for comparison. The correlation co-efficient is established between each linear section or half cycle of the normalised saw-tooth voltage waveform and the normalised sensor signal. Here the correlation factor is 0.9991 averaged over all linear sections. This represents a high level of correlation and an accurate mapping between the normalised APD and sensor signals. If the normalised sensor signal represents a strain range from 0-4170με then the noise superimposed on the signal represents a quasi-static resolution of ±56με. The maximum error found by comparing the voltage applied to the PZT driven stage and a straight line representing an average of the normalised sensor signal is 58με.

In the forward direction, the normalised sensor signal oscillates around the applied voltage. This implies regular fluctuations in the hysteresis due to a resonant process within the stage. The results also show an anomaly from approximately 17 to 21 seconds. This can be seen in fringe pattern results but is not in figure 4.23 above. This can be seen however in figure 4.25 and can be attributed to 'sticking', a slight and momentary increase in friction within the stage within that particular time period.

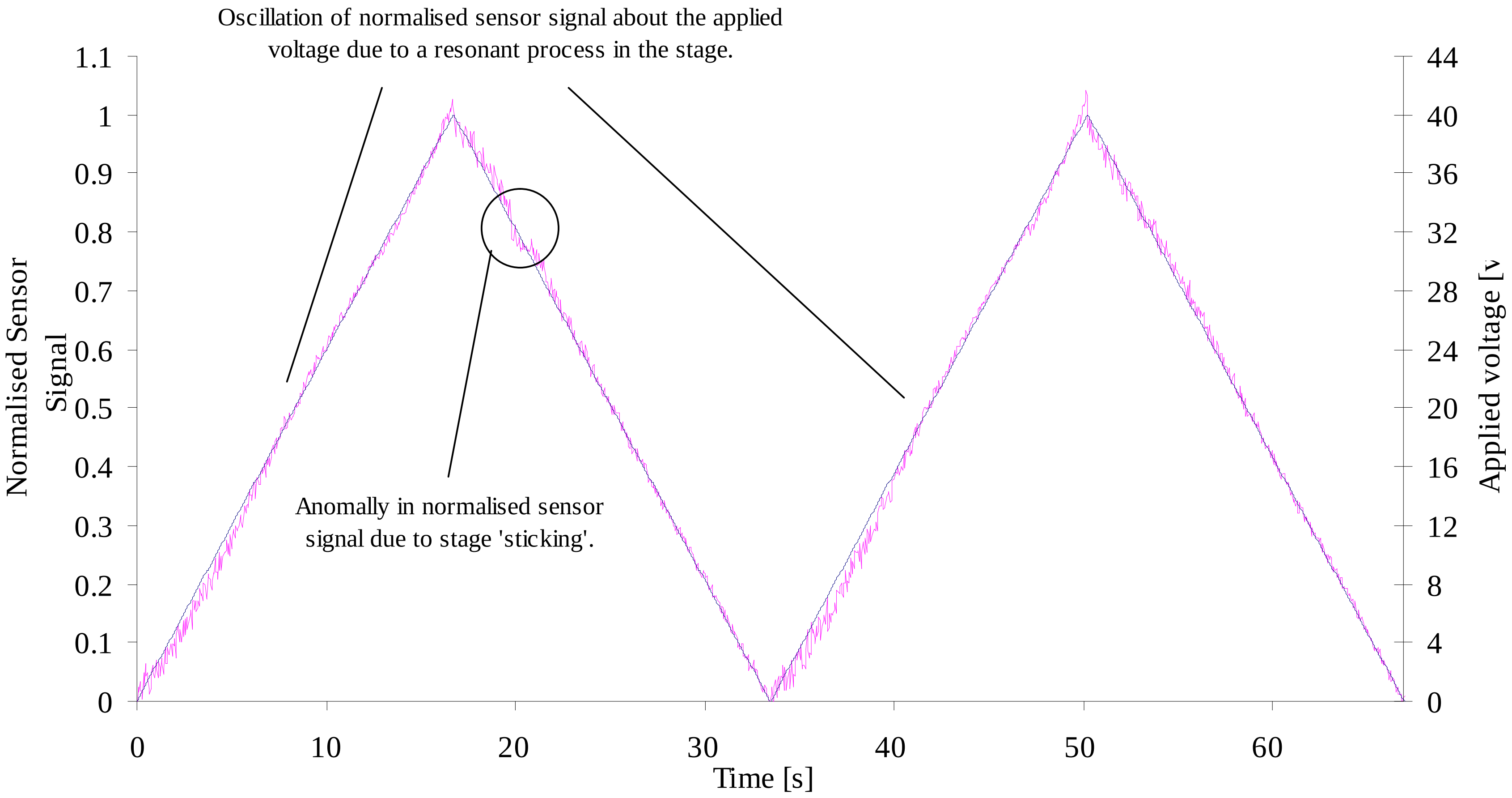

Oscillation of normalised sensor signal about the applied voltage due to a resonant process in the stage.

Anomally in normalised sensor signal due to stage 'sticking'.

Figure 4.25 The normalised sensor signal (—) compared with the normalised voltage applied to the stage (—) upon the demodulation of an FBG sensor signal.

Figure 4.26 shows the demodulation of the single sensor with characteristics previously described within table 4.2 and figure 4.22. Here however a piece of fibre is attached to the ‘pull’ section of the stage to reduce the impact of hysteresis. The piece of fibre serves to reduce tension variations experienced by the central movable stage, as discussed in section 4.5. Figure 4.26 shows the effect of hysteresis being reduced in comparison to initial results shown in figure 4.23. The results however still demonstrate the characteristic second order non-linearity in the forward and reverse directions due to hysteresis. The results further demonstrate a third order non-linearity due to demodulation by a non-linear section of the transfer function.

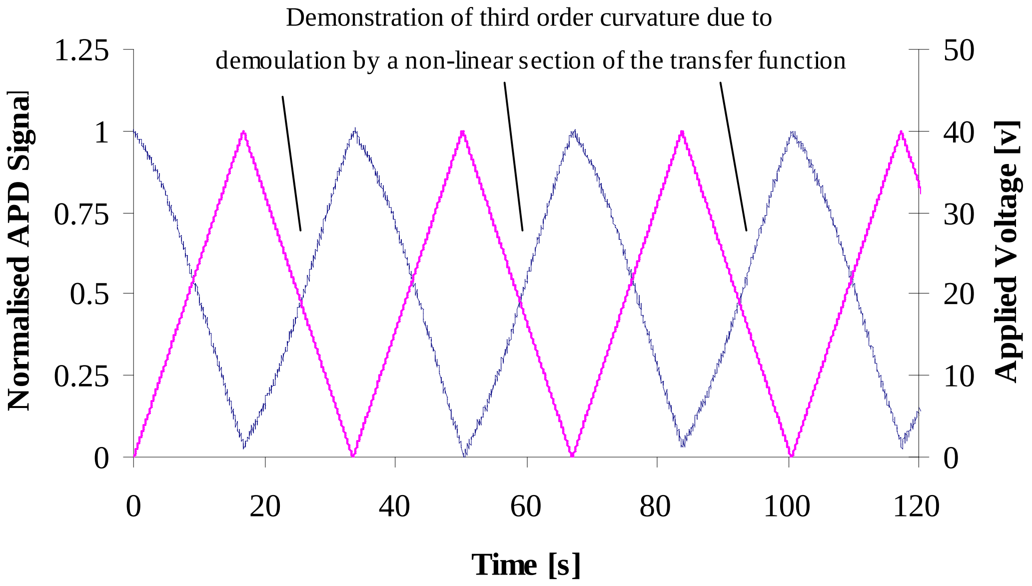
Demonstration of third order curvature due to demoulation by a non-linear section of the transfer function

Figure 4.26 The demodulation of a single sensor by a volume hologram with reduced effect of hysteresis introduced by the PZT.

The normalised voltage applied to the PZT actuator (—) is shown with the normalised APD signal (—). A section of fibre with no inscribed FBG is attached to the ‘pull’ section of the stage to reduce the effects of hysteresis. The results demonstrate the reduction in hysteresis in comparison to that shown in figure 4.23.

The results show that a volume hologram inscribed within a $BaTi0_3$ can demodulate a single FBG sensor. The results further demonstrate that the demodulation scheme can be mathematically represented. The mathematical model can then be used to process raw results to compensate for hysteresis within the stage and any non-linearity within the demodulating holographic transfer function.

4.7. Inscription and Erasure Time Constants

An understanding of inscription and erasure times is important as it is proposed that a holographic array will simultaneously de-multiplex and demodulate elements in an FBG sensor array. The inscription of a hologram however will erase any already hosted within the crystal. A schedule of holographic inscription can be established using equation 3.30 as explained in section 3.3.3. Here the inscription time of a specific hologram is pre-determined so that all elements in a array have the same diffraction efficiency.

Time constants are established by using the experimental configuration detailed in figure 4.8. Here a BPX photo-detector is used to monitor holographic growth over the period of inscription by recording the decrease in object beam power as a result of the two-beam coupling which occurs as the hologram is formed. The time constant is considered as the time taken for the object beam to decay from 10% to 90% of its final value.

To measure erasure times, the fall in diffraction efficiency of a hologram already inscribed within the crystal is recorded as the subsequent hologram in the array is inscribed. Here the object beam is rotated and a photo-detector positioned to monitor the inscription of the subsequent hologram. The detector in the original location monitors changes in diffracted beam intensity from the hologram already inscribed.

The most important factor in determining time constants in the unsaturated regime is the combined interfering beam intensities as explained in section 3.2.3. The unsaturated regime dominates when the grating period is greater than approximately 3μm (Solymar 1996). A mathematical model for the time constants is also presented in section 3.2.3 which is related to combined beam intensities and the material constants. The time constants will aid in establishing the schedule of inscription for a holographic array.

The material constants and inscription half angles used to calculate the inscription time constants are shown in table 4.3.

Table 4.3 Parameters used to determine the value of inscription times. Where λ_i is the wavelength of inscription, $\theta_i/2$ is the half angle between the beams and m is the modulation depth of the interference pattern. The value ε_r is the relative dielectric constant, μ is the mobility, γ_r is the recombination constant and s is the photo-ionisation constant all applicable to $BaTiO_3$. The values N_D^+ and N_D are the ionised donor density and the donor density present within the crystal.

Parameter	Value	Source
λ	780nm	Measured on Spectrum analyser from output of laser source.
$\theta_i/2$	15°	Measured from rotational stage.
M	1	The intensity of interfering beam was equal.
ε_r	600	(Solymar 1996)
S	7.6×10^{-6} m^2 J^{-1}	(Solymar 1996)
μ	5×10^{-5} m^2 V^{-1} s^{-1}	(Solymar 1996)
γ_R	5×10^{-14} m^3 s^{-1}	(Solymar 1996)
N_D^+	9×10^{22} m^{-3}	(Solymar 1996)
N_D	1×10^{25} m^{-3}	(Solymar 1996)
T	272K	N/A

*An approximation based on figures given in (Solymar 1996) but is altered to derive the best fit to experimental time constant results.

Examples of plots to establish inscription times for differing combined beam intensities are shown in figure 4.27. Both the model and experimental results are shown. Here two plots are given, one with the combined beam intensity of 2×10^3 mW/cm^2 and another for 127 mW/cm^2. These represent optical powers of 4mW and 0.25mw respectively for a radial beam width of 0.25mm. Phase changes within the interfering beams imply that a hologram can begin to be inscribed, erased and then inscribed again within one inscription incidence. This implies the time constant for a specific hologram is difficult to pre-determine. The results however represent the best available as they demonstrate an exponential decay to a steady state value. The mathematical model and experimental results are shown and demonstrate a high level of correlation. The time constants (τ) are approximately 1.5s and 25s respectively. The experimental plot for the 25s time constant is noisy due to the low diffraction efficiency of the grating inscribed.

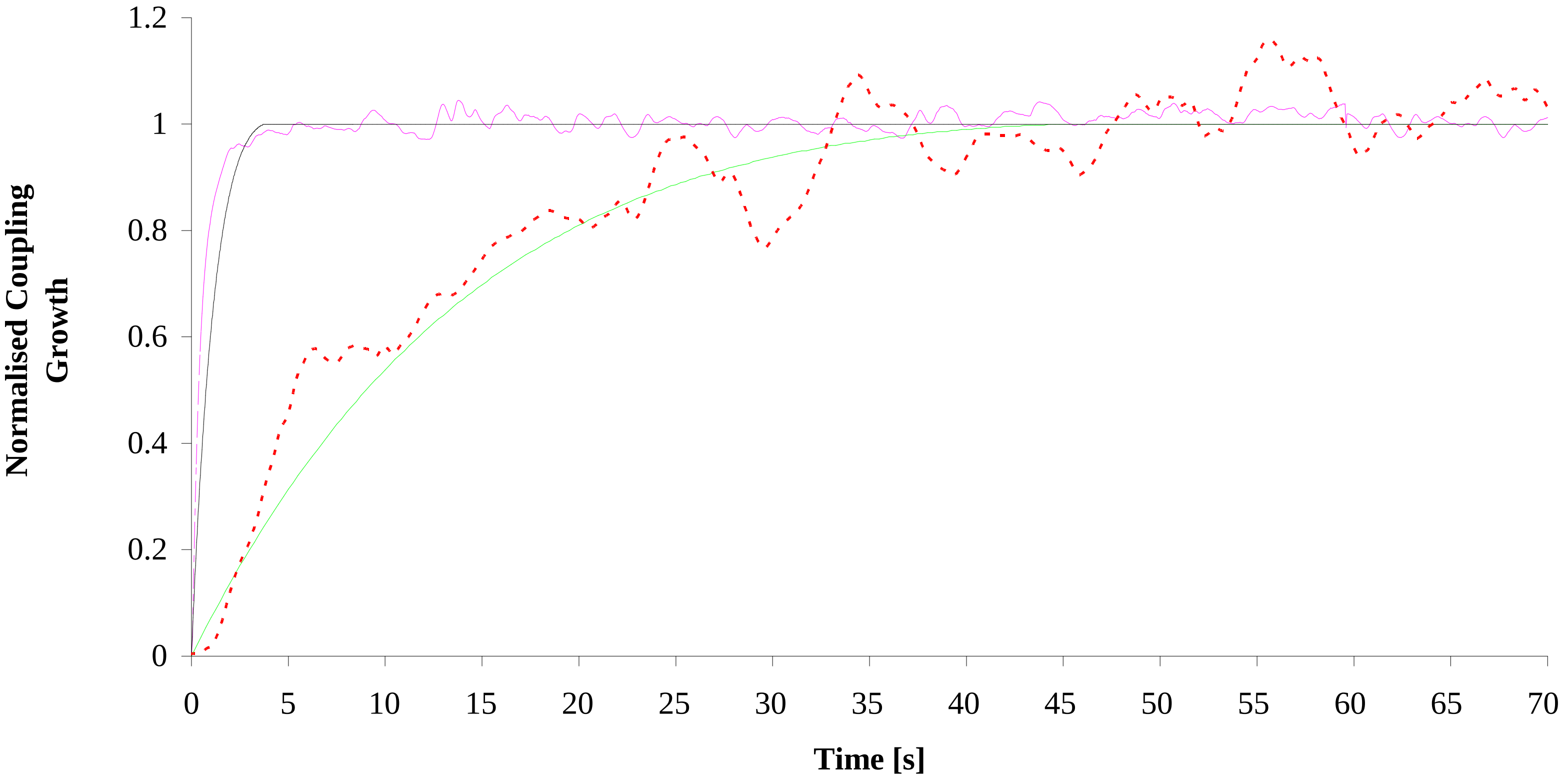

Figure 4.27.Normalised two-beam coupling growth of interfering beams within the $BaTiO_3$ crystal. The experimental (-··-) and theoretical (-·—) coupling growth curves are shown for an incident intensity of $2x10^3$ mW/cm^2. The experimental (- - -) and theoretical (— —) coupling growth curves are also shown for an intensity of 127mW/cm^2.

Similar graphs are plotted to establish inscription times for combined beam intensities from 127 mW/cm^2 to 2x10^3 mW/cm^2. The mathematically modelled time constants are also shown for the range of incident intensities by the solid line. Both are shown in figure 4.28. The measured and modelled time constants demonstrate a high level of correlation. The time constants also show an inverse relationship to beam intensity.

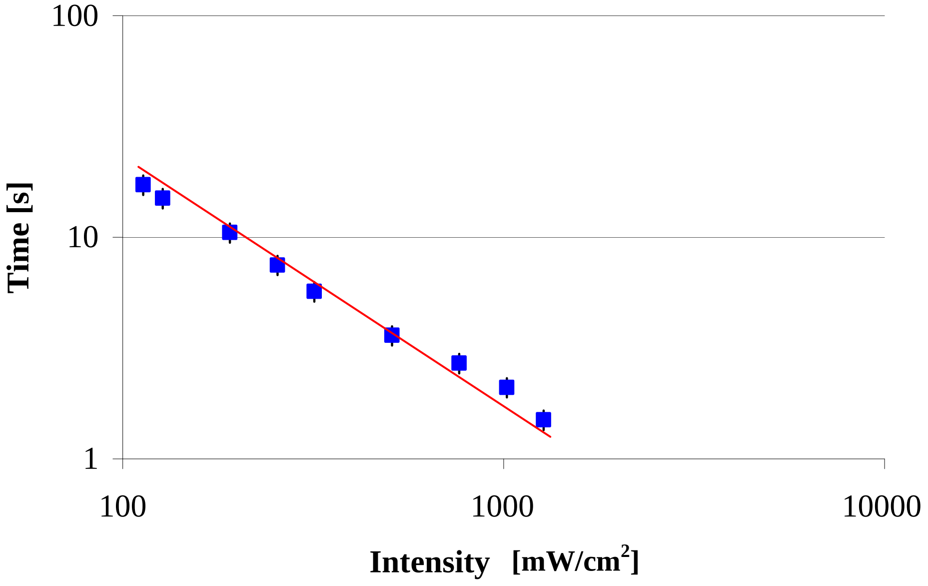

Figure 4.28 Holographic inscription time constants within the BaTiO$_3$ crystal. The mathematically modelled time constants are also shown (—) for the range of intensities from 2x10^3 mW/cm^2 to 127 mW/cm^2.

Examples of plots to establish erasure times for differing beam intensities are shown in figure 4.29. Here two plots are given one with the combined beam intensity of 2x10^3 mW/cm^2 and another of 127 mW/cm^2. The time constants are approximately 5s and 45s respectively, with no beam present the holograms erase overnight due to the thermal generation of charge carriers.

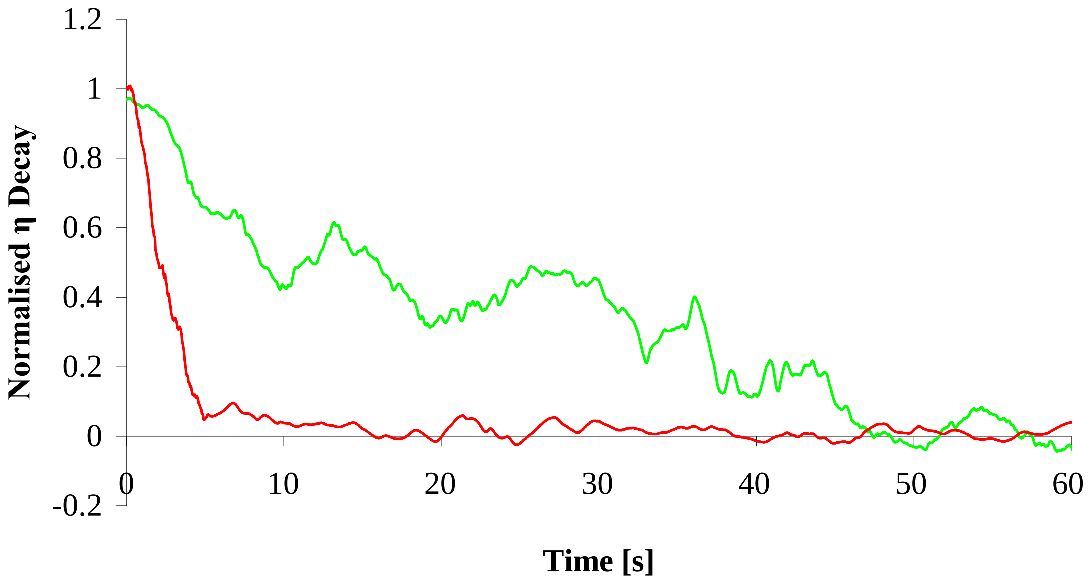

Figure 4.29 Normalised diffraction efficiency decay for a hologram inscribed within the $BaTiO_3$ crystal. Two plots are shown for erasure intensities of 127mW/cm^2 (—) and 2000 mW/cm^2 (—).

Similar graphs are plotted to establish erasure times for combined beam intensities from 127 mW/cm^2 to 2x10^3 mW/cm^2. These are shown in figure 4.30. The erasure times show an inverse relationship to beam intensity as do the inscription times. The time constants for hologram erasure however are consistently longer compared to those of inscription. This is due to the diffracted portion of the erasure beam interfering with the un-diffracted portion to initially reinforce the hologram (Solymar 1996). It is therefore difficult to mathematically model erasure times as discussed in Section 3.2.3.

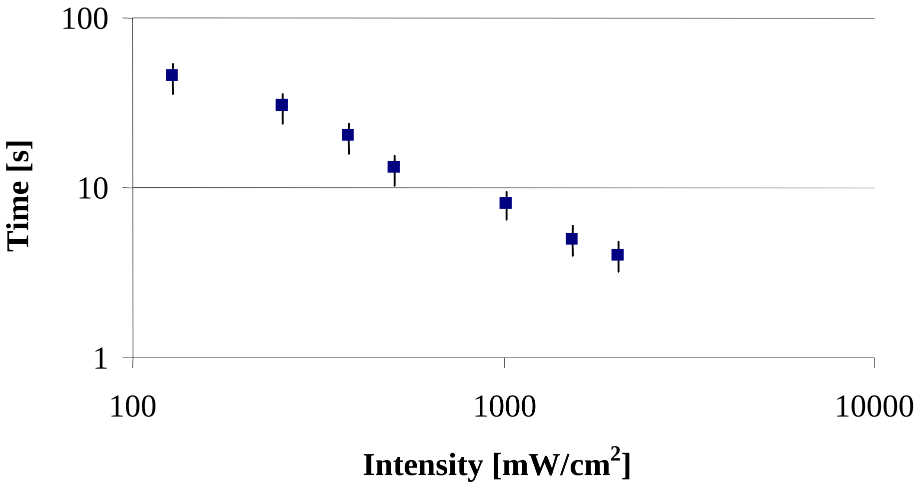

Figure 4.30 Holographic decay time constants within the $BaTiO_3$ crystal.

The errors in the measured time constants are caused by the ambiguity in reading the measured plots. The measured plots do not represent a smooth exponential decay due the process of inscription being irregular. This is clearly seen in the experimental results within figures 4.27 and 4.29 by the variation in diffracted intensity throughout the inscription or erasure process.

The measurement of the inscription and erasure times allows a schedule of inscription to be derived. This is essential to realise a holographic array within the crystal where all elements have the same diffraction efficiency. The schedule is discussed in Section 3.3.3.

An example schedule can then be derived by the using equation 3.30. Here a combined beam intensity of 2x10^3 mW/cm^2 will be assumed. The inscription time for this combined beam intensity is 1.5s whilst the erasure time is 5s. The first hologram is inscribed in 1.5s whilst the second is inscribed in 1.1s, the third in 0.9 of a second and the forth in 0.75 of a second. This will ensure all the holograms in the array will possess the same diffraction efficiency.

4.8. Impact of Optical Components on the Wavelength Response of the Demodulation Scheme

The demodulation scheme relies on the holographic transfer function to demodulate an FBG strain sensor. As explained in Section 4.1 however some optical components within the system possess a wavelength dependent response that can influence the overall transfer function of the demodulation system. The wavelength response of the system is the combination of the responses of individual elements as given by equation 4.4. The response of each component detailed in this equation shall be considered. The important responses are the responsivity of the APD, the split ratio of the 3dB fibre couplers and the power spectrum of the SLD.

4.8.1 Responsitivity of the APD

The APD was not characterised specifically for experiments however the spectral response is available in documentation (Hamamatsu 1997). An image of the spectral response is available in an electronic copy of device documentation. The xyExtract package can then derive x and y vectors to numerically represent the spectral response. The vectors can be imported to Excel to graphically represent the response shown in figure 4.31.

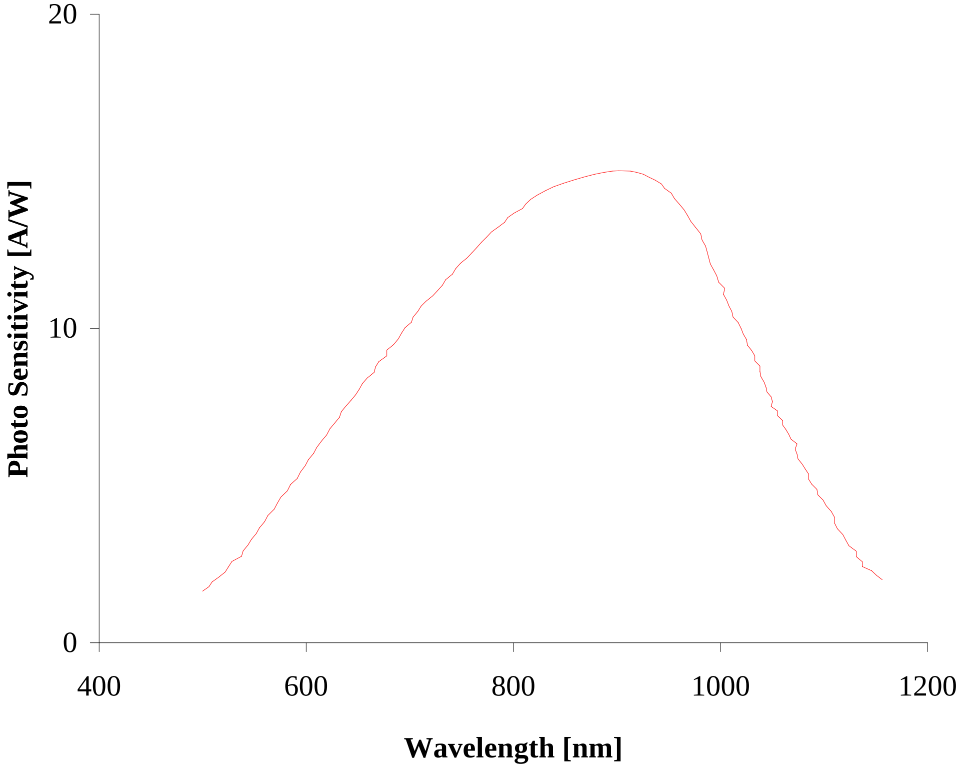

Figure 4.31 Spectral response of the APD.

The response demonstrates a FWHM bandwidth of approximately 400nm centred at 900nm. The response of the APD can therefore be regarded as approximately constant over the operating range of a single FBG sensor.

4.8.2 3dB Fibre Couplers

Two types of couplers are used, one centred at 820 nm and another at 780nm that are based on SM fibre with cut-off wavelengths of 780nm and 750nm respectively. These are used to create two mutually coherent beams from the same laser source for hologram inscription. They are also used to separate the beam illuminating an FBG sensor and the reflected signal. The Ti: Sapphire laser was used to characterise the 820nm coupler by stepping through a wavelength range. A coupler can be characterised by measuring power at the output ports and dividing by the input power at each wavelength increment.

The input power is assumed to be the addition of the powers from the output ports. The wavelength response of a Sifam 3dB coupler PS820 (Serial no D5345) is shown is figure 4.32.

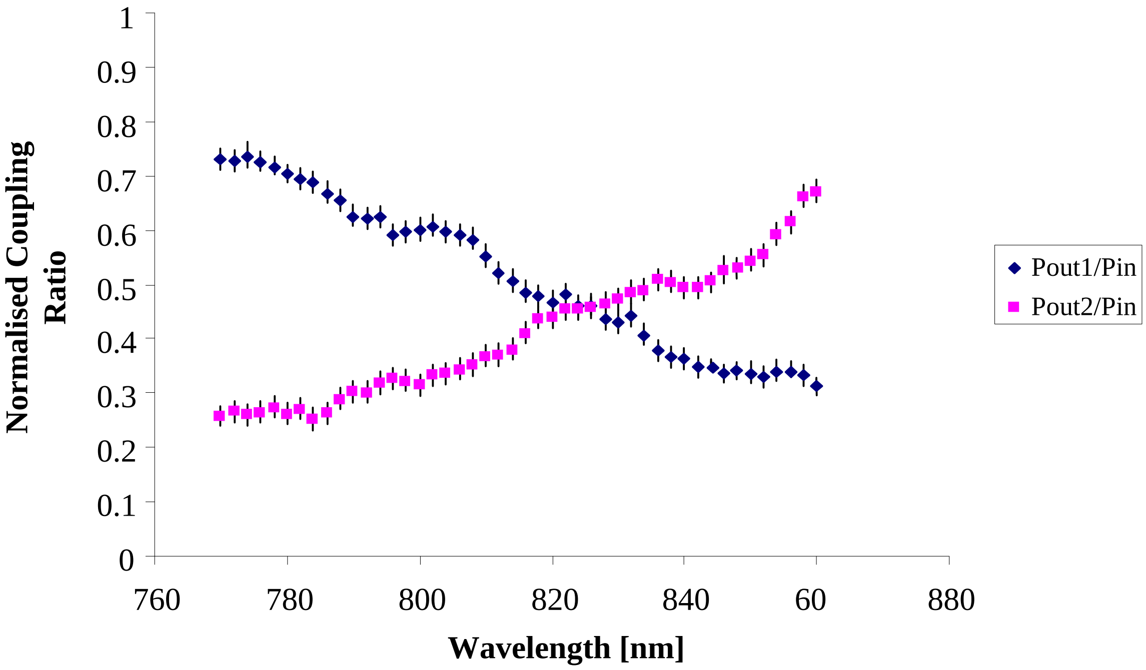

Figure 4.32 Coupling ratio of a 3dB coupler centred an 820nm.

The coupler has a wide FWHM bandwidth of approximately 70nm. As seen in the figure the split ratio changes little over the limited wavelength range of a single FBG sensor, typically 2-4nm. The effects of the wavelength response of the 3dB couplers can therefore be neglected. The error in coupling ratio is due to signal noise recorded by the photo-detector during coupler characterisation.

4.8.3 Power Spectrum of the Super Luminescent Diode

The power spectra of the SLDs used are shown in figure 4.13. The Qphotonics SLD has a central wavelength of 800nm and an approximate FWHM bandwidth of 30nm. The Superlum SLD however has a central wavelength of 820nm and an approximate FWHM bandwidth of 22nm. If the operational range of an FBG sensor lies near the central wavelength of the SLDs, then the change in power with respect to wavelength is small and can be neglected. If however the operational range is within the spectral edge, then the change in power can be significant and will effect demodulation. For example, consider a section of the Qphotonics SLD spectrum between 775nm and 785nm. This is shown in figure 4.33.

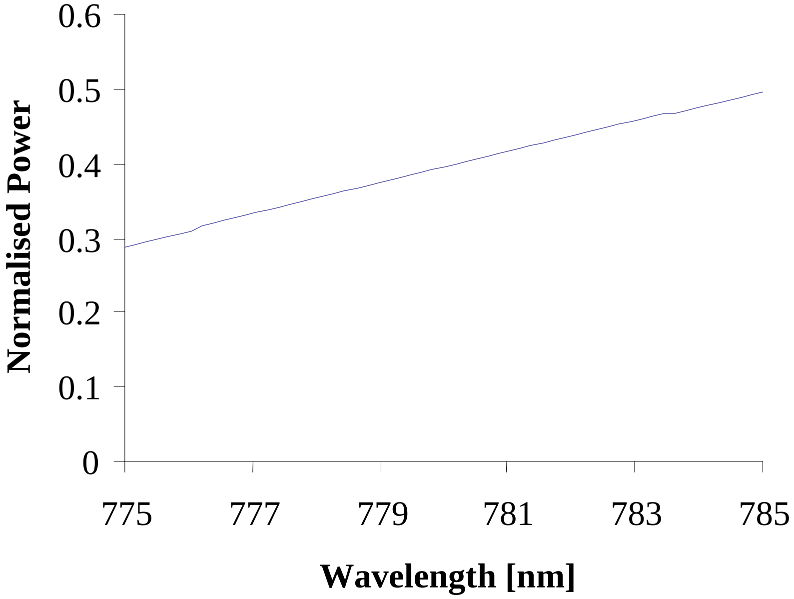

Figure 4.33 Section of the of the Qphotonics SLD power spectrum between 775 and 785nm

This shows a 60% increase in power over a limited wavelength range of 10nm. To investigate the effects of the spectrum on the process of demodulation the following experiment is undertaken.

This phenomenon can seriously affect the correct operation of a holographic demodulation scheme especially if the associated transfer function has a wide optical bandwidth. An experiment was completed to assess the effect where a FBG sensor operating over a 3nm range was demodulated by a wide holographic transfer function inscribed with a narrow beam. The wavelength range of operation coincides with the side of the SLD spectra where the change in power with respect to wavelength is at its greatest.

Table 4.4 indicates the parameters used for the demodulation of an FBG sensor by a wide holographic transfer function using the edge of the Qphotonics SLD spectrum in the 775nm to 785nm range. The parameters of the FBG strain sensor are also included.

Figure 4.34 shows the demodulation scheme including the transfer function of the hologram and the reflection spectrum of the FBG sensor. The holographic transfer function is characterised experimentally as detailed in the figure along with the mathematical model. The characterisation shows an error associated with signal noise recorded by the APD. The measurement of beam diameter is approximate and will possess an associated error. This causes the error in the wavelength bandwidth of the resulting transfer function.

Table 4.4 Parameters used to inscribe the demodulating hologram and the resulting key holographic parameters. λ_i is the wavelength, $\theta_i/2$ the half angle and w the beam width radius of inscription. The FWHM wavelength and angular bandwidth is given by $\delta\lambda$ and $\delta\theta$ respectively. The FBG is attached to the 'pull' section of the stage and is not pre-strained. λ_q is the quiescent wavelength. The peak reflectivity of the FBG sensor is given by R_{fbg}.

Parameter	**Value**
λ_i	775.5nm
$\theta_i/2$	6°
w	0.25±0.3mm
$\delta\lambda$	6.5±0.4nm
$\delta\theta$	1±0.14°
λ_q	776nm
R_{fbg}	63%

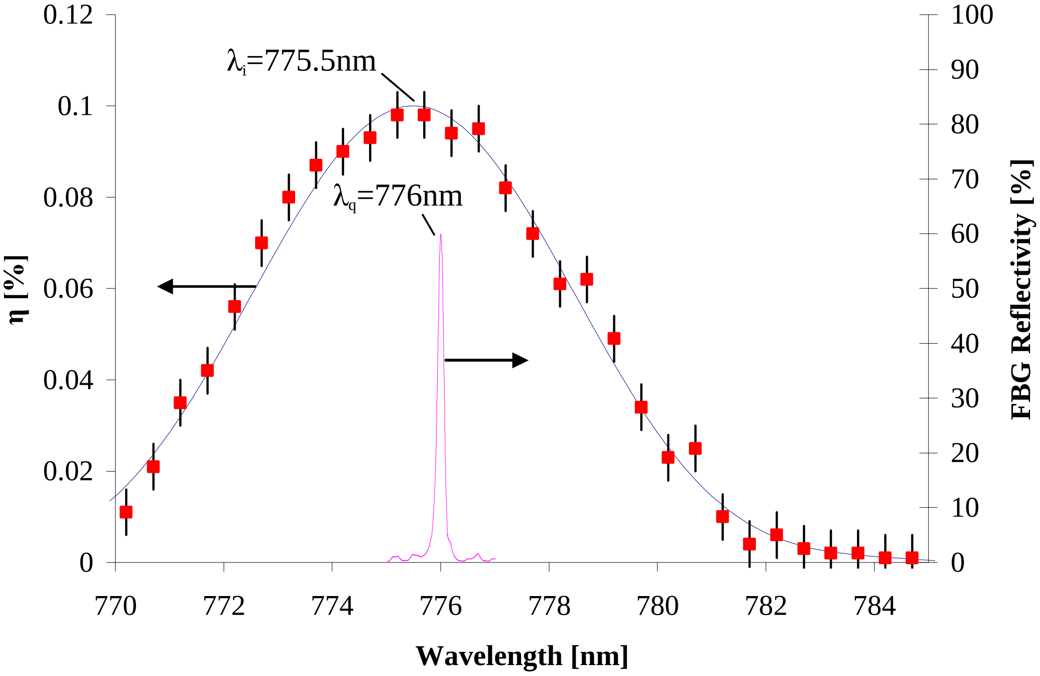

Figure 4.34 Demodulation of an FBG strain sensor by a wide bandwidth holographic transfer function. The inscription variables and the resulting holographic parameters are shown in Table 4.4. The experimental diffraction efficiency is shown (■) as well as the theoretical diffraction efficiency (—).

A 0-40V 30mHz saw-tooth waveform is applied to the PZT. The transfer function of the hologram should then demodulate the sensor signal in a qusai-linear fashion similar to that shown in figure 4.23. The received signal however is shown in figure 4.35.

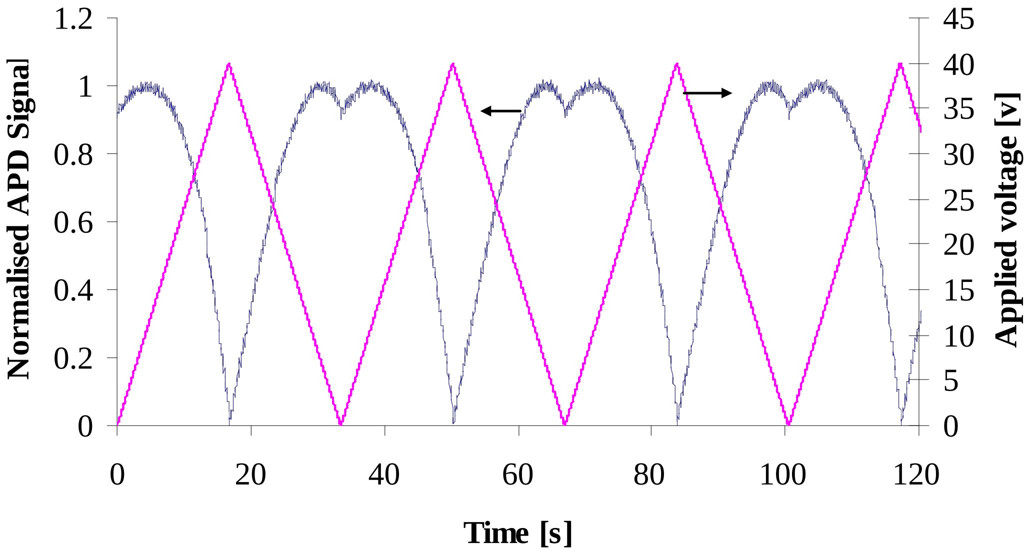

Figure 4.35 Disturbance of the demodulation process of an FBG strain sensor by the spectrum of the SLD. The normalised voltage applied to the PZT actuator (—) is shown with the normalised APD signal (—). The received signal demonstrates a dip at low applied strain due to the slope of the SLD power spectrum possessing a higher differential than the holographic transfer function.

The received signal demonstrates a dip in value at low applied strains. For most of the cycle the slope of the transfer function has a higher differential with respect to wavelength than the SLD power spectrum. At lower applied strains however the slope of the SLD power spectrum has a higher differential and therefore dominates, causing the dip. This issue however can be minimised by reducing the bandwidth of the holographic transfer function or using another section further from the diffraction efficiency peak. This ensures that the slope of the transfer function always has a greater differential than that of the SLD power spectrum.

Most of the elements in the experiment do not interfere with the demodulation process by the holographic transfer function. The only exception is the SLD under certain conditions. If the operating range of an FBG coincides with a steep side of an illuminating SLD spectrum then the optical power in the Bragg signal will change significantly depending on the instantaneous Bragg wavelength. To overcome this problem the sensor operating range will ideally coincide with the peak in the SLD spectrum.

4.9. Demodulation of an FBG Sensor Array

It is possible to extend the scheme described in Section 4.6 to demodulate an FBG sensor array. To demonstrate sensor array demodulation a similar configuration is used to that outlined in figure 4.20. It is necessary however to inscribe an array of holograms within the crystal each demodulating a matching FBG sensor element as demonstrated in Section 4.6. Each signal is then diffracted through a different angle by the matching hologram to a matching element in the APD array to facilitate de-multiplexing. The array is Wavelength Division Multiplexed (WDM) therefore each element is fabricated at a different quiescent wavelength and operates within a separate wavelength range. The wavelength range for each sensor can extend to 2.6nm by the application of approximately 4000με. Crosstalk is a phenomenon where a signal from one channel can be detected in adjacent ones, the closer the operating wavelength ranges of the channels the higher the possibility of crosstalk. A stop-band is implemented to limit crosstalk that is a wavelength range between consecutive operating ranges where no sensor signal is realised. Ideally the stop-band between consecutive ranges is minimised so that the number of sensor elements is at a maximum.

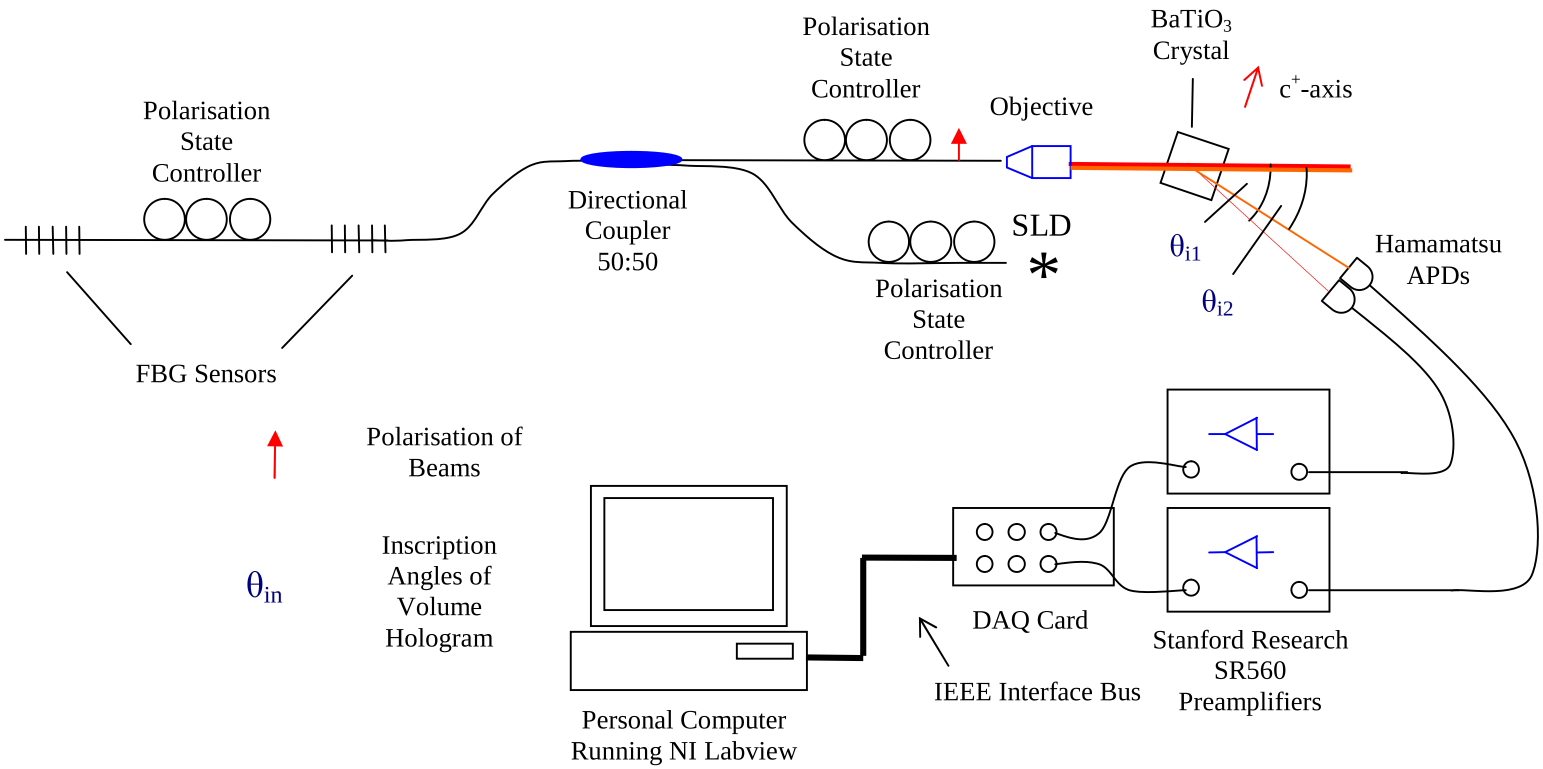

Figure 4.36 Configuration for the demodulation of an FBG strain sensor array by a volume holographic array.

The configuration used to inscribe a holographic array is the same as that detailed in figure 4.8. Here however a writing schedule is derived before inscription begins. The schedule details wavelengths and half angles of inscription, beam widths and inscription times of each hologram. The inscription half-angles and beam-widths are chosen to pre-determine the bandwidth of the inscribed holographic transfer function. The wavelengths of inscription are then chosen so the edge of the transfer function coincides with the operational range of the matching sensor element to demodulate the associated Bragg signal in a linear fashion. The inscription times are chosen to ensure that each element in the holographic array has the same diffraction efficiency.

The crystal is mounted on a fixed post located in the centre of a rotational stage. The objective lens collimating the reference beam is also fixed, however the lens collimating the object beam is located on the rotational stage. This allows holograms to be written at different angles as well as wavelengths.

The schedule details the holograms to be inscribed in a sequential order. Between each inscription however both the object and reference beams are blocked. The object beam is rotated to the required half angle of inscription whilst the laser is altered to the inscription wavelength of the subsequent hologram. The inscription times of each hologram ensure all elements in the array have the same diffraction efficiency. Typically however the beam widths are not altered between inscription instances.

The inscribed holograms are then characterised in the same manner as described in Section 4.3. One sweep of a wavelength range however will characterise a single hologram. Multiple sweeps are therefore required to characterise the holographic array. The holographic transfer functions are pre-determined using the model detailed in Section 3.3.2.

The configuration used to demodulate a two element FBG sensor array is shown in figure 4.36. This is similar to figure 4.20 however a single PSC is deployed between the two sensor elements. This ensures that the polarisations of the reflected Bragg signals are the same. The signals are subsequently manipulated to be of extraordinary polarisation by another PSC before impinging on the crystal. Bragg signals of extraordinary polarisation experience the greatest diffraction efficiency, the importance of polarisation for hologram inscription and interrogation within $BaTiO_3$ being detailed in Section 3.1.

The possibility of crosstalk between channels is considerable due to the stop-band being limited in some cases to 2nm. Crosstalk is measured with the same configuration detailed in figure 4.36. Here however quasi-static strain is applied to one sensor whilst none is applied to the other. The quiescent wavelength of the unstrained sensor is near to the diffraction efficiency peak of the matching hologram to maximise the signal. A 3mHz 0-4000με saw-tooth waveform is applied to the strain sensor. The signal from the unstrained element is then monitored. Specifically signals of 3mHz applied to the strained element are isolated by a filter. Crosstalk is then determined as the RMS signal level at this frequency divided by the average detected from the strained sensor.

Table 4.5 indicates the parameters used for the demodulation of a two element FBG sensor array including the resulting FWHM bandwidths of the holographic transfer functions. The parameters of the sensor elements are also included.

Table 4.5 Parameters used to inscribe demodulating holographic array and the resulting key holographic parameters. λ_i is the wavelength, $\theta_i/2$ the half angle and w the beam width radius of inscription. The FWHM wavelength and angular bandwidths are given by $\delta\lambda$ and $\delta\theta$ respectively. λ_q is the quiescent wavelength of the sensor and $\lambda_s(4170\mu\varepsilon)$ is the Bragg wavelength at 4170με. The peak reflectivity of the FBG sensors is given by $R_{fbg.}$ Sensor 1 is attached to the 'pull' section of the stage and is initially unstrained. Sensor 2 is attached to the 'push' section and is pre-strained to a level of 4170με.

Parameter	**Value**
λ_{i1}	775.3nm
λ_{i2}	782.8nm
$\theta_{i1}/2$	7°
$\theta_{i2}/2$	9°
w_1	0.25±0.03mm
w_2	0.25±0.03mm
$\delta\lambda_1$	5.1±0.3nm
$\delta\lambda_2$	4.1±0.25nm
λ_{q1}	776.8nm
R_{fbg1}	63%
λ_{q2}	779.4nm
$\lambda_{s2}(4170\mu\varepsilon)$	781.5nm
R_{fbg2}	55%

The combined inscribing beam intensity is 510mW/cm^2 with a holographic inscription time of 8s and erasure time of 25s. The first hologram is therefore inscribed in 8s whilst the second is inscribed in 6s.

The measurement of the inscribing beam diameter is approximate and will possess an associated error. This causes the error in the wavelength bandwidth of the resulting holographic transfer function. The demodulation scheme is shown in figure 4.37. This allowed easily fabricated broad bandwidth holograms with a wide difference of inscription wavelengths. The holographic transfer functions are characterised experimentally as detailed in the figure along with the mathematical model. The characterisation shows an error associated with signal noise recorded by the APD.

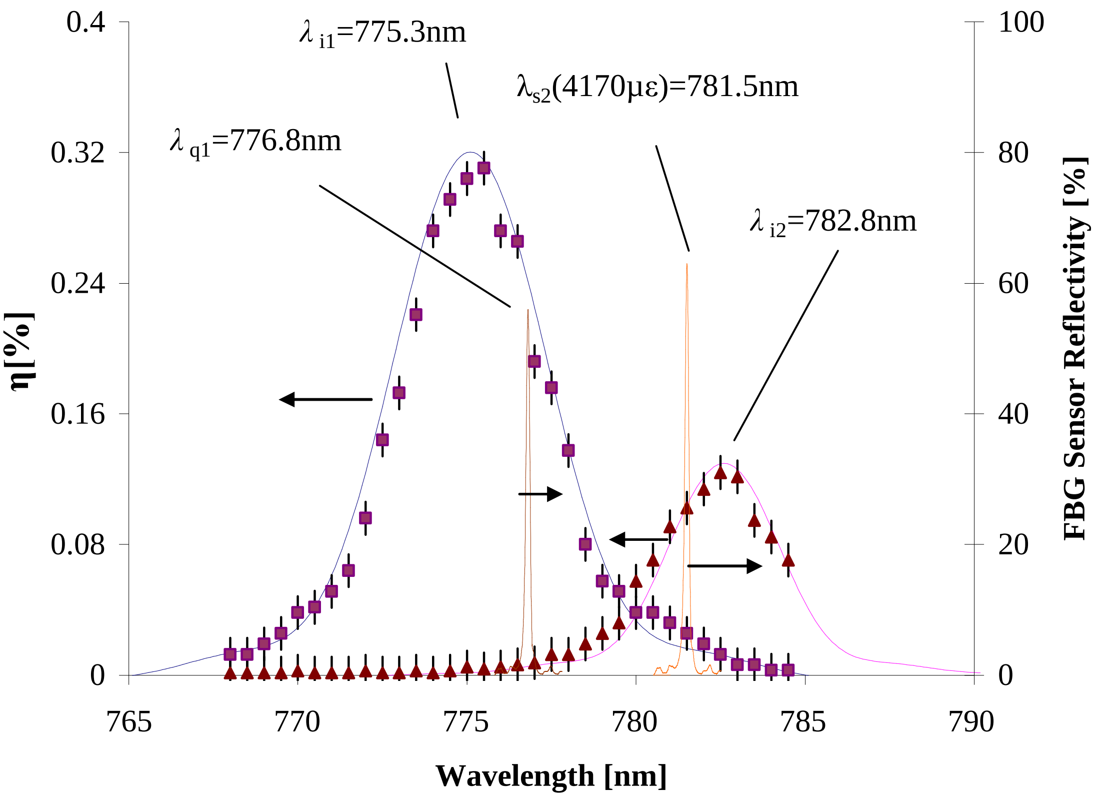

Figure 4.37 The holographic transfer functions used to demodulate an FBG sensor array. The experimental diffraction efficiencies are given by the points (■) and (▲) for the holograms inscribed at 775.3nmm and 782.8nm respectively. The theoretical diffraction efficiencies are given by the lines (—) and (—) for the holograms at 775.3 and 782.8nm respectively.

The peak diffraction efficiencies are not equal even if the timing were adhered to in the schedule of inscription. The inscription process however can lead to partially inscribed holograms as described in Section 4.7. The FBG with a quiescent Bragg wavelength of 779.4nm is attached to the 'push' section of the stage and is pre-strained to 4170με with a Bragg wavelength of 781.5nm at this strain level. The FBG sensor with a quiescent wavelength of 776.8nm is attached to the 'pull' section of the stage and is not pre-strained. The strain range is limited by the limits of linearity of the PZT driven stage. If this limitation did not exist the maximum strain that could be applied is dependent on the response of an individual sensor and the width of the demodulating transfer function. In this case the range can extend to 0-10000με.

A 0-40V 30mHz saw-tooth waveform is applied to the PZT as shown in figure 4.38. The response of the demodulating system is also shown by the normalised APD signals. Both plots are in anti-phase with the applied voltage as FBG_1 initially at the quiescent wavelength is demodulated by the negative slope of one hologram whilst FBG_2 initially strained is demodulated by the positive slope of the other. The signal associated with FBG_2 possesses more noise due the hologram possessing the lower diffraction efficiency.

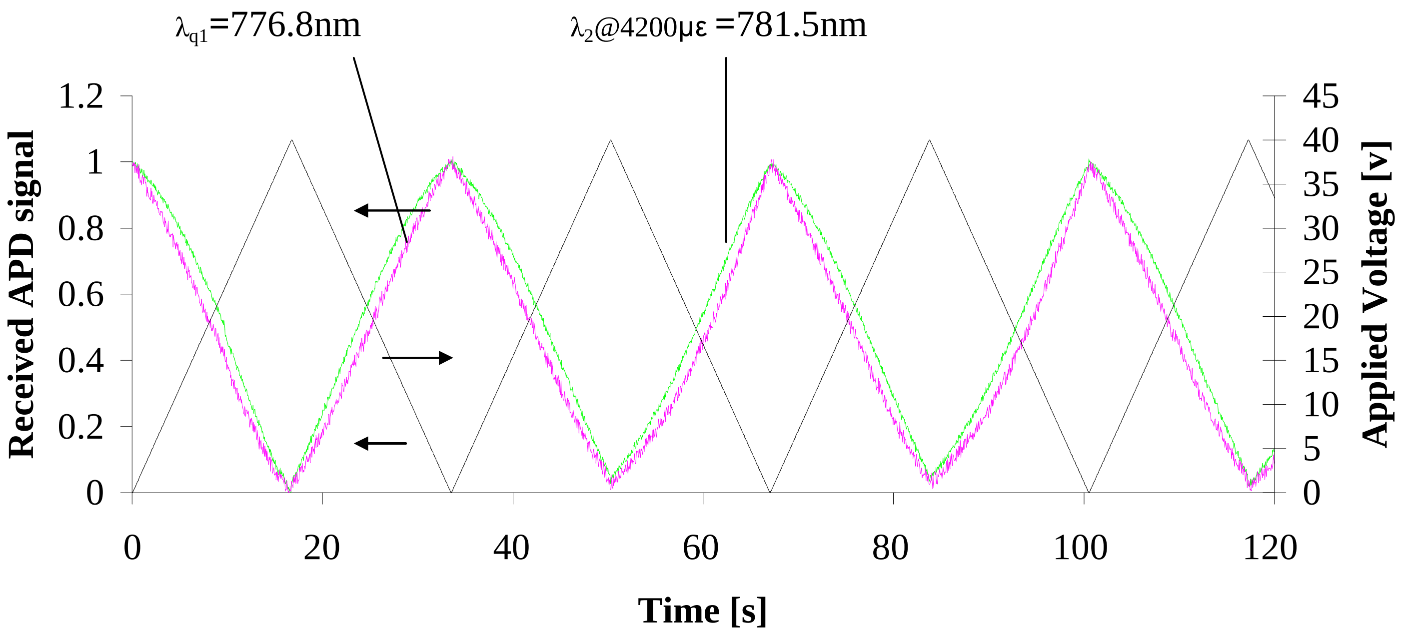

Figure 4.38 The demodulation of a two element FBG sensor array.
The normalised APD signals (—) are the response of the FBG sensor array demodulation scheme to a 30mHz normalised voltage (—) applied to the strain sensor elements.

The results are then processed to map the normalised APD signal to a normalised sensor signal. The mapping shown in figure 4.39 is the multiplication of the applicable section of the demodulating transfer function and the hysteresis of the stage in the forward and reverse directions.

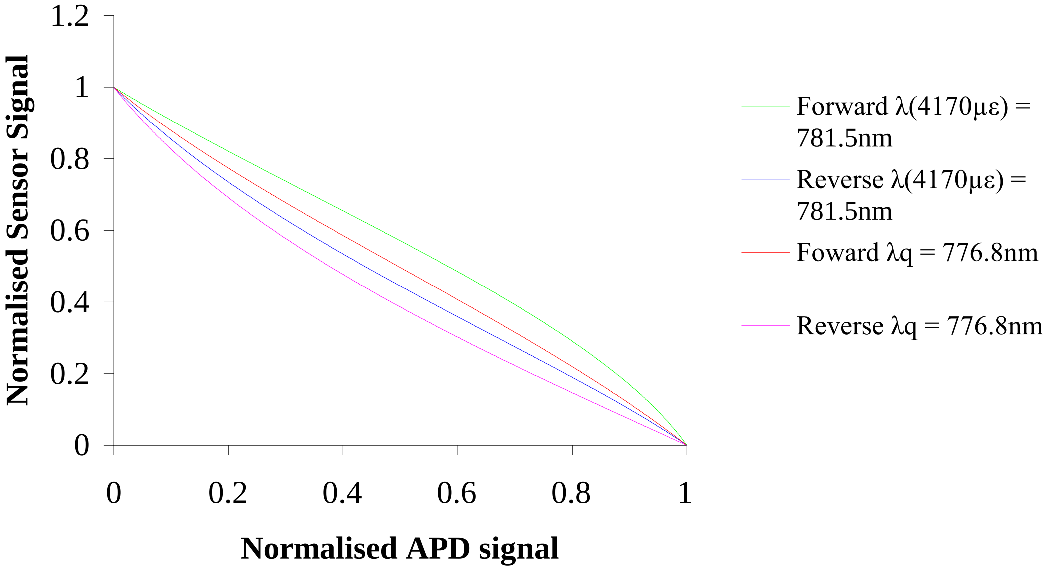

Figure 4.39 The mapping of normalised APD signals to normalised sensor signals for the sensor array demodulation scheme.

The mapping is the multiplication the holographic transfer function over the sensor's wavelength range of operation and two quadratics equations representing the response of the stage in the forward and reverse directions.

The normalised sensor signals are shown in figure 4.40 with the applied voltage for comparison. The results are presented a large format to highlight detail. The Pearson correlation co-efficient is established between each linear section or half cycle of the normalised saw-tooth voltage waveform and the normalised sensor signals. An average factor is then established over all of the linear sections. Here the correlation factor is 0.9997 for the pre-strained sensor at the Bragg wavelength of 781.5nm. For the other sensor whose quiescent wavelength is 776.8nm, the correlation factor is 0.9998. If the normalised sensor signal represents a strain range from 0-4170με then the noise superimposed on the signal represents a quasi-static resolution of ±41με for FBG sensor 1 and ±38με for FBG sensor 2. The maximum error found by comparing the voltage applied to the PZT driven stage and a straight line representing the average of the normalised sensor signal is 50µε for FBG 1 and 63µε for FBG 2. The figures represent a very high level of correlation and an accurate mapping between the normalised APD and sensor signals. The level of crosstalk between the sensors was found to be -11.6dBs.

There is an anomaly in the forward direction of the first cycle recorded by both sensors. This can be attributed to slippage caused by a momentary change in friction within the stage. There is also an anomaly in the reverse direction of the first cycle caused by a significant loss in friction over the complete displacement. Finally both plots show a slight curvature in the reverse directions in later cycles. This represents a departure from the calibrated hysteresis caused by small changes in conditions within the stage between the time of calibration and this particular experiment. This is due to a small change in the response of the PZT or friction within the stage.

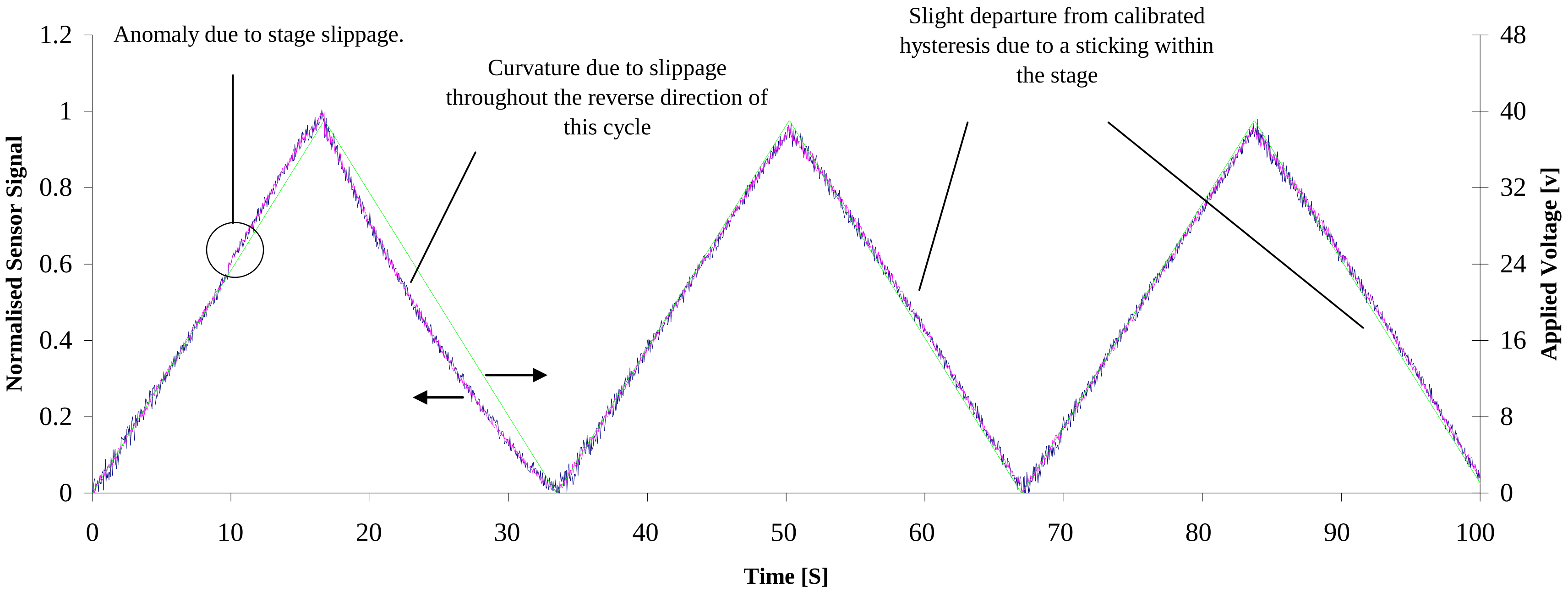
Anomaly due to stage slippage.

Curvature due to slippage throughout the reverse direction of this cycle

Slight departure from calibrated hysteresis due to a sticking within the stage

Figure 4.40 The normalised FBG sensor signals from a de-multiplexed two element array derived from the normalised APD signal. The normalised APD signals (—) are the response of the FBG array demodulation scheme to a 30mHz normalised voltage (—) applied to the strain sensor elements.

The principle of simultaneous de-multiplexing and demodulation is demonstrated by this scheme. However, the wide bandwidth holographic transfer functions imply inefficient use of the illuminating SLD spectrum. Reducing the bandwidth of the transfer functions will allow a densely packed WDM sensor array to be demodulated. A narrow transfer function is achieved by increasing the diameter of an inscribing beam for a given angle and therefore increasing holographic depth as discussed in Section 3.3.2. There is however an increased chance of crosstalk as the band-stop wavelength gap will be reduced. Table 4.6 indicates the parameters of a FBG sensor array demodulation scheme using reduced bandwidth transfer functions. The parameters of the FBG strain sensor are also included.

The measurement of inscribing beam diameter is approximate and will possess an associated error. This causes the error in the wavelength bandwidth of the resulting holographic transfer function. Both FBG sensors are demodulated by the positive slopes of the respective holograms. The demodulation scheme is shown in figure 4.41. The holographic transfer functions are characterised experimentally as detailed in the figure along with the mathematical model. The characterisation shows an error associated with signal noise recorded by the APD. The combined inscribing beam intensity is 510mW/cm^2 with a holographic inscription time of 8s and erasure time of 25s. The first hologram is therefore inscribed in 8s whilst the second is inscribed in 6s.

Table 4.6 Parameters used to inscribe the demodulating holographic array and the resulting key holographic parameters. λ_i is the wavelength, $\theta_i/2$ the half angle and w the beam width radius of inscription. The FWHM wavelength and angular bandwidths are given by $\delta\lambda$ and $\delta\theta$ respectively. λ_q is the quiescent wavelength of the sensor and $\lambda_s(4170\mu\varepsilon)$ is the Bragg wavelength at 4170με. The peak reflectivity of the FBG sensors is given by $R_{fbg.}$ Sensor 1 is attached to the 'pull' section of the stage and is initially unstrained. Sensor 2 is attached to the 'push' section and is pre-strained to a level of 4170με.

Parameter	Value
λ_{i1}	780nm
λ_{i2}	783.9nm
$\theta_{i1}/2$	7°
$\theta_{i2}/2$	9°
w_1	0.5±0.03mm
w_2	0.5±0.03mm
$\delta\lambda_1$	2±0.11nm
$\delta\lambda_2$	2.1±0.13nm
λ_{q1}	777.7nm
$\lambda_{Bs2}(4170\mu\varepsilon)$	779.8nm
R_{fbg1}	73%
λ_{q2}	781.9nm
R_{fbg2}	60%

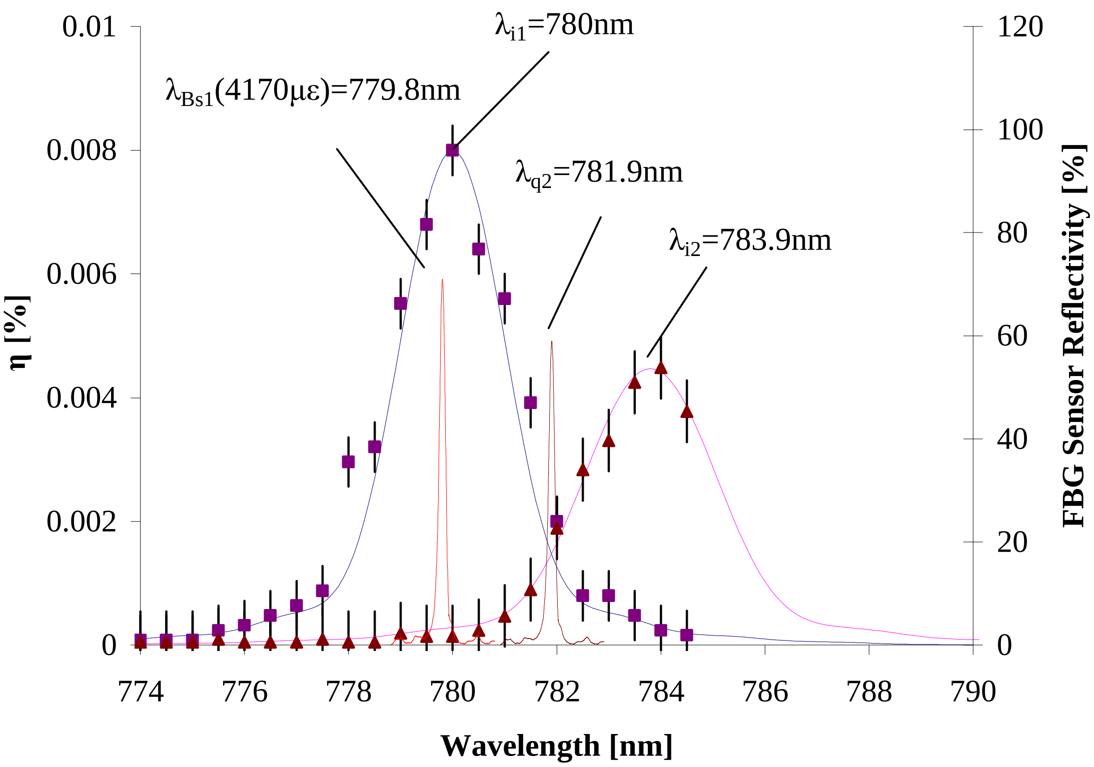

Figure 4.41 The narrow bandwidth holographic transfer functions used to demodulate an FBG sensor array.

The experimental diffraction efficiencies are given by the points (■) and (▲) for the holograms inscribed at 780nm and 783.9nm respectively. The theoretical diffraction efficiencies are given by the lines (—) and (—) for the holograms at 780 and 783.9nm respectively.

A 30mHz 0-40V saw-tooth waveform is applied to the PZT as shown in figure 4.42. The response of the demodulating system is also shown by the normalised APD signals. One is in anti-phase with the applied voltage whilst the other is phase both holograms are demodulated on the positive edge of the respective transfer functions; however sensor 1 is initially pre-strained whilst sensor 2 is at the quiescent wavelength. The strain range is limited by the limits of linearity of the PZT driven stage. If this limitation did not exist the maximum strain that could be applied is dependent on the response of an individual sensor and the width of the demodulating transfer function. In this case the range of strains applied 0-4000με represents the maximum possible.

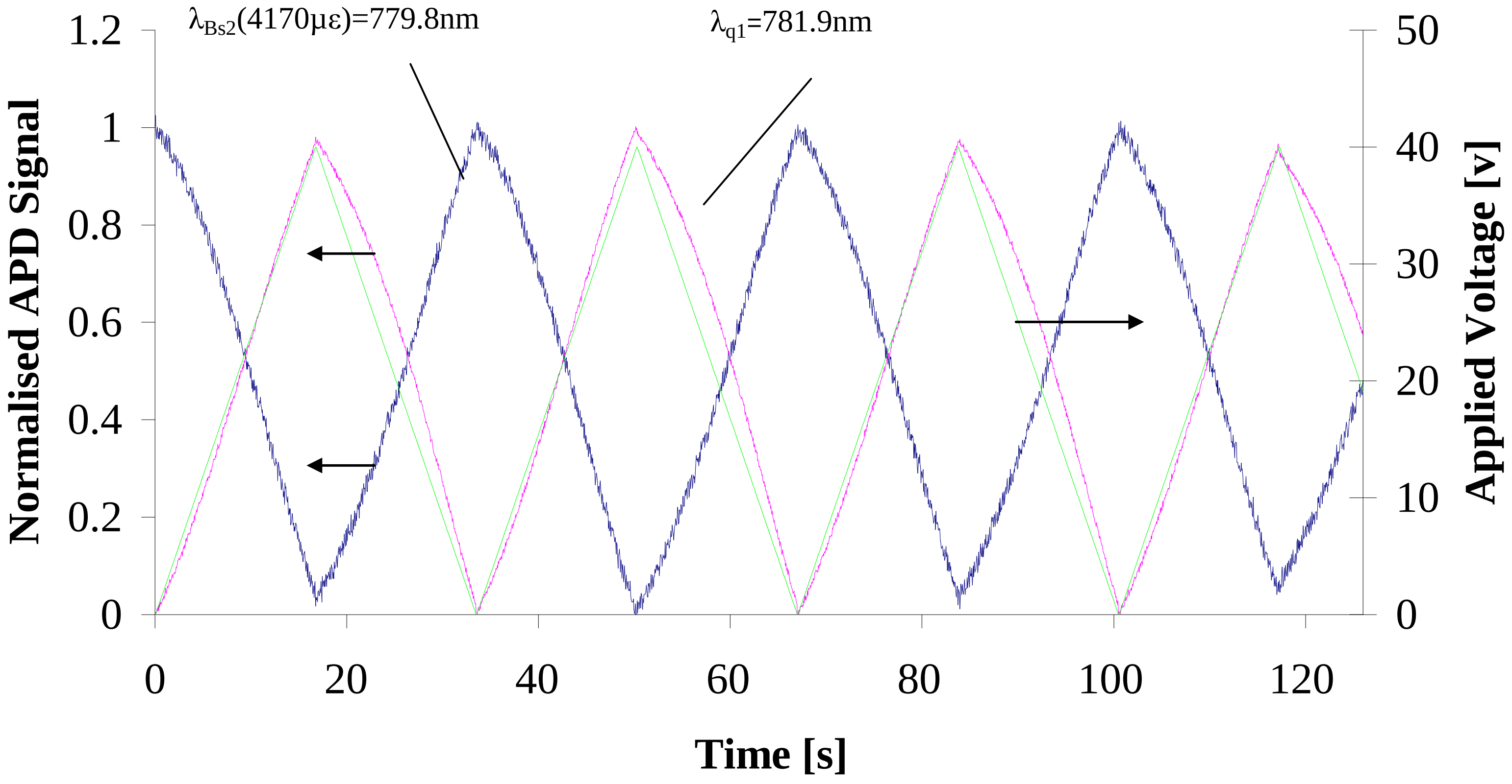

Figure 4.42 The demodulation of a two element FBG sensor array by narrow bandwidth transfer functions. The normalised APD signals (=) are the response of the FBG array demodulation scheme to a 30mHz normalised voltage (—) applied to the strain sensor elements.

The results are then processed to map the normalised APD signal to a normalised sensor signal. The mapping shown in figure 4.43 and is the multiplication of the applicable section of the demodulating transfer function and the hysteresis of the stage in the forward and reverse directions.

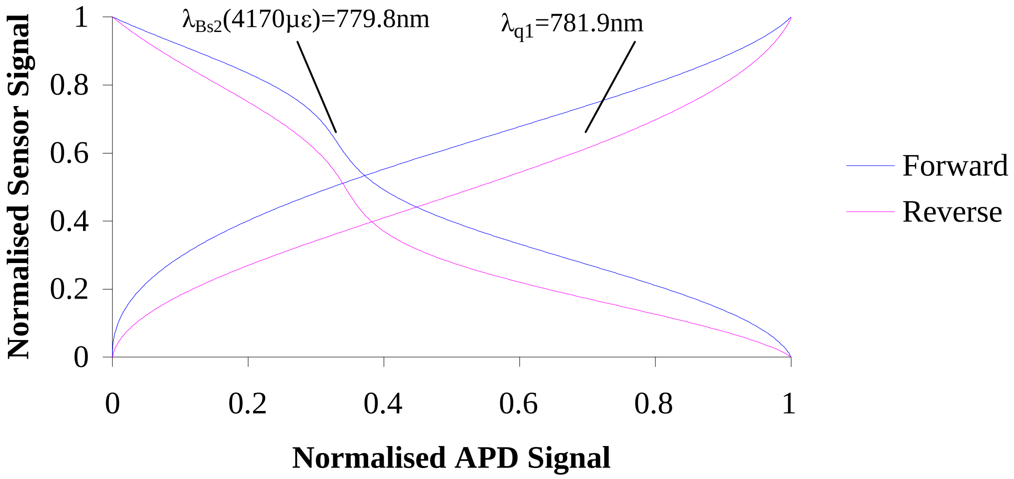

Figure 4.43 The mapping of the normalised APD signals to normalised sensor signals for a demodulation scheme based on narrow bandwidth holographic transfer functions.

The mapping is the multiplication the respective holographic transfer functions over the sensors' wavelength range of operation and two quadratics equations representing the response of the stage in the forward and reverse directions.

The processed results for both sensors are shown in figure 4.44. Both plots show a slight curvature in the reverse directions in later cycles. This represents a departure from the calibrated hysteresis caused by small changes in conditions within the stage between the time of calibration and this particular experiment.

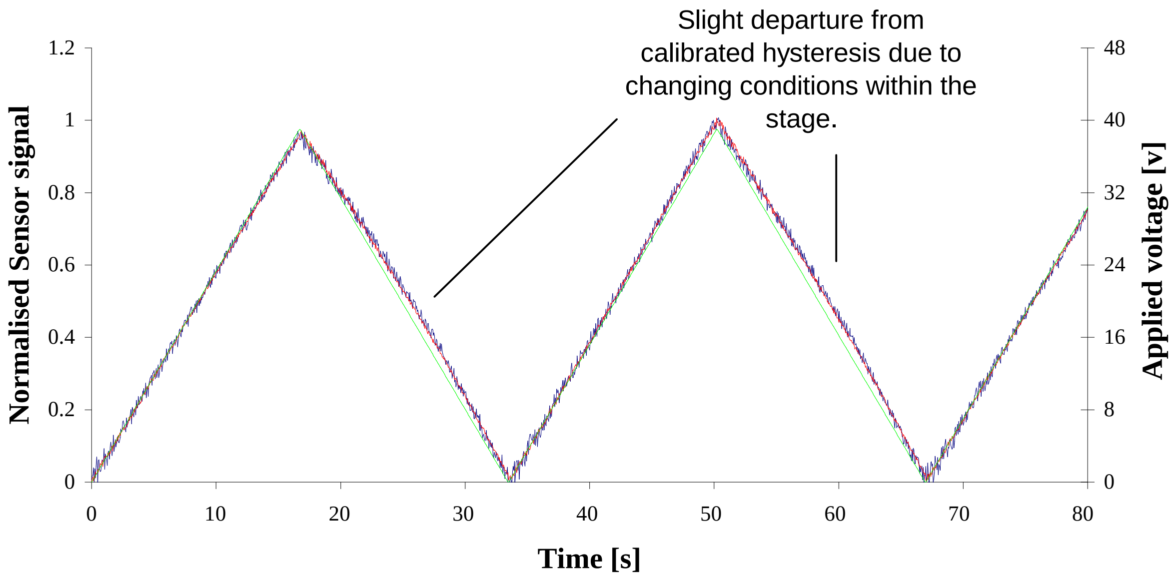

Figure 4.44 The normalised sensor signals from a de-multiplexed two element array by narrow bandwidth holograms derived from the normalised APD signal.
The normalised APD signals (—) are the response of the FBG array demodulation scheme to a 30mHz normalised voltage (—) applied to the strain sensor elements. The processed normalised signals demonstrate a slight departure from a linear function due to slight changes friction within the stage since calibration. .

The Pearson correlation co-efficient is established between each linear section or half cycle of the normalised saw-tooth voltage waveform and the normalised sensor signals. An average factor is then established over all of the linear sections. Here the correlation factor is 0.9992 for the pre-strained sensor at the Bragg wavelength of 779.8nm. For the other sensor whose quiescent wavelength is 781.9nm the correlation factor is 0.998. If the normalised sensor signal represents a strain range from 0-4170με then the noise superimposed on the signal represents a quasi-static resolution of ±40με for FBG sensor 1 and ±45με for FBG sensor 2. The maximum error found by comparing the voltage applied to the PZT driven stage and the a straight line representing the average of the normalised sensor signal is 58με for FBG 1 and 49με for FBG 2. The figures represent a very high level of correlation and an accurate mapping between the normalised APD and sensor signal. The level of crosstalk between the sensors was found to be -8.3dBs.

Both schemes demonstrate that demodulation and de-multiplexing of an FBG sensor array by a holographic array is possible. The second scheme however uses the spectrum of the illuminating SLD more efficiently. The stop-band between the wavelength ranges of the two sensors is reduced for the second scheme; however the level of crosstalk is -8.3dB in comparison to -11.6dB for the first scheme. The normalised sensor signals show a high level of correlation to the applied voltage. The schemes can therefore be mathematically modelled and compensation incorporated for the systematic errors. The demodulation scheme can therefore accurately represent a measurand.

The peak diffraction efficiencies for the holograms demodulating the FBG sensor array is consistently less than 1% and in some cases less than 0.1%. This is caused by numerous factors including the high refractive index of the crystal and inscription geometry. The major contribution however is assumed to be the low absorption coefficient of the crystal at 800nm. This results in a low space charge field and therefore diffraction efficiency due to the number of mobile carriers available for relocation.

The signal level represents a measurand value so excessive noise will be detrimental to the resolution of measurand. The mesurand resolution levels are approximately ±40με that is considerably greater than the industry standard of ±1με. Low diffraction efficiencies coupled with sensor signal levels of approximately 1μW cause high electrical Signal to Noise ratios (SNR) which is responsible for the poor resolution figures. The possible range of the strain readings is comparable with existing demodulation schemes.

To improve measurand resolution the use of modern photorefractive polymers are recommended as these demonstrate significantly improved peak holographic diffraction efficiency over materials such as $BaTiO_3$. This would increase the level of the diffracted signal and reduce the SNR of the signal detected at the APD. A material showing significant potential is PVK (poly (*N*-vinylcarbazole)) (Kippelen *et al.* 2002) that possesses a maximum diffraction efficiency of 70%. This would in turn improve measurand resolution. It is also known that PVK can absorb light within the blue section of the visible spectrum (Taniguchi *et al.* 1964) and can therefore be used in demodulation schemes designed for operation within this wavelength range as recommended in section 4.8. Holograms within this material however are pre-inscribed so cannot be re-used to host holograms with different optical bandwidths.

4.10. Demodulation of an FBG Sensor Array Fabricated in PM Fibre

The polarisation control of the Bragg signals is problematic within the sensor array demodulation schemes described above. Small changes in temperature cause changes within polarisation of beams traversing a length of SM fibre. In an attempt to improve stabilisation therefore the FBG sensor array is fabricated within PM fibre. When aligned with one of the fibre's two cardinal axes, beam polarisation can be maintained along the fibre's length. The sensors are fabricated within the 780nm range and therefore the holograms are inscribed with the Littman external cavity laser. Ideally the complete scheme is to be realised in PM fibre however this could not be achieved as PM 3dB couplers were unavailable for this specific range.

The experimental configuration is shown in figure 4.45. This is similar to the sensor array demodulation scheme shown in figure 4.36 however the length of SM fibre hosting the sensor array is replaced by a length of PM fibre. If the polarisation of the illuminating SLD is aligned with one of the cardinal axes, the polarisations of the reflected Bragg signals are aligned with the same axis. No PSCs are therefore required between sensor elements in this case.

As explained in Section 4.1 the SLDs used to illuminate sensor elements possess a polarisation extinction ratio of approximately 10:1 so despite best efforts light will be coupled into both of the Eigen axes of the PM fibre. The signal reflected from the FBG sensor will therefore have two orthogonal components. These will interfere at some point as they propagate within the SM fibre with a raised cosine response as the orthogonal states are subject to rotation. An important variable is the distance of the splice of the PM and SM fibres and the location of a sensor. The OPD applicable to the interference introduced is then twice this distance multiplied by the difference in refractive indices between the PM fibre's Eigen axes $2d(n_s\text{-}n_f)$. The Free Spectral Range (FSR) of the interferometer is inversely proportional to the OPD as given by equation 4.5. The FSR however can have similar values to the FWHM bandwidth of a holographic transfer function. This implies the interferometer can disturb sensor demodulation by the holographic transfer function.

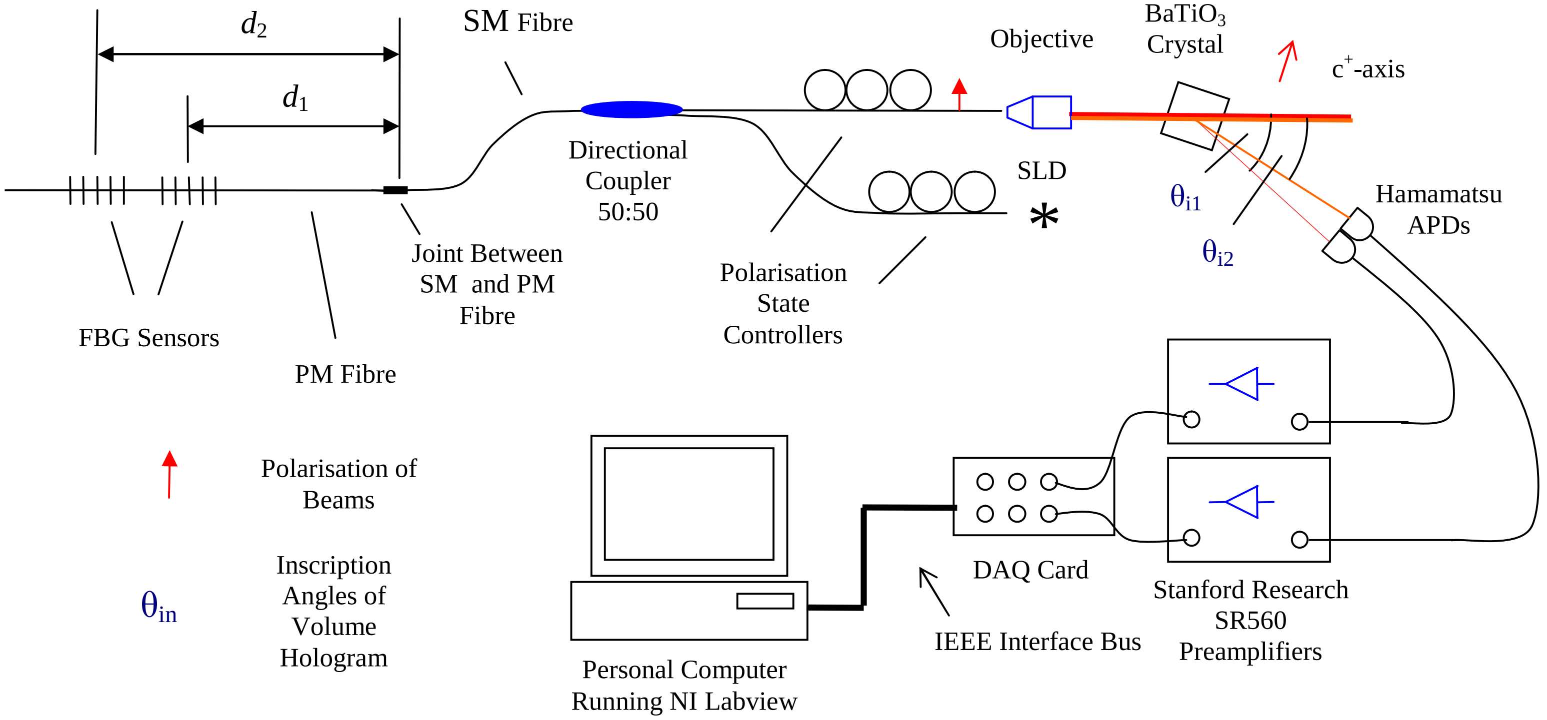

Figure 4.45 Demodulation of a FBG sensor array fabricated in PM fibre.

The detrimental effects of the interferometer can be minimised by firstly ensuring that the polarisation of the illuminating SLD is aligned with one of the cardinal axes. Reducing the distance *d* can also increase the FSR of the interferometer so that it is significantly greater than the FWHM bandwidth of the holographic transfer function (Chung 2001).

The polarisation of the illuminating SLD can be manipulated so that the polarisation aligns with one of the two cardinal axes. For the free space beam emanating from the SuperLum SLD the polarisation is manipulated by a half wave plate. Light from the pigtailed Qphotonics SLD however is manipulated by a PSC. Both possess a polarisation extinction ratio of approximately 10:1 implying that light cannot be launched exclusively into one axis. Remnants of interference will therefore be seen within the results.

To ensure the polarisation of the illuminating SLD is aligned with one of the cardinal axes, two separate techniques are employed. The light that is transmitted through the host PM fibre is monitored by Photon Control detector. Here however the light passes through a plane polariser before impinging on the detector. The device controlling the polarisation is manipulated to maximise the polarisation extinction ratio. The plane polariser is then rotated to minimise the transmitted intensity, a hand is then placed in close proximity to the fibre end. The change in temperature causes a slight change in refractive index difference between the fibre’s cardinal axes. If there are no fluctuations in transmitted intensity the polarisation of the illuminating SLD is aligned with one of the fibre’s cardinal axes.

Another technique uses a spectrum analyser to monitor the spectrum transmitted through the fibre. Here the response of the interferometer is clearly seen by a sinusoidal ripple of constant period superimposed on the spectrum. The spectrum also indicates the Bragg wavelength of the FBG sensors. The device controlling the polarisation of light from the SLD can then be manipulated to minimise the ripple. At this a point the polarisation of the light is aligned to one of the fibre’s cardinal axes.

As explained in Section 4.4 the splicing of individual sensor elements fabricated within PM fibre is problematic. The FBG sensor array is fabricated therefore in a single length of PM fibre. The distance between the splice and the first sensor is 0.1m whilst the second sensor is fabricated a further 0.07m down the fibre. The distances are chosen to allow ease of fabrication and attachment to the stage however also ensuring the interferometers created will possess a wide FSR. The difference in the refractive indices between the fibre's Eigen axes is given within the manufacture's specification and is $4.3\text{x}10^{-4}$. For the second sensor located 0.17m from the splice this creates an interferometer with an FSR of 4nm for wavelengths within the 780nm range, see equation 4.5. This is more than twice the value of the narrow bandwidth holographic transfer function demodulating the FBG array detailed in the previous section.

An experiment was completed similar to that described in Section 4.8. This used narrow bandwidth transfer functions to demodulate two FBG sensors. Table 4.7 indicates the parameters used for the demodulation of an FBG senor array fabricated in PM fibre. The parameters of the FBG strain sensor are also included.

Table 4.7 Parameters used to inscribe the demodulating holographic array and the resulting key holographic parameters. λ_i is the wavelength, $\theta_i/2$ the half angle and w the beam width radius of inscription. The FWHM wavelength and angular bandwidths are given by $\delta\lambda$ and $\delta\theta$ respectively. λ_q is the quiescent wavelength of the sensor and $\lambda_s(4170\mu\varepsilon)$ is the Bragg wavelength at 4170με. The peak reflectivity of the FBG sensors is given by $R_{fbg.}$ Sensor 1 is attached to the 'pull' section of the stage and is initially unstrained. Sensor 2 is attached to the 'push' section and is pre-strained to a level of 4170με. The distance d between the sensor and the splice between the SM and PM fibre is also detailed.

Parameter	Value
λ_{i1}	778nm
λ_{i2}	782.9nm
$\theta_{i1}/2$	7°
$\theta_{i2}/2$	9°
w_1	0.5±0.03mm
w_2	0.5±0.03mm
$\delta\lambda_1$	2±0.11nm
$\delta\lambda_2$	2.1±0.13nm
λ_{q1}	775.8nm
R_{fbg1}	62%
d_1	0.1m
λ_{q2}	780.9nm
$\lambda_{Bs2}(4170\mu\varepsilon)$	782.6nm
R_{fbg2}	59%
d_2	0.17m

The combined inscribing beam intensity is 510mW/cm^2 with a holographic inscription time of 8s and erasure time of 25s. The first hologram is therefore inscribed in 8s whilst the second is inscribed in 6s.

The measurement of inscribing beam diameter is approximate and will possess an error. This causes the error in the wavelength bandwidth of the resulting holographic transfer function. Both FBG sensors are demodulated by the positive slopes of the respective holograms. The demodulation scheme is shown in figure 4.46. The holographic transfer functions are characterised experimentally as detailed in the figure along with the mathematical model. The characterisation shows an error associated with signal noise recorded by the APD.

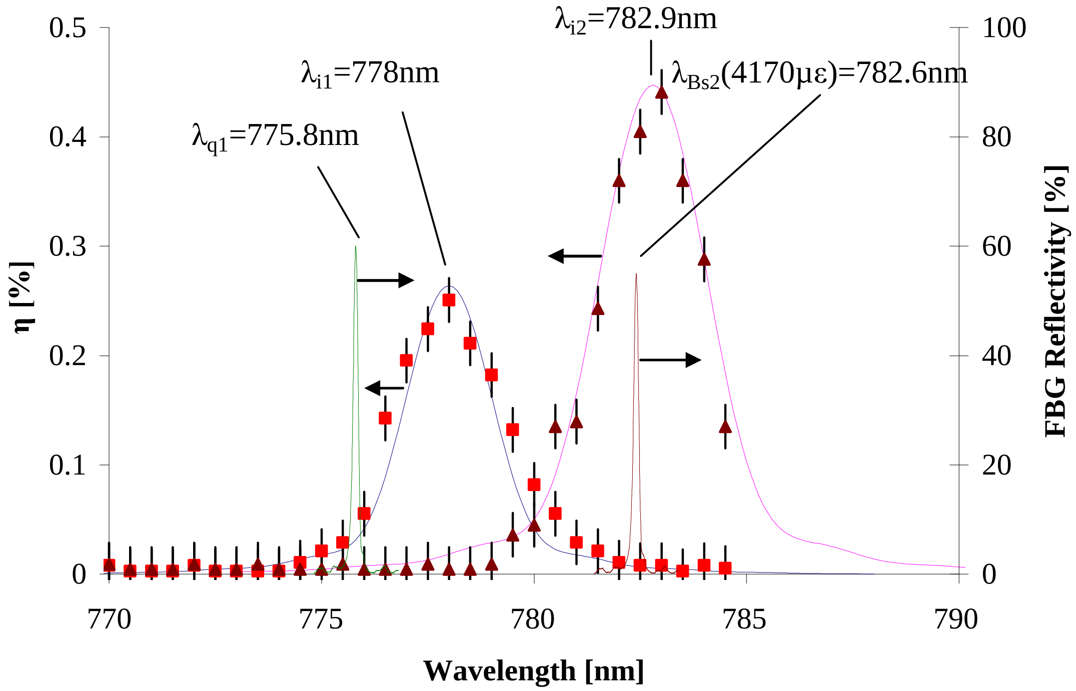

Figure 4.46 The narrow transfer functions used to demodulate an FBG sensor array fabricated in PM fibre. The experimental diffraction efficiency is given by the points (■) and (▲) for the holograms inscribed at 778nm and 782.9nm respectively. The theoretical diffraction efficiency is given by the lines (—) and (—) for the holograms at 778 and 782.9nm respectively.

A 30mHz 0-40V saw-tooth waveform is applied to the PZT as shown in figure 4.47. The response of the demodulating system is also shown by the normalised APD signals. One is in anti-phase with the applied voltage whilst the other is in phase. Both holograms are demodulated on the positive edge of the respective transfer functions however sensor 1 is initially at the quiescent wavelength whilst sensor 2 pre-strained.

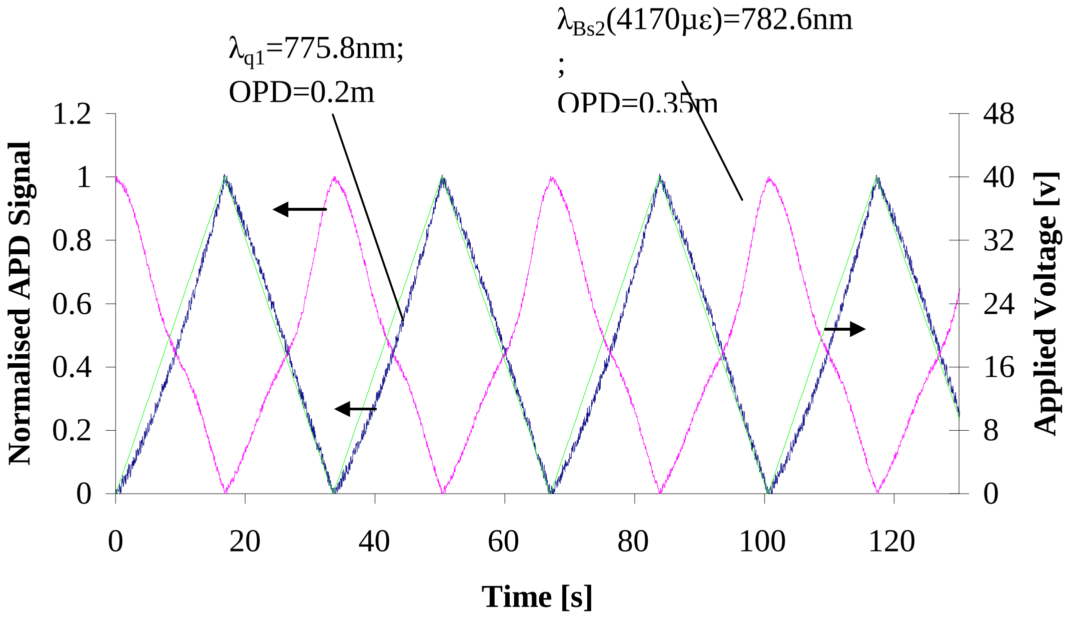

Figure 4.47 Demodulation of an FBG strain sensor array fabricated in PM fibre. The normalised APD signals (═) are the response of the FBG array demodulation scheme to a 30mHz normalised voltage (—) applied to the strain sensor elements.

The results show that for the first element a distance 0.1m from the splice the effects of the interferometer can be neglected. This is due to the FSR being approximately 7nm in width considerably larger than the FWHM of the demodulating holographic transfer function. In contrast the second element a distance 0.17m from the splice has a FSR of approximately 4nm and the remnants of interference can be seen in the results. This manifests as a slight deviation in response during the mid stage of each half cycle.

The results demonstrate that an FBG sensor array fabricated in PM fibre can be demodulated. Certain precautions however are required. Firstly the locations of the sensor elements within the host PM fibre are to be pre-determined. The polarisation of the illuminating SLD must also be aligned with one on the fibre’s Eigen-axes. Both of these precautions minimise the effect of the interference created by the difference in refractive indices of the Eigen-axes within the PM fibre.

The demodulation scheme demonstrates an improved sensitivity over the schemes realised in SM fibre. The signals from both sensors possess the same polarisation when reflected back into the SM fibre as the polarisation of the illuminating SLD is aligned with one of the PM fibre's cardinal axes. The polarisation of both signals can then be controlled by a single PSC improving stability. This is different from the scheme realised in SM fibre alone where the reflection of individual sensor elements need to be controlled. The set-up however still requires reconfiguration before each experiment. This is due to a drift in polarisation states of the sensor signals within the SM fibre. It is recommended therefore that the complete experimental configuration is realised is PM fibre.

4.11. Intensity Referencing

The demodulating scheme is intensity based and so is susceptible to changes in the source intensity and fibre bend losses. An intensity referencing scheme based on holographic transfer functions was therefore developed, as described in Section 4.1. Here two holograms simultaneously demodulate a single FBG sensor fabricated in SM fibre on the positive and negative edges of the respective transfer functions. The Bragg signal is divided by the holograms to diffract the respective portions through different angles to two separate APDs. Ratiometric detection is deployed. However, the Bragg signals are not processed in the usual manner as described by equation. 4.1. The equation is modified to take account of the non-linear nature of the holographic transfer function, as described by equation 4.2.

Ratiometric detection will compensate for fluctuations in fibre bend losses and source intensity but will not compensate for random processes like the noise introduced by the APD. The resolution of the mesurand will therefore still be limited by this factor. Errors between a linearly applied measurand represented by the voltage applied to the PZT stage and the average measurand value derived from results also still exist.

The experimental configuration used is the same as that described in figure 4.36. A fibre length without an inscribed FBG was attached to the 'pull' section of the stage during experimentation to reduce the effect of hysteresis. The characterisation and mathematical modelling of the holograms is the same as that described in section 4.2 and

3.3.2 respectively. A schedule of hologram inscription is also to be derived as described in Section 4.9 for the two element holographic array.

The results will take the form of normalised APD signals as previously demonstrated in figure 4.38. One plot will be in phase with the voltage applied to the PZT whist the other will be in anti-phase as demodulation is on the positive and negative edges of the respective transfer functions.

The quasi-static results however will not be processed as described in Section 4.9 as the compensation for the non-linear transfer function is incorporated into the ratiometric detection scheme. The processing will firstly compensate for hysteresis within the stage alone. Subsequently equation 4.2 will compensate for any non-linearity within the demodulating transfer functions and is used to derive a normalised sensor signal. This will be correlated to the voltage applied to the PZT.

An important part of an intensity referencing scheme is the processing of static signals. A change in the source intensity or bend loss will alter the signal level at both detectors. Under these conditions as explained in Section 4.1 the difference over the sum of the two detected signals will remain at the same value.

An experiment is undertaken to demonstrate principles of the intensity referencing scheme. This uses two narrow bandwidth transfer functions to demodulate a single FBG sensor fabricated in SM fibre. The experimental parameters detailed in Table 4.8 whilst the scheme is detailed in graphical form in figure 4.48. The measurement of inscribing beam diameter is approximate and will possess an associated error. This causes the error in the wavelength bandwidth of the resulting holographic transfer function. The holographic transfer functions are characterised experimentally as detailed in the figure along with the mathematical model. The characterisation shows an error associated with signal noise recorded by the APD.

Table 4.8 Parameters used to inscribe the demodulating hologram and the resulting key holographic parameters. λ_i is the wavelength, $\theta_i/2$ the half angle and w the beam width radius of inscription. The FWHM wavelength and angular bandwidths are given by $\delta\lambda$ and $\delta\theta$ respectively. The FBG is attached to the 'push' section of the stage and is pre-strained. λ_q is the quiescent wavelength and $\lambda_s(4170\mu\varepsilon)$ is the Bragg wavelength at 4170με. The peak reflectivity of the FBG sensor is given by R_{fbg}.

Parameter	Value
λ_{i1}	780.2nm
λ_{i2}	782.8nm
$\theta_{i1}/2$	7°
$\theta_{i2}/2$	9°
w_1	0.5±0.03mm
w_2	0.5±0.03mm
$\delta\lambda_1$	2±0.11nm
$\delta\lambda_2$	2.1±0.13nm
λ_{q1}	780.4nm
$\lambda_{Bs}(4170\mu\varepsilon)$	782.5nm
R_{fbg}	41%

The combined inscribing beam intensity is 510mW/cm^2 with a holographic inscription time of 8s and erasure time of 25s. The first hologram is therefore inscribed in 8s whilst the second is inscribed in 6s.

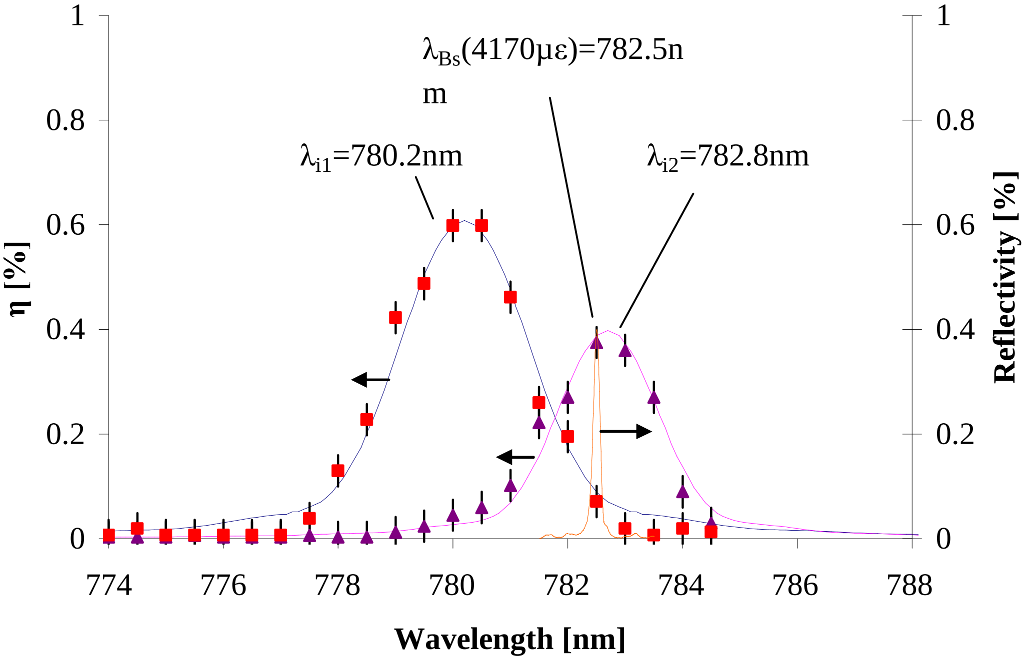

Figure 4.48 The holographic transfer functions used to demodulate a single FBG sensor as a part of an intensity referencing scheme.

The experimental diffraction efficiency is given by the points (■) and (▲) for the holograms inscribed at 780.2nm and 782.8nm respectively. The theoretical diffraction efficiency is given by the lines (—) and (—) for the holograms at 780.2 and 782.8nm respectively.

The FBG sensor is attached to the 'push' section of the stage so it is pre-strained to a level of 4170με. The strain is released as the voltage is applied to the PZT. A 30mHz 0-40V saw-tooth waveform is applied to the PZT as shown in figure 4.49. The response of the demodulating system is also shown by the normalised APD signals. One is in anti-phase with the applied voltage whilst the other is phase as the signal is demodulated on the positive and negative edges of the respective transfer functions.

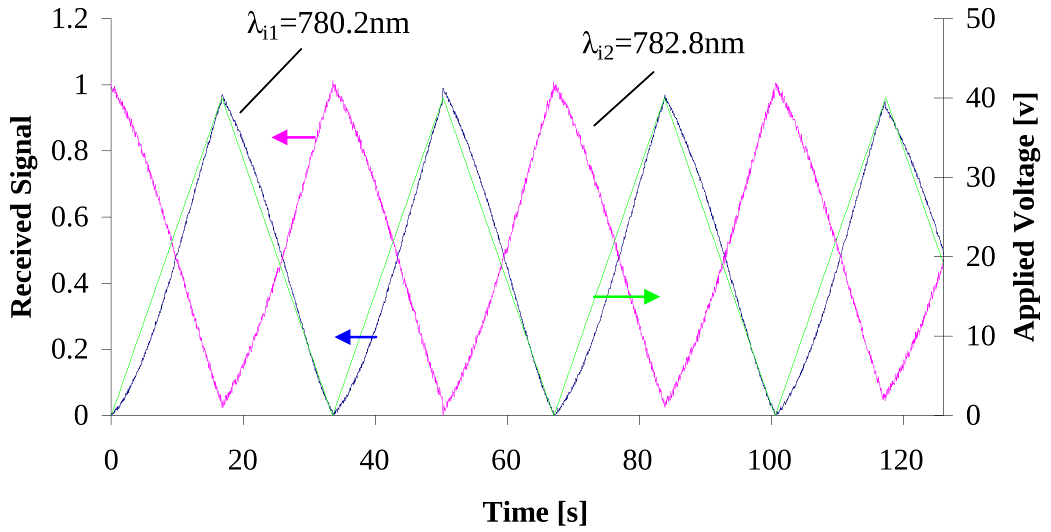

Figure 4.49 Demodulation of a single FBG strain sensor by two volume holograms as a part of an intensity referencing scheme.
The normalised APD signals (=) are the response of the FBG array demodulation scheme to a 30mHz normalised voltage (—) applied to the strain sensor elements, also shown in the figure.

The normalised sensor signals received demonstrate a second-order non-linearity associated with hysteresis within the stage and a third order non-linearity associated with the holographic transfer function. The quasi-static signals are processed to compensate for hysteresis using the quadratic equations 4.9 and 4.10. These represent the hysteresis in the forward and reverse directions respectively. The signals are then processed using equation 4.2 to compensate for the non-linearity within the holographic transfer function. The results are correlated with the sensor signal represented by the normalised applied saw-tooth waveform. The processed results and the normalised saw-tooth waveform are shown in figure 4.50.

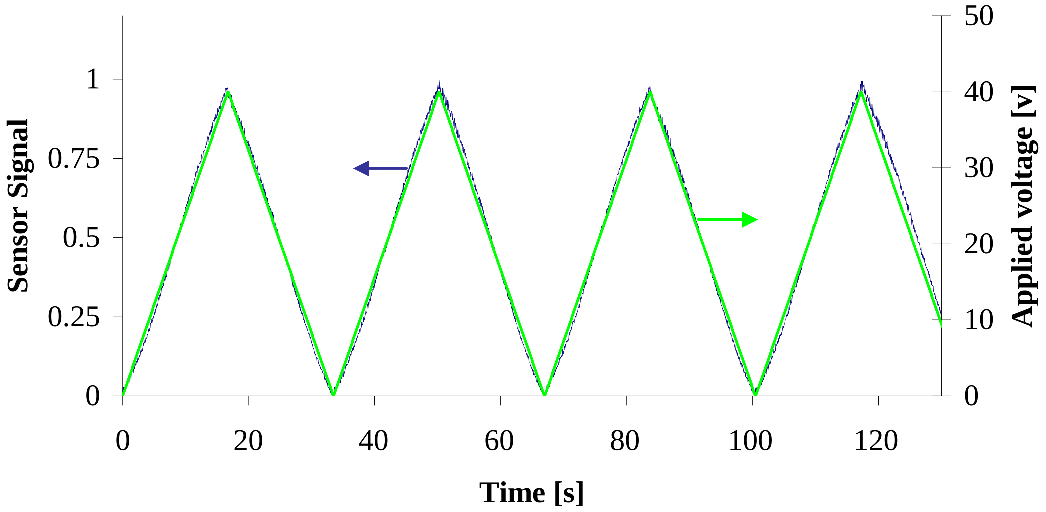

Figure 4.50 Intensity Referencing of quasi-static signals for the FBG sensor demodulation scheme. The normalised sensor signal (—) is shown with the normalised voltage applied to the PZT (—). There a high level of correlation and an accurate mapping between the normalised APD and sensor signals.

The Pearson correlation co-efficient is established between each linear section or half cycle of the normalised saw-tooth voltage waveform and the normalised sensor signal. An average factor is then established over all of the linear sections. Here the correlation factor is 0.9998. The figure represents a very high level of correlation and an accurate mapping between the normalised APD and sensor signals. If the normalised sensor signal represents a strain range from 0-4170με then the noise superimposed on the signal represents a quasi-static resolution of ±32με. The maximum error found by comparing the voltage applied to the PZT driven stage and the average results is 51με.

To assess the performance of the scheme in processing static signals, different levels of static strain are applied to the FBG. Specifically, strains of 0με to approximately 4000με are applied in steps of 1000με, the steps being 40s in duration. The intensity of the SLD is modulated by a 0.5Hz signal as the strain is stepped through this range. The depth of modulation of the SLD is approximately 30%. The output signals then demonstrate a stepped increase or a decrease depending if the hologram demodulates on the negative or positive edge of the respective transfer function. A 0.5Hz signal is superimposed on the individual signals due to the modulation of the SLD. The signals are then processed by equation 4.2 to reconstruct the stepped static strain.

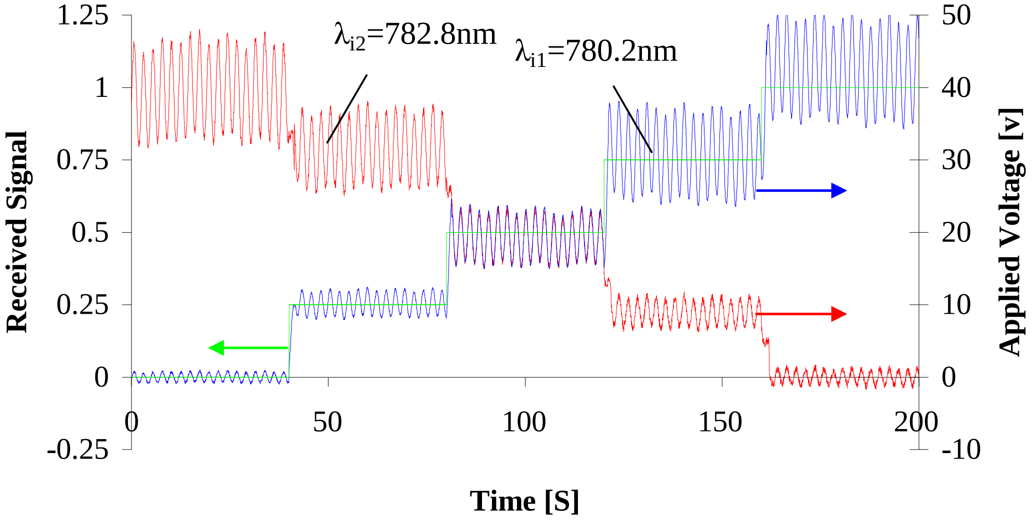

Figure 4.51 Demodulation of a single FBG strain sensor by two volume holograms. The voltage is stepped from 0-40V in 10V increments each with duration of 40s (—). A 0.5Hz frequency signal modulates the SLD throughout the experiment with a 30% depth of modulation. The response of the demodulating system is also shown by the normalised APD signals (=).

A stepped voltage is applied to the voltage controlled PZT as shown in figure 4.51. The steps range from 0V to 40V in increments of 10V each increment having a 40s duration. Throughout the experiment the intensity of the SLD illuminating the sensor is modulated with a 0.5Hz frequency signal with a 30% depth of modulation. The response of the demodulating system is also shown by the normalised APD signals.

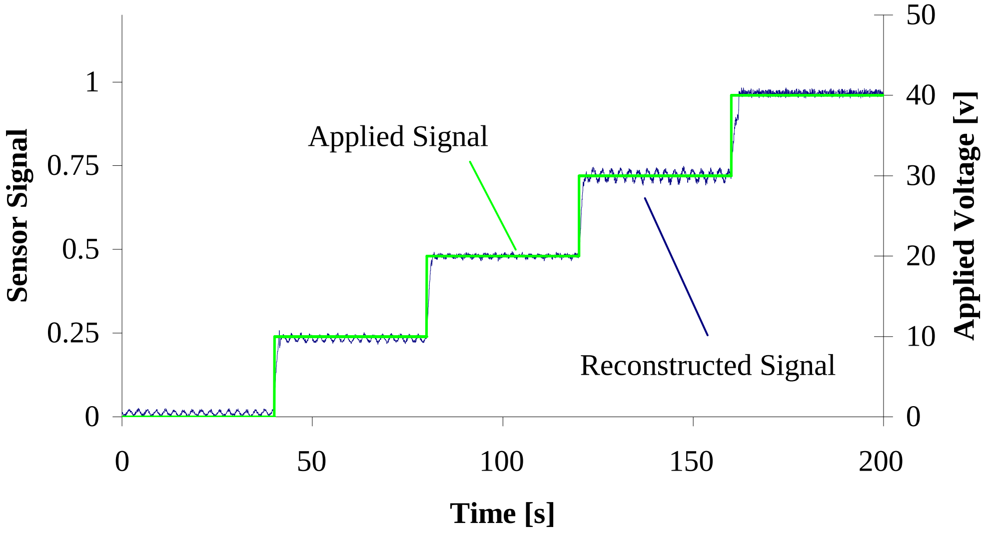

Figure 4.52 Intensity referencing of static signals for the FBG sensor array demodulation scheme. The voltage is stepped from 0-40V in 10V increments each with duration of 40s (—). Also shown is the reconstructed signal (—).

The static results detailed in figure 4.51 are processed by equation 4.2, which represents a modified form of ratiometric detection. This will allow the original static signal to be reconstructed from the normalised APD signals that include the 0.5Hz power fluctuation component. The processed results are shown in figure 4.52. Here the applied stepped voltage and the reconstructed signals are both shown on the same figure for comparison. Here the reconstructed normalised sensor signal broadly correlates to the normalised applied voltage. Errors are present however seen as fluctuations in the reconstructed signal at the 0.5Hz frequency applied to the SLD. The demonstrated technique therefore represents a feasible means to intensity reference an FBG array demodulation scheme.

The intensity referencing technique however suffers from same problems associated with the sensor array demodulation scheme, namely very low holographic diffraction efficiency causing poor measurand resolution. The situation however is compounded as the single Bragg signal is divided between two detectors.

4.12. Summary of Achievements

A two element holographic array has been used in the demodulation of a two element FBG strain sensor array. The first scheme reported used holograms inscribed 7.5nm apart each demonstrating a FWHM bandwidth of approximately 4.5nm. One sensor was demodulated on the positive slope of the hologram inscribed at the higher wavelength whist the other sensor was demodulated on the negative slope of the hologram inscribed at the lower wavelength. Each hologram demodulated a sensor with an operating range of approximately 2.5nm. This corresponds to applying strain to a sensor element in the approximate range 0-4000$\mu\varepsilon$. The crosstalk measured between channels was -11.6dB. The scheme detailed in Section 4.9 however does not use the illuminating spectrum in the most efficient manner.

An improved scheme also demonstrated in Section 4.9 possessed holographic inscription wavelengths 3.9nm apart. This separation is similar to the difference in the FBG quiescent wavelengths that were 4.1nm apart. Both FBG sensors are demodulated on the negative slope of the matching holograms, the bandwidths of which are both approximately 2.1nm. The holograms demodulated sensor elements with an operating range of approximately 2nm. The crosstalk measured between channels was -8.3dB.

Holographic inscription and erasure times where established for a range of beam intensities. The inscription times matched the dielectric relaxation times as the relatively large period of the gratings determined that the space charge field was in the unsaturated regime. The erasure times however are greater than that of inscription and cannot be mathematically modelled. The erasure beam interferes with the diffracted section of the same beam initially reinforcing the hologram to be erased. Establishment of the time constants allow a schedule of inscription to be derived so that all holograms in an array have the same diffraction efficiency.

An intensity referencing technique was realised by demodulation of a single FBG sensor by two holographic transfer functions as detailed in Section 4.11. The respective signals however were processed by a modified version of ratiometric detection to compensate for the third-order non-linearity introduced by the holographic transfer functions as described in Section 4.1. The technique can therefore be used for the intensity referencing of the FBG sensor array demodulation scheme.

The resolution of the scheme however is limited to approximately ±40με by the peak diffraction efficiency of the demodulating hologram. This compares unfavourably with other schemes and is considerably greater than the industry recognised standard of ±1με. The strain range is limited by the limits of linearity of the PZT driven stage. If this limitation did not exist the maximum strain that could be applied is dependent on the response of an individual sensor and the width of the demodulating transfer function. Figures of 0-10000με are possible that compares favourably with other schemes.

Finally some preliminary transient experiments were completed to establish the AC response of the demodulation scheme. This is important as the filter based demodulation schemes have the potential for high speed. Insufficient time however was available to achieve high quality results.

4.13. References

Chung, S., Kim, J., Yu, B.-. & Lee, B. 2001, "A fiber Bragg grating sensor demodulation technique using a polarization maintaining fiber loop mirror", *IEEE Photonics Technology Letters*, vol. 13, no. 12, pp. 1343-1345.

Davis, M.A. & Kersey, A.D. 1994, "All-Fiber Bragg Grating Strain-Sensor Demodulation Technique using a Wavelength-Division Coupler", *Electron. Lett.,* vol. 30, no. 1, pp. 75-77.

Günter, P. and Huignard, J. (1987), *Photorefractive Materials and Their Applications 1: Fundamental Phenomena (Springer Series in Optical Sciences).*

Hamamatsu Solid state Division 1997*, APD Module C5460-SPL-1MHZ Instruction manual*

James, S.W., Dockney, M.L. & Tatam, R.P. 1996, "Photorefractive volume holographic demodulation of in-fiber Bragg grating sensors", *IEEE Photonics Technology Letters,* vol. 8, no. 5, pp. 664-666.

Kippelen, B., Blanche, P, Schuzgen, A., Fuentes-Hernandez, C., Ramos-Ortiz, G., Wang, J.-P., Peyghambarian, N., Marder, S.R., Leclercq, A., Beljonne, D. & Bredas, J.-P. 2002, "Photorefractive polymers with non-destructive readout", *Advanced Functional Materials,* vol. 12, no. 9, pp. 615-620.

Lam, D. K. W. & Garside B. K. 1981, “Characterisation of single-mode optical fibre filters”, *Applied Optics*, vol 20, pp 440-445.

Liu, X., et al., 1997, “The influence of phase mask stitch errors on the performance of UV-written Bragg gratings”, *Bragg grating, photosensitivity, and poling in glass Fibres and waveguides*, vol 17, BMG9-1.

Meltz, G., Morey, W. W. 1991, "Bragg grating formation and germosilicate fibre photosensitivitity”, *Proc. SPIE,* vol 1516, pp 185-199

Nakamura, S., and Fasol, G., 1997, "Room temperature CW operation of InGaN MQW LDs” *The blue laser diode,* pp. 277-300, Springer-Verlag, Berlin.

Parent, M., Bures, J., Lacroix, S. & Lapierre, J. 1985, "Polarizing Properties of Bragg Reflectors Induced by Photosensibility in Monomode Optical Fibers", *Applied Optics,* vol. 24, no. 3, pp. 354-357.

Rajbenbach, H., Delboulbe, A. & Huignard, J.P. 1991, "Low-noise amplification of ultraweak optical wave fronts in photorefractive BiSiO12 20", *Opt. Lett.*, vol. 16, pp. 1481-1483.

Refregier, P., Solymar, L., Rajbenbach, H. & Huignard, J.P. 1985, "Two-beam coupling in photorefractive Bi12SiO 20 crystals with moving grating: Theory and experiments", *Journal of Applied Physics*, vol. 58, no. 1, pp. 45-57.

Ringhofer, K.H., Tao, S., Takacs, J. & Solymar, L. 1991, "The role of the longitudinal component of the electric field vector in two-wave mixing in photorefractive $BaTiO_3$", *Applied Physics B Photophysics and Laser Chemistry*, vol. 52, no. 4, pp. 259-261.

Rodgers, J.L. & Nicewander, W.A. 1988, "Thirteen ways to look at the correlation coefficient", *The American Statistician*, vol. 42, no. 1, pp. 59-66.

Solymar, L. 1996, *The physics and applications of photorefractive materials*, Clarendon Press, Oxford.

Strasser, A.C., Maniloff, E.S., Johnson, K.M. & Goggin, S.D.D. 1989, "Procedure for Recording Multiple-Exposure Holograms with Equal Diffraction Efficiency in Photorefractive Media", *Opt. Lett.*, vol. 14, no. 1, pp. 6-8.

Tanguchi, A., Seiichi, K., Kanda, S., Kusabayashi, S., Mikawa, H., Kazuo, I., 1964, "The electrical properties of PVK tetracyanoquinodimethane charge transfer complex", *Bulletin of the Chemical Society of Japan.*, vol. 37, no. 9, pp. 1386-1388.

Chapter 5 Conclusions and Further Work

The diffraction efficiency of the hologram is related to the space charge field developed in the photorefractive material upon holographic inscription as described in Section 3.2.1. Both a uniform interference pattern and one modified by a Gaussian beam profile have been investigated to understand the space charge field created. An expression for the space charge field which is related to the first spatial differential of the interference pattern is derived in Section 3.2.2. The value of the space charge field therefore approximates to a uniform grating as the rate of change in intensity due to the interference pattern is much greater than that of the Gaussian profile.

The holographic transfer functions used in demodulation are characterised by apodisation and a broadening of bandwidth in comparison with that expected from established coupled mode theory. Coupled mode theory defines a uniform hologram where the associated transfer function bandwidth is determined by the physical depth of the VH material. The bandwidth of a transfer function however was manipulated by altering the diameter of and changing the angle between the inscribing beams. The functions used were modelled mathematically by considering that the hologram formed to be a conic volume within the photorefractive material as described in Section 3.3.2. The rays depending on their lateral position within an interrogating beam then travel different distances through the conic volume. The composite transfer function is then an integration of the transfer functions applicable to individual depths, the maximum depth being the length of the conic section.

The bandwidth of the holographic transfer function was greater by approximately a factor ten to that of the FBG reflection spectrum. The bandwidth of other components in the demodulation scheme for example the 3dB coupler, the SLD spectrum and the APD responsitivity were found to be considerable greater than that of the transfer function. The bandwidth response of the scheme therefore approximates to the holographic transfer function as discussed in Section 4.1. One exception is if wide bandwidth transfer functions are used on an edge of the SLD spectrum. This creates disturbance in the demodulation process as the differential of the SLD spectrum is greater than that of the transfer function as discussed in Section 4.8. This can be overcome by using narrow bandwidth transfer functions or a section of the SLD spectrum near to the peak intensity wavelength.

The maximum diffraction efficiency of the holographic transfer function used for demodulation is much less than expected, the diffraction efficiency being related to the change in the refractive index and therefore the value of the space charge field created within the photorefractive crystal. The space charge field in turn is related to the number of mobile carriers created by the illumination of the crystal as discussed in Section 3.2.3. The absorption coefficient assumed is quoted at 500nm however the experiments described in this thesis were executed at 800nm where the coefficient is known to be significantly less but the value unspecified. This caused the maximum diffraction efficiency to be much less than expected.

Holographic inscription and erasure times where established for a range of beam intensities. The inscription times matched the dielectric relaxation times as the relatively large period of the gratings determined that the space charge field was in the unsaturated regime. The erasure times however are greater than that of inscription and cannot be mathematically modelled. The erasure beam interferes with the diffracted section of the same beam initially reinforcing the hologram to be erased. Establishment of the time constants allow a schedule of inscription to be derived so that all holograms in an array have the same diffraction efficiency. The schedule details wavelengths and angles of inscription as well as inscription times as discussed in Section 4.9. The execution of a schedule however is usually partially successful. This is due to fluctuations in the inscribing process. A hologram can be partially inscribed, erased and then inscribed again within one inscription incidence.

Two critical systematic errors exist within the demodulation scheme. Firstly the PZT controller that applies strain to the FBG sensor array stores energy resulting in hysteresis as discussed in Section 4.5. The stage initially accelerates from a position of rest, enters a period of constant velocity only to decelerate as the stage subsequently comes to rest at the end of a half cycle. The mapping of applied voltage to stage displacement is therefore a quadratic equation that is different in the forward and reverse directions. Secondly the section of a holographic transfer function used for sensor demodulation demonstrates a third order non-linearity as discussed in section 4.6. It is important however to correlate the output of the scheme to the input, a linearly applied voltage to the PZT. Both the hysteresis and the transfer function are therefore mathematically represented and multiplied together to provide a mapping between output and input. The processed results are then correlated to the linearly applied voltage. There exists a high level of correlation between the normalised voltage applied to the PZT and the processed normalised sensor signals implying that the demodulation scheme can be accurately mathematically represented. This is shown in Section 4.7 and 4.9. A demodulation scheme can therefore accurately represent an applied measurand.

Demodulation of a two element FBG strain sensor array by a two element holographic array has been demonstrated. The first scheme reported used holograms inscribed 7.5nm apart each demonstrating a FWHM bandwidth of approximately 4.5nm. The crosstalk measured between channels was -11.6dB. A scheme using the illumining spectrum in a more efficient manner is also detailed in Section 4.9. This possessed holographic inscription wavelengths that were 3.9nm apart. This separation is similar to the difference in the FBG quiescent wavelengths that were 4.1nm apart. Both FBG sensors were demodulated on the negative slope of the matching holographic transfer functions, the FWHM bandwidths of both being approximately 2.1nm. The holograms demodulated sensor elements with an operating range of approximately 2nm and the crosstalk measured between channels was -8.3dB.

The sensor signals received however after diffraction by a hologram were typically $1x10^{-8}$W as described in Section 4.9 and therefore were susceptible to noise introduced by the APD. This was severally detrimental to the measurand resolution which is limited to approximately ±40με. This compares unfavourably with other schemes and is considerably greater than the industry recognised standard of ±1με. The use of recently developed VH materials such as PVK (Poly-*N*-vinylcarbazole) is recommended as this would increase the value of the sensor signal received so reduce susceptibility to noise and improve measurand resolution. Holograms within this material however are pre-inscribed so cannot be re-used to host holograms with different optical bandwidths.

The strain range is limited by the limits of linearity of the PZT driven stage. If this limitation did not exist the maximum strain that could be applied is dependent on the response of an individual sensor and the width of the demodulating transfer function. Figures of 0-10000με are possible that compares favourably with other schemes.

An intensity referencing technique was realised by demodulation of a single FBG sensor by two holographic transfer functions as detailed in Section 4.11. The respective signals however were processed by a modified version of ratiometric detection to compensate for the third-order non-linearity introduced by the holographic transfer functions as described in Section 4.1. The technique can therefore be used for the intensity referencing of the FBG sensor array demodulation scheme.

Polarisation control was a major factor in the stability of the demodulation scheme. This conclusion can be derived from experience using the experimental setup and considering the number of times reconfiguration was needed before and during tests. In an attempt to improve stability sensor arrays where fabricated in PM fibre as discussed in Section 4.10. The use of PM fibre however introduced an interferometer that under certain conditions competed with the holographic transfer function in the demodulation of sensor signals. The effects where minimised however by reducing the lengths of the fibre in which the illuminating beam from the SLD and reflected sensor signals where to travel. The polarisation of the illuminating beam also was to be aligned with one of PM fibre's Eigen-axes. It is recommended however to improve stability further the complete scheme is realised in PM fibre as shown in figure 5.1.

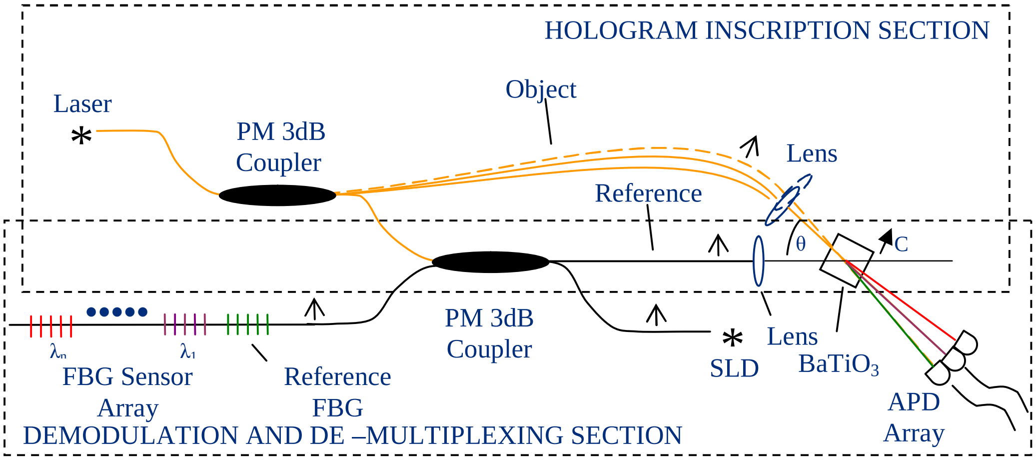

Figure 5.1 A hologram inscription and FBG array demodulation scheme realised totally in PM fibre.

This is similar to the configuration used to derive results presented in Section 4.9. By rotating the fibre the polarisation of the beams inscribing the holograms and the sensor signals can be orientated to be of extraordinary polarisation so ensuring maximum diffraction efficiency. Considering a wavelength span of 4nm is required for the demodulation of a single sensor and an SLD has an optical bandwidth of approximately 40nm the number of elements that can be realistically demodulated is 10. This includes a reference grating used for intensity referencing as shown in figure 5.1.

To improve diffraction efficiency the crystal of $BaTiO_3$ would be replaced with a sample of a modern photorefractive polymer such as PVK (Poly-(*N*-vinylcarbazole)). This allows considerable improvements in sensor signal intensity and therefore the signal to noise ratio. This in turn allows improvements in measurand resolution. Holograms within this material however are pre-inscribed so it cannot be re-used to host holograms with different optical bandwidths. A demodulation scheme incorporating PM fibre and PVK is shown in figure 5.2. This is similar to figure 5.1 however no means of holographic inscription is incorporated.

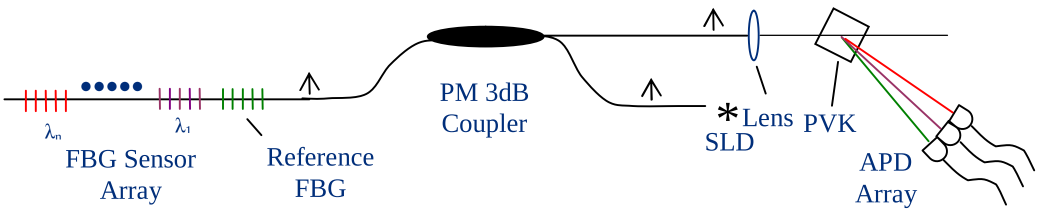

Figure 5.2 An FBG array demodulation scheme realised in PM fibre and using a modern photorefractive polymer to host holograms.

The demodulation scheme described operates within the 800nm wavelength range as discussed in 4.8. This originally existed due to the wavelength characteristics of III-IV semiconductor optoelectronic devices. In the future the wavelength range is set change to the blue section of the visible spectrum due to the advent of Nitride devices. These allow greatly increase storage capability over standard wavelength ranges of 800nm and above. Fibres can host FBG sensors that operate within this range whilst the photorefractive polymer PVK can also absorb blue light. It is recommended therefore that any future scheme shall use components operating within this range.

The use of detector arrays or matrices allows the opportunity to use chirped gratings, discussed in Section 2.2.2. Here the sensor signal would be diffracted by a section of the hologram to a point on a photo-detector array or matrix. As the instantaneous Bragg wavelength changes the signal would be deflected across the matrix. Position information can then be processed to establish wavelength shift. Such schemes have been demonstrated and possess better resolution figures than passive filter based demodulation schemes. The signal is not intensity encoded so there is no need for intensity referencing. Centroid Detection Algorithms (CDAs) can also be used to improve resolution. A photorefractive polymer such as PVK can host multiple chirped gratings to allow the demodulation of an FBG sensor array. The demodulation scheme is shown in figure 5.3.

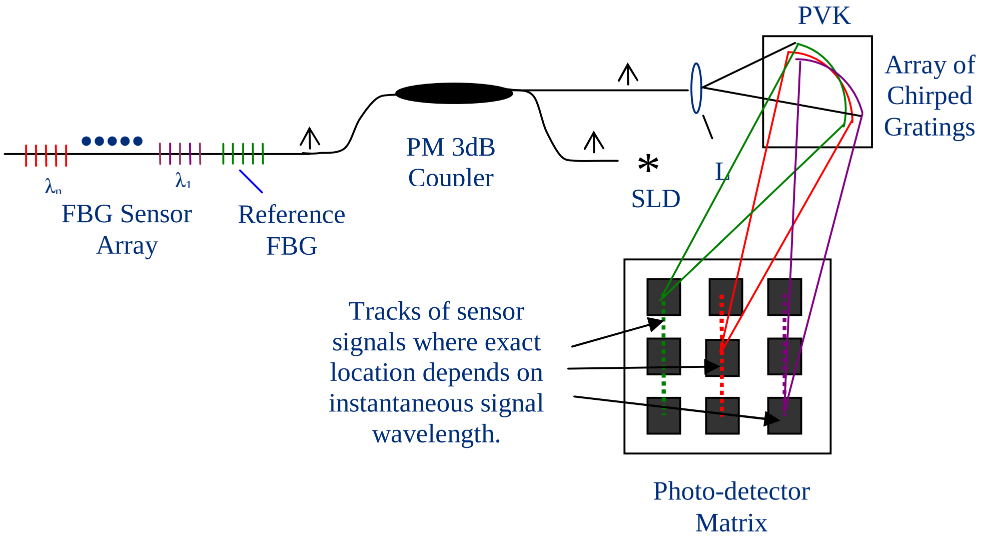

Figure 5.3 An FBG array demodulation scheme realised in PM fibre and using a modern photorefractive polymer to host chirped grating.

The use of MEMS technology is increasing rapidly the scan rates of external cavity lasers as discussed in 2.3.2. Such a laser can be used to demodulate a single sensor or a sensor array as the scan rate of can be up to 20kHz. This implies the use of high speed APDs and Digital Signal Processing (DSP) techniques to determine the instantaneous wavelength of each sensor element.

$(f \otimes g)(x) =$

Summarising the use of holograms for the demodulation of an FBG sensor array has been demonstrated however its potential as a widely used technique is unlikely. Primarily the diffraction efficiency of the holograms implies the demodulated sensor signal is approximately 10^{-8}W degrading the measurand resolution. The SM fibre and VH crystal are sensitive to small fluctuations in temperature and the diffraction efficiency of the hologram is dependent on the polarisation of the sensor signal. Therefore repeated manipulation of polarisation control devices is required that make the demodulation scheme impractical. Measures can be taken to improve polarisation control and hence measurand resolution. This would involve the use of polymer VH material such as PVK and PM fibre to host the FBG sensor array. The use of a chirped grating that allows the deflection of a beam across a CCD array may further improve measurand resolution, whilst removing the need for intensity referencing and reduce costs. The resolution may also be enhanced by the use of Centroid Detection Algorithms. The most likely course of sensor demodulation development however is the enhancement of active schemes. These are widely used at present in commercial systems and can easily be enhanced by incorporating emerging high speed swept laser sources or filters.